

UC Santa Barbara

UC Santa Barbara Electronic Theses and Dissertations

Title

Multiscale Modeling of Mesoscale and Interfacial Phenomena

Permalink

<https://escholarship.org/uc/item/2c938739>

Author

Petsev, Nikolai Dimitrov

Publication Date

2017

Peer reviewed|Thesis/dissertation

UNIVERSITY OF CALIFORNIA

Santa Barbara

Multiscale Modeling of Mesoscale and Interfacial Phenomena

A dissertation submitted in partial satisfaction of the
requirements for the degree Doctor of Philosophy
Chemical Engineering

by

Nikolai Dimitrov Petsev

Committee in charge:

Professor M. Scott Shell, co-chair

Professor L. Gary Leal, co-chair

Professor Matthew E. Helgeson

Professor Frank L H. Brown

March 2017

The dissertation of Nikolai D. Petsev is approved.

Matthew E. Helgeson

Frank L. H. Brown

L. Gary Leal

M. Scott Shell

March 2017

ACKNOWLEDGEMENTS

I am eternally grateful to my parents, who not only started me on a scientific path from an early age and taught me to think skeptically about the world, but also provided me with tremendous support throughout both my undergraduate and graduate studies. In addition, I am thankful to my sister for her encouragement and humor throughout the five years it took me to complete this work.

Furthermore, I consider myself extremely fortunate for the opportunity to work with my PhD advisors, Gary and Scott, whose wonderful mentorship provided me with countless new physical insights about the world, and more generally, a broad perspective on how to think critically, engage with the scientific community, and conduct high-quality work. Gary and Scott each brought a unique perspective to every aspect of my efforts throughout my time at UCSB, and have had a profound effect on my own approach to seemingly intractable challenges, as well as my overall perspective on thinking scientifically.

In addition, I would like to thank the rest of my committee, Matt Helgeson and Frank Brown, whose advice was highly useful in improving this work. I am also indebted to Paul Atzberger for highly useful discussions on many of the subtleties associated with the research described in the following thesis. Additionally, I am grateful to Frank van Swol for his mentorship and conversations throughout the years.

Finally, thank you to members of the Shell and Leal research groups that made my stay in Santa Barbara a positive experience that I will never forget.

NIKOLAI D. PETSEV

316 Mathilda Dr. #7
Goleta, CA 93117
(505) 720 – 8178
npetsev@umail.ucsb.edu

EDUCATION

University of California, Santa Barbara **2011 - Present**
Ph. D. Candidate, Chemical Engineering

University of New Mexico **2006 - 2011**
B.S., Chemical Engineering
Concentration: Materials Processing
Minors: Mathematics, Chemistry
Honors: *magna cum laude*, *summa cum laude* in chemical engineering

RESEARCH EXPERIENCE

Graduate Research Assistant **2012 – Present**
Advisors: M. Scott Shell, L. Gary Leal, University of California, Santa Barbara

- Developed analytical transport model for the stability of interfacial nanobubbles that explains experimental observations in the literature
- Performed numerical simulation of nanobubbles along hydrophobic surfaces using COMSOL package to demonstrate feasibility gas recirculation model for nanobubble stability
- Studied dynamics of gas enrichment at hydrophobic interfaces via molecular dynamics simulation
- Developed new hybrid techniques for multiscale simulation that allow stable bridging between atomistic scales and mesoscale continuum solutions
- Developed novel particle-based techniques for multicomponent mesoscale hydrodynamic problems
- Generalized multiscale smoothed dissipative particle dynamics techniques to multicomponent problems
- Described one of the first approaches for MD-continuum coupling in multicomponent problems
- Developed new integrated boundary framework for colloidal suspensions simulated using particle-based continuum solvers

Chemical and Nuclear Engineering Departmental Honors Program **2010**
Advisor: Frank van Swol, Sandia National Laboratories, University of New Mexico

- Worked on molecular dynamics simulations of ferromagnetic particles subjected to an oscillating uniform magnetic field

Undergraduate Research Assistant **2008 – 2010**
Advisor: Frank van Swol, Sandia National Laboratories, University of New Mexico

- Performed computational/statistical mechanical analysis of anisotropic particle distributions in nanochannels to characterize experimental efforts at the University of New Mexico

SKILLS

Simulation techniques: Molecular dynamics, Brownian dynamics, Monte Carlo, dissipative particle dynamics, smoothed particle hydrodynamics, smoothed dissipative particle dynamics

Programming languages: FORTRAN, Python, MATLAB, Mathematica

HONORS AND AWARDS

- Dow Discovery Fellowship 2013 – 2016
- Member of Tau Beta Pi Engineering Honor Society 2010 – present
- UNM Scholars Scholarship 2006 – 2010
- School of Engineering Dean’s List Award 2006 – 2008

TEACHING

- Tutor (ESTEEM program), University of California, Santa Barbara** 2015
Transport processes (ChE120A)
- Teaching Assistant, University of California, Santa Barbara** 2014
Transport processes (ChE120A)
- Teaching Assistant, University of California, Santa Barbara** 2012
Transport processes (ChE120A)
- Tutor, University of New Mexico** 2011
Physics/math/chemistry tutor, Center for Academic Program Support (CAPS)
- Private Tutor (Physics)** 2011
- Private Tutor (French)** 2003 – 2006

ACTIVITIES

- Co-chair, 2015 Amgen-Clorox Graduate Student Symposium 2015
- Co-organizer for UCSB Graduate Simulation Seminar Series 2015
- UCSB MRL “It’s a Material World!” outreach 2012
- University of New Mexico AIChE chapter officer 2009 – 2010
- Co-organizer for 2010 AIChE regional conference 2010
- MCTP summer math workshop participant 2009

CONFERENCES

1. N. D. Petsev, L. G. Leal, M. S. Shell. “*Hybrid Molecular-Continuum and Multicomponent Simulations Using Smoothed Dissipative Particle Dynamics*”. UCSB Graduate Student Symposium 2014 (poster).
2. N. D. Petsev, L. G. Leal, M. S. Shell. “*Hybrid Molecular-Continuum and Multicomponent Simulations Using Smoothed Dissipative Particle Dynamics*”. American Institute of Chemical Engineers (AIChE) National Conference 2014 (oral).
3. N. D. Petsev, L. G. Leal, M. S. Shell. “*Multiscale from Molecular to Continuum: A Hybrid Simulation Method for Multicomponent Systems*”. Dow Discovery Lecture, UCSB Graduate Student Symposium 2015 (oral).
4. N. D. Petsev, L. G. Leal, M. S. Shell. “*Multiscale from Molecular to Continuum: A Hybrid Simulation Method for Multicomponent Systems*”. American Institute of Chemical Engineers (AIChE) National Conference 2015 (oral).

PUBLICATIONS

1. N. D. Petsev, M. S. Shell, and L. G. Leal. “*Dynamic equilibrium explanation for nanobubbles’ unusual temperature and saturation dependence*”. Phys. Rev. E **88**, 010402 (2013).
2. N. D. Petsev, L. G. Leal, and M. S. Shell. “*Hybrid molecular-continuum simulations using smoothed dissipative particle dynamics*”. J. Chem. Phys. **142**, 044101 (2015).
3. N. D. Petsev, L. G. Leal, and M. S. Shell. “*Multiscale simulation of ideal mixtures using smoothed dissipative particle dynamics*”. J. Chem. Phys. **144**, 084115 (2016).

4. N. D. Petsev, L. G. Leal, and M. S. Shell. “*Coupling discrete and continuum concentration particle models for multiscale simulation*”. In preparation.
5. N. D. Petsev, M. S. Shell, and L. G. Leal. “*An integrated boundary approach for colloidal suspensions simulated using smoothed dissipative particle dynamics*”. In preparation

ABSTRACT

Multiscale Modeling of Mesoscale and Interfacial Phenomena

by

Nikolai Dimitrov Petsev

With rapidly emerging technologies that feature interfaces modified at the nanoscale, traditional macroscopic models are pushed to their limits to explain phenomena where molecular processes can play a key role. Often, such problems appear to defy explanation when treated with coarse-grained continuum models alone, yet remain prohibitively expensive from a molecular simulation perspective. A prominent example is surface nanobubbles: nanoscopic gaseous domains typically found on hydrophobic surfaces that have puzzled researchers for over two decades due to their unusually long lifetimes. We show how an entirely macroscopic, non-equilibrium model explains many of their anomalous properties, including their stability and abnormally small gas-side contact angles. From this purely transport perspective, we investigate how factors such as temperature and saturation affect nanobubbles, providing numerous experimentally testable predictions. However, recent work also emphasizes the relevance of molecular-scale phenomena that cannot be described in terms of bulk phases or pristine interfaces. This is true for nanobubbles as well, whose nanoscale heights may require molecular detail to capture the relevant physics, in particular near the bubble three-phase contact line.

Therefore, there is a clear need for general ways to link molecular granularity and behavior with large-scale continuum models in the treatment of many interfacial problems. In light of this, we have developed a general set of simulation strategies that couple mesoscale particle-based continuum models to molecular regions simulated through conventional molecular dynamics (MD). In addition, we derived a transport model for binary mixtures that opens the possibility for a wide range of applications in biological and drug delivery problems, and is readily reconciled with our hybrid MD-continuum techniques. Approaches that couple multiple length scales for fluid mixtures are largely absent in the literature, and we provide a novel and general framework for multiscale modeling of systems featuring one or more dissolved species. This makes it possible to retain molecular detail for parts of the problem that require it while using a simple, continuum description for parts where high detail is unnecessary, reducing the number of degrees of freedom (i.e. number of particles) dramatically. This opens the possibility for modeling ion transport in biological processes and biomolecule assembly in ionic solution, as well as electrokinetic phenomena at interfaces such as corrosion. The number of particles in the system is further reduced through an integrated boundary approach, which we apply to colloidal suspensions. In this thesis, we describe this general framework for multiscale modeling single- and multicomponent systems, provide several simple equilibrium and non-equilibrium case studies, and discuss future applications.

Table of Contents

Acknowledgements.....	iii
Curriculum Vitae	iv
Abstract.....	vii
Table of Contents	ix
List of Figures	xiii
List of Tables.....	xvii
List of Abbreviations	xviii
List of Symbols.....	xix
1 Introduction.....	1
2 Dynamic Equilibrium Explanation for Nanobubbles' Unusual Temperature and Saturation Dependence.....	6
2.1 Background.....	7
2.2 Diffusive Model for Dynamic Equilibrium Hypothesis.....	10
2.3 Dynamic Equilibrium Model.....	16
2.3.1 Dynamic Equilibrium Outflux.....	17
2.3.2 Dynamic Equilibrium Influx	21
2.3.3 Dynamic Equilibrium Model Predictions for Nanobubbles' Temperature and Saturation Dependence	23
2.4 Appendix.....	32
2.4.1 Model Dependence on the Parameters A and δ	32
2.4.2 Sensitivity Analysis	33
2.4.3 Sensitivity to Parameter A Without Contact Angle Constraint	34

2.5	References.....	35
3	Hybrid Molecular-Continuum Simulations Using Smoothed Dissipative Particle Dynamics.....	39
3.1	Introduction.....	40
3.2	Smoothed Dissipative Particle Dynamics.....	46
3.3	Boundary Conditions.....	50
3.4	Adaptive Resolution Scheme for Coupling MD to SDPD.....	54
3.5	Pairwise Thermodynamic Force.....	58
3.6	Test of MD-SDPD Coupling at Equilibrium.....	63
3.7	Non-Equilibrium Cases Involving the Start Up of Shear Flow.....	69
3.8	Triple-Scale Simulation of Shear Flow.....	73
3.9	Conclusions.....	75
3.10	Appendix.....	79
3.10.1	Equilibrium Multiscale Simulations with and Without Intermediate SDPD Region...	79
3.11	References.....	81
4	Multiscale Simulation of Ideal Mixtures Using Smoothed Dissipative Particle Dynamics.....	85
4.1	Introduction.....	85
4.2	Fluctuating Concentration Model Derivation.....	91
4.3	SDPD Model for Two-Component Ideal Mixture with Flow.....	98
4.4	Equilibrium Properties of Fluid Mixture.....	101
4.5	Multiscale Multicomponent SDPD.....	105
4.6	One-Dimensional Diffusion Across Multiple Length Scales.....	115
4.7	Conclusions.....	117
4.8	Appendix.....	120
4.8.1	Overview of GENERIC Formalism.....	120
4.8.2	Derivation of Concentration Variance for SDPD Particle.....	127

4.8.3 Derivation of SDPD Multicomponent Model Using Chemical Potentials	131
4.9 References.....	136
5 Coupling Discrete and Continuum Concentration Particle Models for Multiscale Simulation	141
5.1 Introduction	141
5.2 Multiscale Modeling Using Smoothed Dissipative Particle Dynamics	147
5.3 Refining Continuous Particles into Particles with Discrete Identities	151
5.4 Coarsening Discrete Particles into Particles with Continuous Concentration Labels.....	156
5.5 Test of Discrete-Continuous SDPD Concentration Coupling at Equilibrium.....	158
5.6 Hybrid MD-Continuum Simulations of an Ideal Mixture at Equilibrium	164
5.7 Non-Equilibrium Multiscale Simulation of a Binary Mixture	171
5.8 Conclusions.....	175
5.9 References.....	179
6 An Integrated Boundary Approach for Colloidal Suspensions Simulated Using Smoothed Dissipative Particle Dynamics	184
6.1 Introduction	184
6.2 Smoothed Particle Methods.....	188
6.3 Approximation of Function near Boundary.....	192
6.3.1 Fluid Particle near Planar Boundary	194
6.3.2 Fluid Particle near Spherical Body.....	198
6.4 Integrated Boundary Approximation for Pressure Term.....	200
6.4.1 Pressure Force near Planar Boundary.....	201
6.4.2 Pressure Force near Spherical Object	202
6.5 Second Derivative Approximation for Viscous Term	203
6.5.1 Fluid Particle near Planar Boundary	204
6.5.2 Particle near Spherical Boundary.....	207

6.6 Integrated Torque Applied to Colloid Due to Surrounding Fluid.....	212
6.7 Colloid Stochastic Force and Torque.....	220
6.8 Equilibrium Simulation of a Colloid Using Integrated Boundaries.....	222
6.9 Conclusions.....	224
6.10 Appendix.....	227
6.10.1 Application of Integrated Boundaries to Mass Transfer in Binary Ideal Mixture	227
6.11 References.....	232
7 Conclusion.....	235
7.1 Implications.....	235
7.2 Future Work	237
7.3 References.....	245

LIST OF FIGURES

Figure 2.1. Schematic for nanobubble dynamic equilibrium mechanism.....	9
Figure 2.2. Combinations of diffusive nanobubble model parameters that give stable bubbles	14
Figure 2.3a. Total flux across bubble surface in dynamic equilibrium model versus bubble radius.....	23
Figure 2.3b. Predicted stable bubble radius versus temperature.....	23
Figure 2.4. Stable radius versus saturation for several temperatures.....	26
Figure 2.5. Total flux across bubble surface versus both radius and contact angle.....	28
Figure A2.1. Influence of dynamic equilibrium model parameters on temperature range where bubbles exist	32
Figure A2.2. Effect of hydrophobic strength parameter on allowed combinations of bubble radii and contact angles.....	34
Figure 3.1. Illustration of boundary particle approach for no-slip boundary condition in SDPD simulations	51
Figure 3.2. Switching function for adaptive resolution approach versus position.....	55
Figure 3.3. Force versus particle separation for pairs located at different locations within the simulation box	59
Figure 3.4a. Average temperature profile versus position from equilibrium MD- continuum simulation	66
Figure 3.4b. Equilibrium density profiles from MD-continuum simulations featuring different thermodynamic force corrections.....	66

Figure 3.5a. Snapshot of multiscale simulation for shear flow case with shear forces perpendicular to MD-continuum interface	71
Figure 3.5b. Snapshot for the non-equilibrium case with shear forces parallel to interface between atomistic and continuum regions.....	71
Figure 3.5c. Velocity profiles at different times for the perpendicular flow case	71
Figure 3.5d. Velocity profiles at different times for the parallel flow case	71
Figure 3.6a. Snapshot of triple-scale hybrid simulation	74
Figure 3.6b. Velocity profiles at different times from triple-scale simulation of shear flow	74
Figure A3.1a. Density profile of multiscale simulation of fluid between two boundaries including atomically-scaled SDPD region	79
Figure A3.1b. Density profile of multiscale simulation of fluid between two boundaries without the atomically-scaled SDPD region.....	79
Figure 4.1. Distribution of concentrations from multicomponent SDPD simulations featuring different degrees of coarse-graining compared to analytical result	104
Figure 4.2. Depiction of multiscale simulation interface between fine and coarse SDPD regions.....	107
Figure 4.3a. Equilibrium density versus position from multiscale SDPD simulations of compressible fluid subjected to gravitational field	110
Figure 4.3b. Smoothing length as a function of position for multiscale SDPD simulation of fluid under influence of gravity	110
Figure 4.4a. Visualization of equilibrium multiscale SDPD simulation	113
Figure 4.4b. Smoothing function versus position for equilibrium multiscale SDPD simulation	113

Figure 4.5a. Equilibrium concentration profiles from multiscale SDPD simulations at different average concentrations.....	114
Figure 4.5b. Probability distributions for concentration in fine and coarse regions from multiscale SDPD simulations compared to analytical result.....	114
Figure 4.6. Concentration profile at different times from multiscale simulation of 1D diffusion compared to analytical result	116
Figure 5.1. Illustration of coupling between “discrete” SDPD fluid and a “continuous” description.....	152
Figure 5.2. Depiction of the three possible scenarios when a continuous SDPD particle splits into two discrete ones	153
Figure 5.3. Equilibrium concentration profiles from coupled discrete-continuous SDPD simulations.....	162
Figure 5.4. Illustration of MD-continuum coupling for binary fluid.....	165
Figure 5.5a. Snapshot of system setup for MD-continuum simulation of mixture.....	170
Figure 5.5b. Concentration profiles from equilibrium MD-continuum simulations of ideal mixture	170
Figure 5.6. Concentration profile at different times for quasi-1D diffusion MD- continuum simulations.....	173
Figure 6.1. Depiction of particle vs. continuum perspective to obtaining SDPD integrated boundary terms.....	194
Figure 6.2. Diagram showing integration variables for determining integrated boundary terms for planar surfaces	196
Figure 6.3. Illustration of integration variables for finding integrated boundary contributions for spherical objects	199

Figure 6.4. Total force acting on spherical particle in uniform flow versus radius computed using integrated boundaries.....	209
Figure 6.5. Depiction of variables in determining torque on colloidal sphere due to single fluid particle.....	213
Figure 6.6. Torque exerted on non-rotating sphere in shear flow versus radius determined using integrated boundary approach.....	218
Figure 6.7a. Probability distribution for linear velocities from integrated boundary simulation of Brownian particle.....	224
Figure 6.7b. Probability distribution for angular velocities for diffusing colloid from integrated boundary simulation.....	224
Figure A6.1. Distribution of concentrations for single fluid particle undergoing dissipative and stochastic exchange of solute with planar boundary.....	230

LIST OF TABLES

Table A2.1. Sensitivity analysis of gas recirculation model with respect to free model parameters	33
Table 6.1. Summary of forces acting on sphere in uniform flow for various sphere radii computed using integrated boundaries.....	211
Table 6.2. Torques exerted on spherical particle in linear shear flow for several sphere radii determined using integrated boundary approach	219

LIST OF ABBREVIATIONS

MD	Molecular dynamics	41
AdResS	Adaptive resolution scheme	42
SDPD	Smoothed dissipative particle dynamics.....	43
SPH	Smoothed particle hydrodynamics.....	43
GENERIC	General equation for non-equilibrium reversible-irreversible coupling	47
LJ	Lennard-Jones	56
DPD	Dissipative particle dynamics	88
SDE	Stochastic differential equation	92
FD	Fluctuation-dissipation.....	94

LIST OF SYMBOLS

$U(z)$	Hydrophobic potential	10
A	Hydrophobic interaction strength.....	10
B	Hydrophobic interaction inverse decay length	10
k_B	Boltzmann's constant	11
T	Temperature.....	11
$C(R)$	Gas concentration at bubble surface (liquid side).....	11
R	Surface nanobubble footprint radius.....	12
θ_c	Surface nanobubble gas-side contact angle.....	12
P_0	Ambient pressure.....	12
γ	Surface tension of liquid-gas interface.....	12
k_H	Henry's law constant	12
C_∞	Gas concentration infinitely far away	18
J_{out}	Total gas outflux from surface nanobubble.....	20
D	Diffusion constant of solute in liquid.....	20
δ	Length scale for onset of microscopic correction to contact angle.....	21
J_{in}	Total gas influx into surface nanobubble	21

ρ	Mass density.....	46
\mathbf{v}	Velocity.....	46
p	Pressure	46
η	Shear viscosity.....	46
ζ	Bulk viscosity.....	46
W_{ij}	Smoothing function	47
N	Total number of particles in the system.....	47
$d\mathbf{W}_{ij}$	Tensorial generalization of stochastic Wiener process	47
h	Smoothing length	49
κ	Factor for truncating smoothing function.....	49
β	Scaling factor for enforcing no-slip using Morris boundary conditions.....	52
λ	Factor used to interpolate between MD and SDPD interactions	55
ε_{ij}	Energy for the MD interaction between particles i and j	57
σ_{ij}	Length scale for interaction between particles i and j	57
r_c	Cut-off radius for molecular interaction	57
κ_T	Isothermal compressibility	60
ρ_0	Target density.....	60
c_s	Speed of sound.....	64

Φ_i	Concentration of the i th particle.....	91
S_i	Entropy of the i th particle.....	93
L	Antisymmetric operator for reversible dynamics.....	93
M	Dissipative matrix.....	93
m_0	Mass of individual solute or solvent atom.....	93
dV_{ij}	Scalar increment of the stochastic Wiener process.....	93
Δt	Simulation time-step magnitude.....	94
Ω	Support domain of point \mathbf{r}	189
Δz	Distance of point from planar boundary.....	194
ν_w	Wall particle number density.....	195
R_c	Colloid radius.....	199
F_{ij}	Scalar function related to W_{ij} derivative, $\nabla_i W_{ij} = -\mathbf{r}_{ij} F_{ij}$	201
\mathbf{n}	Vector normal to boundary.....	201
$\boldsymbol{\omega}$	Colloid angular velocity.....	208
\mathbf{V}_c	Colloid center of mass linear velocity.....	208
M_c	Colloid mass.....	209
$\boldsymbol{\tau}_c$	Torque acting on colloidal particle.....	217

1 Introduction

Due to the advent of technologies at the nanoscale, researchers are faced with numerous problems in molecular and interfacial physics that involve processes spanning many different length scales. These advancements are central to a wide range of applications, yet pose significant challenges in applying traditional modeling techniques. One such problem is surface nanobubbles, which are nanoscopic gaseous domains typically found on hydrophobic surfaces. These bubbles have heights and widths on the order of ~ 10 nm and ~ 100 nm, respectively, and feature a number of surprising properties. First, nanobubbles have high internal Laplace pressures due to their small radii of curvature, which is expected to drive dissolution on microsecond time scales. However, nanobubbles have been observed to stably exist for days. Second, nanobubbles exhibit small gas-side contact angles that appear substrate-independent, and hence violate Young's law. In the second chapter of this thesis, we present a simple non-equilibrium model for the stability of nanobubbles that assumes that the outflux of gas due to their internal pressure is balanced by an influx of gas near the three-phase contact line, driven by the hydrophobic attraction of the gas molecules to the substrate. Next, we demonstrate that this recirculating gas mechanism accounts for the stability and small contact angles of nanobubbles, as well as experimental data showing that nanobubbles nucleate in a narrow range of temperature and gas saturation, and appear larger at lower temperatures.

Ultimately, understanding the stability of nanobubbles and their properties requires fully detailed molecular simulations in order to capture the necessary physics near the substrate and three-phase contact line, where continuum models break down due to the

extremely small bubble heights. This is challenging since the problem of nanobubbles is characterized by multiple length scales, including ones beyond what is traditionally accessible using molecular dynamics (MD). In light of this general difficulty in modeling phenomena at interfaces, we have developed a multiscale simulation strategy using a stochastic particle-based technique called “smoothed dissipative particle dynamics” (SDPD). SDPD is a thermodynamically-consistent formulation of continuum solvers such as smoothed particle hydrodynamics that features scale-dependent thermal fluctuations, making it ideal for selectively coarse-graining regions that require less detail. Using our multiscale approach, it is possible to couple a MD region to a hierarchy of SDPD domains, where each one is characterized by a different length scale. This allows for simulations that simultaneously include regions spanning from the atomistic to the non-fluctuating continuum limit. Using simple case studies, we demonstrate that this technique is applicable to both equilibrium and non-equilibrium situations in Chapter 3.

Extending these types of multiscale techniques to multicomponent systems such as nanobubbles, drug particle margination, corrosion, and many others, remains a major challenge, and in the final part of this thesis, we describe a novel generalization of our multiscale methods to systems that involve one or more dissolved species. In Chapter 4, we develop a new multicomponent formulation of SDPD through a particle discretization of the diffusion equation. This approach is thermodynamically-consistent, featuring thermal noise in the concentration field in accordance with the fluctuation-dissipation theorem. In addition, we extend protocol for coupling two regions containing SDPD fluids with different resolution to miscible fluid mixtures. The interface between these two regions featuring a different degree of coarse-graining is constructed such that mass, momentum, and the amount of solute is conserved. Since domains with different degrees of coarse-graining contain fluid particles with

different masses and number density, it is necessary to perform splitting of large particles into smaller ones, and combining of small particles into large ones over the course of a simulation. We describe the combining splitting rules for multicomponent systems, which makes it possible to simulate binary mixtures for both equilibrium and non-equilibrium problems across a wide spectrum of length scales beyond what is accessible to MD, even all the way to the continuum limit where fluctuations vanish. Finally, we consider several simple case studies and demonstrate that these approaches reproduce correct thermodynamic properties at equilibrium, and proper diffusion dynamics in non-equilibrium problems involving chemical potential gradients.

The MD-continuum method described in Chapter 3 can be generalized to multicomponent systems thanks to the fluid mixture extension of SDPD described in Chapter 4. Hence, the hybrid molecular-continuum approach in Chapter 3 and multicomponent continuum solver in Chapter 4 are unified in Chapter 5, which provides a general framework for coupled MD-continuum simulations of miscible fluid mixtures. The most challenging aspect of reconciling the molecular world with a coarse continuum description is the fact that at the molecular level, matter is composed of distinct units (molecules and atoms), which have discrete identities for the case of fluid mixtures (e.g. a particle is either solute or solvent). Meanwhile, in the continuum description, a fluid particle is interpreted as a volume of fluid or cluster of molecules/atoms, and hence has a concentration associated with it that can assume a continuum of values between 0 and 1. The heart of the problem is how to interface these fundamentally different descriptions for the concentration. Therefore, in Chapter 5 we discuss the protocol for splitting large, coarse continuum particles into fine ones having discrete identities of either solute or solvent, and vice versa. As a simple case study, we consider ideal mixtures and perform MD-continuum simulations for both equilibrium and non-equilibrium

cases, demonstrating that this approach reproduces correct solute properties at equilibrium and captures the solute transport process when gradients in concentration are present.

In addition to multiscale simulation techniques, which reduce the number of particles in the system through coarse-graining, we have developed other tools that significantly lower the computational expense of large-scale multiscale/coarse-grained simulations. This includes a new set of techniques for enforcing boundary conditions in simulations using smoothed particle techniques such as SDPD, as well as more traditional particle-based continuum solvers including smoothed particle hydrodynamics (SPH). Applying boundary conditions (e.g. no-slip) at solid boundaries is challenging with particle-based continuum methods, typically requiring the use of “ghost” boundary particles (which increases the number of pair interactions one must compute). With the integrated boundary method detailed in Chapter 6, the contribution to the dynamics of a single fluid particle due to the wall is integrated out and treated as a single quantity, analogous to the Lennard-Jones 9-3 potential commonly used in MD simulations, in the place of explicit walls. The integral associated with the wall is computed analytically for simple solid geometries (spheres and planar surfaces). Finally, we generalize these integrated boundary methods for problems at the mesoscale, where a boundary may exchange solute or momentum with the surrounding fluid both due to concentration/velocity gradients as well as hydrodynamic fluctuations. In particular, we derive the appropriate integrated boundary expressions for spherical particles, opening the possibility for efficiently simulating colloidal suspensions using SDPD. Combining this boundary approach with our multiscale techniques affords additional computational savings, which makes it possible to consider larger and more complex systems than using traditional simulation techniques. Throughout Chapters 3-6, and in the conclusion in Chapter 7, we

discuss the numerous potential future applications of the modeling framework outlined in this thesis.

2 Dynamic Equilibrium Explanation for Nanobubbles' Unusual Temperature and Saturation Dependence

Surface nanobubbles are nanoscopic gaseous domains that form along hydrophobic substrates when immersed in water. They have been observed to persist for days, in stark contrast to classical predictions that suggest microsecond dissolution times. The so-called “dynamic equilibrium” model suggests that nanobubbles can be stable due to an influx of gas in the vicinity of the bubble contact line, driven by substrate hydrophobicity, that balances the outflux of gas from the bubble apex due to high capillary pressure. We use a variety of thermodynamic, transport, and numerical arguments to critically assess the dynamic equilibrium mechanism and, more generally, understand the determinants of nanobubble stability according to this non-equilibrium picture. First, using the COMSOL software package, we consider a simple diffusive model and explore the general feasibility of this recirculating gas hypothesis by investigating the strength required for the hydrophobic attraction of the gas molecules to the substrate. Following this analysis, we develop a simple, analytical transport model for the dynamic equilibrium mechanism that predicts rich behavior in agreement with experimental measurements. Namely, we find that stable nanobubbles exist in narrow temperature and dissolved gas concentration ranges, that there is a maximum and minimum possible bubble size, and that nanobubble radii decrease with temperature.

2.1 Background

Interfacial nanobubbles form on solid hydrophobic substrates when immersed in water with dissolved gas (e.g. nitrogen, oxygen, argon, etc.), and are spherical-cap-shaped gaseous domains with heights of ~ 20 nm and widths of ~ 100 nm [1–18]. Due to the small radius of curvature, a typical nanobubble has extremely high internal capillary pressure (~ 2 – 10 atm), which provides a substantial driving force for dissolution. Simple diffusion arguments therefore suggest microsecond dissolution times, yet nanobubbles have been observed to persist for days [16]. In addition to this mysterious stability, they exhibit a wealth of other anomalous properties that are not successfully addressed by classical theory, such as a universal contact angle (~ 10 – 30° , gas-side) that appears to be influenced by the gas type [19] and is independent of the substrate chemistry, as well as temperature/saturation-dependent contact angles and radii [12,20–22]. Finally, nanobubbles are observed to form in a very narrow range of temperatures and dissolved gas concentrations [21]. These unusual features represent a fundamental problem in nanoscale interfacial phenomena, even though nanobubbles have already become important in technological applications such as increasing slip along surfaces [23–26], removing biological fouling [27], templating at the nanoscale [28,29], and in a host of other technologies [30,31].

Why are nanobubbles stable? One possibility is surfactant-like impurities aggregating along the liquid-gas interface, which lowers the surface tension and internal capillary pressure that drives dissolution [32]. Furthermore, a coating of contaminants may also pose a kinetic barrier to gas molecules dissolving out of the bubble and diffusing into the fluid [32], although thermal fluctuations would reduce this effect [31]. However, Das et al. have demonstrated that the reduction in the Laplace pressure due to impurities is not substantial

enough to yield stable bubbles, corroborating experimental work that demonstrates contamination alone is an insufficient explanation [31,33–35]. Another possibility is a more recent transport-based idea that suggests nanobubble lifetimes are due to slow gas diffusion (a ‘traffic jam’ effect) across the liquid film above [36]. In this model, gas can only escape the bubble vertically away from the apex since it is assumed that high surface coverage of nanobubbles prevents gas flux in the radial direction. Furthermore, gas can only leave the system by escaping into the atmosphere after diffusing over the full length of the macroscopic liquid film over the bubble. The traffic jam model reproduces the observed nanobubble lifetimes (~40 hours for typical system parameters), although it is yet unclear whether this provides the full picture, since convective currents would dramatically expedite mass transfer in real experiments. Also, this model requires high surface coverage of nanobubbles, which is often but not always observed. Other recent work suggests nanobubbles may exist in a thermodynamically metastable state due to contact line pinning [37–39], although bubbles have been observed to adjust their lateral size [22] and may be moved along the substrate using the tip of an atomic force microscopy apparatus [7,40].

In this chapter, we consider a very different explanation for nanobubble stability: the dynamic equilibrium model [41] (Fig. 2.1, next page), which suggests that the outflux of gas from the top of the bubble is recirculated and re-absorbed near the three-phase contact line due to the attraction and enrichment of dissolved gas at the hydrophobic substrate. If the outflux from the bubble apex and the influx near the contact line are nearly in balance, the bubbles can persist for much longer than predicted by simple diffusion arguments. It was later suggested that the recirculation currents are induced by shear stresses imposed on the liquid-gas interface due to Knudsen diffusion of the gas inside the bubble and the bubble’s

small height [42]. While the ultimate driving force for recirculation is unknown at present (i.e. there must exist an energy source to prevent violation of the second law), one reasonable possibility is subtle temperature gradients due to evaporation [31].

In this chapter, we first assess the feasibility of the dynamic equilibrium picture through a simple diffusive model. We do not attempt to explain the driving force for recirculation; instead, we assume that it exists, and examine the implications of the dynamic equilibrium hypothesis. Specifically, in Section 2.2 we investigate the strength of the hydrophobic attraction necessary to yield a sufficient influx of gas into a nanobubble such that the outflux of gas due to the internal pressure is balanced, giving zero net flux of gas across the bubble surface. This analysis overestimates the strength of the hydrophobic attraction, but gives an order-of-magnitude value suggesting that the gas recirculation model is feasible. In Section 2.3, we develop an analytical transport-based model for the

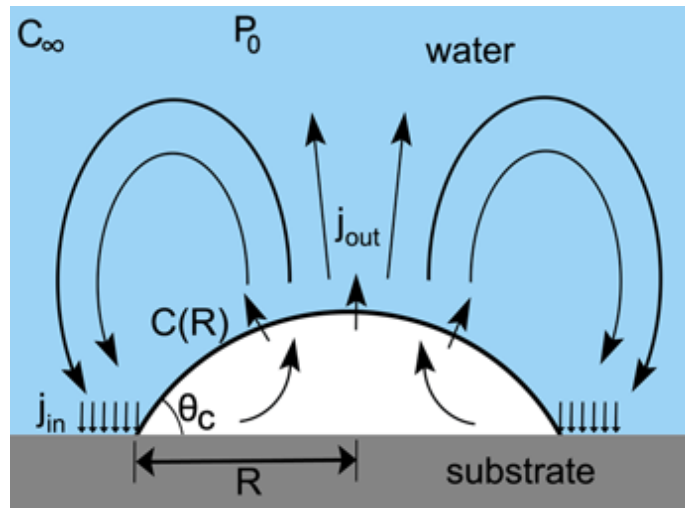


Fig. 2.1. Schematic of the dynamic equilibrium mechanism for nanobubble stability. Here, there is an outflux of gas (j_{out}) near the bubble apex due to the high capillary pressure. This outflux is balanced by an influx of gas (j_{in}) near the bubble three-phase contact line due to the hydrophobic interaction between the dissolved gas and substrate.

temperature and saturation dependence of nanobubbles and discuss its predictions in the context of recent experimental data. Ultimately, full molecular simulations are necessary for a comprehensive understanding of nanobubble stability across all length scales (including molecular ones), although this is challenging due to the large scales involved for parts of the dynamic equilibrium mechanism (e.g. the recirculation currents, which presumably extend over microns). Therefore, we also seek to develop new methodology for hybrid simulations that will enable detailed simulation of nanobubbles, as well as other multiscale phenomena. To this end, we describe a number of novel hybrid simulation strategies in Chapters 3, 4, and 5 that collectively provide a general approach for investigating both single- and multicomponent multiscale systems.

2.2 Diffusive Model for Dynamic Equilibrium Hypothesis

The dynamic equilibrium hypothesis posits that gas lost from the apex of a surface nanobubble is balanced by an influx of gas near the three-phase contact line due to surface hydrophobicity (Fig 2.1). We investigate the feasibility of this mechanism for nanobubble stability from a purely diffusive, continuum perspective. First, we consider the case of a hydrophobic boundary immersed in a liquid that contains a dissolved gas, without any bubbles present in the system. Assuming a simple, experimentally-motivated hydrophobic potential of the form [43]

$$U(z) = -Ae^{-Bz}, \quad (2.1)$$

we can obtain an analytical expression for the equilibrium dissolved gas distribution $C(z)$ (unperturbed due to the presence of a bubble) near the surface from the time-independent equation for diffusion in a field,

$$D\nabla C = -C\nabla U / \zeta. \quad (2.2)$$

Here, ζ is the solute mobility, and D is the diffusion constant of the gas molecules in the liquid. Solving Eq.(2.2) for the simple one-dimensional case with the potential in Eq.(2.1) gives

$$C(z) = C_\infty \exp\left[-\frac{U(z)}{k_B T}\right]. \quad (2.3)$$

Hence, there is an enhancement of the concentration immediately next to the substrate due to the potential given by $C(z=0) = C_\infty \exp(A/k_B T)$. Here, C_∞ is the concentration infinitely far away and k_B is Boltzmann's constant; the concentration at the interface is thus augmented from the bulk value by the field through an exponential factor that depends on the strength of the attraction A , and the system temperature T . Clearly, increasing the factor A results in greater enhancement of the gas concentration near the surface. Similarly, increasing the system temperature acts to decrease the enhancement by giving gas molecules additional thermal energy, which allows them to more readily overcome the attractive influence of the potential $U(z)$. This increase in the gas concentration near the boundary due to its hydrophobicity is known as a gas-enrichment layer [14,44], and is believed to be closely linked to the phenomenon of nanobubbles.

Next, we place a single nanobubble on top of a hydrophobic boundary that features a gas-enrichment layer described by Eq.(2.3). The concentration of dissolved gas in the liquid at the air-water bubble interface (on the liquid-side) $C(R)$ depends on the internal bubble

pressure, and is therefore specified through a combination of Henry's law and the Young-Laplace equation,

$$C(R) = k_H \left(\frac{2\gamma \sin \theta_c}{R} + P_0 \right), \quad (2.4)$$

where θ_c is the bubble contact angle, γ gives the surface tension, k_H is the Henry's law constant, P_0 is the ambient pressure, and R is the bubble footprint radius. By requiring that the concentration at the solid-liquid interface due to gas enrichment is greater than the concentration at the bubble surface in order to drive an influx of gas, $C(z=0) > C(R)$, we obtain an order-of-magnitude estimate for the minimum possible value of the hydrophobic interaction strength,

$$A > k_B T \ln \left(\frac{2\gamma \sin \theta_c}{P_0 R} + 1 \right). \quad (2.5)$$

Using realistic values for the parameters in this expression, we find that for a typical nanobubble with $R = 50$ nm and $\theta_c = 25^\circ$ under normal conditions ($T_0 = 30$ °C, $P_0 = 1$ atm), $A > 1.8$ kcal/mol. Note that this estimate is greater than the actual value required, since we assumed that the influx is driven indirectly by the hydrophobic interaction through a concentration gradient. In principle, this influx occurs purely by the attraction of the gas molecules to the substrate, which is due to a combination of the hydrophobic attraction, as well as van der Waals interactions (ignored altogether in this analysis) that become important over small length scales.

This approximate analysis can be made more precise by explicitly placing a nanobubble on top of a surface featuring a gas-enrichment layer and hydrophobic potential, and numerically calculating the full concentration field, holding the concentration at the bubble surface and substrate constant. Once the steady-state distribution of concentration

across the system is determined, it is possible to evaluate the flux of gas along the bubble surface due to concentration gradients. In order to obtain the value of A necessary for *balanced* flux (i.e. zero net flux across the bubble surface) in this simple diffusive picture, we develop a 2D transport model involving a full solution to the equation for diffusion in a field using the COMSOL package. In this approach, an attractive potential [an approximation for the hydrophobic attraction, Eq.(2.1)] acts on the gas solute molecules in the liquid. If a bubble with fixed concentration at its surface is placed on top of such a hydrophobic substrate, it is possible to drive an influx of gas into the bubble near the contact line if the concentration increase at the surface due to the external field is sufficiently high. Here, there are two free parameters: (1) the ratio of the concentration at the hydrophobic surface to the concentration at the bubble air-water interface (which is related to the parameter A), $C(z=0)/C(R)$, and (2) the decay length for the exponential potential acting on the solute molecules (non-dimensionalized by the bubble width), $B^{-1}/2R$. Provided that $C(z=0)/C(R) > 1$, there will be an influx of gas into the bubble near the contact line (assuming that a continuum level description is sufficient and that concentration gradients alone are responsible for mass transfer in the system).

By varying the two free parameters in this numerical model, we develop a state-space diagram that indicates parameter combinations giving zero total flux across the bubble surface (Fig. 2.2). The diagram is for a bubble with fixed geometry and a gas-side contact angle of 45° . The insets show the concentration profile in the vicinity of the bubble for two different balanced flux points featuring a different decay length for the hydrophobic potential, with red hues corresponding to regions of high dissolved gas concentration. As expected, the stable points asymptote as $C(z=0)/C(R) \rightarrow 1$, since the concentration

difference, and hence driving force for influx, disappears in this limit. As the concentration difference approaches unity, the decay length necessary for balanced flux increases to compensate. Conversely, if the decay length is shortened, the magnitude of the concentration at the substrate surface $C(z=0)/C(R)$ necessary for stability dramatically increases in order to provide adequate influx over a smaller region of the bubble surface.

From this diagram, we can obtain an estimate for the strength of the hydrophobic attraction necessary for balanced flux. The decay length for the hydrophobic interaction has been empirically determined to be ~ 1 nm [43]. Therefore, for a nanobubble with a radius of 50 nm, we have $B^{-1}/2R = 0.01$. A linear interpolation using the data in Fig. 2.2 suggests that for a bubble of this size, $C(z=0)/C(R) \sim 1.9$ for zero net flux across the bubble surface. The value of A that yields $C(z=0)/C(R) = 1.9$ for a typical nanobubble ($T_0 = 30$ °C, $P_0 = 1$ atm) is 2.4 kcal/mol, slightly above the theoretical minimum of 2.1 kcal/mol given by

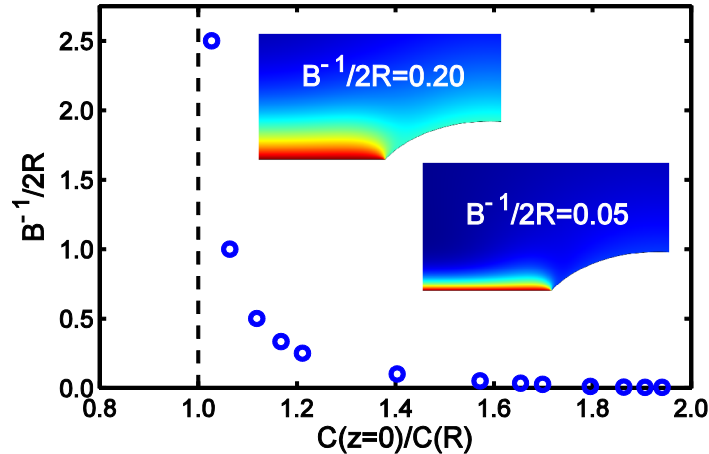


Fig. 2.2. Combinations of allowed parameters for balanced flux in the purely diffusive numerical model. The insets show the concentration profile near the bubble for two of these points, with red corresponding to high gas concentration and blue to low concentration.

Eq.(2.5) for a nanobubble with $\theta_c = 45^\circ$. It is important to note that if a smaller contact angle was used in this analysis, the value of A required for balanced flux would be lower since more bubble surface area would be situated in the high-gas region, giving considerably greater influx across the bubble surface. In addition, decreasing the contact angle while keeping the bubble footprint radius constant leads to a reduction in the bubble internal pressure, and therefore lowers the value of $C(R)$. If $C(R)$ is reduced, this implies that the value of $C(z=0)$ (and therefore A) necessary for influx is decreased as well. Generally, nanobubble contact angles are smaller than the 45° angle used in these simulations, which was selected for numerical reasons.

We can compare this result to values for the strength of the hydrophobic attraction measured from experiment and simulation. Potential of mean force values for two hydrophobes (e.g. methane molecules) associating in water has been found from simulation to be around 0.5 kcal/mol [45]. On the other hand, the energy change per unit area in bringing together two like surfaces (type I) in a medium II equals twice the surface tension of the I-II interface [43]. Thus, we can also approximate the hydrophobic strength parameter as $A \approx 2\gamma_{I-II}a$, where a is the area of contact. The experimental surface tension for a typical hydrocarbon in water is on the order of 50 mJ/m² [43]. Assuming a molecular area of contact of $a \approx 10 \text{ \AA}^2$, we find that $A \approx 0.72 \text{ kcal/mol}$ using the above-formula. The values of A from our diffusive model are approximately three times as large ($A \sim 2.4 \text{ kcal/mol}$), although choosing a smaller contact angle in the calculations would further reduce the required value of A and bring it closer to these estimates. Ultimately, this numerical study demonstrates that given a gas-rich region near the substrate, it is possible to drive an influx of gas into a bubble, even if we neglect molecular effects (though molecular contributions such as disjoining

pressure effects have been recently considered [46], including specifically in the context of the dynamic equilibrium model [47,48]). As discussed previously, this diffusive analysis overestimates the necessary strength of this parameter and only provides an order-of-magnitude assessment. If we assume the hydrophobic potential draws solute molecules across the liquid-gas interface near the contact line, rather than relying on a concentration gradient to drive gas transport, the value required for the parameter A is lower, which we demonstrate in the following sections.

2.3 Dynamic Equilibrium Model

In this section, we develop a new formulation of the dynamic equilibrium mechanism and show that a stability analysis explains many unexpected experimental observations regarding the influence of temperature and gas saturation on nanobubbles. In particular, there is remarkable qualitative agreement with the results of Seddon et al., who reported that nanobubbles nucleate in a narrow temperature range, and that the total volume of nanobubbles decreases with temperature [21]. Moreover, by using a realistic, empirical potential for the hydrophobic attraction, we find that the dynamic equilibrium mechanism does not require unphysical contact angle corrections as in the original model [41]. In Section 2.2, we discussed preliminary numerical calculations in COMSOL for this model, which demonstrate that this hypothesis does not require unrealistic values for the hydrophobic attraction. We now develop a different picture based on the primary diffusive fluxes, neglecting recirculation explicitly, and show that this new formulation of the dynamic equilibrium mechanism explains many unexpected experimental observations regarding the influence of temperature and gas saturation on nanobubbles. Our model treats the influx and

outflux components of the dynamic mechanism independently by assuming that the relevant length scale for the outflux [which is $O(R)$, where R is bubble radius] is much larger than that for the influx (which is on the order of the thickness of the gas-enrichment layer, around a nanometer). Moreover, this approach focuses on the region immediately surrounding the bubble, where mass transfer is diffusion-limited, rather than the full convective recirculation problem. In subsection 2.3.1, we derive an expression for the gas outflux from a flat nanobubble. In 2.3.2, we consider the influx of gas near the contact line, and in 2.3.3, we discuss the predictions of this analytical model in the context of the available experimental literature. Additional details about this model, including a sensitivity analysis to system parameters, are provided in the appendix.

2.3.1 Dynamic Equilibrium Outflux

In this subsection, we derive the outflux of gas from a nanobubble that is approximated as being completely flat (a simplification motivated by the small gas-side contact angles of nanobubbles); readers not interested in the details of this derivation can skip to the following subsections. Assuming there exists a dynamic equilibrium due to a nearly balanced influx and outflux of gas to/from a nanobubble such that the system changes very slowly with time, we can develop an approximate steady-state solution for the outflux by solving the time-independent diffusion equation,

$$\nabla^2 C \approx 0. \tag{2.6}$$

Here, $C(\mathbf{r})$ is the concentration of gas molecules in the liquid. This equation is subject to the boundary conditions

$$\begin{aligned} C(\mathbf{r} = S) &= C(R), \\ C(\mathbf{r} \rightarrow \infty) &= C_\infty. \end{aligned} \tag{2.7}$$

S denotes the bubble surface. In this expression, R is the bubble radius, $C(R)$ is the liquid-side gas concentration at the bubble surface, and C_∞ is its concentration infinitely far away.

We will solve for the case of steady diffusion in all directions from a completely flat bubble in oblate spheroidal coordinates, which are particularly convenient for the problem geometry.

The oblate spheroidal system can be related to Cartesian coordinates via [49]

$$\begin{aligned} x &= a \cosh \eta \sin \theta \cos \psi, \\ y &= a \cosh \eta \sin \theta \sin \psi, \\ z &= a \sinh \eta \cos \theta, \end{aligned} \tag{2.8}$$

where $x = \pm a$ denotes the location of the ellipse foci. The Laplace equation $\nabla^2 C = 0$ in this coordinate system takes the form

$$\begin{aligned} \frac{1}{a^2 (\cosh^2 \eta - \sin^2 \theta)} \left[\frac{\partial^2 C}{\partial \eta^2} + \tanh \eta \frac{\partial C}{\partial \eta} + \frac{\partial^2 C}{\partial \theta^2} + \cot \theta \frac{\partial C}{\partial \theta} \right] \\ + \frac{1}{a^2 \cosh^2 \eta \sin^2 \theta} \frac{\partial^2 C}{\partial \psi^2} = 0. \end{aligned} \tag{2.9}$$

If we assume the problem is axisymmetric, and there is effectively no concentration variation in θ (a consequence of the approximation of two characteristic length scales that can be treated separately), then we can simply write:

$$\frac{d^2 C^*}{d\eta^2} + \tanh \eta \frac{dC^*}{d\eta} \approx 0. \tag{2.10}$$

Here, we have also scaled C such that it vanishes at infinity, $C^* = C - C_\infty$. The boundary conditions are now given by

$$\begin{aligned} C^*(\eta = \varepsilon) &= C(R) - C_\infty, \\ C^*(\eta \rightarrow \infty) &= 0, \end{aligned} \tag{2.11}$$

where $\eta = \varepsilon$ is the surface describing the bubble interface. The height h of the bubble at its apex is given by $h = a \sinh \varepsilon$. A small value for the non-dimensional parameter ε guarantees a flat bubble. We will eventually take the limit as $\varepsilon \rightarrow 0$, which gives the completely flat case.

The general solution to Eq.(2.10) is

$$C^*(\eta) = K_1 \tan^{-1} \left[\tanh \left(\frac{\eta}{2} \right) \right] + K_2. \quad (2.12)$$

Applying the boundary conditions, we find the concentration profile for diffusion from a bubble with arbitrary height described by the surface $\eta = \varepsilon$:

$$C(\eta) = \frac{1 - (4/\pi) \tan^{-1} \left[\tanh(\eta/2) \right]}{1 - (4/\pi) \tan^{-1} \left[\tanh(\varepsilon/2) \right]} \left[C(R) - C_\infty \right] + C_\infty. \quad (2.13)$$

Note that here we have written our solution in terms of the non-rescaled variable C through $C(\eta) = C^*(\eta) + C_\infty$. Allowing ε to go to zero, we recover the concentration profile for gas diffusing from a completely flat bubble:

$$C(\eta) = \frac{4}{\pi} \left[C_\infty - C(R) \right] \tan^{-1} \left[\tanh \left(\frac{\eta}{2} \right) \right] + C(R). \quad (2.14)$$

This concentration profile includes both diffusion in the radial and z -directions.

We now integrate along the bubble surface to obtain the total outflux. The differential element for the integral over the bubble surface (surface of constant η) is given by:

$$dA_{\theta\psi} = a^2 \sqrt{\cosh^2 \eta - \sin^2 \theta} \cosh \eta \sin \theta d\theta d\psi. \quad (2.15)$$

Thus, the outflux of gas from a bubble with arbitrary height is written as

$$\begin{aligned}
J_{out} &= -D \int_S \nabla C \cdot \mathbf{e}_\eta \Big|_{\eta=\varepsilon} dA_{\theta\psi} \\
&= -D \int_S \frac{1}{a \sqrt{\cosh^2 \eta - \sin^2 \theta}} \left(\frac{\partial C}{\partial \eta} \right) \Big|_{\eta=\varepsilon} dA_{\theta\psi}.
\end{aligned} \tag{2.16}$$

Here, D is the diffusion constant for the gas in the liquid. Taking the derivative of the concentration given in Eq.(2.13) and substituting into Eq.(2.16),

$$\begin{aligned}
J_{out} &= \frac{2Da [C(R) - C_\infty] \operatorname{sech}^2(\eta/2) \cosh \eta}{\pi \left\{ 1 - (4/\pi) \tan^{-1} [\tanh(\varepsilon/2)] \right\} [1 + \tanh^2(\eta/2)]} \Big|_{\eta=\varepsilon} \\
&\quad \times \int_0^{2\pi} d\psi \int_0^{\pi/2} d\theta \sin \theta.
\end{aligned} \tag{2.17}$$

Integrating, we find that

$$J_{out} = \frac{4D [C(R) - C_\infty] \sqrt{R^2 - a^2 \sinh^2 \varepsilon}}{1 - (4/\pi) \tan^{-1} [\tanh(\varepsilon/2)]}. \tag{2.18}$$

Here we have used the relationship $a = \sqrt{R^2 - h^2}$ that relates the major and minor axes of an ellipse to its foci. Given the observed small contact angles of nanobubbles [7,12,18,19,40], we approximate the steady-state diffusive gas outflux using a completely flat bubble by taking the limit $\varepsilon \rightarrow 0$, giving the total outflux from a completely flat bubble:

$$J_{out} = 4DR [C(R) - C_\infty]. \tag{2.19}$$

This expression is similar to the result of Bobbert et al. for the problem of diffusion towards a disk-shaped nucleus [50]. Here, C_∞ can be related to the ambient pressure P_0 if the bulk liquid is open to the atmosphere and saturated, with $C_\infty = k_H P_0$, where k_H is a temperature-dependent Henry's law constant. As before, $C(R)$ is specified through the Young-Laplace equation and Henry's law [Eq.(2.4)]. γ gives the surface tension, here described by the Eötvös relation with parameters for an air-water interface. Because

experiments [7,12,18,19,40] suggest the contact angle of small bubbles and drops deviates from the macroscopic value (e.g., due to surface inhomogeneities or line-tension effects [19,51–56]), we introduce an R -dependent θ_c [19,41]:

$$\cos \theta_c = \cos \theta_\infty - \frac{\cos \theta_\infty - \cos \theta_0}{1 + R/\delta}. \quad (2.20)$$

In this expression, θ_∞ is the macroscopic gas-side contact angle, which we take to be 40° . θ_0 is the contact angle as $R \rightarrow 0$, and equals zero. δ sets the length scale for the onset of microscopic corrections, and is a parameter that empirically corrects for the collective contribution of line-tension, surface inhomogeneities/roughness, and other similar effects. Experimental fits to this parameter suggest that it is on the order of a few nanometers, depending on the gas type [19]. An interesting aside is that previous formulations of the dynamic equilibrium model required unrealistically high values of δ (e.g. $\delta = 70$ nm, as in the original Brenner and Lohse model [41]). Because we use a more realistic hydrophobic interaction [Eq.(2.1)], we resolve this issue and find that $\delta = 3.2$ nm yields realistic predictions.

2.3.2 Dynamic Equilibrium Influx

The influx is determined by $J_{in} = -D \int \nabla C \cdot \mathbf{n} dS$, where the integral is over the bubble surface and \mathbf{n} is the surface normal. Gas molecules experience an attractive interaction with the hydrophobic substrate according to a potential $U(z)$; therefore, using Eq.(2.2), we obtain

$$J_{in}(R) = \frac{C(R)}{\zeta} \int \nabla U \cdot \mathbf{n} dS \approx \frac{C(R)}{\zeta} \iint \left[\frac{dU}{dz} \right]_{z=h(r)} \cos \theta_c r dr d\theta, \quad (2.21)$$

where $\zeta = k_b T / D$ is the solute mobility and h is the shape function for the bubble in the vicinity of the contact line, which we approximate as being linear, $h(r) = (R - r) \tan \theta_c$. After substituting the attractive potential [Eq.(2.1)] into Eq.(2.21), the integral over r can be rewritten in terms of h . Eq.(2.21) can be evaluated analytically by assuming that $U(z)$ decays rapidly to yield

$$J_{in}(R) \approx \frac{2\pi DC(R) A \cos \theta_c}{k_b T} \left[\frac{1 - BR \tan \theta_c}{B \tan^2 \theta_c} \right]. \quad (2.22)$$

This expression generally gives a negative value for the flux, indicating mass transfer in a direction opposite to the outward surface normal to the bubble. It is worthwhile to note that for very small values of R and θ_c , J_{in} becomes positive and inaccurate since the separation of length scales and the linear shape approximation fail when the bubble radius or height approach the potential decay length, $B^{-1} = 1$ nm. The magnitude of the attractive potential at the solid-liquid interface (set by A) is treated as approximately constant, and a value of $A \approx 0.40$ kcal/mol was found to yield realistic results. This is on the order of magnitude of the hydrophobic interaction between two methane molecules in water [45], and similar to the values considered by Brenner and Lohse [41]. Furthermore, it is comparable to the estimates for this parameter described in Section 2.2, and considerably lower than the value required in the diffusive model discussed previously. Note that Eq.(2.22) reduces to the expression for the influx derived by Brenner and Lohse in the limit $B^{-1} \rightarrow 0$, and hence their model is a limiting case of the more general one presented in this subsection. This is due to their assumption that $U(z)$ is a step function that equals some value A at the surface and is zero everywhere else, which simplifies the gradient of the potential in Eq.(2.21) to a delta function.

2.3.3 Dynamic Equilibrium Model Predictions for Nanobubbles' Temperature and Saturation Dependence

Fig. 2.3a shows that the net flux of gas into the bubble, normalized by $C(R)$, can have a non-monotonic dependence on bubble radius that is quite sensitive to temperature. These results are shown for the fully saturated case. Stable bubbles of radius R^* occur when $j_{out}(R^*) + j_{in}(R^*) = j_{net}(R^*) = 0$ and $dj_{net}(R^*)/dR > 0$. The derivative condition must be satisfied so that a bubble will return to its original size in response to small perturbations to radius (i.e., perturbations to smaller R cause a net influx, $j_{net} < 0$, and vice versa). Fig 2.3a illustrates that there is only one unstable point at $T = 26$ °C, but at $T = 36$ °C, a stable point occurs at $R^* = 40$ nm in addition to two unstable ones. As temperature is raised, the stable point shifts towards smaller bubble radii, and ultimately vanishes at $T = 56$ °C. Therefore,

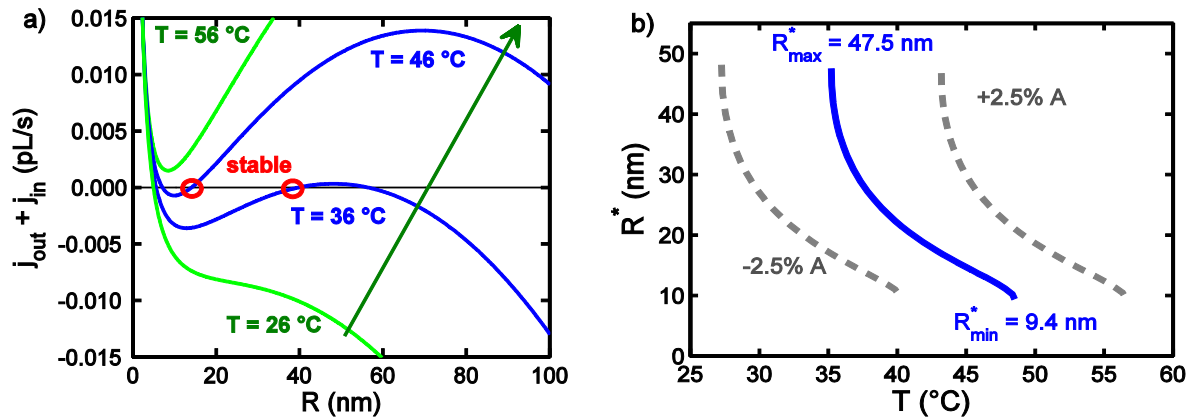


Fig. 2.3. (a) Sum of influx and outflux, scaled by the concentration at the bubble surface versus bubble radius for several different temperatures. The blue curves denote temperatures at which stable points are found. (b) Stable bubble radius versus temperature according to dynamic equilibrium model, shown for different values of A .

this formulation of the dynamic equilibrium model suggests that, for fully saturated liquid in contact with a hydrophobic substrate, stable nanobubbles exist in a narrow range of temperatures, with a minimum and maximum possible bubble size associated with the maximum and minimum temperatures, respectively. The exact breadth of the temperature range depends on the specific parameters used.

Surprisingly, the temperature dependence of gas solubility does not affect nanobubbles in this model, since both influx and outflux scale linearly with k_H . Surface tension only weakly influences nanobubbles since it does not vary dramatically over the considered temperature ranges. The temperature dependence of R^* (Fig. 2.3b) is primarily introduced through the influx, which scales as $\sim 1/T$ due to the solute mobility. With rising temperature, solute mobility increases and dissolved gas molecules more readily overcome the attractive influence of the hydrophobic potential, which shrinks the gas-rich region [as evidenced by the solute concentration profile in the absence of a bubble, given by Eq.(2.3)]. This lowers the influx and the outflux shrinks bubbles until the fluxes balance again. Above some temperature ($T_{\max} \approx 48$ °C), the effect of the potential falls to levels where the influx is too small to ever balance the outflux. Bubbles above this temperature will thus shrink and dissolve. Similarly, below some temperature ($T_{\min} \approx 35$ °C), the action of the attractive field dominates and bubbles grow without bound until the gas is locally depleted or the thermodynamic work required to sustain the influx becomes too great. If a bubble becomes sufficiently large, it may also detach from the substrate due to buoyancy.

The result in Fig. 2.3b qualitatively agrees with the observations of Seddon et al. [21] for the case of a saturated liquid in thermal equilibrium with the substrate. The model presented in this chapter accounts for the sudden appearance of a high density of nanobubbles at a minimum critical temperature, the finite temperature range where bubbles

are observed, and why bubbles at lower temperatures appear coarser. Some studies report a maximum in the total system nanobubble volume versus temperature [19,22]. The decrease in bubble size (Fig. 2.3b), coupled to an experimentally observed increase in bubble number density with temperature [8,12] may explain this non-monotonic behavior. Furthermore, the prediction of larger bubbles at lower temperatures possibly accounts for the increase in average nanobubble separation with decreasing temperature [22], since larger bubbles require a greater surrounding unperturbed gas-rich region.

We do note that other experimental studies have reported more complicated behavior. Recent work finds non-monotonic changes in the average nanobubble radius with decreasing temperature [20,22]. Differences between the model predictions and these observations are possibly due to the complicated temperature dependence of the hydrophobic attractive potential, which we ignore here. The complex nature of this potential may also explain the sensitivity of bubble morphology to the hydrophobicity parameter A (Fig 2.3b) in our simple model. This sensitivity may also be partly responsible for the difficulty in consistently producing nanobubbles among earlier experiments, which for a time cast doubt on whether nanoscale bubbles exist at all [21]. Finally, it is important to note that a number of experimental studies may have observed PDMS droplets rather than nanobubbles due to contamination from syringes [57], which adds further difficulty in meaningful comparisons to experimental literature at present.

Beyond temperature, a second important control parameter is the dissolved gas concentration (C_∞), and Fig. 2.4 shows how it affects the stable radius R^* . There exist large regions in the space of temperature and saturation where stable bubbles cannot exist, which may provide further interpretation for reproducibility problems. Where they do exist,

lowering C_∞ reduces bubble size since this elevates the driving force for outflux but has no effect on the influx (the concentration immediately next to the bubble at the surface is unaffected), as also described by Ref. [41]. As previously discussed, perturbing bubbles to a state outside of the viable region will lead to bubbles either dissolving or growing until the influx expires. The result in Fig. 2.4 is in agreement with experiments indicating that bubbles in supersaturated fluid are larger than those in undersaturated conditions [12]. Interestingly, this model also suggests that there may be middle-range temperatures (e.g., 45 °C in Fig. 2.4) at which the stable bubble radius is quite insensitive to saturation, as reported by Ref. [40], while near the lower temperature limit it can be rather pronounced.

Fig. 2.4 also indicates that there are two limits beyond which stable bubbles cannot exist, one for low bubble radii, and one for larger bubbles. Beyond the lower limit is a region where the outflux dominates, and similarly beyond the upper limit is a domain where the influx is always greater than the outflux and bubbles grow unboundedly. The lower limit is insensitive to changes in saturation since for bubbles with a small radius R , $C(R) \gg C_\infty$ due to the Young-Laplace equation, and hence the concentration at infinity (which is affected by

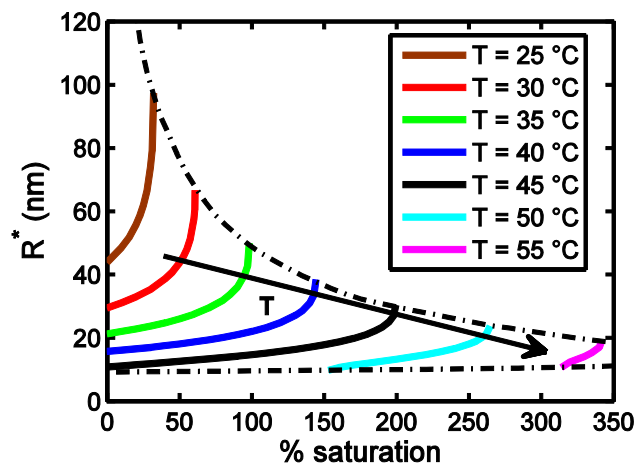


Fig. 2.4. Stable bubble radius versus bulk solute concentration for several different temperatures.

the saturation) is negligible compared to the saturation-independent $C(R)$. By contrast, for the upper limit, $C(R)$ and C_∞ are comparable in magnitude, and therefore the difference between these quantities (which is the driving force for the outflux) depends on the saturation level. As the saturation in the liquid is increases, the concentration difference, and hence the the total outflux, decreases [Eq.(2.19)]. Therefore, for balanced flux, the influx has to decrease as well. The influx does not depend on the concentration at infinity, but is affected by temperature due to the $\sim 1/T$ scaling. Hence, the influx can balance the lowered outflux at higher temperatures, since the additional thermal energy acts to lower J_{in} . In other words, for high levels of saturation in the liquid, stable bubbles can only exist at higher temperature where the influx is lower. For this reason, the temperature range where bubbles can exist becomes increasingly narrow with increasing saturation in Fig. 2.4.

In the model described thus far, we constrained the contact angle such that it depends explicitly on the bubble radius [Eq.(2.20)], which is generally attributed to the combined effect of factors such as line-tension and surface roughness. We now relax the *ad hoc* constraint imposed by Eq.(2.20) and treat the contact angle as an independent variable, which allows us to examine the stability of bubbles to perturbation in θ_c and R separately. Fig. 2.5 (next page) shows the net flux versus both contact angle and radius, where the two are treated as independent. The solid black curve corresponds to the points where the fluxes balance ($j_{net} = 0$). For a fixed contact angle, it is not possible to generate stable bubbles with respect to perturbation in R ; a bubble perturbed to the left of the stable curve at constant angle enters a region where the sum of fluxes is positive and the outflux dominates, and thus will shrink and disappear.

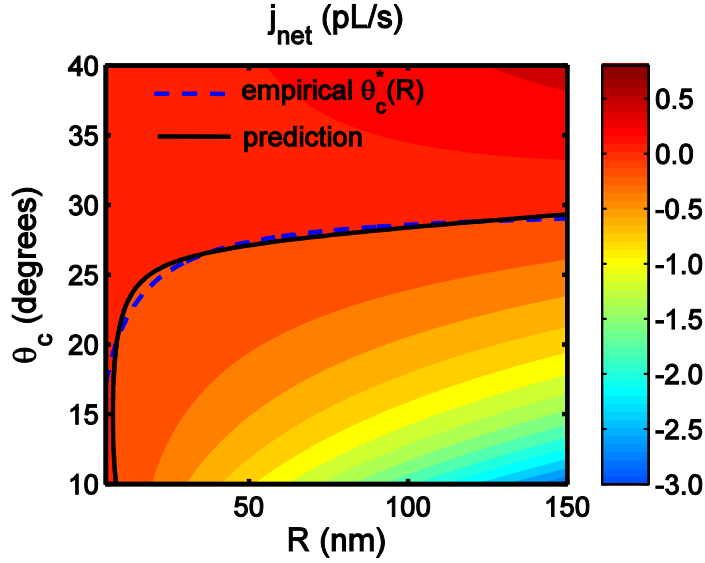


Fig. 2.5. Sum of influx and outflux versus both radius and contact angle for $T = 27\text{ }^\circ\text{C}$. Points where the fluxes balance are shown by the solid curve. The dashed curve is Eq.(2.20), with $\theta_\infty = 30^\circ$ and $\delta = 10\text{ nm}$.

Bubbles are stable, however, to perturbations in θ_c at fixed R . If a bubble pinned at the contact line begins to dissolve and lose vertical height, the contact angle decreases, which leads to an increase in the bubble surface area that is situated within the gas-rich region (which has fixed width). Ultimately, this increases the influx and stabilizes the bubble. Moreover, reducing the contact angle of a pinned bubble increases its radius of curvature and lowers the internal pressure, giving further stability. The size of a pinned bubble exhibits the same qualitative behavior as described previously, with increases in T leading to smaller θ_c^* , and increases in saturation leading to a taller bubble with larger θ_c^* , as observed by Ref. [58]. Without the constraint posed by Eq.(2.20), however, the model does not predict physical limits on the temperature and saturation ranges where bubbles can exist. Furthermore, the model no longer predicts a single preferred radius, but rather a distribution of radii and contact angles for a given temperature. An analytical expression for the allowed

combinations of contact angles and radii within this model can be derived by equating the influx [Eq.(2.22)] and outflux [Eq.(2.19)], and then solving for the stable bubble radius, giving

$$R^* = \frac{1}{2B \tan \theta_c^*} - \frac{2k_B T \gamma \tan^2 \theta_c^*}{\pi A P_0} - \frac{\gamma \sin \theta_c^*}{P_0} + \frac{1}{2P_0} \sqrt{\left(\frac{4k_B T \gamma \tan^2 \theta_c^*}{\pi A} + 2\gamma \sin \theta_c^* - \frac{P_0}{B \tan \theta_c^*} \right)^2 + \frac{8P_0 \gamma \cos \theta_c^*}{B}}. \quad (2.23)$$

Note that the stable contact angle θ_c^* is less than 30° for a wide range of bubble radii in Fig. 2.5, as reported in numerous experimental nanobubble studies. Furthermore, a bubble perturbed in *any* arbitrary direction from the black curve in Fig. 2.5 may be stable if the bubble's response to perturbation in θ_c is more rapid than its response to perturbation in R . This is likely to be the case since surface roughness and inhomogeneities will inevitably lead to at least partial contact line pinning. With this in mind, the predicted curve indicating possible combinations of θ_c and R that yield stable bubbles [solid black curve, Eq.(2.23)] looks remarkably similar to the ad hoc R -dependent contact angle constraint that we applied previously, which is shown for comparison as the blue dashed curve. Therefore, this model suggests that a possible *dynamic* phenomenon may also explain deviations from macroscopic contact angles in nanobubbles.

Even if the dynamic equilibrium model cannot ultimately describe long-term stability, it may still be relevant to the nucleation process since it poses a means by which bubbles may grow. As indicated by the stability analysis, a bubble will tend towards a preferred radius determined by the solution conditions, and may begin as a fluctuation in gas density that inflates via the dynamic equilibrium mechanism until it reaches this size. At this point, the influx may expire and the bubble might be stabilized by different means, such as the

diffusive traffic jam effect described by Weijs and Lohse [36], contact line pinning [37], or some other hitherto undiscovered means. This would also explain why our predictions agree with the experimental data of Seddon et al. [21] where bubbles were explicitly nucleated for every data point.

While the dynamic equilibrium model developed here predicts rich behavior, it may also have limitations. First, the source of energy for recirculation remains an unresolved issue. Also, the model cannot explain the presence of nanoscopic bubbles along hydrophilic substrates. A transient localized gas-rich layer, similar to those in systems with hydrophobic substrates, can develop along a hydrophilic interface during solvent exchange [10], but it is unclear what mechanism might draw gas solute molecules from this gas-rich region into the bubble. Furthermore, a recent study [59] using tracer particles in the vicinity of nanobubbles reported no evidence for an influx near the contact line. However, the particles used are comparable in diameter to the actual nanobubbles, and it is not clear whether velocities localized to a region just a few nanometers over the substrate can be resolved with this technique. Lastly, a study using optical interference-enhanced reflection microscopy [60] reports that nanobubble sizes remained constant over a broad temperature range, in conflict with other experimental studies and our predictions. Ultimately, a more consistent experimental picture is needed under varying conditions, but expounding the detailed behaviors and implications of models like the dynamic equilibrium one remains an essential step in guiding such efforts and in building a deeper understanding of the phenomena at play, even if eventually they are not the full picture.

In summary, we demonstrated through a stability analysis that the dynamic equilibrium hypothesis for nanobubble stability indicates that nanobubbles should only be observed in a narrow range of temperatures and that their radii should decrease

monotonically with temperature. Both predictions have been observed in experiment. Interestingly, the model also predicts large regions of temperature-gas saturation state space where nanobubbles cannot be observed. We believe a thorough understanding of the consequences of this hypothesis may finally settle whether it is a valid picture of nanobubble stability or nucleation through future experimental work.

2.4 Appendix

2.4.1 Model Dependence on the Parameters A and δ

Fig. A2.1 shows the minimum stable bubble temperature (indicated by dotted lines) and maximum temperature (solid lines) versus the strength of the hydrophobic attraction (parameter A). The different colors denote curves generated with a different value of δ . A and δ together constitute the most uncertain parameters in the dynamic equilibrium model. Roughly speaking, the parameter δ controls the width of the temperature range over which bubbles can exist, with smaller values of δ corresponding to narrower temperature ranges. The system is quite sensitive to A , which can shift this range of fixed width to higher or lower temperatures.

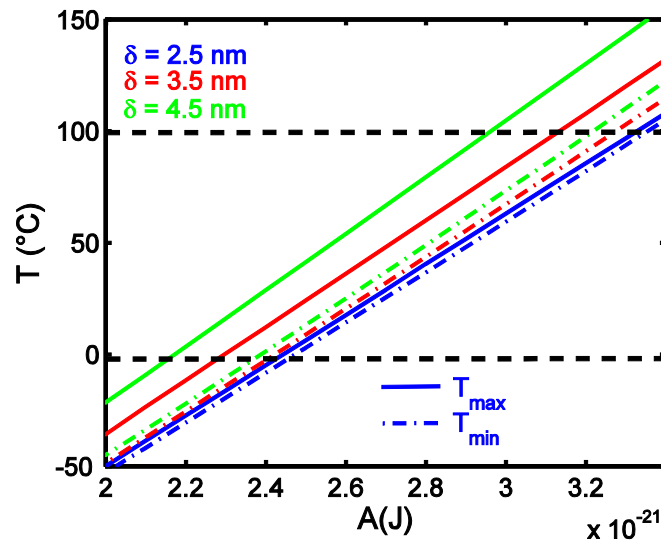


Fig. A2.1. Influence of the strength of the attractive potential (A) and length for the onset of microscopic corrections to the contact angle (δ) on the minimum (dotted lines) and maximum (solid lines) temperatures at which stable bubbles exist.

2.4.2 Sensitivity Analysis

The following table indicates how changing a given parameter by some amount affects the minimum and maximum temperatures at which stable bubbles can exist, and the

Parameter	percent change	R^*_{\min} (nm)	R^*_{\max} (nm)	T_{\min} (°C)	T_{\max} (°C)
A	10%	9.54	44.58	67.2	81.0
	20%	9.64	41.45	99.8	113.7
	-10%	9.90	48.93	3.5	16.1
	-20%	9.50	51.73	-27.9	-16.2
B	10%	8.36	48.08	36.0	54.4
	20%	7.72	50.28	36.6	60.3
	-10%	11.45	42.61	34.3	42.6
	-20%	14.02	37.47	33.0	36.8
δ	10%	9.26	51.11	37.2	54.7
	20%	9.01	53.83	39.0	60.8
	-10%	10.11	41.97	33.1	42.3
	-20%	10.89	36.52	30.8	36.1
θ_{∞}	10%	7.29	62.85	-20.9	6.5
	20%	5.94	79.99	-68.5	-27.4
	-10%	15.09	25.54	101.5	102.6
	-20%				

Table. A2.1. Summary of sensitivity of gas recirculation model with respect to the free model parameters. Parameters are adjusted by some amount, and the resulting minimum/maximum allowed radii and temperatures are listed.

corresponding maximum and minimum stable bubble radii. The predicted temperature ranges are most sensitive to the strength of the hydrophobic interaction (parameter A), and the macroscopic gas-side contact angle (θ_∞). The stable bubble radii associated with the limits of the predicted temperature ranges are relatively insensitive to changes in all parameters other than θ_∞ , which can inhibit the existence of stable bubbles if it is made sufficiently small.

2.4.3 Sensitivity to Parameter A Without Contact Angle Constraint

By relaxing the constraint of an R -dependent contact angle [Eq.(2.20)], the strong influence of the parameter A is partly diminished. Fig. A2.2 indicates that changes in the parameter A by +/- 50% still yield realistic combinations of bubble contact angles and radii.

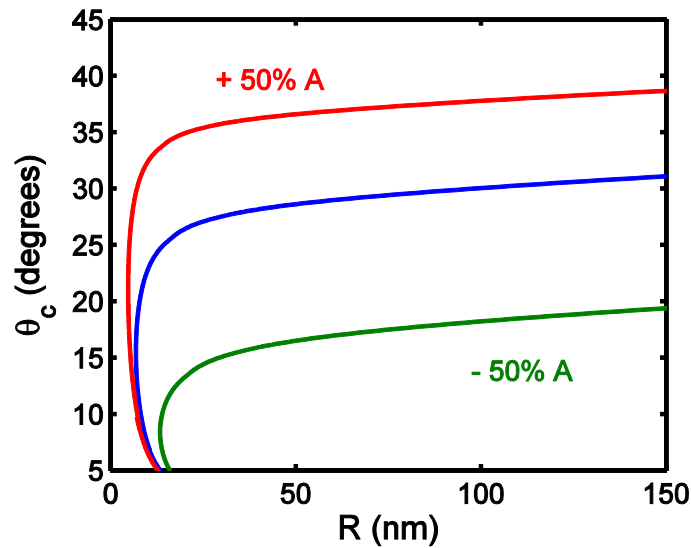


Fig. A2.2. Combinations of stable bubble radii and contact angles that yield zero net flux across the bubble surface, described by Eq.(2.23). The blue curve here is the balanced flux curve that appears in Fig. 2.5 in the chapter. Here, we show the influence of parameter A when the constraint of an R -dependent contact angle is relaxed.

2.5 References

- [1] P. Ball, *Nature* **423**, 25 (2003).
- [2] O. I. Vinogradova, N. F. Bunkin, N. V. Churaev, O. A. Kiseleva, A. V. Lobeyev, and B. W. Ninham, *J. Colloid Interface Sci.* **173**, 443 (1995).
- [3] J. W. G. Tyrrell and P. Attard, *Phys. Rev. Lett.* **87**, 176104 (2001).
- [4] P. Attard, *Adv. Colloid Interface Sci.* **104**, 75 (2003).
- [5] J. L. Parker, P. M. Claesson, and P. Attard, *J. Phys. Chem.* **98**, 8468 (1994).
- [6] M. Holmberg, A. Kühle, K. A. Mørch, and A. Boisen, *Langmuir* **19**, 10510 (2003).
- [7] A. C. Simonsen, P. L. Hansen, and B. Klösgen, *J. Colloid Interface Sci.* **273**, 291 (2004).
- [8] X. H. Zhang, X. D. Zhang, S. T. Lou, Z. Zhang, J. L. Sun, and J. Hu, *CAS OpenIR* **20**, (2004).
- [9] A. Agrawal, J. Park, D. Y. Ryu, P. T. Hammond, T. P. Russell, and G. H. McKinley, *Nano Lett.* **5**, 1751 (2005).
- [10] X. H. Zhang, N. Maeda, and V. S. J. Craig, *Langmuir* **22**, 5025 (2006).
- [11] L. Zhang, Y. Zhang, X. Zhang, Z. Li, G. Shen, M. Ye, C. Fan, H. Fang, and J. Hu, *Langmuir* **22**, 8109 (2006).
- [12] S. Yang, S. M. Dammer, N. Bremond, H. J. W. Zandvliet, E. S. Kooij, and D. Lohse, *Langmuir* **23**, 7072 (2007).
- [13] B. M. Borkent, S. M. Dammer, H. Schönherr, G. J. Vancso, and D. Lohse, *Phys. Rev. Lett.* **98**, 204502 (2007).
- [14] X. H. Zhang, A. Khan, and W. A. Ducker, *Phys. Rev. Lett.* **98**, 136101 (2007).

- [15] S. Yang, E. S. Kooij, B. Poelsema, D. Lohse, and H. J. W. Zandvliet, *EPL Europhys. Lett.* **81**, 64006 (2008).
- [16] X. H. Zhang, A. Quinn, and W. A. Ducker, *Langmuir* **24**, 4756 (2008).
- [17] S.-T. Lou, Z.-Q. Ouyang, Y. Zhang, X. Li, J. Hu, M. Li, and F.-J. Yang, *J. Vac. Sci. Technol. B Microelectron. Nanometer Struct.* **18**, 2573 (2000).
- [18] N. Ishida, T. Inoue, M. Miyahara, and K. Higashitani, *Langmuir* **16**, 6377 (2000).
- [19] M. A. J. van Limbeek and J. R. T. Seddon, *Langmuir* **27**, 8694 (2011).
- [20] Z. Xue-Hua, L. Gang, W. Zhi-Hua, Z. Xiao-Dong, and H. Jun, *Chin. Phys.* **14**, 1774 (2005).
- [21] J. R. T. Seddon, E. S. Kooij, B. Poelsema, H. J. W. Zandvliet, and D. Lohse, *Phys. Rev. Lett.* **106**, 56101 (2011).
- [22] R. P. Berkelaar, J. R. T. Seddon, H. J. W. Zandvliet, and D. Lohse, *ChemPhysChem* **13**, 2213 (2012).
- [23] Y. Wang and B. Bhushan, *Soft Matter* **6**, 29 (2009).
- [24] Y. Wang, B. Bhushan, and X. Zhao, *Langmuir* **25**, 9328 (2009).
- [25] D. C. Tretheway and C. D. Meinhart, *Phys. Fluids* **16**, 1509 (2004).
- [26] E. Lauga and M. P. Brenner, *Phys. Rev. E* **70**, 26311 (2004).
- [27] Z. Wu, H. Chen, Y. Dong, H. Mao, J. Sun, S. Chen, V. S. J. Craig, and J. Hu, *J. Colloid Interface Sci.* **328**, 10 (2008).
- [28] F. Hui, B. Li, P. He, J. Hu, and Y. Fang, *Electrochem. Commun.* **11**, 639 (2009).
- [29] S. Darwich, K. Mougín, L. Vidal, E. Gnecco, and H. Haidara, *Nanoscale* **3**, 1211 (2011).
- [30] W. B. Zimmerman, V. Tesař, and H. C. H. Bandulasena, *Curr. Opin. Colloid Interface Sci.* **16**, 350 (2011).

- [31] J. R. T. Seddon, D. Lohse, W. A. Ducker, and V. S. J. Craig, *ChemPhysChem* **13**, 2179 (2012).
- [32] W. A. Ducker, *Langmuir* **25**, 8907 (2009).
- [33] J. R. T. Seddon and D. Lohse, *J. Phys. Condens. Matter* **23**, 133001 (2011).
- [34] S. Das, J. H. Snoeijer, and D. Lohse, *Phys. Rev. E* **82**, 56310 (2010).
- [35] X. Zhang, M. H. Uddin, H. Yang, G. Toikka, W. Ducker, and N. Maeda, *Langmuir* **28**, 10471 (2012).
- [36] J. H. Weijs and D. Lohse, *Phys. Rev. Lett.* **110**, 54501 (2013).
- [37] Y. Liu and X. Zhang, *J. Chem. Phys.* **138**, 14706 (2013).
- [38] Y. Liu and X. Zhang, *J. Chem. Phys.* **141**, 134702 (2014).
- [39] D. Lohse and X. Zhang, *Phys. Rev. E* **91**, 31003 (2015).
- [40] X. H. Zhang, G. Li, N. Maeda, and J. Hu, *Langmuir ACS J. Surf. Colloids* **22**, 9238 (2006).
- [41] M. P. Brenner and D. Lohse, *Phys. Rev. Lett.* **101**, 214505 (2008).
- [42] J. R. T. Seddon, H. J. W. Zandvliet, and D. Lohse, *Phys. Rev. Lett.* **107**, 116101 (2011).
- [43] J. N. Israelachvili, *Intermolecular and Surface Forces, Third Edition*, 3rd ed. (Academic Press, 2010).
- [44] S. M. Dammer and D. Lohse, *Phys. Rev. Lett.* **96**, 206101 (2006).
- [45] S. Shimizu and H. S. Chan, *J. Chem. Phys.* **113**, 4683 (2000).
- [46] V. B. Svetovoy, I. Devic, J. Snoeijer, and D. Lohse, *Langmuir* (2016).
- [47] K. Yasui, T. Tuziuti, W. Kanematsu, and K. Kato, *Phys. Rev. E* **91**, 33008 (2015).
- [48] K. Yasui, T. Tuziuti, W. Kanematsu, and K. Kato, *Langmuir* (2016).

- [49] P. Moon and D. E. Spencer, *Field Theory Handbook: Including Coordinate Systems, Differential Equations and Their Solutions*, Softcover reprint of the original 2nd ed. 1988 (Springer, 1988).
- [50] P. A. Bobbert, M. M. Wind, and J. Vlieger, *Phys. Stat. Mech. Its Appl.* **141**, 58 (1987).
- [51] A. Checco, P. Guenoun, and J. Daillant, *Phys. Rev. Lett.* **91**, 186101 (2003).
- [52] A. Checco, H. Schollmeyer, J. Daillant, P. Guenoun, and R. Boukherroub, *Langmuir* **22**, 116 (2006).
- [53] P. Jakubczyk and M. Napiórkowski, *J. Phys. Condens. Matter* **16**, 6917 (2004).
- [54] D. Li, *Colloids Surf. Physicochem. Eng. Asp.* **116**, 1 (1996).
- [55] N. Kameda and S. Nakabayashi, *Chem. Phys. Lett.* **461**, 122 (2008).
- [56] N. Kameda, N. Sogoshi, and S. Nakabayashi, *Surf. Sci.* **602**, 1579 (2008).
- [57] R. P. Berkelaar, E. Dietrich, G. A. M. Kip, E. S. Kooij, H. J. W. Zandvliet, and D. Lohse, *Soft Matter* **10**, 4947 (2014).
- [58] X. Zhang, D. Y. C. Chan, D. Wang, and N. Maeda, *Langmuir* **29**, 1017 (2013).
- [59] C. U. Chan and C.-D. Ohl, *Phys. Rev. Lett.* **109**, 174501 (2012).
- [60] S. Karpitschka, E. Dietrich, J. R. T. Seddon, H. J. W. Zandvliet, D. Lohse, and H. Riegler, *Phys. Rev. Lett.* **109**, 66102 (2012).

3 Hybrid Molecular-Continuum Simulations Using Smoothed Dissipative Particle Dynamics

We present a new multiscale simulation methodology for coupling a region with atomistic detail simulated via molecular dynamics (MD) to a numerical solution of the fluctuating Navier-Stokes equations obtained from smoothed dissipative particle dynamics (SDPD). In this approach, chemical potential gradients emerge due to differences in resolution within the total system and are reduced by introducing a pairwise thermodynamic force inside the buffer region between the two domains where particles change from MD to SDPD types. When combined with a multi-resolution SDPD approach, such as the one proposed by Kulkarni et al. [P.M. Kulkarni, C.-C. Fu, M.S. Shell, and L. G. Leal, J. Chem. Phys. **138**, 234105 (2013)], this method makes it possible to systematically couple atomistic models to *arbitrarily* coarse continuum domains modeled as SDPD fluids with varying resolution. We test this technique by showing that it correctly reproduces thermodynamic properties across the entire simulation domain for a simple Lennard-Jones fluid. Furthermore, we demonstrate that this approach is also suitable for non-equilibrium problems by applying it to simulations of the start up of shear flow. The robustness of the method is illustrated with two different flow scenarios in which shear forces act in directions parallel and perpendicular to the interface separating the continuum and atomistic domains. In both cases we obtain the correct transient velocity profile. We also perform a triple-scale shear flow simulation where we include two SDPD regions with different resolutions in addition to a MD domain, illustrating the feasibility of a three-scale coupling. This kind of three-scale coupling requires a finely-

resolved SDPD region to bridge the MD fluid to the coarse SDPD region; therefore, we also describe how this triple-scale approach can be adapted to *directly* couple a MD fluid to coarse SDPD regions featuring more massive particles, without requiring intermediate SDPD zones to bridge the different length scales.

3.1 Introduction

Numerous problems in molecular physics are characterized by multiple time and length scales, a feature that poses significant challenges in applying traditional simulation techniques. For instance, a problem involving localized nanoscale processes or phenomena at a solid surface in contact with a liquid may require molecular-scale resolution (e.g. molecular dynamics) for the solid-liquid boundary, whereas the bulk fluid region away from the surface may not necessitate this kind of detail, and an atomistic treatment of the full system may be prohibitively expensive from a computational standpoint. In fact, the problem of multiple characteristic length scales is one that frequently arises in fluid flow problems involving interfaces, such as the contact line of a three-phase flow [1], slip along hydrophobic substrates [2], dynamics of thin films [3], and surface nanobubbles (see Chapter 2 for a comprehensive discussion). Similarly, a broad range of problems involving biological molecules in explicit solvent (e.g. proteins) may not require the same level of detail for the solvent in the bulk far away from the molecule as in the region immediately surrounding it. In these cases, it is desirable to preserve a detailed description for the system in localized regions where necessary, and use a simpler coarse-grained model such as a continuum or mean-field approximation for parts of the problem domain where less resolution is required [4–8].

In light of this, there have been numerous efforts [9,1,10–15] to directly couple continuum-based (i.e. Navier-Stokes) solutions with molecular dynamics (MD). These studies have generally employed finite-difference/element/volume methods for the continuum region and transferred information between the continuum and MD domains via flux exchange within an overlap region. This is achieved by constraining the MD particle dynamics inside this overlap region such that the averaged particle mass and momentum fluxes equal those in the overlapping continuum solution [9,11]. This approach was extended by Delgado-Buscalioni and De Fabritiis [12] by coupling MD to a finite-volume *fluctuating* continuum domain using the fluctuating hydrodynamic equations of Landau and Lifshitz [16]. However, flux exchange has been challenging in certain situations such as gas-phase calculations where fluctuations in the atomistic region can induce error and instability in the continuum solution [17]. Similarly, molecularly-resolved and continuum domains may be coupled through the Schwarz alternating method, where state-exchange is instead achieved by matching boundary conditions, and the individual regions are iterated until they converge to a steady-state solution [10,1,18]. Due to noise in the MD part of the system, fitting of the local velocity is necessary to smooth the boundary condition from the MD fluid that is applied to the continuum region in a given iteration. The Schwarz alternating method has already been used for multiscale simulations bridging the nano- and meso-scales in coupling MD and lattice Boltzmann domains [19]. Fedosov and Karniadakis [18] also adapted it to interface MD to a mesoscale region simulated using dissipative particle dynamics (DPD), which in turn was coupled to a numerical Navier-Stokes solution. While this strategy decouples both time and length scales, it is less suitable for dynamic problems since each time-step is treated as quasi-steady-state and requires iteration, although often a single iteration per time-step may be sufficient for non-equilibrium systems [1].

A different multiscale approach involves molecular to coarse-grained molecular coupling rather than molecular-continuum coupling, and one such strategy for interfacing atomistic models to a coarse-grained particle-based description has been proposed by Praprotnik et al. [20]. The coarse-grained representation in their work is obtained from the molecular one by structure matching. Their “adaptive resolution scheme” (AdResS) then smoothly interpolates from the molecular to the coarse-grained particles as they pass between an atomistic region and a coarse-grained one [20–26]. Of course, a molecule’s degrees of freedom are not conserved and continuously change as it traverses the intermediate region between the atomistic and coarse domains [20]. This method has been used to develop simulations of liquids with tetrahedral structure, including water, which are coupled to coarse-grained molecules with isotropic pair potentials obtained through Boltzmann inversion [20,21,23,25,26]. While it was originally described in the constant temperature case, recently this technique has been adapted for constant energy simulations, although the latter formulation results in a drift force such that momentum is only weakly conserved [27]. Importantly, this method has also been used in triple-scale simulations of water in which atomistic and coarse-grained mesoscale regions are coupled to a finite-volume continuum solution by exchange of fluxes between the different domains [24]. One issue of concern in such approaches is the lack of transferability in the coarse-grained model. Typically the structure-matched coarse-grained potential is a function of the system thermodynamic state, and thus simulating systems with temperature or density gradients, or across a variety of conditions, can be difficult to implement in a thermodynamically-consistent manner.

Smoothed particle methods offer an alternative and particularly convenient approach to incorporating coarse-grained mesoscale and continuum regions in multiscale simulations, and this is the main strategy that we consider in this chapter. Such particle-based continuum

solvers include smoothed particle hydrodynamics (SPH) [28–30] (also see Chapter 6 for detailed discussion) and smoothed dissipative particle dynamics (SDPD) [31]. In SPH, the problem domain is discretized into a set of Lagrangian particles or nodes. At each time-step, the strain or strain-rate at a selected particle is computed from the particle velocities/positions in the system at that time. With the strain/strain-rate known, the stress at each particle is calculated, from which the corresponding particle acceleration can be determined. Particle positions and velocities are integrated in time as in traditional MD [30], although the equations of motion are distinct and formulated from a top-down, continuum assumption. Thus, SPH is essentially a method for numerically solving the hydrodynamic equations with a formalism that is reminiscent of MD [30]. SDPD is an extension of SPH to the mesoscale proposed by Español and Revenga that introduces thermal fluctuations in the field variables of the continuum solution [31]. In SDPD, the size of the fluid particles is determined by the choice of a parameter called the “smoothing length”. Decreasing the smoothing length results in finer resolution and less massive particles that are subject to larger thermal fluctuations, whereas in the limit of large smoothing lengths, fluctuations disappear and continuum hydrodynamics in the form of SPH is recovered.

Particle-based solvers of the continuum equations offer a natural method of coupling with inherently particle-based descriptions of the molecular world. The use of discrete particle methods for all length scales in a multiscale simulation seems to have been first suggested by Dzwinel et al [32]. This perspective was subsequently adopted by Liu and Liu, who demonstrated that SPH can be stably coupled to MD [30]. These authors provide two possible schemes: (i) In the first approach, particles within an overlap region interact through both MD and SPH forces. (ii) In the second, force-bridging eliminates the need for an intermediate domain; MD particles interact through an atomic potential (e.g. Lennard-Jones),

SPH particles interact through SPH forces, and at the interface between the two regions, MD and SPH particles interact symmetrically through some arbitrarily chosen interaction (SPH or MD). A similar approach was suggested by Ganzenmüller et al. [33], who instead used an algebraic mean of MD and SPH forces for cross interactions. These techniques require a thermostat for the MD region since the (non-fluctuating) SPH particles otherwise dissipate all heat in the MD portion of the system through viscous interactions.

While successful in reproducing velocity profiles for a number of flow types, these existing coupling methods are not ideal if the smoothed particles are subject to fluctuations. For very small particles, the presence of thermal noise can lead a softly-repulsive SPH particle to jump across an interface and instantaneously change type to a MD atom; since MD potentials frequently feature a steeply-repulsive core, catastrophic forces result when such a particle enters the overlap region [approach (i)] or the MD region [approach (ii)] and lands close to another MD atom. Alternatively, if fluid particles are much larger than MD atoms such that fluctuations no longer yield large particle displacements per time-step, mass conservation requires performing particle insertions and deletions when particles cross the fixed boundaries. This is difficult to realize in an efficient manner that does not artificially disrupt either domain's equations of motion.

In our work, we recognize that the tunability of the characteristic length scale (the smoothing length) makes SDPD an ideal candidate for multiscale simulation. Moreover, fluctuations in the MD part of the simulation will not disrupt the continuum solution since SDPD already features thermal noise in the velocity field. Kulkarni et al. [34] demonstrated that it is possible to couple two SDPD regions with different resolutions (i.e. smoothing lengths) and reproduce correct thermodynamic equilibrium properties across an entire simulation box containing both domains. This opens the possibility for multiscale simulations

spanning length scales from the mesoscopic to the continuum. Moreover, these authors showed that there is a smoothing length at the atomistic scale at which a collection of SDPD particles can successfully reproduce both dynamic and thermodynamic properties associated with a Lennard-Jones fluid. Therefore, coupling MD to a reduced-scale SDPD fluid seems to be the major missing link in using such methods to cover the spectrum of length scales from macroscopic to atomistic. Flux/state-exchange between MD and continuum domains is often difficult to implement due to the fundamentally different fluid description in the molecular region (particle-based) versus the continuum one (grid-based); hence, by employing a *particle* description for the continuum fluid, we can readily determine the flow field across all length scales in the Lagrangian frame. Another significant advantage in employing a particle description throughout the simulation box is that conservation of quantities such as mass and momentum is incorporated in a natural and intuitive fashion.

In this chapter, we develop a technique for coupling an atomistic MD region to a fluctuating continuum solution obtained using SDPD, which in turn can be coupled to increasingly coarse SDPD regions via the strategy of Kulkarni et al. [34] Instantaneously changing particle types at a sharp interface can incur catastrophic forces; hence, we follow the adaptive resolution approach and introduce a switching function such that particles change type gradually across an “overlap” region. For the atomistic region, we choose a Lennard-Jones fluid and demonstrate that with the method described here, correct thermodynamic properties are reproduced within the entire system. In order to reduce chemical potential gradients present due to differences in resolution, we introduce a pairwise thermodynamic force that performs work on the particles in the buffer region between the atomistic and continuum fluids. A derivation and discussion of this force is provided in Section 3.5. Finally, in Sections 3.7 and 3.8, we show that our method for coupling MD and

SDPD correctly captures hydrodynamics by performing dual- and triple-scale simulations of shear flow. In order to illustrate the robustness of this approach, we consider two different cases: one in which shear forces act in a direction parallel to the interface between the continuum and atomistic region, and one in which they are perpendicular. This multiscale method is generalized for ideal fluid mixtures in Chapter 5.

3.2 Smoothed Dissipative Particle Dynamics

Because it is the key element of the multiscale approach described in this chapter (as well as essential to Chapters 4-6), we first provide a brief summary of smoothed dissipative particle dynamics. To date, SDPD has been used to simulate a variety of mesoscale hydrodynamic phenomena including simple polymers [35,36], pinned DNA subjected to shear flow [37], colloidal particles [35], the flow of blood [38], suspensions [39], and viscoelastic flows [40]. In this method, the domain is composed of a collection of particles or fluid volumes that evolve in time according to equations of motion obtained from a discretization of the fluctuating Navier-Stokes equations based on interpolation theory. The Navier-Stokes equation in Lagrangian form is [41]

$$\rho \frac{d\mathbf{v}}{dt} = -\nabla p + \eta \nabla^2 \mathbf{v} + \left(\zeta + \frac{\eta}{3} \right) \nabla \nabla \cdot \mathbf{v}. \quad (3.1)$$

In applying the aforementioned particle discretization to this expression, it is possible to obtain an equation of motion for all the particles in the system, i.e. Eq.(3.1) can be solved numerically by deriving an appropriate interaction between particle pairs and integrating particle positions in time. The *reversible* contribution to the dynamics of particle i in the resulting equation is [31,35]

$$m_i \left. \frac{d\mathbf{v}_i}{dt} \right|_{rev} = - \sum_{j=1}^N m_i m_j \left(\frac{p_i}{\rho_i^2} + \frac{p_j}{\rho_j^2} \right) \frac{\partial W_{ij}}{\partial \mathbf{r}_{ij}} \mathbf{e}_{ij}, \quad (3.2)$$

where N is the number of particles in the system, p_i is the pressure at particle i , ρ_i is the density at particle i , m_i is the mass of the i th particle, W_{ij} is the smoothing kernel (discussed below), and \mathbf{e}_{ij} is a unit vector joining the centers of particles i and j , $\mathbf{e}_{ij} \equiv \mathbf{r}_{ij} / |\mathbf{r}_{ij}|$ with $\mathbf{r}_{ij} \equiv \mathbf{r}_i - \mathbf{r}_j$. Eq.(3.2) determines the force on particle i due to the local pressure distribution and corresponds to the discretization of the pressure gradient term in Eq.(3.1). The *irreversible*, viscous contribution to the Navier-Stokes dynamics is represented in SDPD by

$$\begin{aligned} m_i \left. \frac{d\mathbf{v}_i}{dt} \right|_{irr} &= \left(\frac{5\eta}{3} - \zeta \right) \sum_{j=1}^N \frac{m_i m_j}{\rho_i \rho_j} \left(\frac{1}{|\mathbf{r}_{ij}|} \frac{\partial W_{ij}}{\partial r_{ij}} \right) \mathbf{v}_{ij} \\ &+ 5 \left(\frac{\eta}{3} + \zeta \right) \sum_{j=1}^N \frac{m_i m_j}{\rho_i \rho_j} \left(\frac{1}{|\mathbf{r}_{ij}|} \frac{\partial W_{ij}}{\partial r_{ij}} \right) (\mathbf{v}_{ij} \cdot \mathbf{e}_{ij}) \mathbf{e}_{ij}. \end{aligned} \quad (3.3)$$

Here, η is the fluid shear viscosity, ζ is the bulk viscosity, and $\mathbf{v}_{ij} \equiv \mathbf{v}_i - \mathbf{v}_j$ is the relative velocity between particles i and j . The contribution of Eq.(3.3) to the SDPD equations of motion accounts for dissipative interactions between neighboring SDPD particles [i.e., the second and third terms on the right-hand side of Eq.(3.1)].

The last component of SDPD is the presence of thermal noise in the velocity field. Fluctuations are introduced in a thermodynamically-consistent manner through the GENERIC [42–44] formalism (see Appendix 4.8.1 in the following chapter for a brief review), and are described by [31,45]

$$m_i d\tilde{\mathbf{v}}_i = \sum_{j=1}^N \left(A_{ij} d\hat{\mathbf{W}}_{ij} + \frac{1}{3} B_{ij} \text{tr} [d\mathbf{W}_{ij}] \mathbf{I} \right) \cdot \mathbf{e}_{ij}. \quad (3.4)$$

$d\mathbf{W}_{ij}$ is a tensorial generalization of the stochastic Wiener process^{*}, and $d\hat{\mathbf{W}}_{ij}$ is the traceless, symmetric part of $d\mathbf{W}_{ij}$, i.e. $d\hat{\mathbf{W}}_{ij}^{\alpha\beta} = \frac{1}{2}[dW_{ij}^{\alpha\beta} + dW_{ij}^{\beta\alpha}] - \frac{\delta^{\alpha\beta}}{3}\text{tr}[d\mathbf{W}_{ij}]$. The form of this random contribution to the dynamics is postulated such that it is consistent with the tensorial structure of the friction forces in the hydrodynamic equations [45]. This final contribution to the equations of motion is the force on particle i due to random stresses induced by thermal fluctuations in the fluid. Fluctuation-dissipation is satisfied by the following choice for the magnitudes of the noises A_{ij} and B_{ij} :

$$\begin{aligned} A_{ij} &= \left[-\frac{4m_i m_j k_B T}{\rho_i \rho_j} \left(\frac{5\eta}{3} - \zeta \right) \left(\frac{1}{|\mathbf{r}_{ij}|} \frac{\partial W_{ij}}{\partial r_{ij}} \right) \right]^{1/2}, \\ B_{ij} &= \left[-\frac{4m_i m_j k_B T}{\rho_i \rho_j} \left(\frac{5\eta}{3} + 8\zeta \right) \left(\frac{1}{|\mathbf{r}_{ij}|} \frac{\partial W_{ij}}{\partial r_{ij}} \right) \right]^{1/2}. \end{aligned} \quad (3.5)$$

Equations (3.2), (3.3) and (3.4), together with the noise magnitudes given in Eq.(3.5), collectively yield a set of stochastic differential equations governing the velocity field for a SDPD fluid at constant temperature. All these terms, including the viscous and random forces, act symmetrically on pairs of particles so that momentum is conserved; in other words, particle forces are pairwise and depend only on the position and velocity difference vectors.

^{*} We use W in reference to both the Wiener process and the smoothing function for historical reasons, though the two are unrelated.

The smoothing kernel W_{ij} is an even, monotonically-decreasing function of the particle separation r_{ij} with compact support, normalized to unity. Here we use the cubic spline [46,47,30,34],

$$W_{ij}(q) = \frac{1}{\pi h^3} \begin{cases} 1 - \frac{3}{2}q^2 + \frac{3}{4}q^3, & 0 \leq q < 1, \\ \frac{1}{4}(2-q)^3, & 1 \leq q < 2, \\ 0, & q \geq 2, \end{cases} \quad (3.6)$$

where $q = r_{ij}/h$. The support domain of a point is determined by the smoothing kernel and equals κh , where $\kappa = 2$ for the cubic spline. While the sums in Eqs.(3.2), (3.3) and (3.4) extend over all the particles in the system, the compact support condition for the weighting function implies that only nearby particles contribute to the sums.

In the SPH and SDPD approximations, field variables and their spatial derivatives are calculated from a weighted average using properties associated with nearby particles, where the weight is determined by the kernel W_{ij} or its derivative, respectively, at the neighboring particle's location. For instance, the density at particle i is simply a weighted average over neighboring particle masses,

$$\rho(\mathbf{r}_i) = \sum_{j=1}^N m_j W(\mathbf{r}_i - \mathbf{r}_j, h). \quad (3.7)$$

The density field is updated at each time-step by performing this sum; an alternative approach is to use a discretized form of the continuity equation [30]. Note that a different density is obtained from Eq.(3.7) depending on whether particle i itself contributes to the sum. Generally, the particle's own contribution should be included since the particle distribution for an SPH fluid has order [48], although for small smoothing lengths where the distribution of particles is more disordered due to thermal noise, this can lead to an

overestimated density [49,48,34]. In the present work, we include the self-contribution to density. This is an important subtlety that is revisited in later sections.

3.3 Boundary Conditions

Solid boundaries in a SDPD region are treated as a collection of SDPD particles frozen on a lattice with the same number and mass density as the fluid. Hence, a particle near a boundary experiences the same kinds of forces due to surrounding particles as a fluid particle in the bulk far away from any interfaces. The wall-fluid particle pair interactions are the same as the fluid-fluid ones, except the velocity difference in the viscous force between the particles [Eq.(3.3)] is modified by assigning an artificial velocity to the wall (or “virtual”) particle such that no-slip is enforced precisely at the fluid-solid interface. This is achieved by calculating the normal distance of the fluid and wall particles from the surface (d_f and d_w , respectively) and linearly extrapolating the velocity profile due to the fluid particle into the wall such that the velocity is zero at the boundary. New relative velocities between fluid and wall particles are computed for every pair at each time-step as the fluid particle positions and velocities evolve in time. Wall particle densities may be held constant or evolved in time; in this chapter we choose the latter since some work suggests that keeping boundary particle densities fixed gives an inaccurate representation of fluid peak pressures near the fluid-solid interface [50]. For additional discussion on this approach, see Ref. [50], as well as in Chapter 6.

In this section we provide a brief derivation of how this artificial velocity for the virtual particles is computed. For simplicity, we assume a planar boundary located at $z = 0$, though this approach is readily extended for curved surfaces as well [50]. We are interested in calculating the pair interaction between a fluid particle located a distance d_f from the boundary and a wall particle located d_w from the boundary (see Fig. 3.1 below). The fluid particle has velocity \mathbf{v}_f , and the goal is to assign a velocity \mathbf{v}_w to the wall particle such that no-slip is enforced at the boundary located at $z = 0$, which moves with velocity \mathbf{v}_s . Assuming the velocity profile is linear in the vicinity of the surface, we obtain an equation for $\mathbf{v}(z)$ through interpolation of the fluid particle and boundary velocities,

$$\mathbf{v}(z) = (\mathbf{v}_f - \mathbf{v}_s) \left(\frac{z}{d_f} \right) + \mathbf{v}_s. \quad (3.8)$$

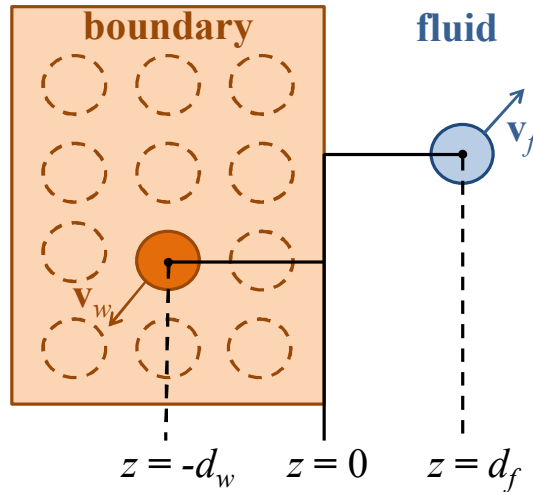


Fig. 3.1. Illustration of the boundary particle approach of Morris et al. Solid objects are treated through a collection of particles frozen on a lattice, and for every pair interaction, a virtual velocity \mathbf{v}_w is assigned to the wall particle such that no-slip is enforced at the fluid-solid boundary ($z = 0$).

Substituting $z = 0$ and $z = d_f$ into Eq.(3.8) gives the velocities of the boundary (\mathbf{v}_s) and the fluid particle (\mathbf{v}_f), respectively. Using this equation for the linearized velocity near the surface, we now extrapolate the velocity to the position of the boundary particle. Hence, we obtain a velocity for the boundary particle that guarantees no-slip at $z = 0$ by substituting $z = -d_w$ into Eq.(3.8),

$$\mathbf{v}_w \equiv \mathbf{v}(-d_w) = -(\mathbf{v}_f - \mathbf{v}_s) \left(\frac{d_w}{d_f} \right) + \mathbf{v}_s. \quad (3.9)$$

The SDPD viscous force depends on the relative velocity between particle pairs [Eq.(3.3)]. Using Eq.(3.9) and following some algebra, we rewrite the velocity difference between the fluid and wall particle $\mathbf{v}_{fw} \equiv \mathbf{v}_f - \mathbf{v}_w$ as

$$\mathbf{v}_{fw} = \left(1 + \frac{d_w}{d_f} \right) (\mathbf{v}_f - \mathbf{v}_s). \quad (3.10)$$

Note that the velocity difference is now between the fluid particle and the nearest point on the solid boundary, rather than between the two particles. If the boundary is stationary ($\mathbf{v}_s = 0$), Eq.(3.10) simplifies to [50]

$$\mathbf{v}_{wf} = \beta \mathbf{v}_f, \quad (3.11)$$

where

$$\beta = \min \left(\beta_{\max}, 1 + \frac{d_w}{d_f} \right). \quad (3.12)$$

Hence, the velocity difference \mathbf{v}_{ij} in Eq.(3.3) is replaced with Eq.(3.10) when one of the particles belongs to the boundary. Note that β diverges in the limit of $d_f \rightarrow 0$, i.e. when the fluid particle closely approaches the fluid-solid interface. This is typically remedied by introducing a constant β_{\max} , which restricts the magnitude of the velocity assigned to the wall

particle. For the work presented in this chapter, we choose $\beta_{\max} = 1.5$ [34,50], which numerical tests suggest is an optimal value for this parameter.

It is important to note that even though an artificial velocity is assigned to the virtual particle, this velocity is not used to integrate the wall particle's position in time since we have fixed boundaries, and a new artificial velocity is assigned to a given wall particle for every pair interaction. For the simulations described here, the positions of wall particles are evolved using the actual boundary velocity \mathbf{v}_s . The use of fictitious, “artificial” velocities as described in Eqs.(3.10) and (3.11) is simply a construct for modifying the pairwise forces that ensures interactions between all particles is consistent with no-slip; since all pair interactions satisfy no-slip at the boundary, the overall velocity field exhibits no-slip as well. If we simply translate the wall particles with the boundary velocity without these modified wall particle velocities, no-slip still applies to the fluid, although the location of where the velocity relative to the surface vanishes becomes ambiguous and the precise location of the surface is no longer clearly defined.

Finally, note that the modified velocity difference in Eq.(3.11) will not rigidly enforce the kinematic boundary condition. Due to the high diffusivity of SDPD particles with a very small smoothing length, additional measures such as specular reflection, a higher wall particle number density, additional interparticle forces [30], or velocity averaging [30,31,51] may be necessary to fully prevent boundary penetration. In the presented work we use specular reflection, i.e. if a fluid particle crosses the boundary, the component of its velocity normal to the boundary is reversed so that the particle leaves the boundary region during the subsequent time integration.

3.4 Adaptive Resolution Scheme for Coupling MD to SDPD

We couple MD to SDPD using the adaptive resolution scheme (AdResS) proposed by Praprotnik et al. [20] This makes it possible to define a fixed overlap domain between the two regions where particles continuously change type from MD to SDPD and vice versa. In this scheme, *reversible* particle pair interactions are turned on/off via a weighting function that depends on their positions within the transition domain. Particles within the MD region interact through an atomistic potential and in the SDPD domain particles interact through SDPD forces [Eqs.(3.2), (3.3), (3.4)]. Within the overlap region, particles interact through a linear combination of both interactions, as described below. AdResS has been considered in the context of coupled MD/finite-volume continuum solutions previously [24], but has not been used with particle-based continuum solvers (e.g. SDPD), even though they present a natural option since one only has to consider particle-particle interactions. Importantly, through this kind of pairwise MD-SDPD coupling, thermal noise in the MD region will not lead to error in the continuum solution since fluctuations are already present in SDPD. Moreover, one can avoid particle insertions and deletions by decreasing the smoothing length of the SDPD fluid such that the SDPD particles are identically massive to the MD ones. This SDPD domain with atomistic resolution can then be coupled to more coarse SDPD regions using the method of Kulkarni et al [34]. An attractive feature of the AdResS approach is that it can be used for coupling to atomistic fluids with complicated molecular geometries [20–23,25,26].

To implement AdResS, we define a switching function $s(z)$ that is zero in the SDPD domain, unity in the MD domain, and smoothly and monotonically transitions between these two values in the buffer region. An example of such a function is shown in Fig. 3.2. With this

switching function, it is possible to define the quantity $\lambda = s(z_i)s(z_j)$, which can be used (as shown below) to interpolate between pairwise particle forces and continuously change particle types within the buffer region. Hence, reversible interactions between particle pairs can be written as a linear combination between the atomistic MD forces and reversible SDPD forces [Eq.(3.2)] [20],

$$\mathbf{F}_{ij}|_{rev} = \lambda \mathbf{F}_{ij}^{MD} + (1-\lambda) \mathbf{F}_{ij}^{SDPD}|_{rev}. \quad (3.13)$$

The form for the MD force depends on the interatomic potential. More generally, Eq.(3.13) describes the reversible dynamics across the entire simulation domain; for example, for particle pairs in the MD region, $s(z)$ for both particles is equal to unity, and thus the second term vanishes, leaving only MD interactions, as we would expect. Similarly, if both particles are within the SDPD region, λ is zero for the pair and the first term involving MD forces vanishes, and the reversible dynamics are described by Eq.(3.2). Note that for the buffer

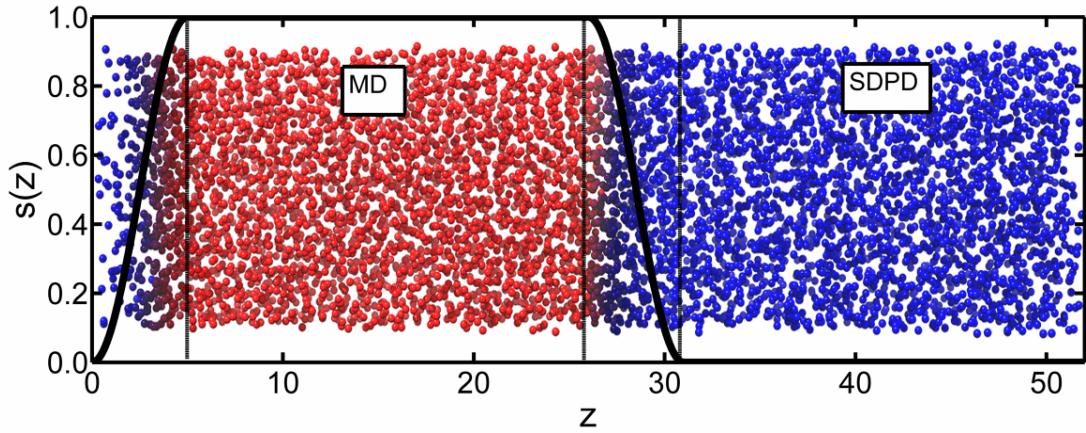


Fig. 3.2. Adaptive resolution weighting function versus position in the problem domain (dark black curve). A snapshot of the system is superimposed for clarity. The part of the domain where $s(z) = 1$ is the MD region, the part where it is zero is the SDPD region, and particles within the remaining “buffer” domains interact through a linear combination of both MD and SDPD forces.

region ($0 < \lambda < 1$), the weighting by λ is only applied to the reversible part of the dynamics, and the viscous and random forces [Eqs.(3.3) and (3.4)] are applied to *all* buffer particles without weighting. This is done in order to thermostat the buffer to the correct temperature and is discussed in more detail below. Because Eq.(3.13) interpolates between pairwise forces, momentum is conserved.

For a simple two-scale AdResS system with periodic boundary conditions in all directions and a vector normal to the two overlap or “buffer” regions between the MD and SDPD regions in the z -direction (Fig. 3.2), an example for the aforementioned weighting function used for interpolating forces inside a buffer bounded by $z = z_{min}$ and $z = z_{max}$ is [20]

$$s(z) = \sin^2 \left[\frac{\pi}{2} \left(\frac{z - z_{min}}{z_{max} - z_{min}} \right) \right], \quad z_{min} \leq z \leq z_{max}. \quad (3.14)$$

This function smoothly transitions from a value of zero in the SDPD domain to unity in the MD region. A similar function may be defined for the second buffer, which is necessary due to the simulation domain periodicity. The form for the global switching function is shown in Fig. 3.2, together with a superimposed example snapshot of the simulation box for a simple system with periodic boundary conditions in all directions.

Additional care is necessary to address the manner in which the MD potential is switched on/off within the buffer since it typically contains a steeply repulsive core. In this work, we choose a Lennard-Jones (LJ) potential for the MD region, which diverges at zero particle separation. The sudden onset of LJ interparticle forces at the MD/buffer interface when λ becomes nonzero can be catastrophic if the SDPD particle enters the buffer region close to another particle. Praprotnik et al. remedy this issue by capping the atomistic interactions [20]. Instead of this approach, we use the weight parameter λ to gradually switch on the atomistic repulsive forces. Specifically, within the buffer region we use core-softened

LJ interactions [52] that continuously approach the normal LJ interactions with decreasing distance from the LJ/buffer interface,

$$\mathbf{F}_{ij}^{MD}(r_{ij}, z_i, z_j) = \begin{cases} 24\varepsilon_{ij}r_{ij}^5 \left(\frac{2\sigma_{ij}^{12}}{[(1-\lambda)\sigma_{ij}^6 + r_{ij}^6]^3} - \frac{\sigma_{ij}^6}{[(1-\lambda)\sigma_{ij}^6 + r_{ij}^6]^2} \right) \mathbf{e}_{ij} & , r_{ij} \leq r_c, \\ \mathbf{0} & , r_{ij} > r_c. \end{cases} \quad (3.15)$$

Here, σ_{ij} and ε_{ij} set the length scale and energy for the interaction, respectively, and r_c is the cut-off radius. For the case of $\lambda = 1$, this expression reduces to the familiar LJ force. Even with these measures, an insufficiently small time-step may still lead to instability, although we find that this scheme is stable for typical MD simulation time-steps. It is worthwhile to note that the core-softened LJ potential is frequently used in alchemical free energy calculations that introduce and remove atoms and their interactions for related numerical reasons [53].

Lastly, it is necessary to apply a thermostat either to the full system or to the buffer region when using the AdResS approach [20,21]. The two domains in such a dual-scale simulation can be considered as different phases in equilibrium [20,21,26], with a corresponding latent heat for particles traveling between the atomistic and coarse regions. Without a thermostat, the loss of heat that occurs within the buffer region results in a MD domain at a lower temperature than the SDPD region that is by construction thermalized to the correct temperature. This undesirable temperature imbalance leads to a pressure differential that is relaxed by a transfer of mass into the MD region, resulting in a non-uniform density distribution. This issue is resolved by applying a thermostat to the entire buffer region. In this study, we use the SDPD thermostat, i.e. the irreversible and stochastic SDPD forces [Eqs.(3.3) and (3.4)] act on all buffer particles without any weighting by the

parameter λ , and the switching function is only used to interpolate between the MD and SDPD reversible dynamics. Hence, at one end of the buffer, the particles are simply a SDPD fluid, while at the other end they are a MD fluid coupled to a SDPD thermostat. This thermostat is similar to the dissipative particle dynamics (DPD) thermostat [54,55] that is frequently used in molecular dynamics simulations, which also introduces pairwise viscous and random forces between particles. The pure MD region itself is not thermostatted, but is still held at fixed temperature due to its interface with the buffer, and thus the correct deterministic dynamics in the MD region are preserved. We note that in addition to AdResS, hybrid explicit/implicit solvent approaches also typically require a similar stochastic buffer region [4,5], as do multiscale simulations using flux exchange [9] and the Schwarz alternating method [10].

3.5 Pairwise Thermodynamic Force

The unphysical mixture of interparticle forces within the buffer region [Eq.(3.13) and Fig. 3.3] can lead to deviations from the target density at equilibrium. For example, Lennard-Jones particles experience both attractions and stiff repulsions, whereas SDPD particles are subject to an effectively soft-repulsive many-body force. A mixture of these two fundamentally different forces can result in particles with very different properties (e.g. effective size, attraction, repulsion) than either of the two original interactions alone—for instance, mixed particles may have a repulsive core at a smaller radius, which leads to a local density increase at equilibrium. Similarly, the mixture of these forces could lead to a larger effective particle size and yield a region of depleted density. The specific implementation of λ in the selected MD potential [e.g. Eq.(3.15)] also affects how the effective particle diameter

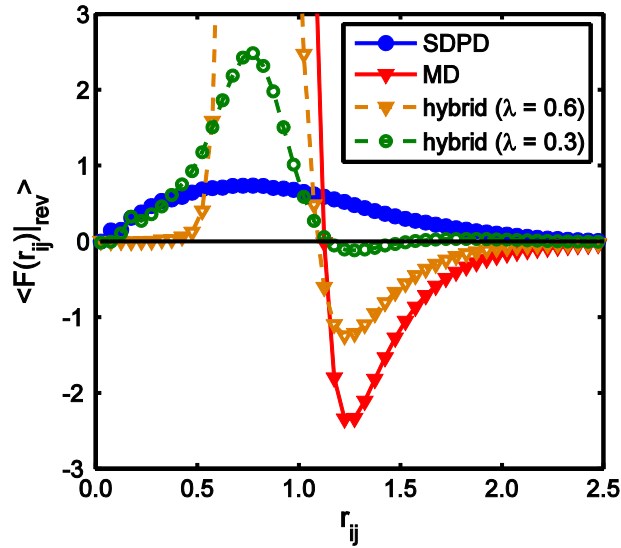


Fig. 3.3. Effective time-averaged force-versus-separation between particle pairs as a function of position within the buffer. Curves were obtained from simulations where all the particles in the system interact through either pure MD or SDPD forces, or some linear combination of the two that is constant throughout the simulation domain. The red (solid triangle) and blue (solid circle) curves denote the force between pure MD and SDPD particles, respectively. The green (hollow circle) and orange (hollow triangle) curves indicate the hybrid force at two different points within the buffer region. The results show that hybrid particles with λ between 0 and 1 can experience effective repulsions corresponding to a modified particle size.

changes with position within the buffer. The emergence of a non-uniform equilibrium density distribution in the transition region can be viewed in terms of chemical potential gradients due to mixed particles. Indeed, simulations using the hybrid methodology described above show significant deviations from the target density in the buffer if no means are taken to correct this (red curve, circle markers, Fig. 3.4b).

To compensate for these unphysical deviations from the target density, we introduce a “thermodynamic” force that performs work on the particles within the transition region such that the density remains approximately flat. A loose physical interpretation of this work is

that it gives the necessary effort required to remove or add degrees of freedom to a particle as it transitions from one type to the other. A similar approach has already been rationalized and tested in work using AdResS [25,26]; specifically, Fritsch et al. introduce a thermodynamic force of the form [26]

$$\mathbf{F}^{th} = \frac{m}{\rho_0} \nabla p(\mathbf{r}). \quad (3.16)$$

To a linear approximation, the force acting on particle i can be rewritten as

$$\mathbf{F}_i^{th} = -\frac{m_i}{\rho_0^2 \kappa_T} \nabla \rho(\mathbf{r}_i), \quad (3.17)$$

where κ_T and ρ_0 denote the isothermal compressibility and density, respectively, of the fluid at the desired thermodynamic state. Here, the pre-factor $1/\rho_0^2 \kappa_T$ is interpreted as the variation of the local chemical potential due to changes in density [26], since $(\partial\mu/\partial\rho)_T = 1/\rho^2 \kappa_T$. It is clear that Eq.(3.17) applies a force to particles only in the presence of density gradients, and that the force promotes particles to move from regions of higher to lower densities, i.e., opposite the gradient.

In order to determine the form for the thermodynamic force, it is necessary to perform a reference simulation and obtain the density profile within the buffer through a binning procedure. With the density profile known, Eq.(3.17) can be used to numerically determine an optimal force as a function of position. Then, a new simulation can be performed using this force and the new density distribution will appear “flatter”. Subsequent modifications to the force may need to be applied through iterations of Eq.(3.17) and additional test simulations until the density distribution is deemed sufficiently flat. A potential drawback of this type of force is that it is single-body and position-dependent, resulting in loss of momentum conservation within the simulation domain.

The ideas above can be reformulated in a particularly convenient way that also leads to improved behavior for the present scenario involving SDPD particles. For our problem we have access to the instantaneous density distribution at every time-step since we calculate SDPD interactions within the buffer; therefore, we seek to write an equivalent thermodynamic force that acts in real-time and does not require iterative simulations. Moreover, we would like to symmetrize this correction force such that it is pairwise and momentum is conserved. First, we write the thermodynamic force as

$$\mathbf{F}_i^{th} = -\frac{m_i}{\rho_0^2 \kappa_T} \frac{1}{\rho(\mathbf{r}_i)} \left[\rho(\mathbf{r}_i) \nabla \rho(\mathbf{r}_i) \right]. \quad (3.18)$$

Since $\rho(\mathbf{r}_i) \nabla \rho(\mathbf{r}_i) = (1/2) \nabla \rho^2(\mathbf{r}_i)$, this expression may be rewritten as

$$\mathbf{F}_i^{th} = -\frac{m_i}{2\rho_0^2 \kappa_T} \frac{1}{\rho(\mathbf{r}_i)} \nabla \rho^2(\mathbf{r}_i) = -\frac{m_i}{2\rho_0^2 \kappa_T} \frac{1}{\rho(\mathbf{r}_i)} \nabla \left[\rho^2(\mathbf{r}_i) - \rho_0^2 \right]. \quad (3.19)$$

Let $g(\mathbf{r}_i) \equiv \rho^2(\mathbf{r}_i) - \rho_0^2$ and note that we can write,

$$\mathbf{F}_i^{th} = -\frac{m_i}{2\rho_0^2 \kappa_T} \left[\nabla \left(\frac{g_i}{\rho_i} \right) + \frac{g_i}{\rho_i^2} \nabla \rho_i \right]. \quad (3.20)$$

Here, we have used the shorthand $g_i \equiv g(\mathbf{r}_i)$. In the SPH approximation, the gradient operator can be expressed as a sum over particles such that

$$\begin{aligned} \mathbf{F}_i^{th} &\approx -\frac{m_i}{2\rho_0^2 \kappa_T} \left[\sum_{j=1}^N \frac{m_j}{\rho_j} \frac{g_j}{\rho_j} \nabla_i W_{ij} + \frac{g_i}{\rho_i^2} \sum_{j=1}^N \frac{m_j}{\rho_j} \rho_j \nabla_i W_{ij} \right] \\ &= -\frac{m_i}{2\rho_0^2 \kappa_T} \sum_{j=1}^N m_j \left(\frac{g_i}{\rho_i^2} + \frac{g_j}{\rho_j^2} \right) \nabla_i W_{ij}. \end{aligned} \quad (3.21)$$

Therefore, we arrive at a pairwise thermodynamic force

$$\frac{\mathbf{F}_{ij}^{th}}{m_i} = -\frac{1}{2\rho_0^2 \kappa_T} \sum_{j=1}^N m_j \left[\frac{(\rho_i^2 - \rho_0^2)}{\rho_i^2} + \frac{(\rho_j^2 - \rho_0^2)}{\rho_j^2} \right] \frac{\partial W_{ij}}{\partial r_{ij}} \mathbf{e}_{ij}. \quad (3.22)$$

In the SPH approximation, the subtracted constant ρ_0 should vanish due to the antisymmetry of the weighting function derivative for a completely uniform particle distribution. If the particles are not distributed uniformly, the subtracted constant will lead to a non-zero contribution to the pairwise correction force and hence penalize deviations from a flat distribution. Note that Eq.(3.22) is equivalent to the reversible SDPD force [Eq.(3.2)] if we choose the following equation of state:

$$p_i = \frac{1}{2\rho_0^2\kappa_T}(\rho_i^2 - \rho_0^2). \quad (3.23)$$

The equation of state for a system that is a linear combination of two systems with identical equations of state may not necessarily be the same as that in the two individual regions [21] and hence we can also think of this thermodynamic force as a modification to the SDPD equation of state within the buffer that minimizes density gradients. Note that both the iterative and SDPD thermodynamic forces are independent of the specific choice for the MD interaction potential and are thus quite general. Here, the density ρ_0 includes the particle self-contribution (discussed in Section 3.2) since the force depends on the density defined at each particle, which will be overestimated for small smoothing lengths. Importantly, the force described by Eq.(3.22) is pairwise in form and thus conserves momentum. This pair force is zero if the density at both particles is precisely equal to the target density, as we would expect. If both particles occupy a high-density region and their densities are higher than the target value, the net force will be repulsive and drive them apart. If both particles are in a low-density region, the net force will be attractive, and thus impede the particles from separating.

One final modification to the thermodynamic force ensures that it only applies to mixed particles in the buffer region and continuously vanishes as both particles approach

either the pure MD or SDPD domains. This is achieved by using the switching function $s(z_i) \equiv s_i$ [Eq.(3.14)] to define a weighting parameter $\xi = 2[s_i(1-s_j) + s_j(1-s_i)]$ for the thermodynamic force, ensuring that it contributes maximally in the buffer center and vanishes at the boundaries. Hence, Eq.(3.13) is modified to include the pairwise thermodynamic force so that the reversible dynamics in the buffer are given by

$$\mathbf{F}_{ij}^{buffer} \Big|_{rev} = \lambda \mathbf{F}_{ij}^{MD} + (1-\lambda) \mathbf{F}_{ij}^{SDPD} \Big|_{rev} + \xi \mathbf{F}_{ij}^{th}. \quad (3.24)$$

3.6 Test of MD-SDPD Coupling at Equilibrium

In order to test this methodology, we first ensure that the coupling scheme yields proper thermodynamic equilibrium, that is, thermodynamic properties like the density and temperature remain uniform across the simulation domain containing both SDPD and MD regions. As a case study, we consider a simple Lennard-Jones fluid with periodic boundary conditions in all directions, as illustrated in Fig. 3.2. Values are reported in reduced Lennard-Jones units and all atoms have a mass of unity. The extent to which MD particles interact with their local environment is determined by the potential cut-off radius r_c , whereas the extent for the SDPD interaction depends on the particles' influence domain κh . Hence, we can ensure symmetric interactions and momentum conservation for the hybrid particles by equating the cut-off radius for the MD potential to the influence domain of the SDPD particles. The latter is chosen so that the SDPD particles are identically massive to the MD atoms ($h = 1.3$). Since $\kappa = 2$ for the cubic spline, it follows that $\kappa h = r_c = 2.6$. MD atoms are held at fixed temperature due to interactions with the buffer particles, which are thermalized using the SDPD thermostat as described in Section 3.4. The simulation box features a SDPD

domain adjacent to a MD domain with identical dimensions, where the two are separated by buffer regions using the AdResS approach discussed in Section 3.4. Periodic boundary conditions are used in the x -, y -, and z -directions, and the z -direction is normal to the interface separating the MD and SDPD regions.

A snapshot of the simulation domain is provided for clarity in Fig. 3.2 together with the switching function appropriate to this problem geometry. The pure MD and SDPD regions of the simulation domain have dimensions $L_x = L_y = 13$ and $L_z = 21$ with a reduced density of $\rho = 0.79$. Particles are initialized on a square $12 \times 12 \times 48$ lattice inside of a box with dimensions $13 \times 13 \times 52$, with those between $z = 0$ and $z = 5$ (and $z = 26$ and $z = 31$) designated as buffer particles. Hence, there are a total of 6912 particles. The region between $z = 5$ and 26 is the MD domain, and between $z = 31$ and 52 is the SDPD one. The MD and SDPD regions are separated by buffers of width 5. The target temperature is $T = 1.0$, and the fluid bulk and shear viscosities are $\zeta = 0.9$ [56] and $\eta = 1.9$ [57,58], respectively. For time-integration, we use a modified velocity-Verlet algorithm where SDPD viscous forces are determined from an extrapolated velocity computed at the previous time-step [54], and we choose a time-step of $\Delta t = 0.002$. The system is equilibrated for 2×10^5 time-steps, and data is averaged over 1×10^5 time-steps.

In pure SDPD simulations, the fluid thermodynamic properties are specified by the equation of state, which is used to obtain the pressure distribution that determines the reversible dynamics given by Eq.(3.2). For simulations of incompressible fluids, a common choice for the equation of state is $p_i = c_s^2 \rho_i$ [30], where c_s is the speed of sound. The parameter c_s is often selected based on convenience such that small density variations yield large pressure gradients, yet not so large that an impractically small time-step is required (i.e. such that the fluid is actually quasi-incompressible). However, the above equation of state

cannot be used directly for MD/SDPD multiscale simulations since the speed of sound of a Lennard-Jones fluid in reduced units at this thermodynamic state is $c_s = 5$ [34], which would result in an excessively high pressure in the SDPD domain and drive a flux of mass into the MD region. Furthermore, for a SDPD fluid characterized by a small smoothing length, the density and hence pressure at a given particle is overestimated due to self-contribution effects (discussed in Section 3.2). Therefore, we modify the aforementioned linear equation-of-state to ensure that the absolute pressure is not altered by changing the speed of sound,

$$p_i = c_s^2 (\rho_i - \rho_0) + p_0. \quad (3.25)$$

Here, p_0 is the target pressure, and ρ_0 is the target density including the overestimation due to self-contribution to density. This expression is simply a local, linear approximation to the full equation of state where the absolute pressure and compressibility can be adjusted independently, hence making it possible to use the appropriate value for the speed of sound and thus match both compressibility and absolute pressure to the target fluid. For the temperature and density investigated here, the target pressure for the LJ fluid with a cut-off $r_c = 2.6$ is $p_0 \approx 1.4$. For SDPD particles with a smoothing length of $h = 1.3$, the overestimated averaged density at each particle from Eq.(3.7) is found to be $\rho_0 \approx 0.804$, which is slightly larger than the actual value of 0.787 due to self-contribution effects. This discrepancy is important to note: this overestimated SDPD density should be used as the target density in the above equation of state [Eq.(3.25)] and the pairwise thermodynamic force [Eq.(3.22)] since both of those quantities depend on the density defined at each particle. This quantity can be obtained by running an inexpensive pure SDPD simulation at the desired thermodynamic state and averaging particle densities. From equilibrium MD simulations, we

find that the compressibility of a LJ fluid at the selected thermodynamic state is $\kappa_T \approx 0.08$, and hence the pre-factor for the thermodynamic force is $1/2\rho_0^2\kappa_T \sim 10$.

The overall approach just described is tested in the absence of flow fields. We find that thermal equilibrium is readily achieved and the pure MD and SDPD fluids converge within 2.0% accuracy to the correct temperature as estimated from the particle kinetic energies. Namely, there are no significant temperature gradients in the direction normal to the interface between the two domains (Fig. 3.4a). This accuracy can be further improved by coupling the buffer more strongly to a thermostat, or applying a thermostat to the full system.

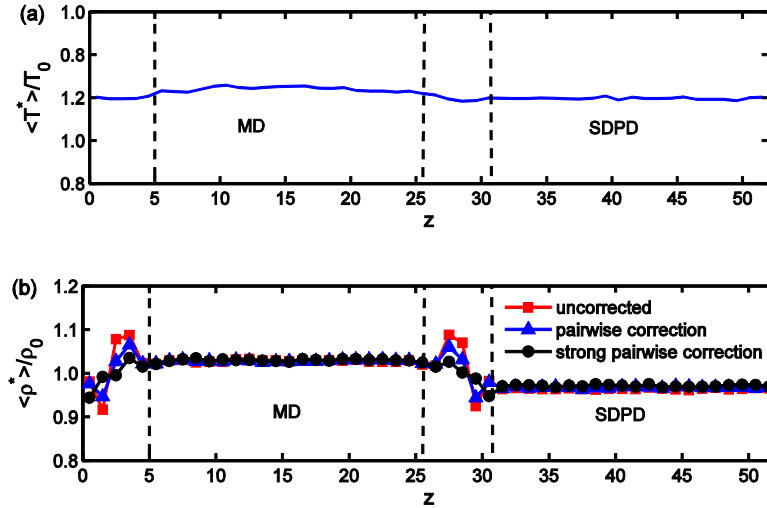


Fig. 3.4. (a) Temperature profile for a LJ system coupled to a SDPD domain at equilibrium with a pairwise correction force. The profile is approximately flat, with deviations less than 2.0% from the target temperature. (b) Density profiles for the system. The red curve (triangles) is the density without corrections, while the blue curve (squares) is with a pairwise correction. The densities within the MD/SDPD domains are within 3.2% of the target value with this correction. The black curve (circles) is the density profile when the strength of the pairwise thermodynamic force is increased by a factor of 10. For the MD and buffer regions, densities are computed by binning the system and counting particles, while for the SDPD part of the system, we use the SPH calculation for density [Eq.(3.7)] at randomly sampled points.

Moreover, the density profile in the system is approximately flat. Fig. 3.4b shows the density profile in the z -direction with and without the pairwise thermodynamic correction force. While the former exhibits some unphysical deviations in the buffer region from the target value, it is improved relative to the case without the thermodynamic force. The uncorrected density profile is within 2.8% and 3.6% of the target value within the MD and SDPD regions, respectively, with more substantial deviations in the buffer. With this force, the average densities inside the MD and SDPD regions are both within 2.9% and 3.2%, respectively, and the deviations inside the buffer are noticeably reduced. The flatness of the density distribution can also be further improved by increasing the prefactor in the pairwise corrective force. Increasing the strength of this force by a factor of 10 reduces deviations in the buffer further and lowers the error in the pure MD and SDPD regions to less than 2.9%. Finite-size effects appear to have a measurable, albeit weak, influence on this approach. We have performed equilibrium tests in the absence of a thermodynamic force with bulk MD/SDPD regions twice as large as the case discussed above, as well as twice as small. Increasing the volume of the bulk MD and SDPD regions by a factor of four, while keeping the buffer domains identical in size, leads to a change in the density in the SDPD region from 0.756 to 0.760, and from 0.805 to 0.810 in the MD region.

We have also investigated fluctuations in key quantities for the equilibrium case. By construction, the multiscale method correctly captures fluctuations in velocity and reproduces the appropriate Maxwell-Boltzmann statistics throughout the entire simulation domain. The standard deviation of the density in the MD, SDPD, and buffer regions is $\sigma_\rho \approx 0.027$, 0.042, and 0.036, respectively. These results suggest that the compressibility is approximately matched in all three regions; a more careful choice for the speed of sound in the equation of state [Eq.(3.25)] may improve these results. We also note that the unphysical deviations from

the target density will affect the compressibilities, and hence some non-uniformity between the compressibility values is expected. Finally, the soft potential in the coarse-grained SDPD domain leads to a slightly higher diffusivity than in the MD region, which is a common feature of coarse-grained systems, and hence mass diffusivity is not completely uniform across the full simulation domain.

We find that the density profile can be further flattened through several approaches. One alternative is to use the iterative non-pairwise thermodynamic force, Eq.(3.17). In principle, with a sufficient number of iterations and appropriate choice for a thermostat, it is possible to obtain a flat density profile to arbitrary precision using this force. This approach would be less suited for non-equilibrium problems, however, since it does not conserve momentum and may require strong thermostating. Alternatively, since the Navier-Stokes solution does not depend on the absolute pressure of the fluid, we can adjust the p_0 parameter in the SDPD equation of state [Eq.(3.25)]. Reducing its value to $p_0 = 0.5$, we find that the error in density in the pure MD and SDPD regions is improved to 0.5% and 1.2%, respectively. It may be possible to reduce the error even further with a more careful tuning of p_0 . Finally, the unphysical density deviations in the buffer region can also be reduced by implementing a three-part overlap domain. In this approach, the MD-to-SDPD and SDPD-to-MD transition regions are separate, with a MD/SDPD coexistence region between them where particles of different types interact via SDPD forces. This approach will be the subject of future work.

3.7 Non-Equilibrium Cases Involving the Start Up of Shear Flow

To levy a more challenging test, we ask how accurately the hybrid method reproduces the correct dynamical behavior in a non-equilibrium scenario, when fluxes of momentum and mass must be preserved across the buffer region. We again consider a Lennard-Jones fluid but in a slab geometry confined between two solid interfaces. After equilibration, we subject it to the start up of shear flow by moving one of the solid boundaries with a constant velocity. In order to demonstrate the robustness of this multiscale technique, we consider two distinct cases: (1) shear forces act in a direction perpendicular to the interface separating the atomistic and continuum regions, and (2) shear forces act in a direction parallel to the buffer region. In the former case, particles are actually convected by the shear forces through the buffer region and thus in some sense are forced (by the flow) to change type. In the latter, particles are not convected across the buffer region but diffuse on their own through Brownian motion. For all of the non-equilibrium simulations considered, we apply the pairwise correction force (Section 3.5) and SDPD thermostat (Section 3.4) in the buffer so that momentum in the fluid is conserved.

In the perpendicular case, fluid is convected across the buffer region between the MD and SDPD domains due to the motion of the solid boundary, as illustrated in Fig. 3.5a. Wall particles within the atomistic region are treated as Lennard-Jones atoms tethered to a fixed position in space using a harmonic potential with a force constant $k = 1000$. For the moving wall, the equilibrium positions of the harmonic potential for the boundary particles are translated at the appropriate velocity. When these atoms enter the buffer region, harmonic forces are turned off and the particles freeze at their instantaneous positions, at which point they are translated at the wall velocity. These transitional wall particles interact with LJ wall

particles through pure LJ interactions and with fluid particles in the buffer through AdResS mixed forces, as described previously. We use an Andersen thermostat for the wall particles in the MD region. Cross interactions involving hybrid boundary particles are treated as described in Sections 3.4 and 3.5, with the pairwise thermodynamic force applied only to fluid particle pairs. In order to prevent boundary penetration within the SDPD/hybrid domains, wall atoms are initialized on a lattice with a higher number density than the fluid ($\rho_n = 1.0$), and transition/SDPD fluid particles are specularly reflected at the solid-liquid interface, i.e., if a particle crosses the wall boundary, the velocity component of the particle normal to the wall is reversed such that it re-enters the fluid domain at the following time-step. The wall is translated in the x -direction with unit velocity. The thickness of the walls is 5 and the channel width is 13; in the x -direction, the SDPD and MD domains have a length of 8 and the buffers have a width of 5. Fluid atoms are initialized at the same number density and temperature as in the equilibrium study, and with the same equation of state and corrective force magnitude for the buffer. The total number of particles is 6836. Due to the large number of hybrid particle interactions, this system setup is not particularly efficient and is included to demonstrate the robustness of the technique with respect to the placement of the transition regions.

For the parallel case (Fig. 3.5b), the box dimensions are $13 \times 13 \times 36$ and the channel width is 26. The fluid atoms are initialized on a $12 \times 12 \times 24$ lattice between $z = 5$ and 31, while wall atoms are initialized between $z = 0$ and 5 and $z = 31$ and 36 with number density $\rho_n = 1.0$. This results in a total of 5146 particles. The buffer region boundaries are at $z = 15.5$ and 20.5. In this case, one solid interface consists entirely of MD particles, while the other is always composed of SDPD particles; no transition between particle types ever occurs within each wall. Specular reflection is only required at the SDPD fluid-wall interface where the

soft SDPD pressure force and high particle diffusivity can lead to boundary penetration. The MD harmonically-tethered wall atoms are again held at a fixed temperature of $T = 1$ using an Andersen thermostat and the equilibrium positions of the harmonic potential are translated with a velocity of 1. For both cases, we select $\Delta t = 0.001$ and equilibrate for 5×10^4 steps before shearing.

Fig. 3.5c shows the velocity profiles for the perpendicular case in the MD, SDPD, and

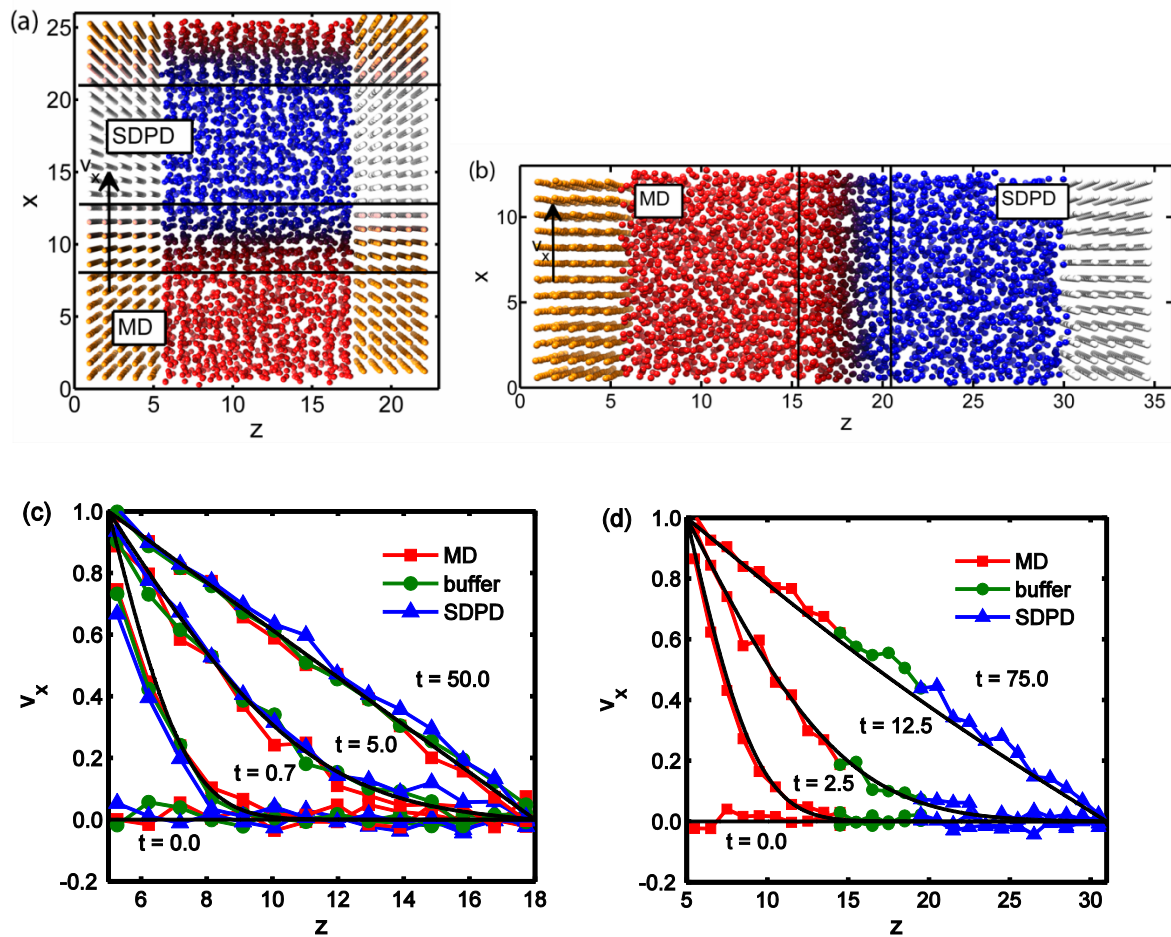


Fig. 3.5. Snapshots of the system for the (a) perpendicular and (b) parallel flow cases. (c) Velocity profiles for the MD, buffer, and SDPD domains for perpendicular start-up shear flow as compared to the analytical solution. (d) Velocity profiles for the parallel case. The velocities are averaged over 20 independent trajectories for both scenarios.

buffer regions at various times in the simulation. Rather than performing a local time average, results are averaged over 20 trajectories initialized with different random seeds in order to correctly capture hydrodynamics [59,60]. The MD fluid is thermostatted by both the harmonic oscillating walls in the atomistic region, as well as through contact with the fluid in the buffer. We find that the observed velocity profile in each region is in good agreement with the exact analytical solution. The absolute error in the velocity per bin, averaged over the simulation production trajectory and treating the analytical solution as exact, is approximately 0.021 in the buffer, 0.025 in the MD region, and 0.035 in the SDPD region. The average velocity in the channel approaches the expected linear profile at steady-state.

The velocity profiles for the parallel case are shown in Fig. 3.5d, and are also in agreement with the exact continuum solution, with an averaged absolute error in the velocity profile of 0.025. At steady-state, there is a subtle deviation from the expected velocity profile in the buffer region between the MD and SDPD domains for the parallel case. This is due to the unphysical, spatially-varying combination of forces, combined with the uniformly applied SDPD thermostat, which results in a fluid with a position-dependent viscosity. If better accuracy is required, this type of artifact in the dynamics may potentially be remedied by introducing a position-dependent thermostat as in Ref. [23]. Since tuning the parameter p_0 may be used to improve the density distribution (Section 3.6), we have also performed simulations for the parallel and perpendicular cases at a reduced absolute pressure of $p_0 = 0.8$ and find no appreciable difference in the results from the case with the true pressure.

3.8 Triple-Scale Simulation of Shear Flow

One of the main motivations behind this multiscale approach is that it provides a natural interface between MD and continuum models. While the SDPD region considered in the examples in Sections 3.6 and 3.7 is of comparable molecular size, it is possible to further couple this domain to a series of continuum models of increasing length scale, all the way up to the non-fluctuating hydrodynamic limit. To illustrate how such a *hierarchy* of resolutions might work, we consider the parallel shear case and include one MD and two SDPD domains of different resolution (Fig. 3.6a). The strategy for bridging SDPD fluids with different smoothing lengths is described in greater detail in Chapter 4 and in Ref. [34], and thus we do not elaborate on that approach here. We choose a smoothing length for the coarse SDPD particles of $h = 1.64$, which gives particles twice as massive as the finer SDPD ones next to the MD part of the system.

The triple-scale simulation is performed as follows. The global box dimensions are $13 \times 13 \times 57$. The MD wall has a thickness of 5 and atoms are again initialized at a higher density than the fluid ($13 \times 13 \times 5$ cubic lattice). Next to the wall, atomically-resolved particles are initialized on a $12 \times 12 \times 24$ lattice across a volume with dimensions $13 \times 13 \times 26$, where particles within a distance of 10.5 to the wall are designated as MD atoms, particles between 10.5 and 15.5 units from the wall are hybrid particles, and beyond that particles are designated as a SDPD fluid with $h = 1.3$. Adjacent to this domain is the coarse SDPD region, where particles are initialized on a square $9 \times 10 \times 19$ lattice over a region with volume $13 \times 13 \times 26$. Coarse particles within a distance of 6 from the box edge are designated as SDPD wall particles. The interface region between the fine and coarse SDPD domains has a width of 6 and is centered at the point initially separating these two regions. The coarse SDPD

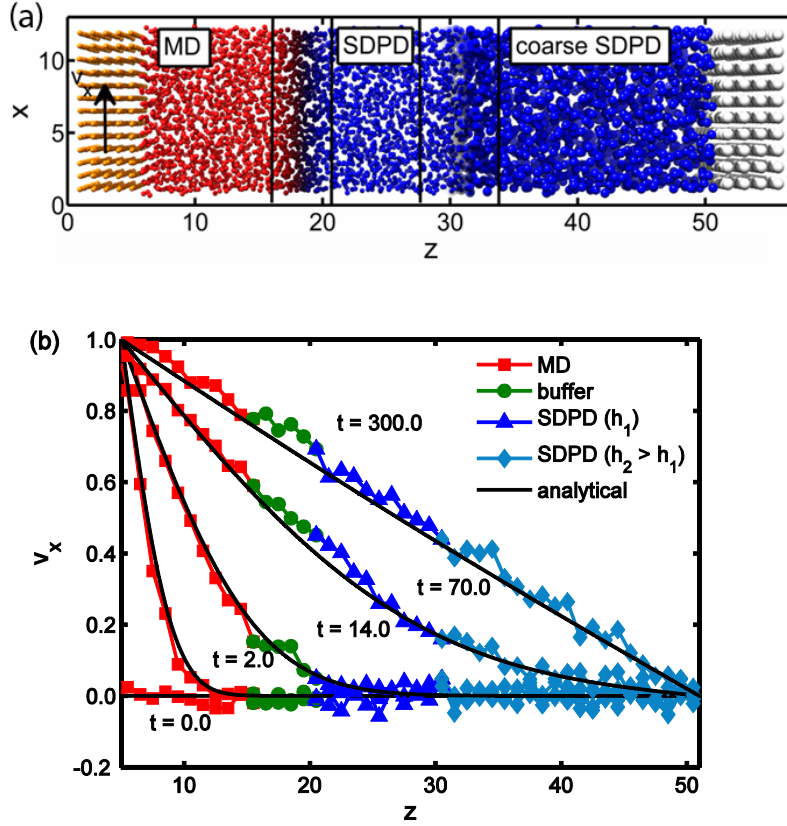


Fig. 3.6. (a) Visualization of the system for the parallel flow, triple-scale simulation. The coarse SDPD particles are twice as massive as the finely-resolved ones, with half the number density. (b) Velocity profiles across the channel width for different times when the fluid is sheared. The exact solution is shown in black.

number density is half of that in the finely-resolved region; hence, the number of particles in the simulation box is reduced by ~ 1746 as compared to the all-atom case to a total of 6011 particles. The equilibration time and time-step magnitude are the same as in Section 3.7.

The system setup and time-dependent velocity profiles are illustrated in Fig. 3.6. Once again, we find that the transient solution, averaged over a set of 20 simulations, is in agreement with the analytical result throughout the entire problem domain. Hence, momentum is correctly transferred across the hierarchy of scales and regions of different resolution such that dynamical flows are accurately reproduced.

Note that this approach requires simulating an atomically-resolved continuum region that acts as a bridge between the molecular region and the coarse-grained continuum one. The number of unphysical atomically-sized continuum particles necessary can be dramatically reduced by shrinking the fine SDPD region to zero size. The buffer region between the MD and continuum region must have width greater than r_c so that pure MD particles do not interact with continuum ones. Similarly, if the transition zone between SDPD domains with different resolution is too small, the abrupt change in smoothing length may result in artifacts in the density [61]. However, there is no limitation for the atomically-resolved SDPD region that separates these transition zones, which can be made arbitrarily small. In this kind of setup, MD particles crossing the buffer region gradually transition into SDPD particles, and immediately enter into the refining part of the transition zone between fine and coarse SDPD particles. We have performed equilibrium tests where the fine SDPD region is removed entirely and find no appreciable difference in the density and temperature profiles. Density profiles from equilibrium simulations comparing the case with and without the atomically-resolved SDPD region are provided in Appendix 3.10.1 and indicate that including the fine SDPD region is not required. Therefore, using the approach described in Sections 3.4 and 3.5, it is possible to couple a MD fluid directly to a coarse SDPD region where the fluid volumes are more massive than the MD atoms, giving additional significant computational savings.

3.9 Conclusions

In this chapter, we describe a new hybrid MD-SDPD coupling strategy for interfacing a hierarchy of regions spanning a broad range of length scales from the molecular to the non-

fluctuating continuum limit. This multiscale modeling approach has both advantages and limitations. In terms of advantages, the method ensures mass conservation in a very intuitive fashion and does not require iterative simulations to derive a new coarse-grained particle model if a different temperature or density becomes of interest, as would be the case for structure-, force-, or energy-matching approaches. Furthermore, there is no constraint on the atomistic model, provided that it is adequately described as a continuum fluid and the appropriate thermodynamic and transport properties at the desired temperature are known. However, as discussed in Sections 3.5 and 3.6, the method does require knowledge of the system target density with corrections due to self-contribution effects, which necessitates running a short, pure SDPD simulation to calculate the overestimated densities at each particle as compared to the global system density.

In the multiscale approach, we couple MD to a region of SDPD particles with the same mass as those in the atomistic region. Since SDPD particles are interpreted as volumes of fluid, one obvious question is the validity of a SDPD fluid where the fluid volumes have the same size as the atoms in the MD region. The viability of a top-down, continuum approach at molecular scales is not immediately clear, particularly for non-homogeneous and complex fluids. In this respect, the atomically-sized SDPD fluid might simply be interpreted as a convenient ansatz that successfully bridges continuum and MD worlds and that satisfies an appropriate number of constraints, including the fluctuation-dissipation theorem and basic conservation laws. Moreover, the continuum approximation often turns out to work surprisingly well when applied to molecular-scale problems (for instance, the accuracy of the Stokes-Einstein relation in predicting diffusivities), and this appears to be the case here. For the systems considered in this chapter the approach is sufficient, although it may not be successful for more complicated fluids. Ultimately, this model provides a bridge between

atomistic models and *increasingly* coarse SDPD regions. Through a hierarchy of SDPD domains with different resolutions, it is possible to coarse-grain to a scale where the SDPD model is appropriate. Finally, it is also possible to shrink this atomically-sized continuum region to zero size such that a very small number of these particles need to be included for a given problem, as described in Section 3.8.

Perhaps the most significant disadvantage of the presented MD-SDPD approach is that it does not decouple time scales. The maximum possible time-step is limited by the smallest characteristic time scale in the system, determined by the most finely-resolved region in the domain. Even if the spatial domains are described by a range of length scales from molecular to highly coarse, all regions will be constrained to evolve over the same time scales. In this respect, the major computational savings would stem from a reduction in the number of particles describing the overall simulation, which of course can be quite significant in a simulation with a hierarchy of SDPD regions. However, an attractive feature of smoothed particle methods is that particle positions and velocity can be integrated in time using algorithms typically used in MD, and there exists a body of literature describing modified integrators that allow for multiple time scales. Hence, it may be possible to use multiple time-step integrators, such as ones originally developed for MD simulations by Tuckerman et al. [62–67], to decouple time scales between the coarse SDPD regions and finely resolved ones. In fact, the problem of decoupling time scales in MD simulations containing particles with disparate masses has already been addressed [63,62], although it is unclear if these techniques will work for SDPD.

In summary, this work demonstrates that it is possible to employ an adaptive resolution scheme in coupling a finely-resolved, molecularly-detailed part of a simulation domain treated via molecular dynamics to a fluctuating continuum domain. In contrast to

earlier approaches that interface particle-based MD simulations with field-based finite-volume discretizations, the approach taken here involves representing the continuum solution using a particle-based technique, namely smoothed dissipative particle dynamics. The overall strategy involves defining a buffer region in which particles smoothly change type when passing from the SDPD to MD domain and vice versa. Here we have described how to design such a buffer in terms of specific interpolations of reversible interactions and the addition of “thermodynamic” forces that account for the change in particle types and minimize boundary artifacts. Such simple, modular, and hierarchical approaches in multiscale simulation are of growing importance in light of the wide range of problems that require the inclusion of multiple length scales. In this work we consider a simple Lennard-Jones fluid and show that the MD-SDPD approach reproduces proper thermodynamic equilibrium globally, as well as accurate transient solutions to simple time-dependent hydrodynamic problems independent of the buffer region placement. Because of the success in previous studies using AdResS to couple MD fluids with more complicated molecular structure to spherically-symmetric coarse-grained particles, we expect that this approach can be readily extended to coupling more complicated MD fluids to multiple SDPD domains.

3.10 Appendix

3.10.1 Equilibrium Multiscale Simulations with and Without Intermediate SDPD

Region

We have performed equilibrium simulations of a fluid in a slab geometry (bounded by walls, where the vector normal to the boundaries is in the z -direction). For these tests, the coarse SDPD fluid particles are four times as massive as the MD particles. All other quantities are the same as the ones described in Section 3.6. Two tests were performed, 1) a simulation featuring an atomically-resolved SDPD region, similar to the one described in

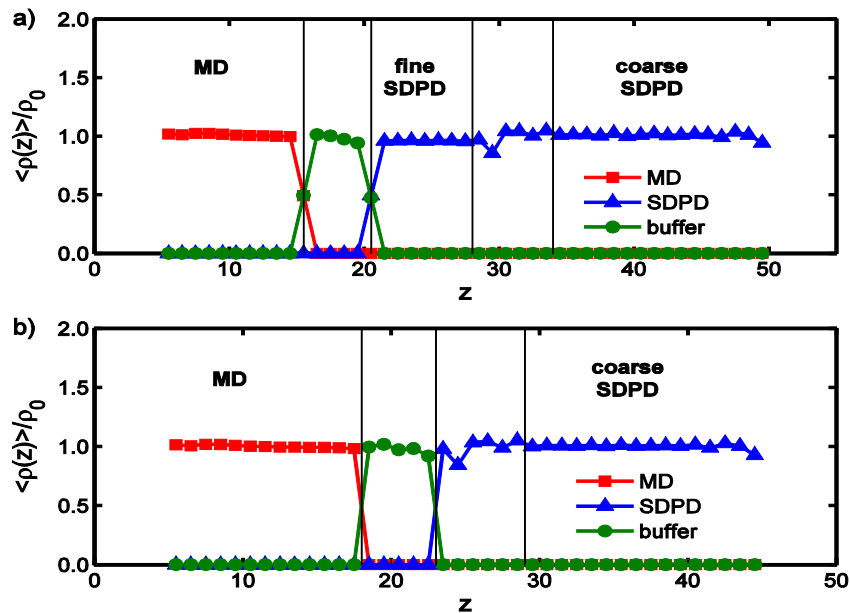


Fig. A3.1. (a) Density profile for fluid between two walls including the atomically-resolved SDPD region. (b) Density profile for a system that is identically set up as in (a), except it does not feature a fine SDPD region. Note that there is no discernible difference due to a lack of this domain. As discussed in Section 3.5, there is a minor mismatch in the densities in the pure MD/SDPD regions, and some deviations of the target density in the transition region.

Section 3.8, albeit without any fluid motion and 2) a simulation that is identical in all respects, except the atomically-resolved SDPD region is removed. For the latter case, the MD-SDPD transition region is immediately adjacent to the fine SDPD-to-coarse SDPD interface. Hence, for a MD particle moving in the positive z -direction, it gradually transitions into a fine SDPD particle, and is immediately combined with another nearby fine SDPD particle.

3.11 References

- [1] N. G. Hadjiconstantinou, *J. Comput. Phys.* **154**, 245 (1999).
- [2] D. C. Tretheway and C. D. Meinhart, *Phys. Fluids* **16**, 1509 (2004).
- [3] S. Thomas, A. Esmaeeli, and G. Tryggvason, *Int. J. Multiph. Flow* **36**, 71 (2010).
- [4] C. L. Brooks III and M. Karplus, *J. Chem. Phys.* **79**, 6312 (1983).
- [5] A. Brünger, C. L. Brooks III, and M. Karplus, *Chem. Phys. Lett.* **105**, 495 (1984).
- [6] D. Beglov and B. Roux, *Biopolymers* **35**, 171 (1995).
- [7] A. Okur, L. Wickstrom, M. Layten, R. Geney, K. Song, V. Hornak, and C. Simmerling, *J. Chem. Theory Comput.* **2**, 420 (2006).
- [8] J. A. Wagoner and V. S. Pande, *J. Chem. Phys.* **134**, 214103 (2011).
- [9] S. T. O’Connell and P. A. Thompson, *Phys. Rev. E* **52**, R5792 (1995).
- [10] N. G. Hadjiconstantinou and A. T. Patera, *Int. J. Mod. Phys. C* **8**, 967 (1997).
- [11] X. B. Nie, S. Y. Chen, W. N. E, and M. O. Robbins, *J. Fluid Mech.* **500**, 55 (2004).
- [12] R. Delgado-Buscalioni and G. De Fabritiis, *Phys. Rev. E* **76**, 36709 (2007).
- [13] R. Delgado-Buscalioni and P. V. Coveney, *Phys. Rev. E* **67**, 46704 (2003).
- [14] R. Delgado-Buscalioni, E. G. Flekkøy, and P. V. Coveney, *EPL Europhys. Lett.* **69**, 959 (2005).
- [15] R. Delgado-Buscalioni, P. V. Coveney, G. D. Riley, and R. W. Ford, *Philos. Trans. R. Soc. Math. Phys. Eng. Sci.* **363**, 1975 (2005).
- [16] L. D. Landau and E. M. Lifshitz, *Fluid Mechanics, Second Edition: Volume 6*, 2nd ed. (Butterworth-Heinemann, Amsterdam, 1987).
- [17] Hadjiconstantinou, N. G., *Bull. Pol. Acad. Sci.* **53**, 335 (2005).
- [18] D. A. Fedosov and G. E. Karniadakis, *J. Comput. Phys.* **228**, 1157 (2009).

- [19] A. Dupuis, E. M. Kotsalis, and P. Koumoutsakos, *Phys. Rev. E* **75**, 46704 (2007).
- [20] M. Praprotnik, L. Delle Site, and K. Kremer, *J. Chem. Phys.* **123**, 224106 (2005).
- [21] M. Praprotnik, L. Delle Site, and K. Kremer, *Phys. Rev. E* **73**, 66701 (2006).
- [22] M. Praprotnik, S. Matysiak, L. D. Site, K. Kremer, and C. Clementi, *J. Phys. Condens. Matter* **19**, 292201 (2007).
- [23] S. Matysiak, C. Clementi, M. Praprotnik, K. Kremer, and L. Delle Site, *J. Chem. Phys.* **128**, 24503 (2008).
- [24] R. Delgado-Buscalioni, K. Kremer, and M. Praprotnik, *J. Chem. Phys.* **131**, 244107 (2009).
- [25] S. Poblete, M. Praprotnik, K. Kremer, and L. D. Site, *J. Chem. Phys.* **132**, 114101 (2010).
- [26] S. Fritsch, S. Poblete, C. Junghans, G. Ciccotti, L. Delle Site, and K. Kremer, *Phys. Rev. Lett.* **108**, 170602 (2012).
- [27] R. Potestio, S. Fritsch, P. Español, R. Delgado-Buscalioni, K. Kremer, R. Everaers, and D. Donadio, *Phys. Rev. Lett.* **110**, 108301 (2013).
- [28] L. B. Lucy, *Astron. J.* **82**, 1013 (1977).
- [29] R. A. Gingold and J. J. Monaghan, *Mon. Not. R. Astron. Soc.* **181**, 375 (1977).
- [30] G. R. Liu and M. B. Liu, *Smoothed Particle Hydrodynamics: A Meshfree Particle Method* (World Scientific Publishing Company, 2003).
- [31] P. Español and M. Revenga, *Phys. Rev. E Stat. Nonlin. Soft Matter Phys.* **67**, 26705 (2003).
- [32] W. Dzwiniel, W. Alda, and D. A. Yuen, *Mol. Simul.* **22**, 397 (1999).
- [33] G. C. Ganzenmüller, S. Hiermaier, and M. O. Steinhauser, *Eur. Phys. J. Spec. Top.* **206**, 51 (2012).

- [34] P. M. Kulkarni, C.-C. Fu, M. S. Shell, and L. Gary Leal, *J. Chem. Phys.* **138**, 234105 (2013).
- [35] A. Vázquez-Quesada, M. Ellero, and P. Español, *J. Chem. Phys.* **130**, 34901 (2009).
- [36] S. Litvinov, M. Ellero, X. Hu, and N. A. Adams, *Phys. Rev. E* **77**, 66703 (2008).
- [37] S. Litvinov, X. Y. Hu, and N. A. Adams, *J. Phys. Condens. Matter* **23**, 184118 (2011).
- [38] N. Moreno, P. Vignal, J. Li, and V. M. Calo, *Procedia Comput. Sci.* **18**, 2565 (2013).
- [39] X. Bian, S. Litvinov, R. Qian, M. Ellero, and N. A. Adams, *Phys. Fluids* **24**, 12002 (2012).
- [40] A. Vázquez-Quesada, M. Ellero, and P. Español, *Phys. Rev. E* **79**, 56707 (2009).
- [41] S. R. D. Groot and P. Mazur, *Non-Equilibrium Thermodynamics*, Dover edition (Dover Publications, New York, 2011).
- [42] M. Grmela and H. C. Öttinger, *Phys. Rev. E* **56**, 6620 (1997).
- [43] H. C. Öttinger and M. Grmela, *Phys. Rev. E* **56**, 6633 (1997).
- [44] H. C. Öttinger, *Beyond Equilibrium Thermodynamics* (Wiley-Interscience, Hoboken, N.J., 2005).
- [45] P. Español, *Phys. Rev. E* **57**, 2930 (1998).
- [46] J. J. Monaghan and J. C. Lattanzio, *Astron. Astrophys.* **149**, 135 (1985).
- [47] J. J. Monaghan, *Comput. Phys. Rep.* **3**, 71 (1985).
- [48] A. P. Whitworth, A. S. Bhattal, J. A. Turner, and S. J. Watkins, *Astron. Astrophys.* 929 (1995).
- [49] O. Flebbe, S. Munzel, H. Herold, H. Riffert, and H. Ruder, *Astrophys. J.* 754 (1994).
- [50] J. P. Morris, P. J. Fox, and Y. Zhu, *J. Comput. Phys.* **136**, 214 (1997).
- [51] J. J. Monaghan, *J. Comput. Phys.* **82**, 1 (1989).
- [52] D. M. Heyes, *J. Chem. Phys.* **132**, 64504 (2010).

- [53] T. C. Beutler, A. E. Mark, R. C. van Schaik, P. R. Gerber, and W. F. van Gunsteren, Chem. Phys. Lett. **222**, 529 (1994).
- [54] R. D. Groot and P. B. Warren, J. Chem. Phys. **107**, 4423 (1997).
- [55] T. Soddemann, B. Dünweg, and K. Kremer, Phys. Rev. E **68**, 46702 (2003).
- [56] K. Meier, A. Laesecke, and S. Kabelac, J. Chem. Phys. **122**, 14513 (2004).
- [57] R. L. Rowley and M. M. Painter, Int. J. Thermophys. **18**, 1109 (1997).
- [58] K. Meier, A. Laesecke, and S. Kabelac, J. Chem. Phys. **121**, 3671 (2004).
- [59] S. Orlandini, S. Meloni, and G. Ciccotti, Phys. Chem. Chem. Phys. **13**, 13177 (2011).
- [60] S. Orlandini, S. Meloni, and G. Ciccotti, in *AIP Conf. Proc.* (AIP Publishing, 2011), pp. 77–95.
- [61] J. A. Backer, C. P. Lowe, H. C. J. Hoefsloot, and P. D. Iedema, J. Chem. Phys. **123**, 114905 (2005).
- [62] M. Tuckerman, B. J. Berne, and G. J. Martyna, J. Chem. Phys. **97**, 1990 (1992).
- [63] M. E. Tuckerman, B. J. Berne, and A. Rossi, J. Chem. Phys. **94**, 1465 (1991).
- [64] M. E. Tuckerman and B. J. Berne, J. Chem. Phys. **95**, 8362 (1991).
- [65] M. E. Tuckerman, B. J. Berne, and G. J. Martyna, J. Chem. Phys. **94**, 6811 (1991).
- [66] M. E. Tuckerman, B. J. Berne, and A. Rossi, J. Chem. Phys. **94**, 1465 (1991).
- [67] M. E. Tuckerman, G. J. Martyna, and B. J. Berne, J. Chem. Phys. **93**, 1287 (1990).

4 Multiscale Simulation of Ideal Mixtures Using Smoothed Dissipative Particle Dynamics

Smoothed dissipative particle dynamics (SDPD) [P. Español and M. Revenga, Phys. Rev. E Stat. Nonlin. Soft Matter Phys. **67**, 026705 (2003).] is a thermodynamically-consistent particle-based continuum hydrodynamics solver that features scale-dependent thermal fluctuations. We obtain a new formulation of this stochastic method for ideal two-component mixtures through a discretization of the advection-diffusion equation with thermal noise in the concentration field. The resulting multicomponent approach is consistent with the interpretation of the SDPD particles as moving volumes of fluid and reproduces the correct fluctuations and diffusion dynamics. Subsequently, we provide a general *multiscale* multicomponent SDPD framework for simulations of molecularly miscible systems spanning length scales from nanometers to the non-fluctuating continuum limit. This approach reproduces appropriate equilibrium properties and is validated with simulation of simple one-dimensional diffusion across multiple length scales.

4.1 Introduction

Stochastic particle descriptions for mesoscale phenomena have become ubiquitous in simulation due to their ability to accurately reproduce hydrodynamic behavior over time and length scales beyond what is feasible in fully resolved molecular dynamics. In this coarse-grained picture, the detailed underlying molecular structure is ignored and the problem

domain is instead decomposed into a collection of fluid volumes or clusters of atoms/molecules, with appropriately chosen interparticle interactions between them such that desired thermodynamic and hydrodynamic properties of the original fluid are preserved. Coarse-grained particle descriptions of fluids are often obtained from a “bottom-up” perspective, where the coarse model is extracted from detailed molecular simulations or principles and features a smoother representation of the free energy landscape that allows for large time-stepping. Alternatively, it is possible to adopt a “top-down” approach and use a coarse-grained fluid description that ignores molecular detail altogether, such as the continuum transport equations. Degrees of freedom absent in the coarse model are approximated by introducing additional features (e.g. fluctuations of field variables).

Smoothed Dissipative Particle Dynamics (SDPD) [1] is one such particle-based top-down approach, and has been applied to a number of phenomena, including pinned DNA in shear flow [2], colloidal particles [3], the flow of blood [4], intravascular drug delivery [5], suspensions [6], and viscoelastic flows [7,8]. Thieulot et al. [9,10] developed a SDPD-like model for a phase-separating fluid mixture by introducing fluctuations through the GENERIC formalism [11–13] following a particle discretization of the appropriate continuum equations. In addition, Ellero et al. [8] used GENERIC to obtain a discretized advection-diffusion equation for a system of Hookean dumbbells in solvent. For the most part, however, SDPD has been limited to single-component systems or suspensions where dissolved particles are equal in size or larger than the SDPD particles (e.g. colloidal or polymeric systems). Multicomponent problems have also been considered in other types of particle-based mesoscale simulations [14,15], although this is done in an *ad hoc* fashion where fluid volumes assume a unique identity (e.g. a particle in a two-component mixture is

either type A or type B). This simple approach is easy to implement and qualitatively adequate in many cases, but not consistent with the interpretation of particles as fluid volumes, since a single particle in a homogeneous fluid mixture should contain some amount of solute and solvent. Therefore, a more rigorous extension of these kinds of particle solvers for solutions should instead include an additional variable associated with each fluid volume specifying the concentration of solute at the particle. Recently, Li et al. extended traditional particle-based solvers to advection-diffusion-reaction systems [16]. There have also been recent developments by Kordilla et al. [17], who derived this type of single-scale multicomponent stochastic particle method through a direct particle discretization of the Landau-Lifshitz fluctuating hydrodynamics equations for mass and momentum transfer [18–20].

In this chapter, we take a different approach and instead develop a multicomponent SDPD model that provides an appropriate basis for multiscale simulation of hydrodynamic phenomena through the GENERIC formalism [11–13] (see Appendix 4.8.1), which guarantees thermodynamic consistency. SDPD and other particle-based fluid solvers are particularly attractive for designing multiscale simulation strategies that reduce computational cost through coarse-graining of select parts of the system, while retaining a high level of detail in others. This is motivated by an abundance of problems in molecular and interfacial physics that involve processes featuring multiple characteristic length scales. In particular, there have been a number of studies describing approaches for coupling molecular dynamics (MD) regions to continuum domains, which makes it possible to preserve molecular resolution where necessary, and use a simpler, coarse-grained description where this level of detail is not required [21–29]. SDPD specifically has already been used in

coupled MD-continuum simulations [30]. While there are a number of hybrid simulation approaches for single-component problems, developing general multiscale strategies for multicomponent systems remains a major challenge. Since SDPD has scale-dependent fluctuations, it is ideally suited for multiscale problems, and an approach for coupling two SDPD regions featuring different degrees of coarse-graining has been developed by Kulkarni et al. [31]. Therefore, generalizing SDPD to multicomponent systems immediately allows for a novel approach to multiscale multicomponent simulation, which is the subject of this work. This kind of particle-based Lagrangian description offers an alternative to spatially-adaptive approaches to solving the fluctuating hydrodynamics equations in the Eulerian frame [32].

SDPD addresses a number of issues present in one of the most widespread bottom-up particle-based techniques, dissipative particle dynamics (DPD) [33,34]. In DPD, the fluid is modeled as a collection of particles, where each particle is interpreted as a cluster of molecules that is locally at thermodynamic equilibrium. These mesoscopic fluid volumes interact with one another and evolve in time through a Langevin-type equation of motion; particles experience a soft repulsion as they approach along the line joining their centers, as well as pairwise viscous and random forces with magnitudes chosen in accordance with the fluctuation-dissipation theorem. This approach preserves Galilean invariance and conserves mass and momentum, giving rise to hydrodynamic behavior [35]. DPD has been applied to a wide range of problems, ranging from polymer solutions and melts [36–39], to the rheology of spherical and non-spherical colloids [40–42], membranes [43,44], surfactant monolayers [45], and vesicles [46,47]. Atomistic interaction potentials, or ones obtained from inverse thermodynamic approaches [48,49], can also be used in place of the softly-repulsive conservative DPD force, i.e. the viscous and fluctuating DPD interactions also

provide a basis for thermostating a fluid in a non-equilibrium setting [50–52]. Despite great success in modeling a broad range of mesoscale phenomena, DPD suffers from a number of limitations. Fluid transport coefficients (e.g. bulk and shear viscosities) do not appear in the equations of motion and are related to the free parameters of the DPD model in an indirect fashion through kinetic theory [53,54]. Moreover, traditional DPD fixes the form of the conservative force and, in turn, the equation of state such that it is always quadratic in the fluid density.

These issues were resolved by Español and Revenga, who derived the so-called “smoothed dissipative particle dynamics” (SDPD) [1] starting from a particle discretization of the hydrodynamic equations known as smoothed particle hydrodynamics, or SPH [55–57]. SPH is a continuum approach originally developed for modeling astrophysical problems, and later modified for simulation of flows in the low Reynold’s number limit [58]. Here, the fluid is approximated as a collection of Lagrangian particles that evolve in time according to an equation of motion obtained from an interpolation theory discretization of the Navier-Stokes equations. By introducing fluctuations into the hydrodynamic variables of the SPH equations in accordance with the second law, Español and Revenga obtain a general model for fluids at the mesoscale that is rigorously derived from a top-down perspective. The resulting approach (SDPD) corresponds to a particle discretization of the Landau-Lifshitz Navier-Stokes equations and offers a number of advantages over traditional particle-based mesoscale techniques such as DPD [1]. Since the basis for SDPD is the continuum hydrodynamic equations, transport coefficients are naturally included and appear in the final equations of motion, and it is possible to use an arbitrary equation of state for calculating the pressure distribution. Importantly, the characteristic length scale in SDPD is properly defined

and determined by a parameter known as the “smoothing length”. For systems involving small smoothing lengths, the corresponding fluid particles are very small and therefore subject to large thermal fluctuations. Similarly, in the limit of large smoothing lengths and hence large particles, fluctuations disappear altogether and the deterministic SPH equations of motion are recovered.

We follow the approach in Ref. [1] in this work and start from a continuum, top-down perspective to derive a discrete particle model for ideal binary mixtures where the concentration field is specified by defining a concentration associated with each fluid particle. Unlike Ref. [17], we introduce thermal noise through the GENERIC framework, and obtain a model that presents a convenient basis for multiscale simulation. Although this approach is only valid for ideal mixtures, it is still useful for a host of problems, such as biological and drug delivery applications where the ideal assumption is valid due to the dilute concentrations. In using the fluctuating hydrodynamic equations for two-component solutions as a basis, we obtain a model where a particle is no longer limited to the discrete choice of assuming identity A or B, but rather has associated with it a variable indicating the mass fraction of solute contained in the particle volume. We reconcile this multicomponent SDPD approach with existing multiscale techniques and provide a general SDPD formalism for multiscale multicomponent simulation. In Section 4.2 we derive a fluctuating concentration smoothed particle model for a quiescent system (i.e., in the absence of any flow fields). In Section 4.3, the model is generalized for systems with flows and fluctuations in the velocity field, and in Section 4.5 we describe how this method is used in multiscale simulation. The approach is validated through some simple multiscale equilibrium and non-

equilibrium benchmark problems in Sections 4.5 and 4.6. In Chapter 5, we extend this approach to coupled MD-continuum simulations.

4.2 Fluctuating Concentration Model Derivation

We first develop a mass diffusion model for a collection of SDPD particles at constant temperature with fixed positions. The model is for a two-component incompressible fluid in the ideal mixing limit. We then extend this to cases with momentum transfer featuring thermal noise in the velocity field in Section 4.3, in which particles are not stationary. The diffusion equation in the Lagrangian frame and in the absence of temperature gradients is given by [59]

$$\frac{d\Phi}{dt} = \frac{1}{\rho} \nabla \cdot (D \nabla \Phi). \quad (4.1)$$

Here, D is the diffusion coefficient for the solute and is defined in terms of units $\text{ML}^{-1}\text{t}^{-1}$, the concentration Φ is a mass fraction (hence, dimensionless), and ρ is the total mass density of the solute-solvent mixture. The time derivative on the left-hand side denotes the material derivative, although for the present case where particle positions are fixed and there are no velocities in the system, it is equivalent to a partial derivative with respect to time.

Discretizing Eq.(4.1) through an interpolant function W , we obtain the SPH approximation for the diffusion equation [60],

$$m_i \frac{d\Phi_i}{dt} = 2D \sum_{j=1}^N \frac{m_i m_j}{\rho_i \rho_j} \left(\frac{1}{|\mathbf{r}_{ij}|} \frac{\partial W_{ij}}{\partial r_{ij}} \right) \Phi_{ij}. \quad (4.2)$$

In this expression, m_i is the mass of the i th particle, ρ_i is the density of the i th particle, $\Phi_{ij} \equiv \Phi_i - \Phi_j$, and \mathbf{r}_{ij} is the relative position vector for the particles i and j , $\mathbf{r}_{ij} \equiv \mathbf{r}_i - \mathbf{r}_j$. W_{ij} is the smoothing function (described below). For simplicity, transport coefficients are assumed to be uniform throughout the system; for the more general case where the diffusion constant varies in space, the quantity $2D$ in Eq.(4.2) is brought inside the summation and replaced with $4D_i D_j / (D_i + D_j)$, where D_i is the diffusion constant for the i th particle [60].

The density at each particle can be updated from a discretization of the continuity equation, or by performing the following summation at each time-step,

$$\rho(\mathbf{r}_i) = \sum_{j=1}^N m_j W(\mathbf{r}_i - \mathbf{r}_j, h). \quad (4.3)$$

In this equation, h is the smoothing length, a parameter that controls the size of the particles and hence the length scale for the fluid. The smoothing kernel $W(\mathbf{r}_{ij}, h) \equiv W_{ij}$ is a normalized bell-shaped function with compact support. One possibility is a cubic spline, which is used for all numerical tests presented in this work [31,57,61],

$$W_{ij}(q) = \frac{1}{\pi h^3} \begin{cases} 1 - \frac{3}{2}q^2 + \frac{3}{4}q^3, & 0 \leq q < 1, \\ \frac{1}{4}(2-q)^3, & 1 \leq q < 2, \\ 0, & q \geq 2, \end{cases} \quad (4.4)$$

where $q = r_{ij}/h$.

The objective of this section is to introduce scale-dependent thermal noise in the concentration field, which is achieved through the GENERIC [11–13] framework (for a review of this formalism, see Appendix 4.8.1 in this thesis). In GENERIC, the system dynamics are governed by the following stochastic differential equations (SDEs):

$$dx = \left[L \cdot \frac{\partial E}{\partial x} + M \cdot \frac{\partial S}{\partial x} + k_B \frac{\partial}{\partial x} \cdot M \right] dt + d\tilde{x}. \quad (4.5)$$

Here, x denotes the independent variables that completely describe the system; in this case it is fully specified by the set of particle positions and the respective concentration at each particle, $x = \{\mathbf{r}_i, \Phi_i, i = 1, \dots, N\}$. M is the dissipative matrix, a positive semidefinite linear operator that acts on the entropy gradients to generate the irreversible dynamics. E denotes the total system energy and L is an antisymmetric operator that translates energy gradients into reversible dynamics. For the present case, this term is zero since the processes under consideration are purely irreversible; this will not be the case in Section 4.3 where fluid motion is considered. In the above-equation, $d\tilde{x}$ is the stochastic contribution. The term $k_B (\partial / \partial x) \cdot M$ appears due to the Itô interpretation of the stochastic integral [11,13].

For a two-component ideal mixture, the entropy of mixing is simply

$$S_i = - \left(\frac{m_i}{m_0} \right) k_B [\Phi_i \ln \Phi_i + (1 - \Phi_i) \ln(1 - \Phi_i)], \quad (4.6)$$

where m_0 denotes the mass of a single atom. Hence $m_i / m_0 = N_i$, where N_i is the number of atoms or molecules inside the i th SDPD particle. The driving force for an irreversible process is given by the entropy gradient,

$$\frac{\partial S_i}{\partial \Phi_i} = - \left(\frac{m_i}{m_0} \right) k_B \ln \left(\frac{\Phi_i}{1 - \Phi_i} \right). \quad (4.7)$$

Next, we postulate a form for the noise term. If we assume pairwise fluxes between particles, the simplest possible choice for introducing noise in a scalar field is

$$m_i d\tilde{\Phi}_i = \sum_{j=1}^N G_{ij} dV_{ij}. \quad (4.8)$$

In this expression, dV_{ij} is an increment of the Wiener process with the antisymmetry $dV_{ij} = -dV_{ji}$, and G_{ij} is the noise amplitude, which is symmetric under exchange of particles i and j , $G_{ij} = G_{ji}$. In practice, dV_{ij} is approximated using a randomly-generated number drawn from a normal distribution with unit variance and zero mean, $dV_{ij} \sim \sqrt{\Delta t} N(0,1)$. Here, Δt is the simulation time-step magnitude. The above-symmetries ensure that the amount of solute is a conserved quantity, i.e.

$$\sum_{i=1}^N m_i d\tilde{\Phi}_i = 0. \quad (4.9)$$

The fluctuation-dissipation (FD) theorem relates the noise in Eq.(4.8) to the dissipative matrix M . For any fluctuating state variable x , the FD theorem can be written as $d\tilde{x}d\tilde{x}^T = 2k_B M dt$. Thus, we use the FD theorem to write the ij th component of the dissipative matrix as

$$M_{ij} = \frac{d\tilde{\Phi}_i d\tilde{\Phi}_j}{2k_B dt}. \quad (4.10)$$

We substitute the postulated noise terms [Eq.(4.8)] into Eq.(4.10), and write M_{ij} in terms of the noise amplitude G_{ij} ,

$$m_i m_j \frac{d\tilde{\Phi}_i d\tilde{\Phi}_j}{dt} = \delta_{ij} \sum_{j'=1}^N G_{ij'} G_{jj'} - G_{ij}^2. \quad (4.11)$$

Here, we have assumed delta correlated noise by applying the mnemotechnical Itô rule $dV_{ii'} dV_{jj'} = [\delta_{ij} \delta_{i'j'} - \delta_{ij'} \delta_{i'j}] dt$ [1,62].

For discrete particle models, the dot operator in Eq.(4.5) corresponds to a sum over particle indices. Hence, the stochastic dynamics for the concentration field are governed by

$$\frac{d\Phi_i}{dt} = \sum_j \frac{d\tilde{\Phi}_i d\tilde{\Phi}_j}{2k_B dt} \left(\frac{\partial S_j}{\partial \Phi_j} \right). \quad (4.12)$$

All the quantities on the right-hand side of this expression are known. Substituting Eqs.(4.7) and (4.11), we arrive at the following evolution equation:

$$m_i \frac{d\Phi_i}{dt} = -\frac{1}{2m_0} \sum_{j=1}^N G_{ij}^2 \left[\ln \left(\frac{\Phi_i}{\Phi_j} \right) + \ln \left(\frac{1-\Phi_j}{1-\Phi_i} \right) \right]. \quad (4.13)$$

In order to compare this with the discretized diffusion equation [Eq.(4.2)], we modify Eq.(4.13) by first writing

$$\ln \left(\frac{\Phi_i}{\Phi_j} \right) = \frac{1}{2} \ln \left(\frac{\Phi_i}{\Phi_j} \right) - \frac{1}{2} \ln \left(\frac{\Phi_j}{\Phi_i} \right). \quad (4.14)$$

Linearizing the logarithmic terms, $\ln(\Phi_i / \Phi_j) \approx \Phi_i / \Phi_j - 1$, and recombining them,

$$\ln \left(\frac{\Phi_i}{\Phi_j} \right) \approx \frac{1}{2} \left(\frac{1}{\Phi_i} + \frac{1}{\Phi_j} \right) \Phi_{ij}. \quad (4.15)$$

Here, it is assumed that Φ_i / Φ_j is close to unity, i.e. that local concentration gradients and deviations from equilibrium are small. This approximation is valid since the accuracy of particle-based methods in reproducing gradients scales with the smoothing length, and large gradients over length scales smaller than typical particle spacing will not be accurately resolved in general. It is possible to derive this type of fluctuating concentration model in terms of chemical potentials, which does not require the linearization in Eq.(4.15). However, this alternate formulation of the method is less numerically stable and robust, and does not offer significant advantages. For completeness, we provide a derivation of this alternate method in Appendix 4.8.3.

The linearization in Eq.(4.15) is applied to both logarithmic terms in Eq.(4.13), which gives the following approximation after some algebra:

$$m_i \frac{d\Phi_i}{dt} = -\frac{1}{4m_0} \sum_{j=1}^N G_{ij}^2 \left(\frac{\Theta_i + \Theta_j}{\Theta_i \Theta_j} \right) \Phi_{ij}, \quad (4.16)$$

where we have defined $\Theta_i = \Phi_i(1 - \Phi_i)$. For fluctuation-dissipation to hold, this equation governing the dissipation of the stochastic noise must be equivalent to the discretized diffusion equation. Hence, by comparing this expression to Eq.(4.2), we find that the following equality must be satisfied:

$$\frac{2Dm_i m_j}{\rho_i \rho_j} \left(\frac{1}{|\mathbf{r}_{ij}|} \frac{\partial W_{ij}}{\partial r_{ij}} \right) = -\frac{1}{4m_0} \left(\frac{\Theta_i + \Theta_j}{\Theta_i \Theta_j} \right) G_{ij}^2. \quad (4.17)$$

Solving for the noise magnitude term G_{ij} ,

$$G_{ij} = \left[-\frac{8Dm_0 m_i m_j}{\rho_i \rho_j} \left(\frac{\Theta_i \Theta_j}{\Theta_i + \Theta_j} \right) \frac{1}{|\mathbf{r}_{ij}|} \frac{\partial W_{ij}}{\partial r_{ij}} \right]^{1/2}. \quad (4.18)$$

This is the SDPD discretized form of the noise amplitude for the stochastic flux in the Landau-Lifshitz Navier-Stokes equations for a binary mixture, $G = \sqrt{2m_0 D \Phi (1 - \Phi)}$ [63].

Finally, we compute the term in Eq.(4.5) involving the divergence of the dissipative matrix, $k_B (\partial / \partial x) \cdot M$, which arises due to the Itô interpretation of the stochastic differential equations (see Appendix 4.8.1). Calculating the divergence of the dissipative matrix is generally undesirable [13], although since the model features multiplicative noise, including this additional term may be important. Hence, we calculate this term from

$$k_B \sum_j \frac{\partial}{\partial \Phi_j} \frac{d\tilde{\Phi}_i d\tilde{\Phi}_j}{2k_B dt} = \frac{1}{2m_i} \sum_j \frac{1}{m_j} \frac{\partial}{\partial \Phi_j} \left(\delta_{ij} \sum_{j'} G_{ij'} G_{jj'} - G_{ij}^2 \right). \quad (4.19)$$

Applying the delta function and simplifying, this reduces to

$$= \frac{1}{2m_i} \sum_j \left(\frac{1}{m_i} \frac{\partial G_{ij}^2}{\partial \Phi_i} - \frac{1}{m_j} \frac{\partial G_{ij}^2}{\partial \Phi_j} \right). \quad (4.20)$$

After substituting Eq.(4.18) into Eq.(4.20) and differentiating, it is possible to write the final SDEs governing the concentration field including the Itô term,

$$m_i d\Phi_i = 2D \sum_{j=1}^N (1 - g_{ij}) \frac{m_i m_j}{\rho_i \rho_j} \left(\frac{1}{|\mathbf{r}_{ij}|} \frac{\partial W_{ij}}{\partial r_{ij}} \right) \Phi_{ij} dt + md\tilde{\Phi}_i. \quad (4.21)$$

Eq.(4.21) is the discretized form of Eq.(4.1) with fluctuations in the concentration field. The noise term is described by Eq.(4.8) with amplitude given by Eq.(4.18). In the above equation, we have defined the quantity:

$$g_{ij} = 2m_0 \left[\frac{(1 - 2\Phi_i) m_j \Theta_j^2 - (1 - 2\Phi_j) m_i \Theta_i^2}{m_i m_j (\Theta_i + \Theta_j)^2 (\Phi_i - \Phi_j)} \right]. \quad (4.22)$$

Note that this contribution to the governing equation scales inversely with particle mass. Hence, for large SDPD particles it is much smaller than the other terms and usually negligible. For example, in subsections 4.4-4.6 we perform tests with particles having masses such that g_{ij} is a hundred times smaller than the irreversible term in Eq.(4.21). Moreover, the SDPD particles cannot be too small or the continuum assumption breaks down, and thus this term's influence will typically be minor relative to the rest. Hence, in all of the numerical tests presented in this chapter, we ignore this contribution (i.e. we assume $g_{ij} \approx 0$). In Appendix 4.8.3, we provide a different derivation of this approach using chemical potentials.

4.3 SDPD Model for Two-Component Ideal Mixture with Flow

We now consider the more general case when particles are allowed to translate due to flow fields in the system. In the presence of fluid motion, the positions of the SDPD particles evolve according to

$$\frac{d\mathbf{r}_i}{dt} = \mathbf{v}_i. \quad (4.23)$$

The velocity \mathbf{v}_i can be determined from the momentum equation in the Lagrangian description [59],

$$\rho \frac{d\mathbf{v}}{dt} = -\nabla p + \eta \nabla^2 \mathbf{v} + \left(\zeta + \frac{\eta}{3} \right) \nabla \nabla \cdot \mathbf{v}. \quad (4.24)$$

Here, p denotes the pressure distribution, and η and ζ are the shear and bulk viscosities, respectively. In discretized form, this equation becomes [1]

$$\begin{aligned} m_i \frac{d\mathbf{v}_i}{dt} = & - \sum_{j=1}^N m_i m_j \left(\frac{p_i}{\rho_i^2} + \frac{p_j}{\rho_j^2} \right) \frac{\partial W_{ij}}{\partial \mathbf{r}_{ij}} \mathbf{e}_{ij} \\ & + \left(\frac{5\eta}{3} - \zeta \right) \sum_{j=1}^N \frac{m_i m_j}{\rho_i \rho_j} \left(\frac{1}{|\mathbf{r}_{ij}|} \frac{\partial W_{ij}}{\partial r_{ij}} \right) \mathbf{v}_{ij} \\ & + 5 \left(\frac{\eta}{3} + \zeta \right) \sum_{j=1}^N \frac{m_i m_j}{\rho_i \rho_j} \left(\frac{1}{|\mathbf{r}_{ij}|} \frac{\partial W_{ij}}{\partial r_{ij}} \right) (\mathbf{v}_{ij} \cdot \mathbf{e}_{ij}) \mathbf{e}_{ij}. \end{aligned} \quad (4.25)$$

As before, transport coefficients are assumed constant for simplicity.

The expression governing the evolution of the concentration field remains unchanged from Section 4.2 since the particles are now free to move, and velocities determined from Eq.(4.25) are included in the material derivative of the equation for the solute transfer, Eq.(4.21). Equilibrium fluctuations in concentration and velocity are statistically independent [64], hence we do not need to impose any correlation between velocity and

concentration in the postulated form for the noise of those quantities. Thus, the appropriate form for the velocity noise for an ideal two-component system with flow at constant temperature is the same as for the single-component case [1,62],

$$m_i d\tilde{\mathbf{v}}_i = \sum_{j=1}^N \left(A_{ij} d\hat{\mathbf{W}}_{ij} + B_{ij} \frac{1}{3} \text{tr} [d\mathbf{W}_{ij}] \mathbf{I} \right) \cdot \mathbf{e}_{ij}. \quad (4.26)$$

In this expression, $d\mathbf{W}_{ij}$ is a tensorial generalization of the Wiener process and $d\hat{\mathbf{W}}_{ij}$ is the traceless, symmetric part of $d\mathbf{W}_{ij}$, $d\hat{W}_{ij}^{\alpha\beta} = \frac{1}{2} [dW_{ij}^{\alpha\beta} + dW_{ij}^{\beta\alpha}] - \frac{\delta^{\alpha\beta}}{3} \text{tr} [d\mathbf{W}_{ij}]$. In non-equilibrium systems, advection of concentration due to velocity fluctuations in the fluid can lead to long-ranged correlations between fluctuations in concentration and velocity, which is responsible for the so-called giant fluctuation phenomenon [63,65]. This effect is naturally incorporated into Lagrangian fluctuating particle models since the velocity that appears in the material derivative of Eq.(4.21) includes the stochastic contribution [17].

The noise magnitudes for the fluctuations in the velocity field are given by [1]

$$A_{ij} = \left[-\frac{4m_i m_j k_B T}{\rho_i \rho_j} \left(\frac{5\eta}{3} - \zeta \right) \frac{1}{|\mathbf{r}_{ij}|} \frac{\partial W_{ij}}{\partial r_{ij}} \right]^{1/2}, \quad (4.27)$$

$$B_{ij} = \left[-\frac{4m_i m_j k_B T}{\rho_i \rho_j} \left(\frac{5\eta}{3} + 8\zeta \right) \frac{1}{|\mathbf{r}_{ij}|} \frac{\partial W_{ij}}{\partial r_{ij}} \right]^{1/2}.$$

The final SDE for the velocity field is [1]

$$\begin{aligned}
m_i d\mathbf{v}_i = & -\sum_{j=1}^N m_i m_j \left(\frac{p_i}{\rho_i^2} + \frac{p_j}{\rho_j^2} \right) \frac{\partial W_{ij}}{\partial r_{ij}} \mathbf{e}_{ij} dt \\
& + \left(\frac{5\eta}{3} - \zeta \right) \sum_{j=1}^N (1-d_{ij}) \frac{m_i m_j}{\rho_i \rho_j} \left(\frac{1}{|\mathbf{r}_{ij}|} \frac{\partial W_{ij}}{\partial r_{ij}} \right) \mathbf{v}_{ij} dt \\
& + 5 \left(\frac{\eta}{3} + \zeta \right) \sum_{j=1}^N (1-d_{ij}) \frac{m_i m_j}{\rho_i \rho_j} \left(\frac{1}{|\mathbf{r}_{ij}|} \frac{\partial W_{ij}}{\partial r_{ij}} \right) (\mathbf{v}_{ij} \cdot \mathbf{e}_{ij}) \mathbf{e}_{ij} dt + m_i d\tilde{\mathbf{v}}_i,
\end{aligned} \tag{4.28}$$

where

$$d_{ij} = \frac{k_B}{4} \left(\frac{1}{C_i} + \frac{1}{C_j} \right). \tag{4.29}$$

Once again, the term arising from the divergence of the dissipative matrix scales inversely with an extensive quantity (in this case the extensive heat capacity), and hence becomes negligible for large SDPD particles. This term is also not included in the present calculations since we only consider situations where particles are massive and this contribution is small. For the cases considered in this chapter, it is not necessary to solve the entropy equation since it is decoupled from the equations of mass and momentum transfer at constant temperature.

Solid surfaces are treated in SDPD using virtual particles frozen on a lattice, and Dirichlet boundary conditions are imposed using the approach of Morris et al. [58], where dissipative and random interactions between fluid and wall particles are modified in order to enforce the correct boundary values for the fields (see Chapters 3 and 6 for additional discussion). For fluid-wall particle pair interactions, the distance of the fluid particle from the wall d_f and the distance of the virtual particle from the wall boundary d_w are calculated. Next, we calculate a factor β from

$$\beta = 1 + \frac{d_w}{d_f}. \quad (4.30)$$

This factor is used to rescale the dissipative terms in both the momentum and diffusion equations, ensuring the solution for the concentration and velocity assumes the correct values at the interface. For every pair interaction, this is equivalent to extrapolating the fluid particle's concentration and velocity across the interface and assigning values to the wall particle such that boundary conditions are satisfied. Note that the stochastic terms are rescaled by $\sqrt{\beta}$ rather than β in order to yield the correct fluctuation-dissipation balance.

4.4 Equilibrium Properties of Fluid Mixture

First, it is necessary to ensure that this model yields the appropriate fluctuations at equilibrium. SDPD particles have constant mass, but do exchange solute and solvent with their neighbors. Therefore, solute and solvent exchange between particle pairs are not independent, and if a particle loses some amount of solute to a neighbor, it must gain the same amount of solvent in order to conserve its mass. The variance of the solute fluctuations at equilibrium for a fluid volume with a constant mass constraint is obtained from a derivation similar to that in Ref. [64], detailed in Appendix 4.8.2. The resulting expression for the concentration variance in a collection of SDPD particles each having dimensionless mass m/m_0 is given by

$$\langle (\Delta\Phi)^2 \rangle = \frac{m_0 \langle \Phi \rangle (1 - \langle \Phi \rangle)}{m}. \quad (4.31)$$

In the following simulations, we choose non-dimensional units such that the mass of a single molecule or atom is unity ($m_0 = 1$). This implies that the dimensionless mass m of a SDPD fluid volume equals the number of molecules N_0 that it contains, $N_0 = m$. Hence, a particle with mass $m = 100$ can be interpreted as a cluster or fluid volume comprised of 100 fluid atoms or molecules.

To evaluate equilibrium fluctuations in the new model, we consider two cases: 1) quiescent fluid at equilibrium with fluctuations in the concentration field alone, as described in Section 4.2 and 2) quiescent fluid at equilibrium with fluctuations in both concentration and velocity (described in Section 4.3). In the first case, particles exist on a cubic lattice and their positions do not evolve in time. As a model fluid, we choose parameters that mimic a simple Lennard-Jones-like liquid, and all values are reported in reduced Lennard-Jones units using the convention described in Refs. [30,31]. According to Eq.(4.31), the concentration fluctuations are affected by the degree of coarse-graining (i.e. the SDPD particle mass) and the average concentration in the system. Hence, we vary these two parameters and perform equilibrium simulations to ensure we obtain the correct distribution of concentrations for all cases. The particle masses considered are $m = 25$, 100, and 200 (with corresponding smoothing lengths $h = 3.75$, 6.00, and 7.50, respectively). The average concentrations tested for each case are $\langle \Phi \rangle = 0.25$, 0.50, and 0.75. For the $m = 25$ case, particles are initialized on a $8 \times 8 \times 8$ cubic lattice inside a box with dimensions of $25 \times 25 \times 25$ and periodic boundary conditions in all directions. For the simulations with particles masses $m = 100$, 1000 particles are initially placed on a $10 \times 10 \times 10$ lattice inside a periodic $50 \times 50 \times 50$ region. Finally, for the $m = 200$ case, we initialize a $8 \times 8 \times 8$ cubic lattice of particles inside a box with size $50 \times 50 \times 50$. The system temperature is $T = 1.0$ and the mass density is $\rho = 0.8$, For scenario

2), we also solve the momentum equation and choose $\zeta = 0.9$ [66] and $\eta = 1.9$ [67] for the viscosities. For convenience, the diffusion constant is assumed constant and set to unity ($D = 1.0$).

Fluid thermodynamic properties are determined by the choice of equation of state, which is an input parameter in SPH and SDPD. In these smoothed particle techniques, fluid motion is driven by local density gradients. Therefore, incompressible flows are typically approximated by choosing a quasi-incompressible equation of state that leads to large pressure gradients for small density perturbations. The equation of state is constructed such that density variations are small (it is recommended that density fluctuations remain within 3% of the target density [58]), while still allowing for practical time-step magnitudes. Presently, we choose $p_i = \rho_i c_s^2$ [31,56,57], where the speed of sound is $c_s = 5.0$ [31], giving average particle density fluctuations within 1.1% of the desired value for all tested fluid resolutions. The selected smoothing kernel is the cubic spline [Eq.(4.4)]. The Euler-Maruyama integrator [68] with a time-step of $\Delta t = 0.001$ is used for time-integration for case 1, where we have fixed particles positions. For case 2, the same time-step is used and particle positions are evolved in time using a modified velocity-Verlet algorithm commonly used for DPD simulations [17,69], where the concentration field is updated at the same points during the integration process as the velocity. The system is equilibrated for 1×10^6 time-steps, and the averaging is over 5×10^6 time-steps.

In Figure 4.1, the distribution of fluctuations determined from the SDPD simulations at three different average concentrations is compared to the analytical result, given by Gaussian distributions with the variance of Eq.(4.31). For clarity, we only show results for the fixed-position tests (case 1). The results for the runs where particles are allowed to move

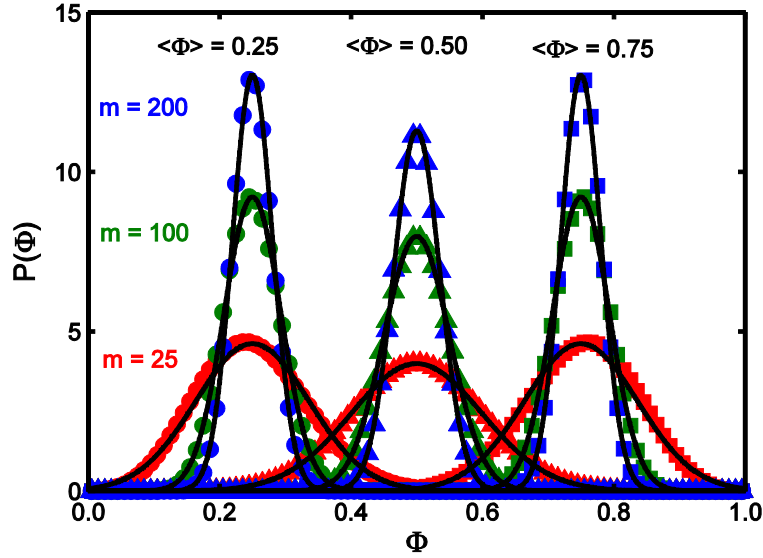


Fig. 4.1. Concentration probability distributions obtained from simulations using multicomponent SDPD (colored markers) as compared to the analytical result (black curves), given by a Gaussian with variance given by Eq.(4.31). Solutions with three different average concentrations are simulated, $\langle \Phi \rangle = 0.25$ (circle markers), 0.50 (triangles) and 0.75 (squares). For each concentration, we also consider three different particle masses, $m = 25$ (red markers), 100 (green) and 200 (blue). The results shown are for the fixed-position tests; simulation results for the case where particle positions evolve in time do not show any appreciable difference and are omitted for clarity.

are indistinguishable from the fixed-position case as expected, since fluctuations in velocity and concentration are statistically independent at equilibrium. For all tests, the numerical calculations show excellent agreement with the analytical result. The time-averaged variance for the $\langle \Phi \rangle = 0.25$ SDPD simulations is within 0.8% of the theoretical result for the case with $m = 200$. The error in the variance for the cases with $m = 100$ and $m = 25$ is 1.7% and 6.5% respectively. For the simulations with $\langle \Phi \rangle = 0.50$, the error in the distribution variance is 0.5% for the $m = 200$ case, 1.1% for $m = 100$, and 4.0% for $m = 25$. These errors are further reduced by decreasing the time-step.

We find that low order integrators such as Euler-Maruyama lead to precision issues if an insufficiently small time-step is used. Concentration cannot assume negative values (or values greater than one), and thus the distribution of concentrations becomes increasingly asymmetric with values of the average concentration approaching zero or unity. This is more prominent for situations involving very small SDPD particles since fluctuations become very large and the distribution of concentrations very broad. A low-order integrator may not be sufficiently accurate to prevent fluctuations that lead to unphysical concentrations ($\Phi_i < 0$ or $\Phi_i > 1$). One possible approach to resolve these kinds of issues when dealing with smaller SDPD particles and dilute concentrations is to use an adaptive time-step integrator for propagating concentrations and/or velocities in time. This can be rigorously implemented through use of a Brownian tree algorithm [70]. With this algorithm, it is possible to detect unphysical concentrations and dynamically reduce the time-step as needed while preserving the original Brownian trajectory of the particle concentrations. For the present work, we simply choose an appropriately small time-step to avoid numerical difficulties.

4.5 Multiscale Multicomponent SDPD

In this section, the multicomponent approach outlined in Sections 4.2 and 4.3 is generalized to a multiscale simulation approach using the formulation of Kulkarni et al [31]. A similar method has been developed for bridging regions featuring traditional DPD particles with a coarse-grained DPD particle description [71]. In both of these works, separate parts of the simulation box contain SDPD/DPD fluids with varying levels of detail. For the SDPD case, the resolution is determined by the smoothing length parameter that controls the particle

masses, and hence the magnitude of the fluctuations. Therefore, it is possible to couple a finely-resolved SDPD particle region (where particles have smoothing length h_1 and some corresponding mass m_1) to a more coarse one (containing particles with $h_2 > h_1$ and $m_2 > m_1$) by carefully constructing an interface between the two different representations of the bulk fluid. Fig. 4.2 illustrates how to interface two SDPD fluids with different level of detail for the case of large particles twice as massive as the fine particles, where the large particles therefore split into twos. The interface region is itself divided into three separate subdomains 1) an overlap region, 2) a coarsening region, 3) and a refining region. Particles in the system are free to traverse the interface and mass transfer between domains with different resolution is unrestricted. Mass is conserved through particle splitting and combining when moving across this boundary.

If a large SDPD particle is transported into the interface region, either due to advection or Brownian motion, and then eventually moves into the refining subregion, it splits into two small SDPD particles. Here, we have assumed that the small SDPD particles in the finely resolved part of the simulation box have half the mass of the large particles in the coarse region, $m_2 = 2m_1$. It is possible to generalize this kind of approach for situations where the massive particles are n times more massive than the small particles, where n is an integer greater than one, and hence large particles can split into n smaller particles. For simplicity, we assume $n = 2$. The remaining splitting rules are constructed such that momentum and the amount of solute are also conserved. Note that there are multiple ways to assign new positions to the daughter particles upon splitting. In the work of Backer et al. [71], both particles are inserted at the same location as the parent particle. Due to the soft DPD interactions, the system remains stable in spite of both particles occupying the same

point, and the thermostat dissipates heat generated due to particle overlap after the insertion. However, for fluids with quasi-incompressible equations of state, this heating may be substantial. Therefore, Kulkarni et al. adopt an alternative perspective where both particles are inserted randomly inside a region that corresponds to the influence domain of the parent particle (i.e. within a sphere surrounding the parent particle with radius equal to the parent’s smoothing length). This reduces the problem of heating, although the center of mass of the original particle is no longer conserved.

Here, we take a different approach and only insert one of the two daughter particles

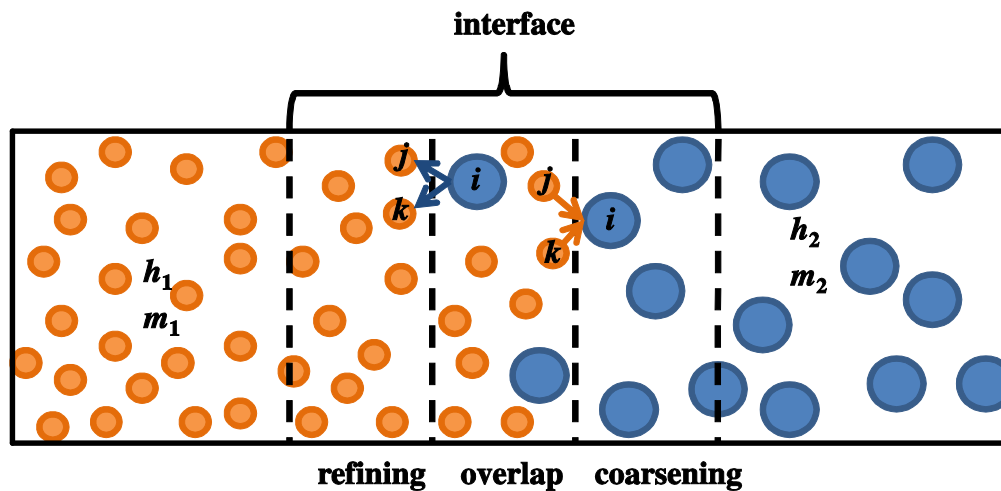


Fig. 4.2. Depiction of the multiscale SDPD simulation interface region between fluids with different resolution. The “fine” SDPD fluid has smoothing length and mass h_1 and m_1 , respectively. The “coarse” fluid in this example has a smoothing length of h_2 and mass of $m_2 = 2m_1$. The interface is divided into three parts, 1) refining, 2) overlap, and 3) coarsening subdomains. Once a large particle crosses into the refining region, it splits into two small SDPD particles each having half the mass of the parent particle. When a small particle crosses into the coarsening region, it is combined with another nearby particle into a large one. Large and small particles coexist within the overlap domain.

randomly inside the parent particle's influence domain. After particle j is inserted at random inside a sphere with radius h_i surrounding the parent particle i , the second particle k is inserted at a position such that the center of mass of the parent particle is preserved. In other words, if a large particle i splits into small particles j and k , we generate a random displacement vector $\Delta\mathbf{r}_{ij} = \mathbf{r}_i - \mathbf{r}_j$ according to $\Delta\mathbf{r}_{ij} = \text{random}(h_i)$. Then, the appropriate rules are

$$\begin{aligned}
m_j &= m_k = 0.5m_i, \\
\mathbf{v}_j &= \mathbf{v}_k = \mathbf{v}_i, \\
\mathbf{r}_j &= \mathbf{r}_i - \Delta\mathbf{r}_{ij}, \\
\mathbf{r}_k &= \mathbf{r}_i + \Delta\mathbf{r}_{ij}, \\
\Phi_j &= \Phi_k = \Phi_i.
\end{aligned} \tag{4.32}$$

This procedure also ensures that potential energy is conserved upon splitting in simulations that feature a linear external potential acting on the particle masses (e.g. gravity).

The rules for combining smaller particles into larger ones are more straightforward. If a small particle j is transported to the interface region and crosses into the coarsening region, the nearest small particle k is located, and the two are combined into large particle i using the following rules:

$$\begin{aligned}
m_i &= m_j + m_k, \\
\mathbf{v}_i &= 0.5(\mathbf{v}_j + \mathbf{v}_k), \\
\mathbf{r}_i &= 0.5(\mathbf{r}_j + \mathbf{r}_k), \\
\Phi_i &= 0.5(\Phi_j + \Phi_k).
\end{aligned} \tag{4.33}$$

We note that with the particle splitting and combining steps in this top-down multiscale approach, it is not strictly possible to satisfy detailed balance because the coarsening and refining subregions, where the ‘‘forward’’ and ‘‘reverse’’ moves take place, are spatially separated. However, this splitting/combining scheme maintains conserved physical

quantities and has been shown to accurately reproduce hydrodynamic behavior [31,71]. For the single-component case, this method yields a flat density distribution at equilibrium [31], as well as accurate solutions for the flow field in simple problems such as shear flow. Specifically, Backer et al. consider cases where the flow is both perpendicular and parallel to the interface separating the regions with different resolution, and in both cases there is good agreement of the numerical result with the analytical solution from Navier-Stokes.

In this and the following section, we benchmark the multiscale multicomponent approach by performing simple equilibrium and non-equilibrium problems. Due to the presence of multiple length scales, a few additional details require discussion. Note that previously it was possible to hold the smoothing length constant for all particles. In the present multiscale scenario where the fluid resolution changes with position, the smoothing length for every particle must be allowed to vary since the number density varies in space, and each particle must maintain the appropriate number of nearest neighbors. Thus, each particle is assigned a smoothing length variable that is updated at each time-step based on the local SDPD particle number density [31],

$$h_i = h_0 v_i^{-1/3}. \quad (4.34)$$

Here, v_i is the local number density computed from $v_i = \sum_j W_{ij}$. h_0 is a constant parameter selected so that each particle has ~ 56 neighbors within its own influence domain, which is required for the accuracy of the particle approximation [57]. In this work, we choose $h_0 = 1.2$ [31,57]. In order to ensure symmetric interactions, we use the arithmetic mean of particle smoothing lengths when computing pair interactions, $h_{ij} = (h_i + h_j) / 2$.

We have tested the procedure implied by Eqs.(4.32) and (4.33) in the presence of an external field by placing two fluids with different resolution next to a wall in a semi-infinite domain, with a uniform gravitational force in the direction perpendicular to the wall. The results are shown in Fig. 4.3 and compared to the analytical solution for the density, given by $\rho(z) = \rho(0)\exp(-gz)$. Here, g is the gravitational constant; presently, we choose $g = 0.01$. $\rho(z = 0)$ is a parameter giving the density at the surface and is fit to the simulation data. The computed density profiles do in fact show the correct equilibrium Boltzmann distribution,

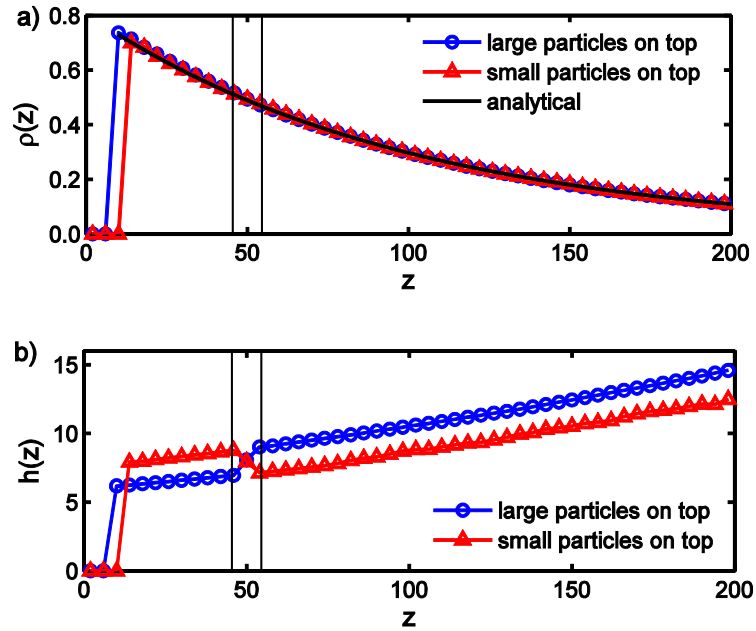


Fig. 4.3. (a) Density distribution for fluid in semi-infinite domain next to a solid boundary, located at $z = 0$. A uniform external potential is applied and acts to pull particles towards the boundary. We consider both cases where the massive, coarse-grained particles are on top (blue/circle markers) and where they are on bottom (red/triangles). Both results are compared to the exact analytical solution, shown in black. (b) Smoothing function versus position. As expected, $h(z)$ is large in the coarse region and small in the fine one. Moreover, $h(z)$ increases with separation from the boundary since the number density of particles decreases.

without artifacts due to the interface. Moreover, this test is successful whether or not the more massive-particle fluid is on top or bottom. Note that while the smoothing length is larger in the coarse region than the fine one, it also increases with distance from the surface. This is due to the decrease in the particle number density away from the surface. The smoothing length is updated such that each particle has ~ 56 neighbors in its influence domain; as the number density decreases, the smoothing length must increase to include a sufficient number of particles, as described by Eq.(4.34).

Unlike previous studies that only focused on single-component systems, Eqs.(4.32) and (4.33) include the appropriate splitting and combining rules for a binary mixture. We confirm that this approach reproduces correct equilibrium properties uniformly across the simulation box by considering a fluid at reduced temperature $T = 1$ with density $\rho = 0.8$ and viscosities $\eta = 1.9$ and $\zeta = 0.9$. Initially, we divide the global simulation box (with volume $50 \times 50 \times 100$) in two parts, with 1000 fine particles in the region located at $z < 50$, and 512 coarse particles in the region at $z > 50$. The fine particles are initialized on a $10 \times 10 \times 10$ lattice inside a $50 \times 50 \times 50$ volume. These “fine” particles have mass $m = 100$ and smoothing length $h = 6.0$. For the coarse region, particles are initially placed on a $8 \times 8 \times 8$ lattice inside a volume with dimensions $50 \times 50 \times 50$. These “coarse” particles have a mass of $m = 200$ and smoothing length $h = 7.5$. The z -coordinate is perpendicular to the interface separating the coarse and fine SDPD domains [see Fig. 4.4a]. Periodic boundary conditions are used in all directions. The interface regions have a width of 9.0 and are located between $z = 0.0$ and 9.0, and $z = 50.0$ and 59.0. It is necessary to include two transition zones due to the periodicity of the simulation box. Each of the interface coarsening, refining, and overlap subdomains has a width of 3.0. The interface region should be sufficiently large to allow for a smooth transition

of the smoothing length; when an inadequately sized transition region is used, particles near the interface have a different number of neighbors from particles in the bulk, which can result in unphysical density gradients [71]. After initializing positions, all the particles are translated in the z -direction by half the interface region width so that the initial boundary between the coarse and fine particle lattices are located precisely half-way inside the interface regions, within the overlap subdomains ($z = 4.5$ and $z = 29.5$). We use a time-step of $\Delta t = 0.001$ and collect data for 5×10^6 steps after equilibrating for 1×10^6 . Five cases with average concentrations $\langle \Phi \rangle = 0.25, 0.40, 0.50, 0.60,$ and 0.75 are considered. The neighbor list is updated every ten steps, unless the number of particles in the system changes due to splitting/combining of particles, in which case it is also rebuilt.

The system is illustrated in Fig. 4.4a, and the smoothing length as a function of position is obtained from a binning procedure and shown in Fig. 4.4b. The regions where the smoothing length is low ($h = 6.0$) contains particles with mass $m = 100$, and the part where $h = 7.5$ features particles with mass $m = 200$, with a smooth transition between the two values of h across the interface separating the two domains. Fig. 4.5a gives the concentration profiles for the five different average concentrations investigated. There are no unphysical concentration gradients perpendicular to the interface between the fine and coarse regions, and the distribution of solute is uniform. The average error per bin in the profiles across all five cases is 0.0003%. We also compare the concentration distributions in the fine and coarse regions to the exact analytical result [Eq.(4.31)] in Fig. 4.5b and find that both the finely-resolved and coarse-grained regions in the multiscale simulation exhibit fluctuations in concentration appropriate for their respective scales. The distributions for the $\langle \Phi \rangle = 0.40$ and 0.60 are omitted for clarity.

In addition, we have tested this approach for $n = 4$, i.e. when the coarse-grained fluid particles are 4 times as massive as the fine ones. Larger values of n give significant computational savings, since the number of particles in the coarse region is significantly reduced relative to the fine region. For the particle splitting step, three particles are inserted at random, and the final particle is inserted such that the center of mass of the parent particle is preserved; an alternative approach is to insert particles in pairs, where each pair preserves the center of mass, though this requires that n is an even integer. The concentration profile in

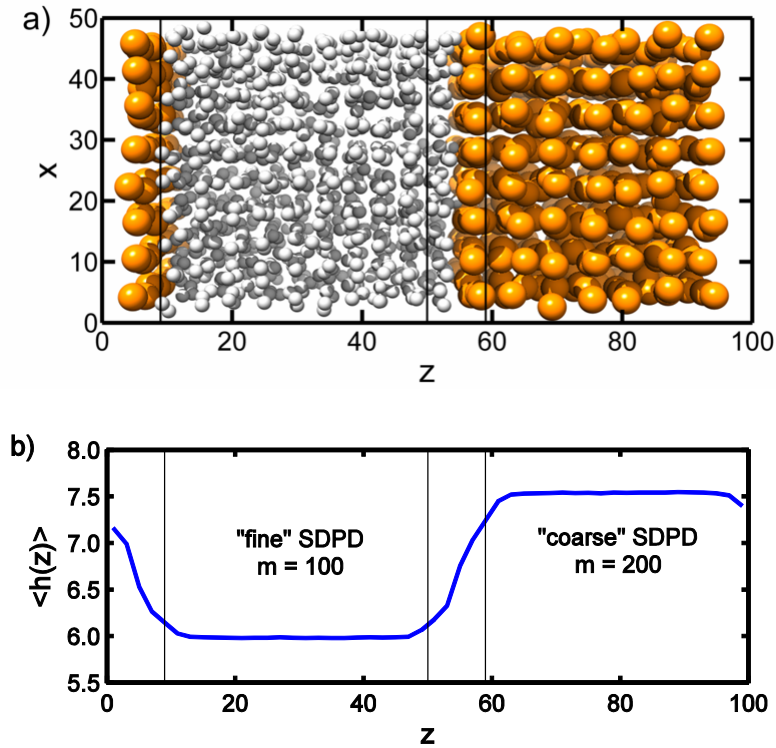


Fig. 4.4. (a) Visualization of equilibrium multiscale SDPD simulation. The left bulk region (white particles) is the finely-resolved SDPD fluid with smoothing length $h = 6.0$, and the particles on the right (orange) are the coarse ones with $h = 7.5$. These coarse particles are twice as massive as the fine ones, and their number density is half as much. Periodic boundary conditions are used for the x -, y -, and z -directions. (b) The corresponding smoothing length versus position for an equilibrium multiscale SDPD simulation. The interface regions are located between $z = 0.0$ and 9.0 , and between $z = 50.0$ and 59.0 .

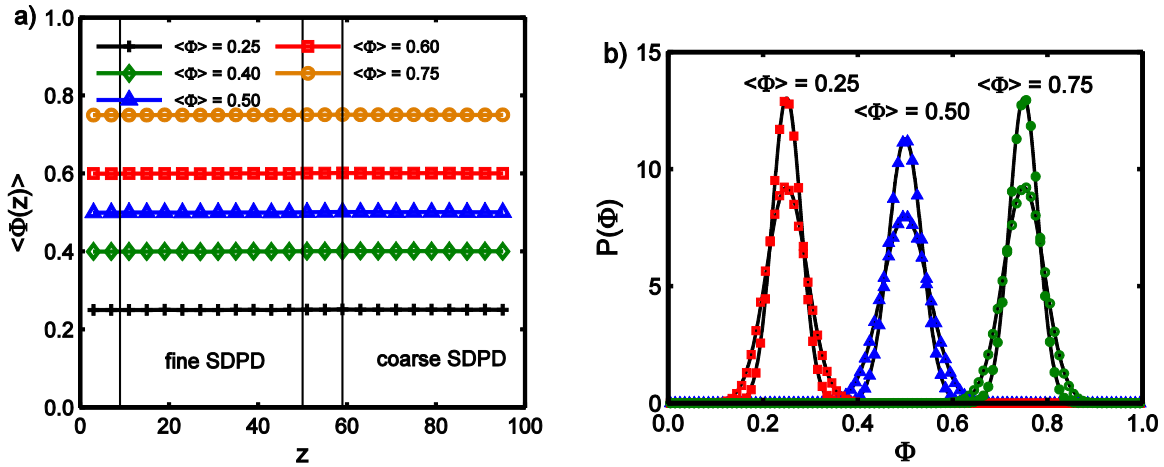


Fig. 4.5. (a) Concentration profiles for equilibrium multiscale SDPD simulations. We have performed tests at several different average concentrations, $\langle \Phi \rangle = 0.25, 0.40, 0.50, 0.60,$ and 0.75 , where the results from each simulation are shown with a different marker/color. (b) Concentration probability distributions from equilibrium multiscale simulations. For clarity, we show results for three of the five cases: $\langle \Phi \rangle = 0.25$ (red/square markers), 0.50 (blue/triangle markers), and 0.75 (green/circle markers). The solid markers represent the probability distribution in the “coarse” SDPD region, and the hollow markers represent the “fine” SDPD region. The black curves are the exact analytical solution. The distributions for $\langle \Phi \rangle = 0.40$ and 0.60 are omitted for clarity.

these tests is also completely flat, similar to the $n = 2$ case shown in Fig.4.5a, without artifacts near the interface (results not shown). Note that as the degree of coarse-graining in the coarse region is increased, the number of particle insertions one must perform increases as well. Since particle insertions can lead to heating due to the strong repulsion between particle pairs, large values of n can lead to sizeable temperature spikes. For the choice of $n = 4$, we found more substantial temperature increases than for the $n = 2$ case, although the thermostat kept the fluid stably near the $T = 1$ target temperature.

4.6 One-Dimensional Diffusion Across Multiple Length Scales

Next we demonstrate that our multiscale multicomponent method captures diffusion dynamics correctly across multiple length scales by performing a multiscale simulation of quasi-1D diffusion. Once again, we choose $T = 1$ and $\rho = 0.8$ as the state point, and $D = 1.0$, $\zeta = 0.9$ and $\eta = 1.9$ for the transport coefficients. The system is set up as follows: the global simulation box has dimensions $50 \times 50 \times 200$, where one side initially contains 2000 fine particles, and the other side contains 1024 coarse particles. At the start of the simulation, the finely-resolved particles are initialized on a $10 \times 10 \times 20$ lattice inside a region with dimensions $50 \times 50 \times 100$, which is a subset of the whole simulation box. These particles have a mass of 100 and smoothing length of 6.0. Next to this region, we initialize the coarse SDPD particles (with mass of 200 and smoothing length of 7.5) on an $8 \times 8 \times 16$ lattice inside a part of the global simulation box with lengths $50 \times 50 \times 100$. The vector normal to the interface separating the coarse and fine regions is in the z -direction. The interface region separating the coarse and fine domains has a width of 9.0 and is centered at $z = 100$. The simulation box features periodic boundary conditions in the x - and y -directions. The walls are located $z = 20$ and $z = 180$, and particles located $z < 20$ and $z > 180$ are labelled as virtual particles; their positions and concentrations are not evolved in time. The fluid particles are initialized with an average concentration of 0.4. We use a time-step of $\Delta t = 0.01$, and equilibrate for 1×10^6 steps.

After equilibration a concentration gradient is imposed on the system by increasing the concentration of the wall particles located at $z > 180$ to 0.6. Boundary conditions are enforced using the approach described in Section 4.3. The gradient is perpendicular to the interface separating the fine and coarse regions, and hence drives solute transfer across the

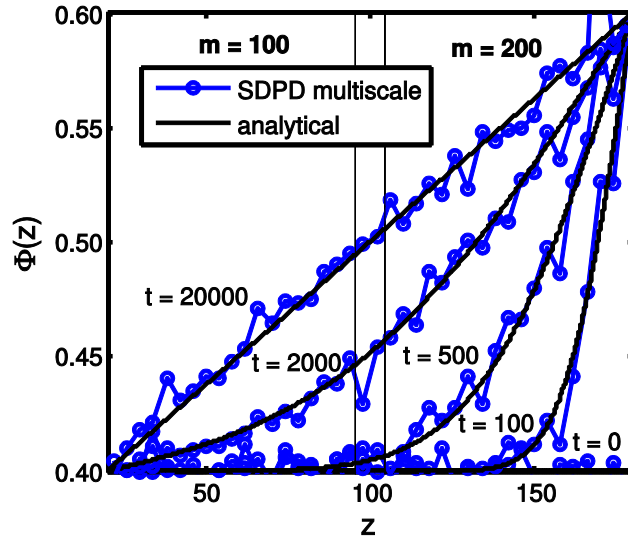


Fig. 4.6. Concentration profile at different times for the quasi-one-dimensional diffusion problem across multiple length scales. A fluid region is situated between two walls, and the fluid itself is divided into finely-resolved and coarse-grained domains, where particles have masses $m = 100$ and $m = 200$, respectively. After equilibrating, a concentration gradient is imposed by holding the concentration fixed at 0.4 at the left boundary, and 0.6 at the right boundary, and the time-evolution of the concentration profile is computed. The numerical results (blue curve, circle markers) are shown against the exact solution of the non-fluctuating diffusion equation (black curve).

boundary from the region with coarse resolution to the finely-resolved SDPD region. The resulting transient concentration profile is shown for several different times and compared to the exact analytical solution of the non-fluctuating diffusion equation in Fig. 4.6. The results show excellent agreement with the exact solution, mass transfer is correctly mediated across domains with different levels of detail and diffusion is independent of the degree of coarse-graining. At steady-state, the time-averaged concentration profile is perfectly linear and does not exhibit unphysical artifacts due to the interface between the two SDPD regions with different resolution.

4.7 Conclusions

In this work, we provide a new multiscale fluctuating continuum particle approach for ideal solutions. The stochastic differential equations governing the concentration field are obtained by introducing thermal noise in the Lagrangian SPH equation for diffusion using the GENERIC formalism. Random fluxes of solute are pairwise between particles and constructed such that fluctuation-dissipation is satisfied. When solved concurrently with the SDPD equations of motion, this set of SDEs allows for treatment of advection-diffusion problems across length scales ranging from nanometers to microns and the non-fluctuating continuum limit. The characteristic length scale of the fluid is controlled by the smoothing length parameter, which influences both the distribution of momenta as well as solute concentrations. We illustrate that this new multicomponent SDPD reproduces the correct fluctuations by performing equilibrium simulations at different average concentrations and resolutions (i.e., smoothing lengths). In all cases, the results show excellent agreement with the analytical result for the probability distribution of concentrations.

Importantly, the ability to control the smoothing length parameter makes multicomponent SDPD ideal for multiscale simulation. Thus, we use this approach to extend the single-component multiscale SDPD techniques of Kulkarni et al. to binary solute-solvent systems, and propose refining and coarsening rules for particle splitting/combining such that mass, momentum, and solute are conserved. In order to validate this framework for multicomponent multiscale simulation, we perform equilibrium simulations involving SDPD fluids with different degrees of coarse-graining and demonstrate that there are no unphysical artifacts in the concentration profile near the interface between the two regions, and each

region features the appropriate fluctuations for its corresponding length scale. Finally, we apply these tools to a simple non-equilibrium problem (one-dimensional diffusion across a narrow channel), and we demonstrate that this multiscale method correctly captures the propagation of a concentration gradient across multiple length scales, and accurately reproduces the expected diffusion dynamics with solute transfer from the coarse region to the fine one.

The presented multiscale multicomponent approach does have a number of limitations, however. First, for very small SDPD particles with concentration close to zero or unity such that the analytical Gaussian distribution of concentrations is truncated, precision issues can lead to unphysical negative concentrations (or concentrations greater than one). It is possible to remedy this problem either by reducing the time-step, or by using a dynamic time-step approach, such as the Brownian tree algorithm described in Ref. [70]. Second, the method is based on a discretization of the diffusion equation, which is relevant to a very wide range of different problems, but which ultimately assumes ideal mixing. Moreover, constant temperature conditions and a quasi-incompressible fluid are also assumed. These simplifications may be relaxed, although the resulting equations of motion become more complex and for the case of temperature gradients, it is necessary to solve the entropy equation in addition to the ones for momentum and solute diffusion. Finally, while this approach provides a basis for coarse-graining regions where a high level of detail is unnecessary, it is still purely a continuum approach. The power of this framework lies in the ability to reduce the number of particles in bulk regions where high detail is not required, lowering computational cost. However, for certain problems, it may be necessary to retain atomistic resolution in select regions to capture important effects. In a prior study, we

developed an approach for embedding a MD region inside a coarse-grained SDPD fluid (Chapter 3), and constructing these kinds of MD-SDPD hybrid approaches for multicomponent systems is described in Chapter 5.

4.8 Appendix

4.8.1 Overview of *GENERIC Formalism*

In this subsection of the appendix, we provide a brief review of *GENERIC*, since it is central to the approaches presented in Chapters 3-6. For additional details, see Refs. [31,44,68,69]. *GENERIC* (“General Equation for Non-Equilibrium Reversible-Irreversible Coupling”) provides a framework for beyond-equilibrium problems, which is comparable to existing formalisms in traditional equilibrium thermodynamics. Consider that in equilibrium thermodynamics, the total change in energy of the system can be divided into two separate yet intimately related quantities, 1) “work” (a mechanical, “macroscopic” quantity and 2) “heat”,

$$dE = \delta W + \delta Q. \quad (4.35)$$

This is of course the first law of thermodynamics, which tells us that energy (a conserved quantity) for a given system changes through exchange of heat or work with the surroundings. The work contribution is specified using mechanical terms (e.g. $-pdV$ and μdN), and the heat term depends on temperature through the second law, TdS . Substituting these terms into Eq.(4.35) gives the fundamental equation, which in turn can be used to obtain expressions for other thermodynamic potentials that depend on different independent variables through Legendre transformations.

The idea of *GENERIC* is to provide an analogous approach for systems that are not at equilibrium. In particular, we make the distinction between “reversible” and “irreversible” contributions to the dynamics of the system (similar to the distinction between “work” and

“heat” in the equilibrium case) as the starting point, and the process of interest is the evolution towards an equilibrium state. The reversible contribution is interpreted under mechanistic terms and is associated with Hamiltonian dynamical systems. The structure of the reversible terms translates energy gradients into vector fields through linear operators. In classical irreversible thermodynamics, it is assumed that entropy gradients drive irreversible time evolution towards equilibrium (for small perturbations from the equilibrium state), similar to how energy gradients drive reversible dynamics. Thus, it is also necessary to introduce a linear operator that translates entropy gradients into vector fields. Combining these two distinct contributions, one arrives at a general time-evolution equation for systems beyond equilibrium, referred to as GENERIC:

$$\frac{dx}{dt} = L(x) \cdot \frac{\delta E(x)}{\delta x} + M(x) \cdot \frac{\delta S(x)}{\delta x}. \quad (4.36)$$

Here, x is a set of independent variables that are required to fully describe the state of the non-equilibrium system. $E(x)$ and $S(x)$ are real-valued functionals for the energy and entropy, respectively, which depend on the state variables x . $L(x)$ and $M(x)$ are the Poisson and friction matrices that represent geometric structures and dissipative properties in terms of linear operators. The first term on the right-hand side of Eq.(4.36) corresponds to the reversible part of the dynamics, and the second term corresponds to the irreversible one. The dot product implies summations over discrete indices and/or integration over continuous labels. Generally, the derivatives of the energy and entropy functions are functional derivatives. The GENERIC equation can be viewed as a generalization of the Ginzburg-Landau equation, which is a simple equation that is found to successfully describe irreversible relaxation towards an equilibrium state in many systems.

With the described formalism, it is possible to show that the matrices $L(x)$ and $M(x)$ must satisfy a number of properties. In addition to Eq.(4.36), we have the following complementary degeneracy requirements:

$$\begin{aligned} L(x) \cdot \frac{\delta S(x)}{\delta x} &= 0, \\ M(x) \cdot \frac{\delta E(x)}{\delta x} &= 0. \end{aligned} \tag{4.37}$$

The first condition is due to the reversible nature of the L -matrix contribution to the dynamics, i.e. the entropy function is unaffected by the action of the reversible dynamics-generating L operator. In other words, the first condition is a statement of the 2nd law of thermodynamics (the time derivative of the entropy will always be greater than or equal to zero). The second condition is a statement of conservation of energy in an isolated system; dissipated mechanical energy is converted into internal energy, and globally energy must be conserved. Below, we explicitly demonstrate how these conditions, in combination with the GENERIC equation, yield energy conservation and irreversible entropy production. In addition to these conditions, the matrix $L(x)$ must be antisymmetric, and the dissipative or friction matrix $M(x)$ must be symmetric and positive semidefinite.

We now incorporate the structure of Hamiltonian dynamics into the reversible part of the non-equilibrium process. This is done by defining a bracket operator through the antisymmetric matrix $L(x)$,

$$\{A, B\} = \frac{\delta A(x)}{\delta x} \cdot L(x) \cdot \frac{\delta B(x)}{\delta x}. \tag{4.38}$$

This operator inherits the antisymmetry of the matrix $L(x)$,

$$\{A, B\} = -\{B, A\}. \quad (4.39)$$

It also satisfies Liebnitz' rule,

$$\{AB, C\} = A\{B, C\} + B\{A, C\}. \quad (4.40)$$

These identities hold for arbitrary functionals A , B and C . Finally, the bracket operator must satisfy the Jacobi identity,

$$\{A, \{B, C\}\} + \{B, \{C, A\}\} + \{C, \{A, B\}\} = 0. \quad (4.41)$$

Note that we have essentially defined the Poisson bracket, which guarantees Hamiltonian dynamics.

Similarly, it is possible to define a bracket operator with the dissipative matrix $M(x)$

$$[A, B] = \frac{\delta A(x)}{\delta x} \cdot M(x) \cdot \frac{\delta B(x)}{\delta x}. \quad (4.42)$$

This bracket operator has the symmetry property $[A, B] = [B, A]$. Since $M(x)$ is positive semidefinite, this implies the operator must satisfy the condition $[A, A] \geq 0$ for any arbitrary functional A .

Using these definitions, we can reformulate GENERIC. Consider writing the time evolution of some arbitrary functional A as

$$\frac{dA}{dt} = \frac{\delta A(x)}{\delta x} \cdot \frac{dx}{dt}. \quad (4.43)$$

Substituting Eq.(4.36) into Eq.(4.43), we rewrite the GENERIC equation using the bracket notation as

$$\begin{aligned}\frac{dA}{dt} &= \frac{\delta A(x)}{\delta x} \cdot \left[L(x) \cdot \frac{\delta E(x)}{\delta x} + M(x) \cdot \frac{\delta S(x)}{\delta x} \right] \\ &= \{A, E\} + [A, S],\end{aligned}\tag{4.44}$$

where, of course, E and S denote energy and entropy functionals, and $A(x)$ is a functional that depends on state variables x . In the second line, we have distributed the $\delta A / \delta x$ term and used the definitions of the brackets.

We now show that the degeneracy requirements and bracket properties lead to energy conservation. Suppose that the function of interest $A(x)$ is, in this particular case, the energy $E(x)$. Eq.(4.44) becomes

$$\frac{dE}{dt} = \{E, E\} + [S, E].\tag{4.45}$$

Here, we have also used the symmetry of the dissipative bracket, $[E, S] = [S, E]$. Thus, we are left with

$$\frac{dE}{dt} = \{E, E\} + \frac{\delta S(x)}{\delta x} \cdot M(x) \cdot \frac{\delta E(x)}{\delta x}.\tag{4.46}$$

The second term on the right-hand side is zero due to the degeneracy requirement for the dissipative matrix, Eq.(4.37). The first term is zero due to the Poisson bracket property that $\{E, E\} = 0$. Hence, we have energy conservation, i.e.,

$$\frac{dE}{dt} = 0.\tag{4.47}$$

Similarly, by applying the GENERIC equation to entropy and instead using the degeneracy requirement for the $L(x)$ operator, it is possible to prove irreversibility. Once again, we start with the GENERIC equation of motion, Eq.(4.44). In this case, we let the functional $A(x)$ be the entropy, $S(x)$,

$$\frac{dS}{dt} = \{S, E\} + [S, S]. \quad (4.48)$$

Using the antisymmetry of the Poisson bracket $\{S, E\} = -\{E, S\}$,

$$\begin{aligned} \frac{dS}{dt} &= -\{E, S\} + [S, S] \\ &= -\frac{\delta E(x)}{\delta x} \cdot L(x) \cdot \frac{\delta S(x)}{\delta x} + [S, S]. \end{aligned} \quad (4.49)$$

The first term on the right-hand side of Eq.(4.49) is zero due to the degeneracy requirement $L \cdot \delta S / \delta x = 0$, Eq.(4.37). The remaining term will always be equal to or greater than zero since the dissipative matrix is positive semidefinite. Hence, we can write,

$$\frac{dS}{dt} = [S, S] \geq 0. \quad (4.50)$$

This is of course a statement the second law of thermodynamics.

Finally, it is possible to incorporate thermal fluctuations into GENERIC. Note that Eq.(4.36) is purely deterministic, although noise can be incorporated in a natural manner by formulating a diffusion/Fokker-Planck equation that governs the time evolution of the configurational distribution function $f(x, t)$,

$$\frac{\partial f(x, t)}{\partial t} = -\frac{\delta}{\delta x} \cdot \left[\left(L \cdot \frac{\delta E}{\delta x} + M \cdot \frac{\delta S}{\delta x} \right) f(x, t) \right] + k_B \frac{\delta}{\delta x} \cdot \left[M \cdot \frac{\delta}{\delta x} f(x, t) \right]. \quad (4.51)$$

Omitting the second term on the right-hand side, this equation becomes simply the Liouville equation corresponding to GENERIC. The corresponding SDE for trajectories given particular realizations of the stochastic process is:

$$dx = L \cdot \frac{\delta E}{\delta x} dt + M \cdot \frac{\delta S}{\delta x} dt + k_B \frac{\delta}{\delta x} \cdot M dt + B \cdot dW_t. \quad (4.52)$$

Here, $B(x)$ is the noise amplitude; it is a matrix that is related to the dissipative matrix $M(x)$ through the fluctuation dissipation theorem:

$$B(x) \cdot B(x)^T = 2k_B M(x). \quad (4.53)$$

k_B is Boltzmann's constant and dW_t is the stochastic Wiener process with first and second moments:

$$\begin{aligned} W_t &= 0, \\ W_t W_t^T &= \min(t, t') \mathbf{I}. \end{aligned} \quad (4.54)$$

Taking the limit $k_B \rightarrow 0$ reduces Eq.(4.52) to the non-fluctuating form of GENERIC, Eq.(4.36). The term involving the divergence of the dissipative matrix in the Fokker-Planck equation is a consequence of the Itô interpretation of the SDE. This occurs because the friction matrix $M(x)$ is positioned between the two functional derivatives in the second order term, which is necessary to reproduce the appropriate Boltzmann distribution at equilibrium. In practice, it is desirable to avoid calculating the term involving the divergence of the friction matrix.

In summary, modeling through GENERIC requires the definition of four building blocks $E(x)$, $S(x)$, $L(x)$, and $M(x)$ (or the brackets that correspond to these matrix operators). The matrix $L(x)$ can be determined through consideration of symmetries, whereas dynamical information enters through the friction matrix $M(x)$. As long as the four building blocks satisfy the constraints described in this appendix, the system they describe will be thermodynamically-consistent by construction, i.e. the first and second laws of thermodynamics will be satisfied.

4.8.2 Derivation of Concentration Variance for SDPD Particle

Here, we provide a derivation for the variance in concentration of a SDPD particle, Eq.(4.31). Note that this closely follows the derivation for the variance in a binary mixture described in Ref. [64]. To this end, we consider a small control volume in a large bulk solution where that volume contains N solvent and n solute particles. This region of fluid is a SDPD particle (defined as a volume of fluid that is locally in equilibrium) and corresponds to our system, whereas the remaining SDPD particles constitute the surrounding bath. Assuming that the total number of atoms or molecules inside the system does not change, we write

$$N_{total} = N + n, \quad (4.55)$$

where n and N can vary, though N_{total} is fixed. This constraint is due to the SDPD particles having constant mass. Ultimately, we are interested in the probability distribution for the concentration of the solute inside the fluid volume (i.e. SDPD particle), which is allowed to exchange solute with the surroundings (or remaining SDPD particles). Here, we define the solute concentration as $\Phi = n / N_{total}$.

At equilibrium, the temperature, pressure, and concentration of this small control region are equal to their values in the rest of the solution, which acts as a bath. We need to determine the minimum work needed to bring the temperature, pressure, and number of solute particles in this volume to values which differ from the equilibrium ones by small but finite amounts of δT , δP , δn , and δN . These perturbations change the entropy by some quantity. Note that the perturbations in n and N are not independent due to the constraint in Eq.(4.55). The probability of this thermodynamic fluctuation is

$$P \propto \exp(\Delta S_t). \quad (4.56)$$

Here, ΔS_t is the change in entropy from the maximum value due to the fluctuation. This entropy difference can be written as

$$\Delta S_t = \frac{-R_{min}}{k_B T_0}. \quad (4.57)$$

R_{min} is the minimum work done by the region on the external medium to modify the temperature, pressure, and number of solute molecules by δT , δP , δn , and δN . T_0 denotes the temperature in the surrounding fluid. Note that this minimum in the work occurs when the process is reversible.

The work done by an external force is equal to the change in energy of the system,

$$\delta R_{min} = \delta E + \delta E_0. \quad (4.58)$$

In this expression, the zero subscript indicates changes in the external medium (surroundings), and the variables without a subscript indicate changes in the small region we are considering (system). We rewrite δE_0 in terms of changes in the independent variables,

$$\delta R_{min} = \delta E + T_0 \delta S_0 - P_0 \delta V_0 + \mu_0^a \delta n_0 + \mu_0^b \delta N_0, \quad (4.59)$$

where μ_0^a indicates the chemical potential of the solute in the surrounding fluid, and μ_0^b denotes the solvent chemical potential.

Since the process is assumed to be reversible, we have the condition

$$\delta S_0 = -\delta S. \quad (4.60)$$

Moreover, if we assume that volume and the number of solute and solvent molecules are conserved quantities, we can also write

$$\begin{aligned}
\delta V &= -\delta V_0, \\
\delta n &= -\delta n_0, \\
\delta N &= -\delta N_0.
\end{aligned}
\tag{4.61}$$

Substituting these expressions into (4.59), we obtain a new expression for the minimum work done,

$$\delta R_{min} = \delta E - T_0 \delta S + P_0 \delta V - \mu_0^a \delta n - \mu_0^b \delta N. \tag{4.62}$$

We assume that the total number of particles within the system is fixed [Eq.(4.55)]. Hence, this expression simplifies to

$$\begin{aligned}
\delta R_{min} &= \delta E - T_0 \delta S + P_0 \delta V - \mu_0^a \delta n - \mu_0^b \delta (N_{tot} - n) \\
&= \delta E - T_0 \delta S + P_0 \delta V - (\mu_0^a - \mu_0^b) \delta n.
\end{aligned}
\tag{4.63}$$

At thermal equilibrium, the temperature, pressure, and chemical potential values are uniform at their equilibrium values. Thus, we drop the zero subscript and assume T , P , μ denote equilibrium values,

$$\delta R_{min} = \delta E - T \delta S + P \delta V - (\mu^a - \mu^b) \delta n. \tag{4.64}$$

The minimum work necessary to change n by Δn is hence given by

$$R_{min} = \Delta G - \mu^{ab} \Delta n. \tag{4.65}$$

Here G denotes the Gibbs' free energy and we have defined $\mu^{ab} = \mu^a - \mu^b$. This is an effective chemical potential that emerges due to the fact that the two species are not independent.

Next, we Taylor expand the free energy in the solute change Δn

$$\begin{aligned}
\Delta G &\cong \left(\frac{\partial G}{\partial n} \right)_{P,T} \Delta n + \frac{1}{2} \left[\left(\frac{\partial^2 G}{\partial n^2} \right)_{P,T} (\Delta n)^2 \right] + O[(\Delta n)^3] \\
&\cong \mu^{ab} \Delta n + \frac{1}{2} \left[\left(\frac{\partial \mu^{ab}}{\partial n} \right)_{P,T} (\Delta n)^2 \right].
\end{aligned}
\tag{4.66}$$

Substituting this expression for ΔG into Eq.(4.65) gives the following for the minimum work,

$$R_{min} = \frac{1}{2} \left[\left(\frac{\partial \mu^{ab}}{\partial n} \right)_{P,T} (\Delta n)^2 \right]. \quad (4.67)$$

Combining Eqs.(4.56), (4.57), and (4.67) gives the probability distribution formula

$$P \propto \exp\left(-\frac{R_{min}}{k_B T}\right) = \exp\left\{-\frac{1}{2k_B T} \left[\left(\frac{\partial \mu^{ab}}{\partial n} \right)_{P,T} (\Delta n)^2 \right]\right\}. \quad (4.68)$$

The general formula for a Gaussian distribution is

$$P(x) dx = \frac{1}{\sqrt{2\pi \langle x^2 \rangle}} \exp\left(-\frac{x^2}{2 \langle x^2 \rangle}\right) dx. \quad (4.69)$$

Comparing Eqs.(4.68) and (4.69) yields the following relationship for the variance of the solute:

$$\frac{1}{2 \langle (\Delta n)^2 \rangle} = \frac{1}{2k_B T} \left(\frac{\partial \mu^{ab}}{\partial n} \right)_{P,T}. \quad (4.70)$$

Solving for the variance,

$$\langle (\Delta n)^2 \rangle = \frac{k_B T}{\left(\frac{\partial \mu^{ab}}{\partial n} \right)_{P,T}} = \frac{k_B T}{\left(\frac{\partial \mu^a}{\partial n} \right)_{P,T} - \left(\frac{\partial \mu^b}{\partial n} \right)_{P,T}}. \quad (4.71)$$

Assuming ideal mixing, the chemical potentials are defined as

$$\begin{aligned} \mu^a &= \mu_s^a + k_B T \ln\left(\frac{n}{N_{tot}}\right), \\ \mu^b &= \mu_s^b + k_B T \ln\left(\frac{N}{N_{tot}}\right) = \mu_{id}^b + k_B T \ln\left(\frac{N_{tot} - n}{N_{tot}}\right). \end{aligned} \quad (4.72)$$

Here, the s subscript denotes the pure species chemical potential. Using Eq.(4.72), we can find the derivatives

$$\begin{aligned}\left(\frac{\partial\mu^a}{\partial n}\right)_{P,T} &= \frac{k_B T}{n}, \\ \left(\frac{\partial\mu^b}{\partial n}\right)_{P,T} &= -\frac{k_B T}{N_{tot} - n}.\end{aligned}\tag{4.73}$$

Substituting Eq.(4.73) into Eq.(4.71),

$$\langle(\Delta n)^2\rangle = \frac{1}{\frac{1}{n} + \frac{1}{N_{tot} - n}}.\tag{4.74}$$

Finally, we divide Eq.(4.74) by N_{tot}^2 , and define the solute concentration as $\Phi = n / N_{tot}$ and solvent concentration as $(1 - \Phi) = (N_{tot} - n) / N_{tot}$. Using these definitions, Eq.(4.74) simplifies after some algebra to

$$\langle(\Delta\Phi)^2\rangle = \frac{\langle(\Delta n)^2\rangle}{N_{tot}^2} = \frac{\Phi(1 - \Phi)}{N_{tot}}.\tag{4.75}$$

Note that for a SDPD particle, we can write $N_{tot} = m / m_0$, where m is the mass of the SDPD fluid volume, and m_0 is the mass of an individual solute or solvent atom, giving Eq.(4.31).

4.8.3 Derivation of SDPD Multicomponent Model Using Chemical Potentials

In deriving the SDPD model presented in Section 4.2, we linearized the chemical potentials for direct comparison with the discretized diffusion equation. Here, we provide an alternative derivation of this model using chemical potentials where this simplification is not necessary. This different approach first requires deriving the appropriate transport equation

for an ideal mixture with the constant mass constraint discussed in Appendix 3.8.2. For small concentration gradients, the flux of solute is a linear of function of the chemical potential gradient, i.e.

$$\mathbf{j} = -\alpha \nabla \hat{\mu}. \quad (4.76)$$

The general relationship between the diffusion constant and the coefficient α and the derivative of the chemical potential is given by [18]

$$D = \frac{\alpha m_0}{\rho} \left(\frac{\partial \hat{\mu}}{\partial \Phi} \right)_{p,T}. \quad (4.77)$$

Here, we have an effective chemical potential due to the constant mass constraint (see Appendix 4.8.2, Ref. [18,19]).

$$\hat{\mu} = \frac{k_B T}{m_0} \ln \Phi - \frac{k_B T}{m_0} \ln(1 - \Phi). \quad (4.78)$$

From α , we can also obtain the fluctuation correlation for the components of the stochastic flux vector $\tilde{\mathbf{j}}$ [19],

$$\langle \tilde{j}^m(\mathbf{r}_1, t_1) \tilde{j}^n(\mathbf{r}_2, t_2) \rangle = 2\alpha k_B T \delta_{mn} \delta(t_1 - t_2) \delta(\mathbf{r}_1 - \mathbf{r}_2). \quad (4.79)$$

Substituting Eq.(4.78) into Eq.(4.77),

$$D = \frac{\alpha k_B T}{\rho} \frac{\partial}{\partial \Phi} [\ln \Phi - \ln(1 - \Phi)]_{p,T} = \frac{\alpha k_B T}{\Phi(1 - \Phi)\rho}. \quad (4.80)$$

Solving for the coefficient α ,

$$\alpha = \frac{\rho D \Phi(1 - \Phi)}{k_B T}. \quad (4.81)$$

Combining Eq.(4.81) with Eq.(4.79) gives the correlation for solute fluctuations in ideal fluid mixtures,

$$\langle \tilde{\mathbf{j}}(\mathbf{r}_1, t_1) \tilde{\mathbf{j}}(\mathbf{r}_2, t_2) \rangle = 2\rho D\Phi(1-\Phi)\mathbf{I}\delta(t_1 - t_2)\delta(\mathbf{r}_1 - \mathbf{r}_2). \quad (4.82)$$

Next, we substitute Eq.(4.81) into Eq.(4.76), which results in the following expression for the flux of solute,

$$\mathbf{j} = -\frac{\rho D\Phi(1-\Phi)}{k_B T} \nabla \hat{\mu}. \quad (4.83)$$

By defining a dimensionless chemical potential $\mu = \hat{\mu} / k_B T$ and a diffusion constant in terms of units $\text{ML}^{-1}\text{t}^{-1}$, Eq.(4.83) can be written more simply as

$$\mathbf{j} = -D\Phi(1-\Phi)\nabla\mu. \quad (4.84)$$

Taking the divergence of this flux, we obtain the transport equation

$$\rho \frac{d\Phi}{dt} = \nabla \cdot [D\Phi(1-\Phi)\nabla\mu]. \quad (4.85)$$

As before, the left-hand side is the material derivative. Substituting the appropriate form of the chemical potential [Eq.(4.78)] reduces this expression to the familiar diffusion equation. For this alternate derivation, we preserve the driving force written in terms of chemical potential, rather than concentration, gradients.

Discretizing Eq.(4.85) using the interpolant W results in

$$m_i \frac{d\Phi_i}{dt} = 4D \sum_{j=1}^N \frac{m_i m_j}{\rho_i \rho_j} \left(\frac{\Theta_i \Theta_j}{\Theta_i + \Theta_j} \right) \left(\frac{1}{|\mathbf{r}_{ij}|} \frac{\partial W_{ij}}{\partial r_{ij}} \right) \mu_{ij}, \quad (4.86)$$

where we have defined $\Theta_i = \Phi_i(1-\Phi_i)$ and the chemical potential difference $\mu_{ij} = \mu_i - \mu_j$,

where $\mu_i = \ln \Phi_i - \ln(1-\Phi_i)$.

We again postulate noise in the solute number with the form

$$m_i d\tilde{\Phi}_i = \sum_{j=1}^N G_{ij} dV_{ij}. \quad (4.87)$$

Following the same procedure described in Section 4.2 (using the fluctuation-dissipation theorem and GENERIC), we obtain an equation of motion describing how gradients due to concentration fluctuations induced by Eq.(4.87) are relaxed,

$$m_i \frac{d\Phi_i}{dt} = -\frac{1}{2m_0} \sum_{j=1}^N G_{ij}^2 \left[\ln \left(\frac{\Phi_i}{\Phi_j} \right) + \ln \left(\frac{1-\Phi_j}{1-\Phi_i} \right) \right]. \quad (4.88)$$

With the definition of the dimensionless chemical potential given previously, Eq.(4.88) becomes simply

$$m_i \frac{d\Phi_i}{dt} = -\frac{1}{2m_0} \sum_{j=1}^N G_{ij}^2 \mu_{ij}. \quad (4.89)$$

Earlier, we obtained a discrete transport equation in terms of chemical potential differences, Eq.(4.86). Comparing Eq.(4.86) to Eq.(4.89), it is possible to determine the unknown coefficient for the noise G_{ij} without having to linearize the logarithmic terms,

$$G_{ij} = \left[-\frac{8Dm_0 m_i m_j}{\rho_i \rho_j} \left(\frac{\Theta_i \Theta_j}{\Theta_i + \Theta_j} \right) \frac{1}{|\mathbf{r}_{ij}|} \frac{\partial W_{ij}}{\partial r_{ij}} \right]^{1/2}. \quad (4.90)$$

Summarizing, we have the evolution equation for the particle concentrations,

$$m_i d\Phi_i = 4D \sum_{j=1}^N \frac{m_i m_j}{\rho_i \rho_j} \left(\frac{\Theta_i \Theta_j}{\Theta_i + \Theta_j} \right) \left(\frac{1}{|\mathbf{r}_{ij}|} \frac{\partial W_{ij}}{\partial r_{ij}} \right) \mu_{ij} dt + m_i d\tilde{\Phi}_i, \quad (4.91)$$

with fluctuations given by Eqs.(4.87) and (4.90). Linearizing the logarithms in the quantity μ_{ij} reduces Eq.(4.91) to the model presented in Section 4.2. Note that the noise amplitude for the alternate model [Eq.(4.90)] is the same as for the linearized case. This approach reproduces the correct fluctuations at equilibrium and dynamics in non-equilibrium problems (results not shown).

While the derivation in this appendix is more elegant, this alternate formulation is less numerically stable. Note that in the limit $\Phi_i \rightarrow 0$ (or similarly, $\Phi_i \rightarrow 1$), the μ_{ij} term in Eq.(4.91) approaches $-\infty$ (or $+\infty$) since the chemical potential is not finite for these cases. At the same time, the concentration-dependent pre-factor in Eq.(4.91) goes to zero for both of these limiting scenarios. Hence, this version of the multicomponent model is not numerically suited for problems involving really dilute concentrations, or concentrations approaching unity. However, the linearized model presented in Section 4.2 resembles the traditional SPH diffusion equation and does not have this stability issue.

4.9 References

- [1] P. Español and M. Revenga, *Phys. Rev. E Stat. Nonlin. Soft Matter Phys.* **67**, 26705 (2003).
- [2] S. Litvinov, X. Y. Hu, and N. A. Adams, *J. Phys. Condens. Matter* **23**, 184118 (2011).
- [3] A. Vázquez-Quesada, M. Ellero, and P. Español, *J. Chem. Phys.* **130**, 34901 (2009).
- [4] N. Moreno, P. Vignal, J. Li, and V. M. Calo, *Procedia Comput. Sci.* **18**, 2565 (2013).
- [5] K. Müller, D. A. Fedosov, and G. Gompper, *Sci. Rep.* **4**, (2014).
- [6] X. Bian, S. Litvinov, R. Qian, M. Ellero, and N. A. Adams, *Phys. Fluids* **24**, 12002 (2012).
- [7] A. Vázquez-Quesada, M. Ellero, and P. Español, *Phys. Rev. E* **79**, 56707 (2009).
- [8] M. Ellero, P. Español, and E. G. Flekkøy, *Phys. Rev. E* **68**, 41504 (2003).
- [9] C. Thieulot, L. P. B. M. Janssen, and P. Español, *Phys. Rev. E* **72**, 16713 (2005).
- [10] C. Thieulot, L. P. B. M. Janssen, and P. Español, *Phys. Rev. E* **72**, 16714 (2005).
- [11] M. Grmela and H. C. Öttinger, *Phys. Rev. E* **56**, 6620 (1997).
- [12] H. C. Öttinger and M. Grmela, *Phys. Rev. E* **56**, 6633 (1997).
- [13] H. C. Öttinger, *Beyond Equilibrium Thermodynamics* (Wiley-Interscience, Hoboken, N.J., 2005).
- [14] P. V. Coveney and P. Español, *J. Phys. Math. Gen.* **30**, 779 (1997).
- [15] M. Laradji and M. J. A. Hore, *J. Chem. Phys.* **121**, 10641 (2004).
- [16] Z. Li, A. Yazdani, A. Tartakovsky, and G. E. Karniadakis, *J. Chem. Phys.* **143**, 14101 (2015).
- [17] J. Kordilla, W. Pan, and A. Tartakovsky, *J. Chem. Phys.* **141**, 224112 (2014).

- [18] L. D. Landau and E. M. Lifshitz, *Fluid Mechanics, Second Edition: Volume 6*, 2nd ed. (Butterworth-Heinemann, Amsterdam, 1987).
- [19] C. Cohen, J. W. H. Sutherland, and J. M. Deutch, *Phys. Chem. Liq.* **2**, 213 (1971).
- [20] J. M. O. de Zarate and J. V. Sengers, *Hydrodynamic Fluctuations in Fluids and Fluid Mixtures*, 1 edition (Elsevier Science, 2006).
- [21] S. T. O'Connell and P. A. Thompson, *Phys. Rev. E* **52**, R5792 (1995).
- [22] N. G. Hadjiconstantinou and A. T. Patera, *Int. J. Mod. Phys. C* **8**, 967 (1997).
- [23] N. G. Hadjiconstantinou, *J. Comput. Phys.* **154**, 245 (1999).
- [24] X. B. Nie, S. Y. Chen, W. N. E, and M. O. Robbins, *J. Fluid Mech.* **500**, 55 (2004).
- [25] R. Delgado-Buscalioni and P. V. Coveney, *Phys. Rev. E* **67**, 46704 (2003).
- [26] R. Delgado-Buscalioni and G. De Fabritiis, *Phys. Rev. E* **76**, 36709 (2007).
- [27] R. Delgado-Buscalioni, K. Kremer, and M. Praprotnik, *J. Chem. Phys.* **128**, 114110 (2008).
- [28] D. A. Fedosov and G. E. Karniadakis, *J. Comput. Phys.* **228**, 1157 (2009).
- [29] I. Korotkin, S. Karabasov, D. Nerukh, A. Markesteijn, A. Scukins, V. Farafonov, and E. Pavlov, *J. Chem. Phys.* **143**, 14110 (2015).
- [30] N. D. Petsev, L. G. Leal, and M. S. Shell, *J. Chem. Phys.* **142**, 44101 (2015).
- [31] P. M. Kulkarni, C.-C. Fu, M. S. Shell, and L. Gary Leal, *J. Chem. Phys.* **138**, 234105 (2013).
- [32] P. J. Atzberger, *J. Comput. Phys.* **229**, 3474 (2010).
- [33] P. J. Hoogerbrugge and J. M. V. A. Koelman, *EPL Europhys. Lett.* **19**, 155 (1992).
- [34] P. Español and P. Warren, *EPL Europhys. Lett.* **30**, 191 (1995).
- [35] P. Español, *Phys. Rev. E* **52**, 1734 (1995).

- [36] Y. Kong, C. W. Manke, W. G. Madden, and A. G. Schlijper, *Int. J. Thermophys.* **15**, 1093 (1994).
- [37] Y. Kong, C. W. Manke, W. G. Madden, and A. G. Schlijper, *J. Chem. Phys.* **107**, 592 (1997).
- [38] W. Jiang, J. Huang, Y. Wang, and M. Laradji, *J. Chem. Phys.* **126**, 44901 (2007).
- [39] P. Nikunen, I. Vattulainen, and M. Karttunen, *Phys. Rev. E* **75**, 36713 (2007).
- [40] E. S. Boek, P. V. Coveney, H. N. W. Lekkerkerker, and P. van der Schoot, *Phys. Rev. E* **55**, 3124 (1997).
- [41] A. Chatterjee and L.-M. Wu, *Mol. Simul.* **34**, 243 (2008).
- [42] R. D. Groot, *J. Chem. Phys.* **136**, 64901 (2012).
- [43] D.-W. Li and X. Y. Liu, *J. Chem. Phys.* **122**, 174909 (2005).
- [44] A. Grafmüller, J. Shillcock, and R. Lipowsky, *Phys. Rev. Lett.* **98**, 218101 (2007).
- [45] L. Rekvig, M. Kranenburg, J. Vreede, B. Hafskjold, and B. Smit, *Langmuir* **19**, 8195 (2003).
- [46] S. Yamamoto, Y. Maruyama, and S. Hyodo, *J. Chem. Phys.* **116**, 5842 (2002).
- [47] M. Laradji and P. B. Sunil Kumar, *Phys. Rev. Lett.* **93**, 198105 (2004).
- [48] D. Reith, M. Pütz, and F. Müller-Plathe, *J. Comput. Chem.* **24**, 1624 (2003).
- [49] M. S. Shell, *J. Chem. Phys.* **129**, 144108 (2008).
- [50] A. P. Lyubartsev, M. Karttunen, I. Vattulainen, and A. Laaksonen, *Soft Mater.* **1**, 121 (2002).
- [51] T. Soddemann, B. Dünweg, and K. Kremer, *Phys. Rev. E* **68**, 46702 (2003).
- [52] C.-C. Fu, P. M. Kulkarni, M. S. Shell, and L. G. Leal, *J. Chem. Phys.* **139**, 94107 (2013).

- [53] C. A. Marsh, G. Backx, and M. H. Ernst, *Phys. Rev. E* **56**, 1676 (1997).
- [54] M. Ripoll, M. H. Ernst, and P. Español, *J. Chem. Phys.* **115**, 7271 (2001).
- [55] L. B. Lucy, *Astron. J.* **82**, 1013 (1977).
- [56] R. A. Gingold and J. J. Monaghan, *Mon. Not. R. Astron. Soc.* **181**, 375 (1977).
- [57] G. R. Liu and M. B. Liu, *Smoothed Particle Hydrodynamics: A Meshfree Particle Method* (World Scientific Publishing Company, 2003).
- [58] J. P. Morris, P. J. Fox, and Y. Zhu, *J. Comput. Phys.* **136**, 214 (1997).
- [59] S. R. D. Groot and P. Mazur, *Non-Equilibrium Thermodynamics*, Dover edition (Dover Publications, New York, 2011).
- [60] J. J. Monaghan, *Rep. Prog. Phys.* **68**, 1703 (2005).
- [61] J. J. Monaghan, *Comput. Phys. Rep.* **3**, 71 (1985).
- [62] P. Español, *Phys. Rev. E* **57**, 2930 (1998).
- [63] A. Donev, J. B. Bell, A. de la Fuente, and A. L. Garcia, *J. Stat. Mech. Theory Exp.* **2011**, P06014 (2011).
- [64] L. D. Landau, E. M. Lifshitz, and L. P. Pitaevskii, *Statistical Physics Part I*, 3rd ed. (Butterworth-Heinemann, Oxford [England], 1980).
- [65] A. Donev, J. B. Bell, A. de la Fuente, and A. L. Garcia, *Phys. Rev. Lett.* **106**, 204501 (2011).
- [66] K. Meier, A. Laesecke, and S. Kabelac, *J. Chem. Phys.* **122**, 14513 (2004).
- [67] K. Meier, A. Laesecke, and S. Kabelac, *J. Chem. Phys.* **121**, 3671 (2004).
- [68] P. E. Kloeden and E. Platen, *Numerical Solution of Stochastic Differential Equations* (Springer, Berlin, 2010).
- [69] R. D. Groot and P. B. Warren, *J. Chem. Phys.* **107**, 4423 (1997).

[70] V. Sotiropoulos and Y. N. Kaznessis, *J. Chem. Phys.* **128**, 14103 (2008).

[71] J. A. Backer, C. P. Lowe, H. C. J. Hoefsloot, and P. D. Iedema, *J. Chem. Phys.* **123**, 114905 (2005).

5 Coupling Discrete and Continuum Concentration Particle

Models for Multiscale Simulation

Multiscale simulation techniques afford a number of advantages for problems in the rapidly burgeoning area of nanoscale engineering and technology, though they are typically quite complex to implement and limited to single-component fluid systems. We describe an approach for modeling multicomponent hydrodynamic problems spanning multiple length scales when using particle-based descriptions for both the finely-resolved and coarse-grained regions. This technique is based on the multiscale methodology previously developed for mesoscale binary fluids [N. D. Petsev, L. G. Leal, and M. S. Shell, *J. Chem. Phys.* **144**, 84115 (2016)], simulated using a particle-based continuum method known as smoothed dissipative particle dynamics (SDPD). An important application of this approach is the ability to perform coupled molecular dynamics (MD) and continuum modeling of molecularly miscible binary mixtures. In order to validate this technique, we investigate multicomponent hybrid MD-continuum simulations at equilibrium, as well as non-equilibrium cases featuring concentration gradients.

5.1 Introduction

Over the last two decades, numerous approaches for concurrently modeling phenomena across multiple length scales have been proposed, driven by a broad spectrum of emergent technologies at interfaces and the nanoscale. One tactic is to employ a molecular

description for spatial regions that necessitate high detail (e.g. a surface where a nanoscale physical or chemical process occurs), and a simpler continuum approximation for other bulk regions where high resolution is not required [1–9]. The first approach of this type was proposed by O’Connell and Thompson [1], who coupled molecular dynamics (MD) simulations to a continuum fluid, where the Navier-Stokes solution was obtained using finite-element methods, with exchange of fluxes between the two regions. Hadjiconstantinou and Patera [3] provided an alternative formulation through the Schwarz alternating method, making it possible to couple MD and continuum domains by iteratively matching their boundary conditions. This method was subsequently applied to the moving contact line problem, resolving singularities that appear in the continuum solution by using a molecular description for the region near the boundary [2]. More recently, we developed a different MD-continuum approach featuring a MD region coupled to a continuum region simulated via a fluctuating hydrodynamic solver called “smoothed dissipative particle dynamics” (SDPD) [9]. Unlike previous hybrid simulation methodologies, we used this stochastic *particle*-based technique for the continuum part of the simulation [10,11], allowing for a consistent and intuitive particle-based description throughout the entire system [12].

However, a major shortcoming of all of these so-called “multiscale” simulation strategies is that they are limited to single-component scenarios, even though systems involving solvated species are ubiquitous in modern molecular and interfacial physics. A significant challenge is faithfully reproducing the dynamics of the dissolved species in solute-solvent systems across multiple spatiotemporal scales, including atomistic ones, which is essential to a number of fundamental problems and applications. For example, a number of time and length scales appear in drug delivery and particle transport in cardiovascular

flow [13,14], where surface chemistry and functionalization is important over small scales while hydrodynamics dominates over larger ones. Other applications include electrolyte solutions at interfaces and corrosion [15,16], in which oxidation occurs at the molecular level, and transport and the microstructure of the material are relevant over micrometer lengths and beyond. Hybrid multiscale techniques may also be useful in coarse-graining solvent in bulk regions when simulating biomolecules in solutions containing salt, including protein interactions in biomolecular assembly [17] and ion channels in cellular membranes [18–20]. Another such example is modeling surface nanobubbles and nanodroplets [21–25], where transport over potentially large length scales may occur in bulk solvent away from the bubble or drop. In light of the vast body of applications, the goals of this chapter are: 1) to outline an intuitive and generalizable framework for capturing the transport of solute in a miscible mixture due to diffusion and advection across multiple length scales and 2) to assess the applicability of the method in simple and appropriately devised test cases.

A major difficulty in multiscale multicomponent simulations is that at the sub-nanometer level matter is discrete (e.g. a molecule is either a solute or solvent), whereas over larger length scales and in the continuum approximation, the fluid is described in terms of fields that can assume a continuum of values (i.e. a fluid volume in solution has a concentration associated with it). Therefore, in traditional MD-continuum hybrid methods, it is necessary to perform spatial or temporal averages that can translate properties in the “discrete” molecular region into continuum variables. Conversely, for free exchange of solute, mass, and momentum between the two regions, conveying the averaged information contained in the continuum fields to a collection of particles with discrete identities is also

required. A hybrid simulation strategy for bridging MD regions to finite-difference continuum solutions that allows for heat and solute transport was provided by Alexiadis et al. [26,27]. In this work, the authors couple MD simulations of a fluid mixture to finite-element solutions of the transport equations by solving a Poisson-type equation for the continuum variables, where information from the atomistic region enters through the non-homogeneous term. Techniques for interfacing MD regions to numerical solutions of Navier-Stokes have also been extended to allow for modeling electroosmotic transport [28]. For the most part, however, multiscale multicomponent simulations schemes are largely absent in the literature, in spite of an abundance of important systems.

In this chapter, we provide a simple framework for coupling discrete concentration descriptions (MD or coarse-grained) to particle-based continuum ones, opening the possibility for multiscale modeling of ideal mixtures, including simulations featuring atomically-resolved regions. In particular, we focus on an algorithm for interfacing discrete particle models, applicable to finer scales, to a SDPD fluid representing the continuum region. SDPD is a Lagrangian particle-based approach for solving the fluctuating hydrodynamic equations of Landau and Lifshitz [29–31], and has been applied to a number of problems at the nano- and mesoscales [11,14,32–35]. An attractive feature of SDPD is that the characteristic length scale (i.e. the degree of coarse-graining in the fluid) is a tunable parameter, controlled by a quantity h known as the “smoothing length”, which determines the size of the fluid volumes (or “particles”) into which the fluid is discretized. The SDPD continuum region can then, in turn, be coupled to increasingly coarse SDPD fluids (i.e. regions with more massive SDPD particles having larger h and at a lower number density), giving significant computational savings due to the reduction in the number of

particles [9,36,37]. SDPD is a thermodynamically-consistent formulation of smoothed particle hydrodynamics (SPH), which is a numerical approach for solving the Navier-Stokes equations by decomposing the fluid into a collection of Lagrangian volumes, or interpolation nodes, whose positions evolve in time according to an equation of motion that approximates the hydrodynamic equations [38–40]. SDPD is obtained by using GENERIC [41–43] to incorporate thermal noise in the evolution equations for the SPH particles through the fluctuation-dissipation theorem. While the techniques described in this chapter are applicable to both SPH and SDPD as the continuum description, we focus on the latter.

Using the coupling techniques described in this chapter, it is possible to perform particle-based hybrid MD-continuum simulations of multicomponent systems. Previously, we described a fluctuating continuum multiscale generalization of the SDPD method for fluid mixtures [37] that provides a particle approach to solving the fluctuating hydrodynamic equations for miscible solutions. In addition, we developed a strategy for hybrid MD-SDPD simulations [9], allowing for multiscale modeling that includes an atomistic MD fluid embedded inside a fluctuating SDPD continuum region. For brevity, we do not discuss these methods in detail here, and refer the interested reader to Ref. [9] (Chapter 3) for the MD-continuum method, and Ref. [37] (Chapter 4) for the multiscale multicomponent extension of SDPD. Instead, we focus on a discrete-continuous coupling strategy for MD-continuum simulations of a homogeneous fluid mixture, hence reconciling the multiscale techniques in Ref. [9] to the multicomponent generalization of SDPD in Ref. [37]. To illustrate this point, we perform simple equilibrium simulations, as well as non-equilibrium tests of quasi-1D diffusion. Though the ideas presented here are limited to ideal solutions, they are still valid for numerous problems where the ideal mixing approximation is appropriate due to dilute

concentrations, i.e. any situation where the solute dynamics is governed by the classic advection-diffusion equation. Moreover, the technique outlined in the following sections may be extensible to non-ideal solutions as well.

In the first part of this chapter, we focus on the algorithm for coupling discrete particle descriptions (i.e. a fluid where a particle is either solute or solvent) to a continuum fluid having a concentration value associated with each particle. For the continuum description, we use SDPD. In order to test this algorithm, we consider the simplest possible case: a multiscale simulation featuring a “fine” SDPD fluid where each particle assumes a discrete identity of either $\Phi_i = 1$ (solute) or $\Phi_i = 0$ (solvent), coupled to a more coarse SDPD fluid where the concentration at each fluid volume can have any value between 0 and 1*. This coupling of multiple scales is achieved by allowing larger, coarse-grained particles to split into finer particles, and for fine particles to combine into coarse ones. The question we address is how to split continuous particles into smaller ones having discrete identities, and vice versa. Refining and coarsening rules for a single-component SDPD fluid are already known [36,37]. Hence, we only need rules for the splitting and combining steps for the concentration. First, we provide a brief overview of SDPD and the coupled MD-SDPD approach for single-component systems in Section 5.2. The MD-SDPD techniques require modification for simulating fluid mixtures, and in Section 5.3 we consider the refining step, where a large, continuous SDPD particle enters the refining region and must split into small, discrete particles. In Section 5.4, we discuss the combining step, where two (or more) fine particles with discrete identities of either $\Phi_i = 1$ or $\Phi_i = 0$ are combined into a single coarse particle having a concentration Φ_j . In Sections 5.5 and 5.6, we test this approach by

* As in Chapter 4, we define concentration in terms of a dimensionless mass fraction.

performing simple multiscale simulations (both continuum-continuum and MD-continuum), demonstrating that proper equilibrium solute distribution is recovered. Finally, in Section 5.7 we extend this multiscale multicomponent approach to non-equilibrium situations featuring concentration gradients, and consider the simple problem of quasi-1D diffusion as a case study.

5.2 Multiscale Modeling Using Smoothed Dissipative Particle Dynamics

Smoothed dissipative particle dynamics is a particle-based approach for solving the hydrodynamic equations in the Lagrangian frame. For the case of an incompressible Newtonian fluid and ideal mixing, the appropriate transport equations governing the momentum and solute dynamics are [44]

$$\rho \frac{d\mathbf{v}}{dt} = -\nabla p + \eta \nabla^2 \mathbf{v} \quad (5.1)$$

and

$$\frac{d\Phi}{dt} = \frac{1}{\rho} \nabla \cdot (D_F \nabla \Phi). \quad (5.2)$$

Here, ρ is the mass density of the fluid (combined mass density of the solute and solvent for the case of a binary mixture), Φ is the concentration defined as the ratio of solute mass to total mass, η is the fluid (or fluid mixture) viscosity, and D_F denotes the diffusivity of the solute with units $ML^{-1}t^{-1}$. In SDPD, the fluid domain is decomposed into a collection of fluid volumes or “particles” whose positions, concentrations, and velocities are evolved using forms of Eqs.(5.1) and (5.2) obtained from a discretization using an interpolant function $W_{ij}(\mathbf{r}_i - \mathbf{r}_j, h)$. The resulting equations of motion for the SDPD particles are [10,34,37]

$$m_i \frac{d\mathbf{v}_i}{dt} = -\sum_{j=1}^N m_i m_j \left(\frac{p_i}{\rho_i^2} + \frac{p_j}{\rho_j^2} \right) \frac{\partial W_{ij}}{\partial r_{ij}} \mathbf{e}_{ij} + 2\eta \sum_{j=1}^N \frac{m_i m_j}{\rho_i \rho_j} \left(\frac{1}{|\mathbf{r}_{ij}|} \frac{\partial W_{ij}}{\partial r_{ij}} \right) \mathbf{v}_{ij} \quad (5.3)$$

for the particle momenta, while the concentration of each particle evolves according to

$$m_i \frac{d\Phi_i}{dt} = 2D_F \sum_{j=1}^N \frac{m_i m_j}{\rho_i \rho_j} \left(\frac{1}{|\mathbf{r}_{ij}|} \frac{\partial W_{ij}}{\partial r_{ij}} \right) \Phi_{ij}. \quad (5.4)$$

In the SDPD governing equations (5.3) and (5.4), \mathbf{v}_i , Φ_i , m_i , ρ_i , and p_i denote the velocity, concentration, mass, density, and pressure of the i th particle, respectively. Additionally, we have the relative position, velocity, and concentration of particles i and j , given by $\mathbf{e}_{ij} \equiv \mathbf{r}_{ij} / |\mathbf{r}_{ij}|$ with $\mathbf{r}_{ij} \equiv \mathbf{r}_i - \mathbf{r}_j$, $\mathbf{v}_{ij} \equiv \mathbf{v}_i - \mathbf{v}_j$, and $\Phi_{ij} \equiv \Phi_i - \Phi_j$. $r_{ij} \equiv |\mathbf{r}_i - \mathbf{r}_j|$ is the separation between particles i and j . The level of coarse-graining in SDPD is an input parameter controlled by the smoothing length h , which determines the extent of the smoothing function W_{ij} and controls the size of the SDPD particles.

Small values of h give mesoscopic fluid volumes that stochastically exchange momenta and solute with each other due to thermal fluctuations. Therefore, in addition to the reversible and dissipative interactions between SDPD particles in Eqs.(5.3) and (5.4), we have the additional random contributions to the equations of motion [10,34,37],

$$\begin{aligned} m_i d\tilde{\mathbf{v}}_i &= \sum_{j=1}^N A_{ij} d\hat{\mathbf{W}}_{ij} \cdot \mathbf{e}_{ij}, \\ m_i d\tilde{\Phi}_i &= \sum_{j=1}^N G_{ij} dV_{ij}, \end{aligned} \quad (5.5)$$

where $d\mathbf{W}_{ij}$ and dV_{ij} are tensorial and scalar increments of the stochastic Wiener process, respectively, and $d\hat{\mathbf{W}}_{ij}$ is the traceless and symmetric part of $d\mathbf{W}_{ij}$. A_{ij} and G_{ij} are noise amplitudes chosen such that the fluctuations introduced into the particle momenta and

concentrations by Eq.(5.5) balance the viscous/dissipative terms in Eqs.(5.3) and (5.4) in accordance with the fluctuation-dissipation theorem. The noise amplitudes are given by [10,34,37]

$$\begin{aligned}
 A_{ij} &= \left[-\frac{8\eta m_i m_j k_B T}{\rho_i \rho_j} \left(\frac{1}{|\mathbf{r}_{ij}|} \frac{\partial W_{ij}}{\partial r_{ij}} \right) \right]^{1/2}, \\
 G_{ij} &= \left[-\frac{8D_F m_0 m_i m_j}{\rho_i \rho_j} \left(\frac{\Theta_i \Theta_j}{\Theta_i + \Theta_j} \right) \frac{1}{|\mathbf{r}_{ij}|} \frac{\partial W_{ij}}{\partial r_{ij}} \right]^{1/2}.
 \end{aligned} \tag{5.6}$$

Above, m_0 is the mass of a single solute or solvent molecule or atom, and we have defined $\Theta_i = \Phi_i(1 - \Phi_i)$. The smoothing length h (i.e. SDPD resolution) can vary spatially in order to selectively coarse-grain parts of the simulation by allowing large SDPD particles to split into small ones, and small particles to combine into more massive ones (see Ref. [37] and Chapter 4). The rules for splitting particles are constructed such that particle momenta, solute, and center of mass are conserved [37].

While a purely continuum method, the equations of motion governing the SDPD particles [Eqs.(5.3) and (5.5)] are similar to those in molecular dynamics, and hence we can perform coupled MD-continuum simulations by allowing particles to change type from MD to SDPD and vice versa depending on their location inside the simulation box using an adaptive resolution approach [45–51]. We previously coupled MD to SDPD for the single-component case using a switching function $s(\mathbf{r})$ that is unity in the MD region, zero in the SDPD region, and smoothly and monotonically transitions between these values inside a buffer zone between the atomistic and continuum domains. Then, the pair interaction between particles i and j is written as a sum between MD and SDPD reversible forces with weighting given by $\lambda = s(\mathbf{r}_i)s(\mathbf{r}_j)$ [9],

$$\mathbf{F}_{ij}|_{rev} = \lambda \mathbf{F}_{ij}^{MD} + (1 - \lambda) \mathbf{F}_{ij}^{SDPD}|_{rev}. \quad (5.7)$$

Here, $\mathbf{F}_{ij}^{SDPD}|_{rev}$ denotes the pressure force in the SDPD equation of motion [i.e. the first term on the right-hand-side of Eq.(5.3)]. Eq.(5.7) guarantees that particles interact through MD forces in the atomistic region, SDPD interactions in the continuum one, and through a linear combination of both force types inside the intermediate (i.e. “buffer”) zone between the MD and SDPD fluids. The dissipative [second term on the right-hand-side of Eq.(5.3)] and random [Eq.(5.5)] SDPD forces are applied to all particles inside the buffer region without weighting in order to thermostat the fluid.

Note that there is a work associated with transforming particles from MD to SDPD type due to the different fluid description, which is supplied by a so-called “thermodynamic force” that acts on particles in the buffer to counter chemical potential gradients that emerge due to multiple resolutions [9,51] (see Chapter 3). By incorporating a thermodynamic force and using the MD-SDPD force interpolation approach outlined above, a MD region can be coupled to an atomically-scaled SDPD fluid (i.e. one where continuum particles have the same mass as the MD ones, ensuring mass conservation). This finely-resolved SDPD domain can in turn be coarse-grained by coupling to SDPD regions having more massive particles and larger values for the smoothing length h by allowing the fine particles to combine into more coarse ones, and coarse particles to split into fine ones. This approach has been applied to single-component systems and is detailed in Ref. [9] and Chapter 3, and extended to binary fluid mixtures in the following sections.

5.3 Refining Continuous Particles into Particles with Discrete Identities

Previously, we described how to interface two SDPD fluids featuring a different resolution using a transition zone that is divided into three parts: 1) splitting, 2) overlap, and 3) combining subregions [37] (see Chapter 4). In this approach, the coarse region is discretized into large fluid volumes, whereas the finely-resolved one is composed of a collection of less massive particles at a higher number density. If a large particle is transported to the refining region, it splits into fine SDPD particles. Similarly, a fine particle that crosses into the combining region is merged with another nearby fine particle into a single coarse one (see Fig. 5.1). The fine and coarse particles coexist in the overlap region, whose presence ensures a smooth transition of fluid properties across the interface between the two different scales [52]. In this section, we focus on the refining region. Note that in the prior work described in Chapter 4, we used a uniform continuum description for the entire problem domain, and combining/splitting rules were straightforwardly determined from conservation laws, i.e. such that the total mass, momentum, and solute remain constant. The rules in Ref. [37] are still used for the particles' masses and momenta upon splitting and combining, and in this chapter we focus on the concentration variable alone, and how concentration values are assigned upon splitting and combining of particles. Unlike Chapter 4, we now consider the case where fine particles assume discrete identities (solute/solvent), whereas the coarse particles adopt a continuum of concentration values for the solute. Hence, when a continuum particle splits into two or more discrete particles (or vice versa), some of the dissolved species may be lost or gained, and will not be precisely conserved globally.

Therefore, in the following, we do not preserve the total solute number exactly, and instead enforce a constant chemical potential.

For simplicity, we first consider the case where coarse particles are twice as massive as the fine ones (Fig. 5.1), i.e. we have fine particles with mass and smoothing length m_1 and h_1 , and large particles with $m_2 = 2m_1$ and $h_2 > h_1$. Thus, when a coarse particle enters the refining region, it splits into two particles, each having half the mass of the parent. Later, we generalize this approach for situations involving large fluid volumes that are n times more massive than the fine ones, where n is an integer greater than one. For the present case, when a large particle i enters the refining region, it divides into two discrete particles j and k . When assigning concentrations to the daughter particles j and k , we have the following possibilities

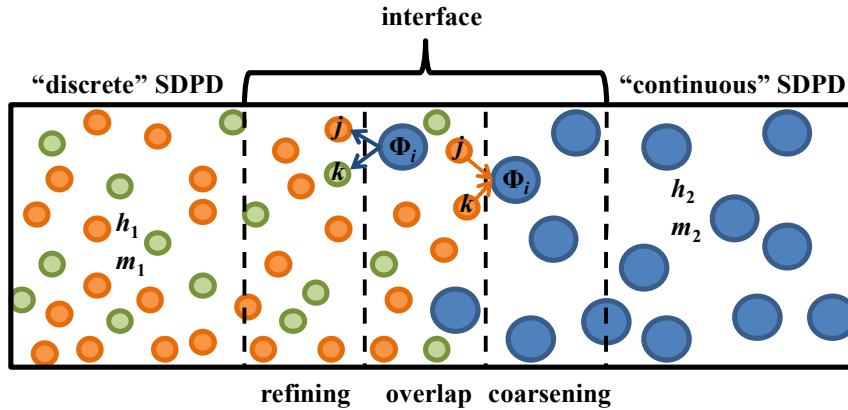


Fig. 5.1. Illustration of discrete-continuous coupling. The left-hand-side of the simulation box features a “discrete” SDPD fluid with mass and smoothing length m_1 and h_1 , respectively, where concentrations can only assume values of 1 or 0, and hence each particle is either solute (orange) or solvent (green). On the right-hand-side, we have a normal SDPD fluid where particles are twice as massive ($m_2 = 2m_1$, $h_2 > h_1$) and can have any concentration Φ . The large, continuous SDPD particles are able to split into fine, discrete ones when crossing into the refining region. Similarly, fine, discrete particles can combine into large particles upon entering the coarsening region.

(Fig. 5.2): 1) The large particle i splits into two solute particles ($\Phi_j = \Phi_k = 1$), 2) the large particle splits into one solute and one solvent particle (e.g. $\Phi_j = 1$ and $\Phi_k = 0$), and 3) the large particle splits into two solvent ($\Phi_j = \Phi_k = 0$). Note that for case 2), there are actually two possibilities: either $\Phi_j = 1$ and $\Phi_k = 0$, or $\Phi_j = 0$ and $\Phi_k = 1$. Therefore, this splitting move has a degeneracy of two ($\Omega_2 = 2$). For the other two splitting options, there is no degeneracy ($\Omega_1 = \Omega_3 = 1$).

Next, we construct rules for selecting from these three possibilities such that a constant chemical potential is enforced. Consider a mixture of two types of particles (i.e. one where the j th particle has concentration of either $\Phi_j = 1$ or $\Phi_j = 0$) with average bulk solute concentration $\langle \Phi \rangle$. From simple combinatorics, we know that the probability of drawing a solute particle ($\Phi_j = 1$) from the box is proportional to the average concentration, $P(\Phi_j = 1) \propto \langle \Phi \rangle$, i.e. a lower concentration of solute particles corresponds to a lower probability of drawing a solute particle at random from the box. Therefore, the probability for drawing two solute particles (i.e. particles with concentration $\Phi_j = \Phi_k = 1$) is given by

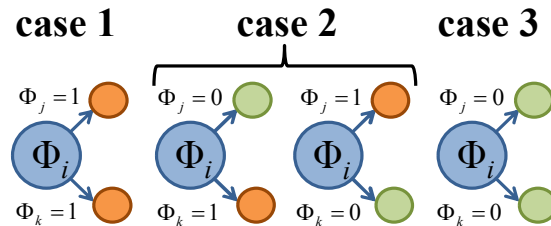


Fig. 5.2. Three different possibilities when splitting a continuous particle into two discrete ones. For case 1, the large particle divides into two solute particles. In case 2, the particle splits into one solute and one solvent, and finally for case 3, the large particle breaks up into two solvent particles.

$P(\Phi_j = 1)P(\Phi_k = 1) \propto \langle \Phi \rangle^2$. Note that this is only exactly true if the first particle is replaced before drawing the second. However, for large systems comprised of many particles, this is a good approximation without replacement as well. Moreover, when the chemical potential is fixed this is exact, since drawing a particle would not affect the average concentration, which is maintained constant by contact with a bath. Hence, the probability for case 1) is:

$$P_1 = \Omega_1 \langle \Phi \rangle^2. \quad (5.8)$$

Similarly, the probability for drawing a solvent molecule is $P(\Phi_j = 0) = 1 - \langle \Phi \rangle$. Therefore, the probability for drawing one solvent and one solute is $P(\Phi_j = 1)P(\Phi_k = 0)$, and thus for case (2) we have

$$P_2 = \Omega_2 \langle \Phi \rangle (1 - \langle \Phi \rangle). \quad (5.9)$$

Finally, the probability for a large particle splitting into two solvent particles [case (3)] is:

$$P_3 = \Omega_3 (1 - \langle \Phi \rangle)^2. \quad (5.10)$$

Therefore, Eqs.(5.8), (5.9), and (5.10) with degeneracies $\Omega_1 = \Omega_3 = 1$ and $\Omega_2 = 2$ give the probabilities for each of the three cases in Fig. 5.2. When a particle crosses into the refining region and divides into two daughter particles, we have to choose from one of these three possibilities, and therefore the total probability that we pick one of these three outcomes must be unity. Due to the definition of the concentrations as mass fractions, the probabilities are normalized, i.e. $\sum_l \Omega_l P_l = 1$. Summarizing, P_1 gives the probability to split into two solute particles relative to the probabilities for the other two options, P_2 is the probability to split into one solute and one solvent relative to the other possibilities, and P_3 is the probability of splitting into two solvents relative to cases 1 and 2. In practice, selecting

from one of these three outcomes is done using a Monte Carlo algorithm, where a uniformly distributed random number X is generated [$X \sim U(0,1)$]. Then, if $X < P_1$, the particle splits into two solutes, $P_1 \leq X < P_1 + P_2$ results in a solute and solvent, and $X \geq P_1 + P_2$ gives two solvent particles.

It is straightforward to extend these rules for large fluid volumes splitting into more than two small particles. For the general case of a coarse particle splitting into n fine particles, the probabilities become

$$\begin{aligned}
 P_1 &= \Omega_1 \langle \Phi \rangle^n (1 - \langle \Phi \rangle)^0, \\
 P_2 &= \Omega_2 \langle \Phi \rangle^{n-1} (1 - \langle \Phi \rangle)^1, \\
 P_3 &= \Omega_3 \langle \Phi \rangle^{n-2} (1 - \langle \Phi \rangle)^2, \\
 &\dots \\
 P_{n+1} &= \Omega_n \langle \Phi \rangle^0 (1 - \langle \Phi \rangle)^n.
 \end{aligned} \tag{5.11}$$

Here, the l th degeneracy factor is the $\binom{n}{l-1}$ binomial coefficient. By coupling to a fluid with coarse particles significantly more massive than the fine ones, there is greater reduction in the total number of particles used, giving further computational savings. However, note that if the discrepancy in the particle masses is too large, this leads to artifacts in properties such as the density distribution, as well instability due to heating upon particle insertion [52,37]. We have performed tests with $n = 2, 4$, and 6 , and in this work present results from the $n = 2$ and 6 cases.

5.4 Coarsening Discrete Particles into Particles with Continuous Concentration Labels

We now consider the converse situation, when two small, discrete particles are combined into a single continuous particle. This combining step occurs inside the coarsening region (Fig. 5.1) and is the reverse move to the particle splitting illustrated in Fig. 5.2. Note that for the particle splitting discussed in the previous section, the amount of solute is not conserved exactly, and instead we enforce the desired chemical potential. Similarly, we construct a coarsening procedure that imposes the same target chemical potential (i.e. average concentration) as the splitting rules. This guarantees that at equilibrium, there is no net loss or gain of solute due to the splitting and combining steps, even if the total amount of solute is not conserved precisely. The concentration inside a small, finite region within a binary mixture can assume a number of different values due to thermal fluctuations, since this region is free to exchange solute with its surroundings. At equilibrium, this results in a distribution of concentration values. For a collection of SDPD particles, each having dimensionless mass m/m_0 , these concentration values are described by a Gaussian distribution with variance

$$\langle (\Delta\Phi)^2 \rangle = \left(\frac{m_0 k_B T}{m} \right) \left(\frac{\partial(\Delta\mu)}{\partial\Phi} \right)_{P,T}^{-1}, \quad (5.12)$$

where $\Delta\mu$ denotes the difference between the solute and solvent chemical potential, a consequence of the constant mass constraint for the SDPD particles. Eq.(5.12) is obtained following a derivation similar to the one for concentration fluctuations in Ref. [53]. Assuming an ideal solution, i.e. $\Delta\mu = k_B T \ln \Phi - k_B T \ln(1-\Phi)$, the variance in Eq.(5.12)

becomes simply $\langle (\Delta\Phi)^2 \rangle = m_0 \langle \Phi \rangle (1 - \langle \Phi \rangle) / m$ [37] (also, see Appendix 4.8.2), and the concentration distribution is therefore

$$P(\Phi) d\Phi = \sqrt{\frac{m}{2\pi m_0 \langle \Phi \rangle (1 - \langle \Phi \rangle)}} \exp\left[-\frac{m(\Phi - \langle \Phi \rangle)^2}{2m_0 \langle \Phi \rangle (1 - \langle \Phi \rangle)}\right] d\Phi. \quad (5.13)$$

Here, m is the mass of the coarse SDPD particle, and m_0 is the mass of an individual solute or solvent molecule; hence, the dimensionless mass m/m_0 is also equivalent to the total number of molecules contained in a single fluid particle. We can therefore assign a concentration value to the newly-formed daughter particle upon coarsening by sampling this distribution. Similar to the splitting move, the amount of solute contained in the parents is irrelevant to the concentration of the newly formed fluid volume, which only depends on the chemical potential of the bath. Note that by drawing values at random from Eq.(5.13), the new continuous particle is automatically equilibrated with the surrounding fluid. Furthermore, this is readily extensible to coarsening steps where the large particle is arbitrarily more massive than the fine particles, since the parameter n is proportional to the coarse particle's mass, m , which affects the distribution in Eq.(5.13). Eq.(5.12) gives a basis for determining the distribution one needs to sample in a coarsening step when dealing with non-ideal solutions where the chemical potential features a different functional form.

Alternative approaches for combining particles include giving the daughter particle a concentration that is equal to the equilibrium concentration ($\Phi_i = \langle \Phi \rangle$), or assigning a value based on the concentrations of the parent particles such that solute is conserved (e.g. a pair of discrete particles with concentrations $\Phi_j = 1.0$ and $\Phi_k = 0.0$ combine into a single coarse particle with concentration $\Phi_i = 0.5$). However, these approaches bias the solute distribution

inside the coarsening region such that it no longer represents the appropriate equilibrium one, given by Eq.(5.13). When coarse particles that do not comply with the equilibrium distribution are then destroyed to form smaller fluid volumes, this may result in a net loss or gain of solute over time. In other words, when considering the distributions of solute left over after a collection of coarsening steps, and after a collection of refining steps, the distributions are perfectly symmetric when using Eq.(5.13). On the other hand, if a different approach is used for the coarsening step, the average solute left over from the combining steps may not balance the leftover solute from the refining steps. There will thus be a net creation or destruction of solute over time (depending on the average concentration) that is balanced by an unphysical constant outflux or influx of solute from the bath. Therefore, in this work we assign coarse particle concentrations by sampling Eq.(5.13).

5.5 Test of Discrete-Continuous SDPD Concentration Coupling at Equilibrium

We use simple two-scale SDPD simulations to test this approach at equilibrium. Specifically, we perform a multiscale simulation having a finely-resolved SDPD fluid coupled to a coarse one where the particles are twice as massive, and the number density is halved. Concentrations are defined as dimensionless mass fractions, and all values are reported with the reduced unit convention in Refs. [36] and [37]. The particles in the fine region are “discrete” and can only take on values of $\Phi_j = 1$ (solute) or $\Phi_j = 0$ (solvent), whereas the particles in the coarse region have a concentration assigned to them that can have any value between 0 and 1. The simulation of a discrete SDPD fluid coupled to a more

coarse continuous one is a toy model for testing the discrete-coupling splitting and combining rules in Sections 5.3 and 5.4. Hence, the splitting probabilities are given by Eqs.(5.8), (5.9), and (5.10), and the concentration of a coarse particle resulting from a combining step is drawn from Eq.(5.13). Initially, 1000 fine particles are placed on a $10 \times 10 \times 10$ cubic lattice inside a volume with dimensions $25 \times 25 \times 25$. The coarse region is prepared by creating 512 particles on a $8 \times 8 \times 8$ lattice inside a $25 \times 25 \times 25$ region. This coarse fluid is placed adjacent to the fine one such that the normal vector to the interface between fine and coarse regions points in the z -direction. The system features periodic boundary conditions in all directions, and the two transition regions are located between $z = 0$ and 6, and $z = 25$ and 31, with each transition zone being divided into refining, overlap, and coarsening subregions having a width of 2. Hence, the total simulation box has dimensions $25 \times 25 \times 50$, with the fine-grained region located at $6 < z < 25$, and the coarse-grained one at $31 < z < 50$. Before starting the equilibration, the particle lattice positions are translated in the positive z -direction by half the transition region width so that initially the interfaces between fine and coarse particle domains are precisely centered inside the overlap subregions.

For the SDPD model, we choose parameters that correspond to a Lennard-Jones fluid at reduced temperature $T = 1.0$ and mass density $\rho = 0.8$. With this mass density and lattice number density, the resulting particles have mass $m_1 = 12.5$ in the fine region, and $m_2 = 25.0$ in the coarse (henceforth the 1 subscript denotes the fine region, and 2 is the coarse-grained one). The corresponding smoothing lengths are $h_1 = 3.00$ and $h_2 = 3.75$, respectively. At the selected state point, the fluid bulk and shear viscosities are $\zeta = 0.9$ [54] and $\eta = 1.9$ [55]. Finally, in SDPD it is necessary to specify the equation of state for the fluid, and thus its thermodynamic properties, in order to calculate the pressure force between particle pairs.

Rather than using the full Lennard-Jones equation of state, we use a simple linearized version with the form $p_i = c_s^2 \rho_i$ [36,39,40], where p_i is the pressure at particle i , ρ_i is the density at the i th particle, and c_s is the speed of sound. Incompressible fluids in SDPD are approximated as quasi-incompressible by choosing a large value for the speed of sound, such that particles are highly-repulsive and density variations are low [40,56,57], typically within 3% of the target density [56]. Hence, we select $c_s = 5.0$ [36], which gives small fluctuations in density without requiring a prohibitively small time-step. The particle concentrations are updated using the Euler-Maruyama integrator [58] with a time-step of $\Delta t = 0.01$.

An important detail is that the self-diffusivity of the fine, discrete particles (MD or SDPD) must equal the effective solute diffusion constant in the continuum part of the simulation, i.e. the diffusive transport of solute should be uniform throughout the system independent of the degree of coarse-graining. In the fine region, solute diffusion occurs purely due to the motion of the discrete particles, and hence it is described by the discrete particles' self-diffusion constant. However, the solute diffusivity in the coarse, continuous SDPD region has two distinct contributions since particles not only move, but also exchange solute with each other in a pairwise fashion. In other words, solute transfer occurs in the coarse SDPD region even if the particles are stationary due to solute fluxes between particle pairs [described by Eqs.(5.4) and (5.5)], and the actual thermal motion of the SDPD particles enhances solute transport further. Matching diffusivities in this case requires care since for small fluid volumes, velocity fluctuations lead to an enhancement of diffusive transport [59,60]. In light of this, the diffusion constant characterizing the total or “effective” rate of solute transfer in the continuous SDPD region is written as a combination of these two contributions: 1) the “bare” Fickian diffusion constant D_F for the solute transferred from one

particle to a neighbor (either due to a difference in chemical potential between the two particles, or due to a stochastic flux of solute), and 2) an additional quantity D_2 that accounts for the random motion of the fluid particles due to velocity fluctuations. The effective diffusion constant for the coarse SDPD fluid is therefore given by summing these two distinct parts [61]

$$D_{eff} = D_F + D_2, \quad (5.14)$$

where D_2 is simply the self-diffusivity of the continuous SDPD particles due to thermal stresses. From mean-square-displacement calculations, we find that the self-diffusion constant of the SDPD fluid particles with mass $m_2 = 25.0$ is $D_2 = 0.0162$. $D_1 = 0.0325$ for SDPD particles with $m_1 = 12.5$, which is the self-diffusivity of a discrete SDPD particle in the fine region [note that in the discrete SDPD domain we do not solve the diffusion equation Eq.(5.4), and hence $D_F = 0$ and solute transport is purely due to the Brownian motion of the SDPD particles].

Summarizing, the fine and coarse SDPD particles in a multiscale simulation feature a different self-diffusivity, and hence the solute dynamics need to be modified to equalize the rate at which solute diffuses throughout the simulation box. In the coarse, continuous region the overall solute diffusivity is $D_{eff} = D_F + D_2$ since 1) solute can be transported between particle pairs, and 2) the particles themselves move and undergo a random walk, advecting solute in the process and enhancing its transport. In the fine, discrete region, however, solute diffusivity is simply D_1 since particles cannot exchange solute with one another ($D_F = 0$) and solute transfer only occurs due to the random motion of the SDPD particles. In order to have uniform diffusivity across the simulation box, the finely-resolved fluid self-diffusion

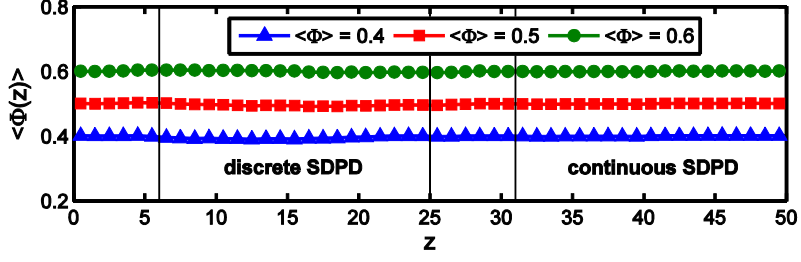


Fig. 5.3. Concentration profiles versus position at equilibrium for a discrete SDPD fluid (located at $6 < z < 25$) coupled to a continuum one ($31 < z < 50$). There are two transition regions due to the box periodicity, located at $0 < z < 5$ and $25 < z < 31$. Results from three separate simulations are shown, having average concentrations of 0.4, 0.5, and 0.6.

constant D_1 therefore must equal the effective diffusion constant in the coarse SDPD region, D_{eff} [Eq.(5.14)], i.e. $D_1 = D_{eff}$, which is achieved by tuning D_F for the continuous SDPD particles. Eq.(5.14) suggests a choice of $D_F = D_1 - D_2 = 0.0162$ for the constant that enters the discretized diffusion equation in order to achieve this matching. Note that the diffusion constant in the discrete part of the simulation box D_1 must be greater than the self-diffusivity of the coarse SDPD particles ($D_1 > D_2$); if this condition is not met, having uniform diffusivity would require a negative value for the bare diffusion constant D_F . If a simulation features a hierarchy of continuum SDPD domains, each having a different level of coarse-graining (i.e. smoothing length) [37], then the Fickian diffusion constant D_F may need to be adjusted for each region such that the effective diffusivity is uniform [although for large particles, D_2 is vanishingly small compared to D_F , and thus Eq.(5.14) becomes simply $D_{eff} \approx D_F$. Hence, modifying the value of D_F for more coarse fluids is not necessary].

Equilibration of the fluid mixture features two stages. This is necessary since initially there is a slight transfer of mass from the fine region into the coarse one, a consequence of

the higher self-diffusivity of the smaller SDPD particles relative to the coarse ones, $D_1 > D_2$ [36]. After the distribution of particles across the system is equilibrated, and the number of particles in the fine and coarse regions stabilizes and fluctuates around an equilibrium value, the concentrations are reset to the average and thermally equilibrated. In other words, we equilibrate the total mass distribution first, and the solute distribution second. The total process is over 1×10^6 time-steps, and the production run is over 1×10^7 time-steps, with a time-step magnitude of $\Delta t = 0.01$. Three separate cases, each having a different average concentration, are studied: *i*) $\langle \Phi \rangle = 0.4$, *ii*) $\langle \Phi \rangle = 0.5$, and *iii*) $\langle \Phi \rangle = 0.6$. The equilibrium concentration profiles from the production runs are shown in Fig. 5.3. The profiles are flat, without significant deviations due to the interface between the discrete and continuous regions, with errors in the three profiles of 1.36%, 0.88%, and 0.02% in the discrete region for cases *i*), *ii*), and *iii*), respectively. In the continuous region, the concentrations are within 0.05%, 0.04%, and 0.03% of the target value. By construction, the continuous SDPD region reproduces the correct fluctuations [37], i.e. the distribution of concentrations is given by Eq.(5.13). Throughout the simulation for case *i*), there are a total of 109712 refining events and 109717 coarsening ones, with particle splitting or combining occurring on average every 73 time-steps. The average solute lost/gained in case *i*) due to a refining/coarsening step over the course of the production run is 0.0144 for particles splitting and 0.032 for particles combining; hence, there is approximately no net creation or destruction of solute, which is on average conserved. Similarly, the average solute gained or lost per splitting/combining move is 0.0052 and 0.0004 for case *ii*), and 0.0355 and 0.0171 for case *iii*).

5.6 Hybrid MD-Continuum Simulations of an Ideal Fluid Mixture at Equilibrium

We now demonstrate how this technique is used to facilitate MD-continuum coupling for fluid mixtures. In particular, we consider a binary fluid modeled across multiple resolutions, with a molecular region for the small scales, and a continuum description for the large ones. The hybrid molecular-continuum approach for single-component systems described in Chapter 3 is an essential element in this test. The method involves a MD region coupled to a SDPD fluid composed of molecularly-sized particles, using an adaptive resolution approach [45–51] that gradually interpolates between MD and SDPD interactions across a buffer region using Eq.(5.7). Due to the particle description employed across all length-scales, momentum and mass conservation is intuitively prescribed. Note that to mediate the MD-to-SDPD transition, this technique requires SDPD fluid “volumes” that have the same size as the individual molecules/atoms, which is unphysical [9]. Despite being atomically-sized, these particles are Markovian due to their coupling to a momentum bath, similar to MD fluids with a DPD thermostat [62]. However, this kind of highly-resolved SDPD fluid still satisfies conservation laws and fluctuation-dissipation, and is used to bridge MD to coarser continuum domains. Importantly, we previously demonstrated in Chapter 3 that it is possible to shrink the atomically-resolved SDPD region to zero size, minimizing the number of ultrafine SDPD particles required for a multiscale simulation. Thus, the only parts of the simulation box where atomically-sized SDPD particles appear is in the refining and overlap regions in the interface between the MD and SDPD fluids (see Fig. 5.4).

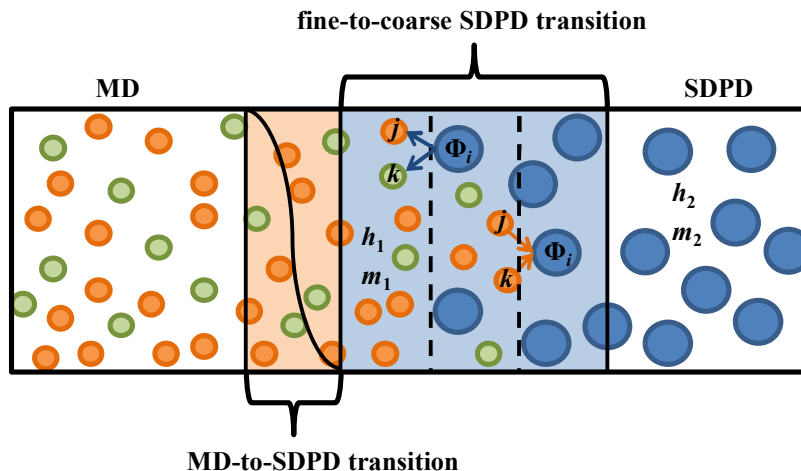


Fig. 5.4. Illustration of MD-continuum coupling for a binary mixture. On the left-hand-side is the MD region, comprised of a collection of solute and solvent atoms. On the right-hand-side is the continuum region, simulated using SDPD. The interface between them is divided into two separate parts: 1) the MD-to-continuum transition (orange) and 2) the fine-to-coarse SDPD particle transition (blue). Note that this arrangement is identical to the set-up for the hybrid MD-continuum simulations in Chapter 3, except the atomically-sized SDPD fluid region has been removed. In the MD-to-SDPD region, particles transition from MD atoms to atomically-sized SDPD fluid particles, and vice versa, where their interactions are gradually turned on/off using a switching function (shown in black). Here, a solute MD atom changes into a SDPD particle with $\Phi_i = 1$, and a solute MD atom becomes a SDPD particle with $\Phi_i = 0$. The fine-to-coarse SDPD transition region (blue) is itself divided into coarsening, overlap, and refining subregions. Here, discrete SDPD particles are combined into continuous particles, and continuous ones are split into discrete ones.

Since the single-species MD-continuum approach briefly summarized in Section 5.2 has been discussed at length (Chapter 3), we focus only on how concentration is treated across the simulation box. In generalizing the MD-continuum approach from Chapter 3 to multicomponent systems, there is no ambiguity in how the molecular region is handled; we simply have a MD region featuring more than one species. Similarly, the continuum region is unambiguously modeled using the multicomponent SDPD formulation described in Chapter

4, where each fluid particle carries solute, has a concentration value assigned to it, and these concentrations are evolved according to the discretized diffusion equation. The MD-continuum coupling is handled as follows: using Eq.(5.7), a solute MD atom/molecule becomes a discrete SDPD particle with concentration $\Phi_i = 1$ upon crossing the MD-to-continuum transition zone (orange area, Fig. 5.4) into the SDPD region, and vice versa. A solvent MD atom/molecule becomes a SDPD particle with $\Phi_i = 0$. Then, these fine, discrete SDPD particles are coupled to more coarse, continuous ones across the fine-to-coarse SDPD transition zone (blue area, Fig. 5.4) using the discrete-continuous coupling described in Sections 5.3-5.5 of this chapter. Note that there is no pure atomically-scaled SDPD fluid region as in Chapter 3; by removing this domain, the MD-to-continuum and fine-to-coarse SDPD transition regions are placed immediately next to each other. Hence, the overall interface is divided into these two parts, one where MD particles transition to continuum ones, and a second part where these fine SDPD particles are coarsened (see Fig. 5.4).

A test for this coupling methodology is set up as follows: a MD wall is created by initializing 845 atoms on a $13 \times 13 \times 5$ lattice inside a volume with dimensions $13 \times 13 \times 5$. Immediately next to this region, we place the MD fluid domain by creating a $12 \times 12 \times 12$ lattice of atoms inside a $13 \times 13 \times 13$ volume. This region is located adjacent to the MD wall such that the z -direction is normal to the liquid-solid interface. Next, the transition zone is created by placing 1056 particles on a $11 \times 12 \times 8$ lattice inside a region with side lengths $13 \times 13 \times 8$. Once again, this part of the simulation box is positioned next to the MD one such that the interface between them has a normal in the z -direction. Finally, we initialize the coarse SDPD fluid by generating a region with dimensions $13 \times 13 \times 26$, and placing a $6 \times 7 \times 14$ lattice of particles inside. This fluid domain is next to the transition region, where the normal

vector to the interface between them is in the z -direction. This setup is illustrated in Fig. 5.5a. The system features a MD boundary between $z = 0$ and $z = 5$ and a MD fluid between $z = 5$ and $z = 18$. The region between $z = 18$ and 23 is the MD-to-continuum transition zone, where MD and SDPD interactions are turned on and off using the adaptive resolution approach from Ref. [9], Eq.(5.7). Between $z = 23$ and $z = 29$ is the fine-to-coarse particle transition described in Sections 5.3 and 5.4, as well as Ref. [37], where fine SDPD particles are transformed into coarse ones, and vice versa. This part is itself divided into a refining region (located $23 < z < 25$), overlap region ($25 < z < 27$), and coarsening region ($27 < z < 29$). Particles situated between $z = 29$ and $z = 46$ are coarse SDPD fluid particles. The SDPD particles between $z = 46$ and $z = 52$ constitute the wall, and their positions and concentrations are not evolved in time. For more details about boundaries in SDPD, see Chapters 3 and 4, and Ref. [56].

We investigate the same thermodynamic state point ($T = 1.0$ and $\rho = 0.8$), and hence use identical values for the shear and bulk viscosities as in Section 5.5. In order to approximately match both the compressibility and absolute pressure in the MD region, we use a linear equation of state with the form $p_i = c_s^2(\rho_i - \rho_0) + p_0$ (here ρ_0 and p_0 are the target density and pressure, respectively, where for the present case $p_0 = 1.4$) [9]. Matching the absolute pressure of the SDPD fluid to the one in the MD region is required, since a pressure mismatch will result in a transfer of mass across the interface separating the domains with different resolution. For this test, we couple the MD fluid to a SDPD region with particles six times more massive; hence, splitting probabilities are given by Eq.(5.11) with $n = 6$, and the concentration of a newly-formed coarse particle is drawn from a numerically pre-computed probability distribution of a single-scale SDPD fluid with

$m / m_0 = 6$ (discussed in more detail below). Given the initial lattice and choice of mass density, the coarse SDPD particles have a mass of 6 and smoothing length $h = 2.35$, while the fine particles (MD and discrete SDPD) have a mass of unity and $h = 1.30$. Since we have an ideal mixture, the SDPD model corresponds to a reference MD fluid where atom interaction energies and sizes are uniform, and the distinction between solute and solvent atoms is purely in terms of labels.

Recall that for very small fluid particles, matching diffusivities requires additional care since velocity fluctuations result in enhanced diffusion. In other words, the self-diffusivity of the solute MD molecules should match the effective diffusion constant in the continuum part of the simulation, which is composed of a Fickian and self-diffusion contribution, as described by Eq.(5.14). Using mean-square-displacement calculations, the self-diffusion constant of the SDPD fluid volumes with $m = 6.0$ is calculated to give $D_{SDPD} = 0.0486$. Our MSD calculations are in agreement with the results of Kulkarni et al. [36], who found that SDPD particles with mass between $m = 2.0$ and 6.0 approximately match the self-diffusivity of their Lennard-Jones atom counterparts at the current thermodynamic state point. $D_{LJ} = 0.0737$ in the MD region, which is the self-diffusivity of a Lennard-Jones particle at the present conditions in a fluid with interaction energy and length $\varepsilon = 1$ and $\sigma = 1$, respectively, and potential cut-off $r_c = 2.6$. Uniform diffusivity across the simulation box requires that the MD diffusion constant D_{LJ} equals the effective diffusion constant in the SDPD region, $D_{eff} = D_F + D_{SDPD}$, i.e. $D_{LJ} = D_{eff}$, where D_F is the diffusion constant that enters the discretized SDPD form of the diffusion equation. Eq.(5.14) therefore suggests a choice of $D_F = 0.0252$ for the Fickian diffusion constant that ensures this matching.

As in Section 5.5, three separate equilibrium simulations are performed, each having a different average concentration ($\langle\Phi\rangle=0.4$, $\langle\Phi\rangle=0.5$, and $\langle\Phi\rangle=0.6$). For the continuum part of the system, a Dirichlet boundary condition is applied at the solid boundary such that the concentration at this location equals the average, equilibrium value. In addition, a no-slip condition is applied to the velocity at the continuum solid-liquid interface. The system is equilibrated for 1×10^6 time-steps, and data is collected for 8×10^6 time-steps. We choose a time-step value of $\Delta t = 0.001$. Care must be taken to use a sufficiently small time-step due to precision issues associated with very small particles that result in SDPD particles having a negative concentration, or concentration greater than one.

An issue that appears as a consequence of the small size of the continuum particles when coupling to a MD region is that the distribution for the coarsening step [Eq. (5.13)] assumes large particles; when particles are small such that concentration fluctuations are significant, the breadth of the distribution becomes larger than the interval between 0 and 1. In such a case, the probability distribution is no longer Gaussian and it is not possible to directly use Eq.(5.13). Hence, the distribution for the solute $P(\langle\Phi\rangle)$ is numerically precomputed beforehand from a single-scale SDPD simulation, and a truncated Gaussian fit of this distribution is used in place of the analytical result given by Eq.(5.13). Note that like the atomically-sized continuum particles it describes, this distribution is not entirely physical, but an artificial construction necessary for mediating the MD-continuum coupling. The resulting distribution can also be viewed as a Gaussian approximation to the true distribution for small systems with ideal mixing.

Concentration profiles from these equilibrium simulations are shown in Fig. 5.5b. The error in the MD region is 0.89%, 1.31%, and 0.46% for the $\langle\Phi\rangle = 0.4$, 0.5, and 0.6 cases, respectively, while in the continuum region it is within 0.57%, 0.13%, and 0.77% for the three tests. The time-average of the solute destroyed per splitting event for the $\langle\Phi\rangle = 0.4$ case is 0.0081, while the solute created due to coarsening is 0.0110. For the $\langle\Phi\rangle = 0.5$ test, the solute destroyed and created is 0.0076 and 0.0092, respectively, and for the $\langle\Phi\rangle = 0.6$ simulation we have 0.0044 solute created and 0.0085 solute destroyed. As before, the net solute created or destroyed per refining/coarsening step is approximately zero. The frequency

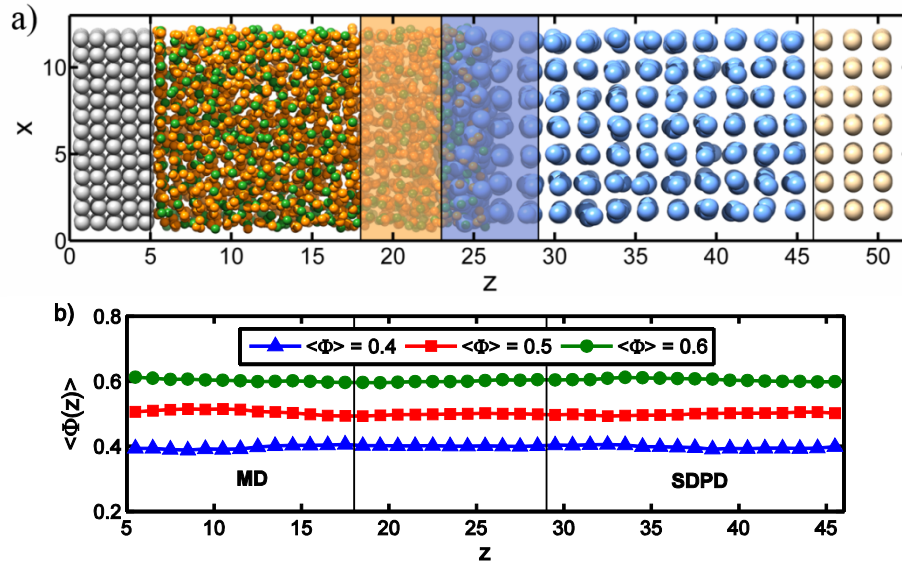


Fig. 5.5. (a) Illustration of system setup. The left-hand-side is a binary MD fluid, whereas the right-hand-side is a continuum region modeled using SDPD. The orange zone is the MD-to-continuum transition, and the blue is the fine-to-coarse SDPD coupling zone. (b) Equilibrium concentration versus position. We show results from three separate simulations, having average concentrations of 0.4, 0.5, and 0.6. The transition region between the MD and continuum domains is divided into two parts, 1) the MD-to-continuum transition region, and 2) the fine-to-coarse particle transition zone.

for splitting and combining particles averaged over the three tests is every 206 time-steps. Over the course of the simulation, we have 96820 splitting events and 96845 coarsening ones. These two numbers are approximately the same, implying no net mass transfer between regions at equilibrium. Note that while we focus on MD-continuum simulations in this section, this approach is general to any situation involving a particle description for the fluid, even ones where molecular regions are not present altogether. For example, the widely used, bottom-up, coarse-grained particle technique known as dissipative particle dynamics (DPD) [64,65] has been applied to qualitative multicomponent simulations where DPD particles are assigned a unique identity (e.g. type A or type B) [66,67]; using the discrete-continuum technique described here, it is possible to couple a binary DPD fluid region to a more coarse continuum one modeled using SDPD. Another possibility is to interface a fine binary fluid composed from particles with potentials obtained from Boltzmann inversion to a more coarse SDPD continuum fluid.

5.7 Non-Equilibrium Multiscale Simulation of a Binary Mixture

In this section, these methods are extended to non-equilibrium situations, where the chemical potential is no longer uniform across the system, giving rise to fluxes of solute. We specifically focus on the problem of quasi-1D diffusion as a case study, where a concentration gradient is imposed across the system perpendicular to the interface between the MD and continuum parts of the simulation box. The system is set up identically to the one in Section 5.6, with a fluid bounded by two walls (see Fig. 5.5a). As before, a MD wall is placed next to a MD fluid, which is coupled to a SDPD fluid where particles are six times as

massive. The difference is that we previously assumed a fixed chemical potential, which corresponded to some equilibrium concentration, when performing the splitting and coarsening steps. Note that the interface region between fine and coarse SDPD fluids is the portion of the simulation box that is coupled to a bath. When gradients are present, we need to adjust the chemical potential of the bath to match the chemical potential that would exist at this location in the absence of multiple degrees of coarse-graining, i.e. if a uniform fluid description was used throughout. In order to generalize this approach to non-equilibrium simulations, we therefore calculate the average concentration in the fluid left of the interface region, as well as the average concentration to the right of the interface, and then perform a linear interpolation to determine the average inside the transition zone (where this average is used for the splitting and refining steps). In other words, the average concentration that appears in Eqs.(5.11) and (5.13) is no longer a constant value across the simulation box, but is calculated from a linear interpolation across the interface region, and the bath enforces a chemical potential based on this value. Therefore, we make a local equilibrium assumption and linearize the concentration profile near the interface. The accuracy of this approach requires that the length scale characterizing concentration gradients is larger than the width of the interface region.

As in the previous section, the probability distribution for the coarsening step is not given by Eq.(5.13) owing to the small particle size and requires additional care. Moreover, since the average concentration is no longer fixed, the distribution will change as the average concentration inside the interface varies while the system evolves towards its equilibrium state. Hence, we first set up a series of equilibrium SDPD simulations at a number of different average concentrations at regular intervals in order to numerically determine the

concentration probability distribution for each one. Next, we use a truncated Gaussian function to fit these results. Once the fitting parameters for a number of different average concentrations are known, we can interpolate between these values to approximate the solute probability distribution for any average concentration that may appear in the transition region. Hence, we determine $P(\langle\Phi\rangle)$ for any $\langle\Phi\rangle$ that may potentially appear within the interface region between the discrete and continuous domains, and therefore we are able to sample the probability distribution appropriate to the instantaneous average concentration inside the transition zone. This procedure assumes that the time-scale for the evolution of $\langle\Phi\rangle$ inside the transition region is slow relative to other time-scales (e.g. the motion of the individual particles), and that sufficiently large volumes are used to calculate this average value in order to remove effects of statistical noise.

For the present test, the concentration is initially 0.4 across the entire simulation box, and after equilibration, the concentration at the SDPD wall is increased to 0.6, and a gradient

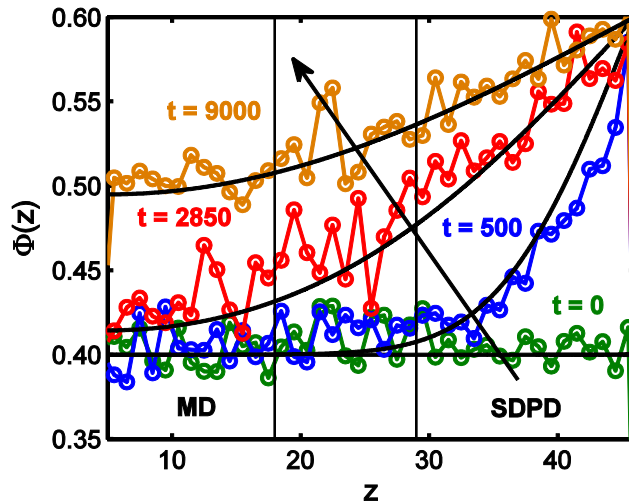


Fig. 5.6. Concentration profiles at different times in a hybrid MD-continuum simulation. The blue curves (circle markers) are the results from simulations, averaged over 10 independent simulations. The black curve is the exact, analytical solution of the diffusion equation.

begins to propagate across the box. The MD wall naturally provides a no-flux boundary condition. Since the concentration can vary between 0.4 and 0.6 inside the interface region, prior to starting we perform a separate series of equilibrium pure SDPD simulations at the following concentrations: $\langle\Phi\rangle=0.40, 0.45, 0.50, 0.55, 0.60$. For each one, the distribution $P(\langle\Phi\rangle)$ is calculated, fit to a truncated Gaussian function, and the values for the fitting parameters are tabulated. Then, if we are running the full hybrid simulation and the value of the concentration inside the buffer is determined to be 0.47 (as an example), we perform a linear interpolation using the fitting parameters for the 0.45 and 0.50 distributions, giving the distribution for that instant $P(\langle\Phi\rangle=0.47)$. This distribution is used in place of Eq.(5.13) if it is necessary to perform a coarsening step. The splitting probabilities are the same as before, except the average concentration in Eq.(5.11) is replaced with the interpolated value. To perform the interpolation and determine the average transition region concentration, the average concentration is calculated using bins of width 5 immediately to the left and to the right of the transition zone. Prior to switching on the concentration gradient, the system is equilibrated at an average concentration of $\langle\Phi\rangle=0.40$ for 1×10^6 time-steps. Due to significant statistical and thermal noise, we average the time-dependent concentration profile over 10 separate trajectories, each initialized using a different random seed. The concentration profile at several different instants is shown in Fig. 5.6 (previous page), compared to the analytical solution from the diffusion equation. Note that while we capture the correct overall diffusion dynamics, the numerical solution may advance slightly ahead or behind of the analytical one since the linear interpolation inside the buffer region can

overestimate/underestimate the average concentration depending on the curvature of the concentration profile.

5.8 Conclusions

In this chapter, we described an approach for hydrodynamic simulations with bridging between high-resolution regions where particles represent individual solute or solvent molecules/clusters, to lower-resolution continuum ones where each particle is a fluid volume that may contain some amount of solute and solvent. This approach is general to any discrete concentration model for the high-resolution molecular region (MD or coarse-grained), and any continuum particle approach for the more coarse-grained part, though in our work we focus on using SDPD. This is achieved by allowing large continuum particles to split into finer discrete ones, and vice versa. The splitting and combining rules are constructed such that an average concentration (i.e. chemical potential) is enforced, allowing for straightforward multiscale equilibrium simulations of fluid mixtures. Moreover, by performing a linear interpolation of the concentration profile across the interface region, it is possible to adjust the bath chemical potential on-the-fly and perform non-equilibrium simulations as well. A simple binning average was used in Section 5.7 to determine the concentration profile values to the left and right of the interface region, which gives an interpolated value for the concentration inside the transition zone. This approach can be generalized to more complicated concentration profiles with variation in all directions by calculating bin averages in three dimensions or performing local SPH averages instead, though the length scale characterizing gradients in concentration should be larger than the

transition zone width to minimize errors due to this local linearization. Importantly, we demonstrated how the applicability of this method by performing both equilibrium and non-equilibrium MD-continuum simulations of a binary ideal mixture.

This approach features several shortcomings, however. First, it is limited to ideal mixing, where the distinction between solute and solvent is only based on particle identities, and interactions between all particles in the fine (e.g. molecular) region are identical. Of course, ideal mixing is a good approximation for many situations, and this approach is still applicable to any problem where the solute flux is proportional to the gradient of concentration. The simple splitting and refining rules can be adjusted for more complicated non-ideal fluid mixtures if the functional form of the entropy and chemical potential or activity coefficients are known (e.g. a regular solution having an enthalpy of mixing), though this would require deriving a new model for the concentration dynamics through GENERIC and concurrently solving an equation for the entropy production. Another potential drawback is that the self-diffusivity of the atomically-scaled, discrete SDPD particles in a MD-continuum simulation may not match the diffusivity of the MD atoms precisely, since coarse-grained particles typically have softer interactions and therefore larger diffusion constants. Moreover, this puts a limit on the allowed level of coarse-graining for the SDPD region, because an unphysical, negative Fickian diffusion constant is required if the self-diffusivity of the SDPD particles is larger than the MD ones. Finally, as the size of the SDPD particles shrinks, fluctuations in concentration become increasingly large. In such situations it is no longer possible to use Eq.(5.13) for the coarsening steps, and instead the probability distribution must be pre-computed numerically prior to starting the multiscale simulation.

Ultimately, multiscale simulation methods have been historically difficult to implement, and we believe this general extension to multicomponent problems provides a basis for not only large-scale modelling of problems involving binary mixtures, but also future advancements in the field towards methods that are more efficient and refined. Importantly, the framework provided in this chapter opens the possibility for a number of applications, including the transport and margination of porous drug particles in intravascular drug delivery [13,14]. Here particles experience complex interactions due to surface chemistry at the nanoscale, van der Waals and lubrication forces at micron separations, and long-range hydrodynamics over larger scales. Using multiscale multicomponent techniques, it is possible to perform simulations that also capture the dynamics of the active ingredient lost to the surrounding fluid. Another important system is surface nanobubbles and nanodroplets, nanoscale bubbles and drops that form along hydrophobic boundaries and stably exist over time scales orders of magnitude beyond classical predictions [21–25]. All current models that explain this unusual stability feature multiple length scales and multiscale multicomponent techniques, such as the one in this work, are essential for capturing the key physics at all levels. While everything discussed in this work is for uncharged systems, the adaptive resolution approach for bridging MD and coarse-grained fluid representation is also applicable to systems featuring electrostatic interactions [47–49], and coarse particle fluid descriptions similar to the ones used here have been modified to include the evolution of the electrostatic potential [68]. Therefore, the approach presented in this chapter is extensible and useful for a host of important electrokinetic phenomena, including corrosion [15,16], modeling of biomolecules solvated in ionic solution [17], and bioprocesses featuring ion transport (e.g. ion channels) [18–20]. These techniques allow for molecular detail in the

region surrounding the surface, protein, or membrane, while having a more coarse-grained description for the bulk fluid further away.

5.9 References

- [1] S. T. O’Connell and P. A. Thompson, *Phys. Rev. E* **52**, R5792 (1995).
- [2] N. G. Hadjiconstantinou, *J. Comput. Phys.* **154**, 245 (1999).
- [3] N. G. Hadjiconstantinou and A. T. Patera, *Int. J. Mod. Phys. C* **8**, 967 (1997).
- [4] X. B. Nie, S. Y. Chen, W. N. E, and M. O. Robbins, *J. Fluid Mech.* **500**, 55 (2004).
- [5] R. Delgado-Buscalioni and G. De Fabritiis, *Phys. Rev. E* **76**, 36709 (2007).
- [6] R. Delgado-Buscalioni and P. V. Coveney, *Phys. Rev. E* **67**, 46704 (2003).
- [7] R. Delgado-Buscalioni, E. G. Flekkøy, and P. V. Coveney, *EPL Europhys. Lett.* **69**, 959 (2005).
- [8] R. Delgado-Buscalioni, P. V. Coveney, G. D. Riley, and R. W. Ford, *Philos. Trans. R. Soc. Math. Phys. Eng. Sci.* **363**, 1975 (2005).
- [9] N. D. Petsev, L. G. Leal, and M. S. Shell, *J. Chem. Phys.* **142**, 44101 (2015).
- [10] P. Español and M. Revenga, *Phys. Rev. E Stat. Nonlin. Soft Matter Phys.* **67**, 26705 (2003).
- [11] A. Vázquez-Quesada, M. Ellero, and P. Español, *J. Chem. Phys.* **130**, 34901 (2009).
- [12] W. Dzwinel, W. Alda, and D. A. Yuen, *Mol. Simul.* **22**, 397 (1999).
- [13] P. Decuzzi, S. Lee, B. Bhushan, and M. Ferrari, *Ann. Biomed. Eng.* **33**, 179 (2005).
- [14] N. Moreno, P. Vignal, J. Li, and V. M. Calo, *Procedia Comput. Sci.* **18**, 2565 (2013).
- [15] D. R. Gunasegaram, M. S. Venkatraman, and I. S. Cole, *Int. Mater. Rev.* **59**, 84 (2014).
- [16] I. S. Cole and A. E. Hughes, *Corros. Eng. Sci. Technol.* **49**, 109 (2014).
- [17] M. Lund, P. Jungwirth, and C. E. Woodward, *Phys. Rev. Lett.* **100**, 258105 (2008).

- [18] D. H. Mackay, P. H. Berens, K. R. Wilson, and A. T. Hagler, *Biophys. J.* **46**, 229 (1984).
- [19] S. W. Chiu, J. A. Novotny, and E. Jakobsson, *Biophys. J.* **64**, 98 (1993).
- [20] A. Skerra and J. Brickmann, *Biophys. J.* **51**, 969 (1987).
- [21] N. D. Petsev, M. S. Shell, and L. G. Leal, *Phys. Rev. E* **88**, 10402 (2013).
- [22] J. H. Weijs and D. Lohse, *Phys. Rev. Lett.* **110**, 54501 (2013).
- [23] D. Lohse and X. Zhang, *Rev. Mod. Phys.* **87**, 981 (2015).
- [24] X. Zhang, Z. Lu, H. Tan, L. Bao, Y. He, C. Sun, and D. Lohse, *Proc. Natl. Acad. Sci.* **112**, 9253 (2015).
- [25] Y. Liu and X. Zhang, *J. Chem. Phys.* **141**, 134702 (2014).
- [26] A. Alexiadis, D. A. Lockerby, M. K. Borg, and J. M. Reese, *Comput. Methods Appl. Mech. Eng.* **264**, 81 (2013).
- [27] A. Alexiadis, D. A. Lockerby, M. K. Borg, and J. M. Reese, *J. Heat Transf.* **137**, 91010 (2015).
- [28] L. Guo, S. Chen, and M. O. Robbins, *Eur. Phys. J. Spec. Top.* **225**, 1551 (2016).
- [29] L. D. Landau and E. M. Lifshitz, *Fluid Mechanics, Second Edition: Volume 6*, 2nd ed. (Butterworth-Heinemann, Amsterdam, 1987).
- [30] C. Cohen, J. W. H. Sutherland, and J. M. Deutch, *Phys. Chem. Liq.* **2**, 213 (1971).
- [31] J. M. O. de Zarate and J. V. Sengers, *Hydrodynamic Fluctuations in Fluids and Fluid Mixtures*, 1 edition (Elsevier Science, 2006).
- [32] S. Litvinov, M. Ellero, X. Hu, and N. A. Adams, *Phys. Rev. E* **77**, 66703 (2008).
- [33] S. Litvinov, X. Y. Hu, and N. A. Adams, *J. Phys. Condens. Matter* **23**, 184118 (2011).

- [34] X. Bian, S. Litvinov, R. Qian, M. Ellero, and N. A. Adams, *Phys. Fluids* **24**, 12002 (2012).
- [35] A. Vázquez-Quesada, M. Ellero, and P. Español, *Phys. Rev. E* **79**, 56707 (2009).
- [36] P. M. Kulkarni, C.-C. Fu, M. S. Shell, and L. Gary Leal, *J. Chem. Phys.* **138**, 234105 (2013).
- [37] N. D. Petsev, L. G. Leal, and M. S. Shell, *J. Chem. Phys.* **144**, 84115 (2016).
- [38] L. B. Lucy, *Astron. J.* **82**, 1013 (1977).
- [39] R. A. Gingold and J. J. Monaghan, *Mon. Not. R. Astron. Soc.* **181**, 375 (1977).
- [40] G. R. Liu and M. B. Liu, *Smoothed Particle Hydrodynamics: A Meshfree Particle Method* (World Scientific Publishing Company, 2003).
- [41] M. Grmela and H. C. Öttinger, *Phys. Rev. E* **56**, 6620 (1997).
- [42] H. C. Öttinger and M. Grmela, *Phys. Rev. E* **56**, 6633 (1997).
- [43] H. C. Öttinger, *Beyond Equilibrium Thermodynamics* (Wiley-Interscience, Hoboken, N.J., 2005).
- [44] S. R. D. Groot and P. Mazur, *Non-Equilibrium Thermodynamics*, Dover edition (Dover Publications, New York, 2011).
- [45] M. Praprotnik, L. Delle Site, and K. Kremer, *J. Chem. Phys.* **123**, 224106 (2005).
- [46] M. Praprotnik, L. Delle Site, and K. Kremer, *Phys. Rev. E* **73**, 66701 (2006).
- [47] M. Praprotnik, S. Matysiak, L. D. Site, K. Kremer, and C. Clementi, *J. Phys. Condens. Matter* **19**, 292201 (2007).
- [48] S. Matysiak, C. Clementi, M. Praprotnik, K. Kremer, and L. Delle Site, *J. Chem. Phys.* **128**, 24503 (2008).

- [49] R. Delgado-Buscalioni, K. Kremer, and M. Praprotnik, *J. Chem. Phys.* **131**, 244107 (2009).
- [50] S. Poblete, M. Praprotnik, K. Kremer, and L. D. Site, *J. Chem. Phys.* **132**, 114101 (2010).
- [51] S. Fritsch, S. Poblete, C. Junghans, G. Ciccotti, L. Delle Site, and K. Kremer, *Phys. Rev. Lett.* **108**, 170602 (2012).
- [52] J. A. Backer, C. P. Lowe, H. C. J. Hoefsloot, and P. D. Iedema, *J. Chem. Phys.* **123**, 114905 (2005).
- [53] L. D. Landau, E. M. Lifshitz, and L. P. Pitaevskii, *Statistical Physics Part I*, 3rd ed. (Butterworth-Heinemann, Oxford [England], 1980).
- [54] K. Meier, A. Laesecke, and S. Kabelac, *J. Chem. Phys.* **122**, 14513 (2004).
- [55] K. Meier, A. Laesecke, and S. Kabelac, *J. Chem. Phys.* **121**, 3671 (2004).
- [56] J. P. Morris, P. J. Fox, and Y. Zhu, *J. Comput. Phys.* **136**, 214 (1997).
- [57] J. J. Monaghan, *Rep. Prog. Phys.* **68**, 1703 (2005).
- [58] P. E. Kloeden and E. Platen, *Numerical Solution of Stochastic Differential Equations* (Springer, Berlin, 2010).
- [59] A. Donev, J. B. Bell, A. de la Fuente, and A. L. Garcia, *Phys. Rev. Lett.* **106**, 204501 (2011).
- [60] A. Donev, J. B. Bell, A. de la Fuente, and A. L. Garcia, *J. Stat. Mech. Theory Exp.* **2011**, P06014 (2011).
- [61] J. Kordilla, W. Pan, and A. Tartakovsky, *J. Chem. Phys.* **141**, 224112 (2014).
- [62] T. Soddemann, B. Dünweg, and K. Kremer, *Phys. Rev. E* **68**, 46702 (2003).
- [63] V. Sotiropoulos and Y. N. Kaznessis, *J. Chem. Phys.* **128**, 14103 (2008).

- [64] P. J. Hoogerbrugge and J. M. V. A. Koelman, *EPL Europhys. Lett.* **19**, 155 (1992).
- [65] P. Español and P. Warren, *EPL Europhys. Lett.* **30**, 191 (1995).
- [66] P. V. Coveney and P. Español, *J. Phys. Math. Gen.* **30**, 779 (1997).
- [67] M. Laradji and M. J. A. Hore, *J. Chem. Phys.* **121**, 10641 (2004).
- [68] M. Deng, Z. Li, O. Borodin, and G. E. Karniadakis, *J. Chem. Phys.* **145**, (2016).

6 An Integrated Boundary Approach for Colloidal Suspensions Simulated Using Smoothed Dissipative Particle Dynamics

One of the most significant challenges in particle-based continuum solvers such as smoothed particle hydrodynamics (SPH) and smoothed dissipative particle dynamics (SDPD) is the treatment of solid boundaries, whose presence leads to a truncation of the integral approximation to functions and their higher derivatives, and hence, error in the numerical solution. In this work, we describe an integrated boundary framework for modeling colloidal suspensions composed of rigid spherical particles. The integral corresponding to the colloid's contribution is analytically evaluated, giving a simple and computationally inexpensive approach relative to other commonly-used boundary particle techniques. We formulate a thermodynamically-consistent version of this top-down method for mesoscale simulations, where the fluid exchanges momentum and solute with the suspended particles due to thermal fluctuations, giving a framework for modeling the dynamics of colloids at arbitrary Reynolds and Péclet numbers. The resulting evolution equations are validated for a single colloidal particle in a fluid at constant temperature.

6.1 Introduction

Smoothed particle hydrodynamics (SPH) [1–4] is a particle-based continuum solver, originally formulated for the simulation of astrophysical phenomena and more recently adapted to problems in solid and continuum mechanics. In this numerical scheme, the fluid is

decomposed into a collection of volumes whose positions, velocities, and other properties evolve in time following appropriately discretized forms of the transport equations. This type of meshless, Lagrangian strategy to computational fluid dynamics offers a number of advantages for certain types of problems over traditional Eulerian grid-based methods, such as applications involving interfaces and deformable or free boundaries [3]. In addition, these techniques incorporate advection in a natural way and are easily extensible to include more complex physics.

Furthermore, SPH can be reformulated using the GENERIC formalism [5–7] to account for entropy production and include scale-dependent thermal fluctuations in the relevant hydrodynamic variables (e.g. momentum, concentration, etc.) associated with each material volume [8]. This thermodynamically-consistent version of SPH is known as smoothed dissipative particle dynamics (SDPD), and features a random noise term in the equations of motion that introduces stochastic fluxes of momentum and solute between particles [8,9], giving a generalization of SPH to the mesoscale. SDPD is useful for a number of applications ranging from polymer physics [10,11] and pinned DNA dynamics under shear [12], to blood flow modeling [13]. Importantly, SDPD has been applied to particles dispersed in a fluid medium [10,14], a problem ubiquitous in physics and relevant to numerous industrial applications including paints, slurries, composite materials, and ceramics. These kinds of suspensions are generally composed of particles that interact through interparticle (e.g. electrostatic, van der Waals, etc.), hydrodynamic, and thermal forces, a consequence of their dimensions ranging from nanometers to microns, and are thus ideally suited for modeling using SDPD.

One major challenge in adapting these particle-based approaches to problems in continuum mechanics, including colloidal dispersions, is the presence of solid interfaces and rigid objects. When considering low Reynold's number flows in particular, it is desirable to impose the kinematic and no-slip boundary conditions precisely at the solid-liquid interface. To this end, numerous techniques in SPH have been proposed over the years. For example, boundaries may be introduced by renormalizing the integral approximation for points near surfaces [15–17,16], modifying the smoothing kernel [18–20], or through Taylor series expansions [17]. Most often, they are modeled through “ghost” boundary particles frozen on a lattice, or particles generated on the fly through a mirroring algorithm [4,21]. These ghost particles exert repulsive forces on the fluid particles in order to enforce the kinematic boundary condition and prevent boundary penetration, as well as additional interactions that impose other constraints on the flow near the surface. For instance, Morris et al. freeze particles in place for solid objects and assign fictitious, “virtual” velocities to these ghost particles by extrapolating the velocity profile into the surface such that the modified viscous force gives no-slip along a well-defined interface [22]. These types of algorithms for extending functions into the boundary domain (see Maciá et al [23]) successfully modify the particle dynamics to impose the no-slip condition, though they require additional pair force calculations. An elegant solution was provided by Takeda et al. [24], who integrate out the contribution of the “ghost” boundary particles and remove the need for computing additional forces between pairs. A similar approach has been used in simulations using the so-called “dissipative particle dynamics” (DPD) method [25,26], where solid objects interact with fluid particles through an effective force contribution that replaces individual boundary particle interactions [27–29], and this is the perspective we adopt in this chapter.

Colloidal dispersions alternatively may be modeled using Brownian dynamics, where the solvent is treated implicitly and the velocity of each suspended particle is evolved according to the Langevin equation. Brownian dynamics offers a computationally inexpensive basis for large-scale modeling of dilute suspensions, though it typically ignores hydrodynamic interactions between colloids and is only valid in the zero Péclet number limit (though hydrodynamic interactions may be incorporated through the Oseen tensor for the friction terms [30]). It may also be generalized to the so-called “Stokesian dynamics” method [31–34], which includes hydrodynamic interactions between particles and is applicable to any Péclet number, though it assumes creeping flow and therefore ignores inertia altogether. Inertial terms are included when using a Lattice-Boltzmann description for the fluid [35,36], though this approach is quantitative and traditionally applicable when density variations are small, i.e. for systems with incompressible fluids. Another popular modeling tool for nano- and micro-scale suspensions is DPD, a bottom-up approach where the fluid is divided into clumps of molecules that interact through coarse-grained, softly-repulsive interactions in addition to dissipative and fluctuating ones. However, the free parameters in the DPD model are related to fluid properties (e.g. viscosity) in an indirect fashion, and there is no physical length scale associated with the DPD interactions [8,10]. SDPD addresses these issues, and hence the integrated SDPD approach in this work can be viewed as a top-down alternative to DPD that is rigorously obtained from the continuum transport equations. The work in this chapter is a fluctuating Lagrangian equivalent to “direct numerical simulation”, which involves no physical approximation for the flow beyond the usual continuum assumption [37], and is valid for arbitrary Reynolds and Péclet numbers, including scenarios where inertia is important.

In this work, we provide a framework for treating colloidal particles as continuum solid objects in SDPD, rather than being composed of discrete particles that necessitate the calculation of additional pair interactions and rigid-body dynamics. This gives a method that is less computationally costly than traditional boundary particle methods, since every fluid particle that is near a boundary receives a single contribution to its evolution equation due to the nearby colloid. In particular, we obtain analytical expressions for simple planar and spherical boundaries, and incorporate scale-dependent thermal fluctuations for stochastic fluxes of momentum and solute between the fluid and boundary. In Section 6.2, we provide a brief summary of SPH and SDPD and the problem of interfaces. Section 6.3 describes the integrated boundary approach and gives analytical results for approximating functions near surfaces with planar and spherical geometries. In Section 6.4, we develop an integrated pressure force that prevents fluid particles from penetrating the solid boundary. A boundary term for the Laplacian operator, which is essential to a number of transport problems, is derived in Section 6.5, and we generalize the boundary approach to the mesoscale by allowing for thermal fluctuations in linear and angular momenta in Section 6.7. In Section 6.6 we derive an expression for the total torque acting on the colloid due to surrounding fluid particles. Finally, in Section 6.8 we perform full scale simulations of a single colloidal sphere using these results, and show that they reproduce the correct diffusive behavior.

6.2 Smoothed Particle Methods

To illustrate the problem posed by solid boundaries when using smoothed particle methods, we begin with a brief overview of this subject. A more comprehensive review can

be found in Refs. [3,4]. The key to these approaches is the so-called “integral approximation”, where a function $f(\mathbf{r})$ (assumed continuous on Ω) at some point \mathbf{r} is written as,

$$\langle f \rangle(\mathbf{r}) = \frac{1}{\gamma(\mathbf{r})} \int_{\Omega} f(\mathbf{r}') W(\mathbf{r} - \mathbf{r}', h) d\mathbf{r}'. \quad (6.1)$$

In this work, the bracket $\langle \rangle$ indicates the approximation. The smoothing kernel W is a normalized, positive function with compact support, which reduces to the Dirac delta function in the limit $h \rightarrow 0$. h is the “smoothing length”, a quantity that controls the spread of the kernel, and therefore the extent of the integral in Eq.(6.1). Later, we decompose the fluid domain into a collection of fluid “particles” and write these integrals as sums over the neighboring particles. Note that the delta function requirement for W implies that Eq.(6.1) becomes exact in the limit $h \rightarrow 0$. Hence, h is a factor that controls the accuracy of the numerical solution in SPH; choosing a smaller value gives a more precise result, but requires using more particles and hence more calculated pair interactions. In the above expression, we also have the Shepard normalization factor, which is typically unity due to the normalization requirement for the smoothing function,

$$\gamma(\mathbf{r}) = \int_{-\infty}^{\infty} W(\mathbf{r} - \mathbf{r}', h) d\mathbf{r}'. \quad (6.2)$$

In order to obtain the SPH approximation to a function, the problem domain is discretized into a collection of N fluid volumes or “particles”, in which case the integral in Eq.(6.1) is approximated as the sum

$$\langle f \rangle(\mathbf{r}) \approx \sum_j^N \frac{m_j}{\rho_j} f(\mathbf{r}_j) W(\mathbf{r} - \mathbf{r}_j, h). \quad (6.3)$$

Here, m_j and ρ_j are the mass and density of the j th particle, respectively. While the sum extends over all the particles in the system, the compact support condition for the function W ensures that only nearby ones contribute to the average, and the sum is actually performed over all the particles within a sphere with radius κh (where κ is a constant that controls this cut-off radius for interaction). Similar sum-over-particles approximations can be obtained for spatial derivatives of functions as well. The application of the integral and particle approximations to the hydrodynamic equations is the basis for SPH, giving equations of motion for the particles that are used to evolve their properties such as positions, velocities, densities, and concentrations using integrators typically used in molecular dynamics (MD) simulations. For example, the incompressible Navier-Stokes equation in the Lagrangian frame is given by [38]

$$\rho \frac{d\mathbf{v}}{dt} = -\nabla p + \eta \nabla^2 \mathbf{v}. \quad (6.4)$$

In this expression, the differential on the left-hand-side is a material derivative, ρ is the fluid mass density, and η is the viscosity. Applying the integral and particle approximation to the right-hand-side (i.e. the forces acting on a fluid element) gives the following evolution equation for the momenta of the i th fluid particle [22], with pairwise interactions between fluid particles resulting from the symmetrized discretization,

$$m_i \frac{d\mathbf{v}_i}{dt} = -\sum_{j=1}^N m_i m_j \left(\frac{p_i}{\rho_i^2} + \frac{p_j}{\rho_j^2} \right) \frac{\partial W_{ij}}{\partial r_{ij}} \mathbf{e}_{ij} + 2\eta \sum_{j=1}^N \frac{m_i m_j}{\rho_i \rho_j} \left(\frac{1}{|\mathbf{r}_{ij}|} \frac{\partial W_{ij}}{\partial r_{ij}} \right) \mathbf{v}_{ij}. \quad (6.5)$$

Here, m_i , p_i , and ρ_i give the mass, pressure, and density of the i th particle, respectively. \mathbf{v}_{ij} is the relative velocity between particles i and j , $\mathbf{v}_{ij} \equiv \mathbf{v}_i - \mathbf{v}_j$, and $\mathbf{e}_{ij} \equiv \mathbf{r}_{ij} / |\mathbf{r}_{ij}|$ with $\mathbf{r}_{ij} \equiv \mathbf{r}_i - \mathbf{r}_j$.

It is also possible to include thermal fluctuations in the velocity field for simulations at mesoscopic length scales, giving a thermodynamically-consistent version of SPH known as “smoothed dissipative particle dynamics” (SDPD). For the isothermal incompressible case, an additional term is included in the equation of motion given by Eq.(6.5) with the form [8,39]

$$m_i d\tilde{\mathbf{v}}_i = \sum_{j=1}^N A_{ij} d\hat{\mathbf{W}}_{ij} \cdot \mathbf{e}_{ij}. \quad (6.6)$$

$d\mathbf{W}_{ij}$ is a tensor of Brownian process increments and $d\hat{\mathbf{W}}_{ij}$ is the traceless, symmetric part of $d\mathbf{W}_{ij}$. The noise coefficient A_{ij} is determined through the fluctuation-dissipation theorem, giving [8,39]

$$A_{ij} = \left[-\frac{8\eta m_i m_j k_B T}{\rho_i \rho_j} \left(\frac{1}{|\mathbf{r}_{ij}|} \frac{\partial W_{ij}}{\partial r_{ij}} \right) \right]^{1/2}. \quad (6.7)$$

Note that when fluctuations appear in SPH, the parameter h takes on a slightly different meaning. Previously, h controlled the precision of the numerical solution, similar to the level of mesh refinement in a finite-element calculation. In SDPD, however, h controls the size of each particle, which is interpreted as a fluid volume locally in equilibrium. Decreasing the size of a thermodynamic system produces greater relative thermal fluctuations. Hence, a smaller h gives finer particles subject to larger fluctuations, whereas increasing h results in more massive SDPD particles with diminished fluctuations. In other words, when thermal noise is included, adjusting h actually produces distinct particle dynamics by changing the coarse-graining level [10].

The problem posed by boundaries is immediately apparent when considering the integrals in Eqs.(6.1) and (6.2), which are truncated by the interface for any point \mathbf{r} located

near a boundary. From the particle perspective [Eq.(6.3)], this truncation corresponds to a particle deficiency when summing over neighbors in the support domain of points near the surface. This issue is remedied in this work by assuming that functions are defined over a space extending into the boundary such that a Dirichlet boundary condition is imposed precisely at the interface between the solid and liquid. This is consistent with existing particle-based boundary approaches, where sums over particles for points near a boundary include both fluid and “ghost” wall particles. Therefore, the support domain for any point Ω does not only include the fluid domain, but consist of both the fluid and wall, i.e. $\Omega = \Omega_f + \Omega_w$ resulting in an additional integral over Ω_w that provides the necessary support for points near the boundary. Since the maximum interaction length between particles is given by κh , Ω_w is the set of points inside the boundary located within a distance κh from the liquid-solid interface (though as a convenient approximation, Ω_w may be defined as all points inside a surface or colloidal particle, including ones beyond this maximum interaction distance since they contribute weakly to the final expressions). The purpose of this chapter is therefore to provide analytical results for the wall contribution resulting from integration over the wall domain Ω_w when simulating colloidal suspensions.

6.3 Approximation of Function near Boundary

In order to demonstrate how the integrated boundary approach works, we first discuss the simplest application: approximating a function near planar and spherical surfaces. Consider a point \mathbf{r} in a continuum fluid near a boundary. Using the integral approximation [Eq.(6.1)] and the linearity of the integral operator, we can write

$$\langle f \rangle(\mathbf{r}) = \int_{\Omega_f} f(\mathbf{r}') W(\mathbf{r} - \mathbf{r}', h) d\mathbf{r}' + \int_{\Omega_w} f(\mathbf{r}') W(\mathbf{r} - \mathbf{r}', h) d\mathbf{r}', \quad (6.8)$$

where Ω_f is the part of the support domain of \mathbf{r} that lies in the fluid, and Ω_w is the part inside the wall. Hence, we assume the function is defined and continuous over a space that extends into the boundary, $\Omega = \Omega_f + \Omega_w$, and the Shepard normalization factor [Eq.(6.2)] is unity. The first term in Eq.(6.8) is the familiar integral representation of a function and therefore does not merit further discussion; discretizing this term using the particle approximation yields the familiar SPH sum over nearby fluid particles for approximating a function, Eq.(6.3). However, this sum is incomplete due to a deficiency of neighboring particles, a consequence of the neighboring boundary that occupies the space Ω_w . Hence, we are interested in the second integral in Eq.(6.8), which is due to the surface and compensates for this lack of surrounding particles,

$$f_w \int_{\Omega_w} W(\mathbf{r} - \mathbf{r}', h) d\mathbf{r}'. \quad (6.9)$$

In writing Eq.(6.9), Dirichlet boundary conditions are assumed, i.e. $f(\mathbf{r})$ adopts some constant value f_w at the boundary and can be pulled in front of the integral operator. In this section, we focus on Eq.(6.9), which is the contribution of the wall to the function's value at some point \mathbf{r} in the integral approximation. In principle, this quantity can be numerically determined for objects with complicated shapes and boundaries featuring local curvature (though the length scale characterizing surface features or curvature should be larger than length scale associated with each fluid particle, given by h). For simple boundary geometries and Gaussian kernels, it is possible to evaluate Eq.(6.9) analytically. Previously, Eq.(6.9) has been determined for simple cases involving 1D flow past a flat boundary [24]. The goal of

this chapter is to generalize this to include thermal fluctuations, and evaluate it for hard spheres, allowing for the simulation of suspended spherical particles.

6.3.1 Fluid Particle near Planar Boundary

Eq.(6.9) is analytically determined for simple geometries assuming the kernel $W(|\mathbf{r}-\mathbf{r}'|, h)$ is Gaussian (this is an approximation, discussed below). For a function evaluated at a point \mathbf{r} located a distance Δz from a flat surface with vector normal in the z -direction, we can explicitly write the integral Eq.(6.9) using cylindrical coordinates,

$$f_w \int_{\Omega_w} W(\mathbf{r}-\mathbf{r}', h) d\mathbf{r}' \approx 2\pi f_w \int_{-\infty}^{-\Delta z} dZ \int_0^{\infty} R dR W\left[\left(R^2 + Z^2\right)^{1/2}\right]. \quad (6.10)$$

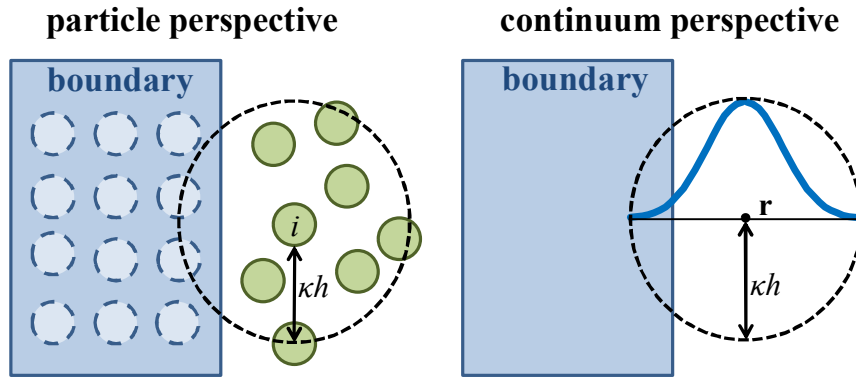


Fig. 6.1. Illustration of the particle perspective to the integrated boundary approach versus the continuum one. In the former, a function evaluated at the location of particle i depends on a sum over neighboring fluid particles (green) and virtual particles that comprise the boundary (light blue). The sum is partitioned into a sum over fluid particles, and one over wall particles that is rewritten as an integral. In the continuum perspective, the function evaluated at point \mathbf{r} is obtained from an integral over a volume that is decomposed into an integral over the fluid domain, and an integral over the boundary, where the latter is evaluated explicitly.

Note that the integral limits extend to infinity. In principle, the compact support condition for the function W limits the integral to the support domain of point \mathbf{r} .

It is possible to arrive at the result in Eq.(6.10) from a different perspective. Assuming virtual or “ghost” particles are used for the boundary, the particle approximation to a function, Eq.(6.3), can be decomposed into a sum over fluid particles, and a sum over the wall particles within the point’s support domain,

$$\langle f \rangle(\mathbf{r}) \approx \sum_{j, \text{fluid}}^{N_f} \frac{m_j}{\rho_j} f(\mathbf{r}_j) W(\mathbf{r} - \mathbf{r}_j, h) + \sum_{j, \text{wall}}^{N_w} \frac{m_j}{\rho_j} f(\mathbf{r}_j) W(\mathbf{r} - \mathbf{r}_j, h). \quad (6.11)$$

We consider the second sum on the right hand side, which accounts for the wall particles’ contribution to the sum,

$$\frac{m_w}{\rho_w} f_w \sum_{j, \text{wall}}^{N_w} W(\mathbf{r} - \mathbf{r}_j, h). \quad (6.12)$$

Here, we have again assumed Dirichlet boundary conditions [$f(\mathbf{r}) = f_w$ at the wall, where f_w is a constant], as well as uniform mass and density for the wall particles. Similar to the derivation of the Lennard-Jones 9-3 potential, this sum-over-particles is replaced with an integral scaled by the particle number density of the wall $v_w = \rho_w / m_w$,

$$\frac{m_w}{\rho_w} f_w \sum_{j, \text{wall}}^{N_w} W(\mathbf{r} - \mathbf{r}_j, h) \approx \frac{m_w}{\rho_w} f_w v_w \int_0^{2\pi} d\phi \int_{-\infty}^{-\Delta z} dZ \int_0^{\infty} R dR W \left[(R^2 + Z^2)^{1/2} \right]. \quad (6.13)$$

Simplifying, we arrive at the same result as Eq.(6.10). This illustrates that, when deriving the integrated contributions of boundaries, we can begin either with the general integral approximation to a function, or from a fluid particle near a boundary composed of subparticles, and in both cases obtain the same result (Fig. 6.1).

Eq.(6.10) is evaluated straightforwardly for the Gaussian smoothing function,

$$W(r, h) = \frac{1}{\pi^{3/2} h^3} \exp \left[- \left(\frac{r}{h} \right)^2 \right]. \quad (6.14)$$

Substituting Eq.(6.14) into Eq.(6.10) and integrating, we obtain the following result:

$$\frac{f_w}{2} \left[1 - \operatorname{erf} \left(\frac{\Delta z}{h} \right) \right]. \quad (6.15)$$

This is the expression derived by Takeda et al. for approximating the density near a boundary [24]. Note that Eq.(6.15) is an approximation to the actual integral representation of a function since one of the requirements for smoothing kernels in SPH is compact support, and therefore the integral in Eq.(6.10) should extend over a finite region where the smoothing function is nonzero. In practice, when using a Gaussian smoothing function in SPH, the kernel is truncated beyond some point to give compact support. However, in the above derivation, we integrate to infinity and hence have additional contributions that would not exist with a properly local smoothing function. Due to the exponential kernel, these contributions are typically negligible.

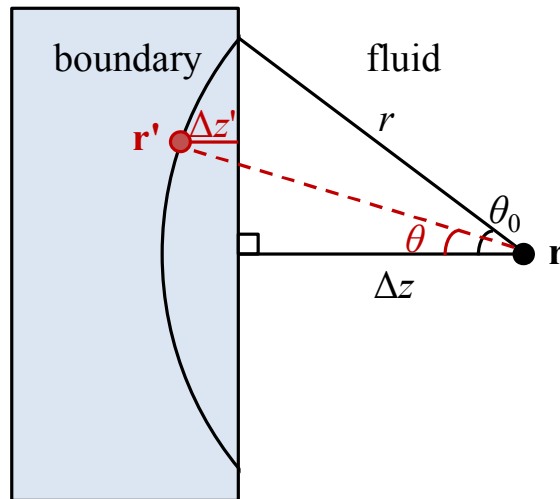


Fig. 6.2. Illustration showing the integration variables for the planar boundary contribution in spherical coordinates. The coordinate origin is set at the position in the fluid r .

To obtain a more precise expression, we must integrate over a region that corresponds to a sphere surrounding the point \mathbf{r} where we are approximating the function, with size determined by the support domain of the point, namely κh . We therefore exactly compute the integral approximation in Eq.(6.9) for a planar boundary using spherical coordinates,

$$f_w \int_{\Delta z}^{\kappa h} dr \int_0^{2\pi} d\phi \int_0^{\theta_0} d\theta W(r, h) r^2 \sin \theta, \quad (6.16)$$

where we have defined $\theta_0 = \cos^{-1}(\Delta z / r)$ and the coordinate origin is set at the position \mathbf{r} in the fluid where $f(\mathbf{r})$ is approximated. Fig. 6.2 illustrates the variables used to write Eq.(6.16). Integrating over the angular coordinates, we are left with

$$2\pi f_w \int_{\Delta z}^{\kappa h} dr W(r, h) r(r - \Delta z). \quad (6.17)$$

Substituting the Gaussian kernel [Eq.(6.14)] and applying the remaining integral operator, we find that the exact contribution to the function near a boundary is

$$\frac{f_w}{2} \left[\operatorname{erf}(\kappa) - \operatorname{erf}\left(\frac{\Delta z}{h}\right) \right] - \frac{f_w}{\pi^{1/2} h} \exp(-\kappa^2)(\kappa h - \Delta z). \quad (6.18)$$

Note that the limit $\kappa \rightarrow \infty$, this reduces to the approximate expression derived by Takeda et al., Eq.(6.15). Therefore, the full approximation of a function at a point \mathbf{r} located near a boundary is

$$\begin{aligned} \langle f \rangle(\mathbf{r}) = & \sum_{j, \text{fluid}}^{N_f} \frac{m_j}{\rho_j} f(\mathbf{r}_j) W(\mathbf{r} - \mathbf{r}_j, h) \\ & + \frac{f_w}{2} \left[\operatorname{erf}(\kappa) - \operatorname{erf}\left(\frac{\Delta z}{h}\right) \right] - \frac{f_w}{\pi^{1/2} h} \exp(-\kappa^2)(\kappa h - \Delta z), \end{aligned} \quad (6.19)$$

where Δz is the distance of the point \mathbf{r} from the surface. The summation is only over nearby fluid particles, and the second term on the right-hand-side gives the contribution of to the

boundary. Without this term, Eq.(6.19) is simply the normal SPH approximation of a function. This additional contribution is included when the interface is located within the support domain of the point \mathbf{r} , $\Delta z \leq \kappa h$, and compensates for the lack of surrounding particles.

Eq.(6.19) can be applied to the density evaluated at each particle's position, a quantity that appears in the equations of motion in SPH [see Eq.(6.5)], giving

$$\begin{aligned} \langle \rho \rangle(\mathbf{r}_i) = & \sum_{j, fluid}^{N_f} m_j W(\mathbf{r}_i - \mathbf{r}_j, h) \\ & + \frac{\rho_w}{2} \left[\operatorname{erf}(\kappa) - \operatorname{erf}\left(\frac{\Delta z_i}{h}\right) \right] - \frac{\rho_w}{\pi^{1/2} h} \exp(-\kappa^2)(\kappa h - \Delta z_i). \end{aligned} \quad (6.20)$$

Here, Δz_i is the distance of the i th particle from the boundary. The sum in Eq.(6.20) is performed at each time-step to evolve the density of each particle. This is the so-called “summation density” approach, which now features an additional term due to the presence of a nearby solid object. The density update equation given by Eq.(6.20) matches the one used by Takeda et al. in the limit $\kappa \rightarrow \infty$. Note that assuming a constant density for the boundary does not reproduce peak pressures as accurately as evolving the densities of the wall particles [22], though we find it sufficient in the test studies that follow below.

6.3.2 Fluid Particle near Spherical Body

The goal of this chapter is to apply this approach to suspensions composed of hard spheres, and therefore we also evaluate Eq.(6.9) for a point in the fluid located near a solid spherical object. Writing this integral in spherical coordinates by setting the coordinate origin at the point in the fluid \mathbf{r} ,

$$f_w \int_{R-R_c}^{R+R_c} dr \int_0^{2\pi} d\phi \int_0^{\theta_0} d\theta r^2 \sin\theta W(r, h). \quad (6.21)$$

Here, R is the distance between the center of the spherical body and \mathbf{r} , R_c is the radius of the sphere, and we have the relationship $R_c^2 = R^2 + r^2 - 2rR \cos\theta_0$. These quantities are illustrated in Fig. 6.3. Integrating over the angular variables and substituting Eq.(6.14),

$$\frac{f_w}{\pi^{1/2} h^3} \int_{R-R_c}^{R+R_c} dr \exp\left[-\left(\frac{r}{h}\right)^2\right] \frac{r}{R} \left[R_c^2 - (R-r)^2 \right]. \quad (6.22)$$

Integrating again yields the final result,

$$\frac{f_w}{2} \left\{ \frac{h}{\pi^{1/2} R} \left[\exp(-A_+^2) - \exp(-A_-^2) \right] + G_- \right\}. \quad (6.23)$$

The following quantities are defined for convenience:

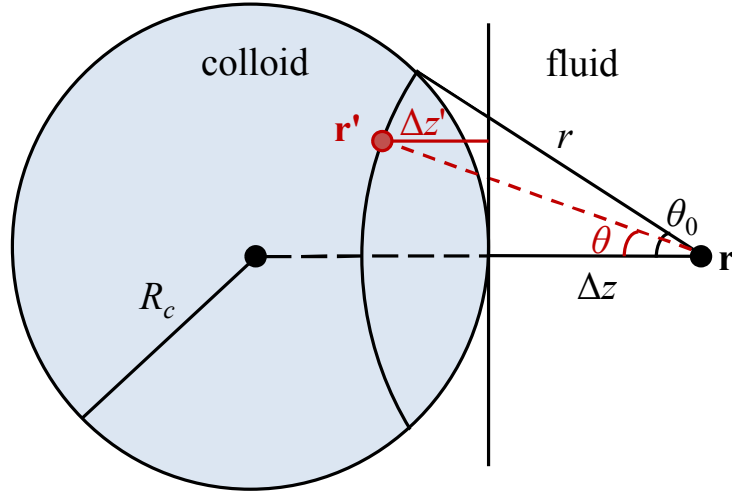


Fig. 6.3. Illustration of integration variables in spherical coordinates for the boundary contribution for a fluid point near a spherical solid object (e.g. colloid) with radius R_c . The coordinate origin is once again set at the position in the fluid \mathbf{r} .

$$\begin{aligned}
A_+ &= \frac{R + R_c}{h}, \\
A_- &= \frac{R - R_c}{h}, \\
G_- &= \text{erf}(A_+) - \text{erf}(A_-).
\end{aligned} \tag{6.24}$$

The approximation for the density at the position of the i th fluid particle, located a distance R from the center of a solid spherical object having radius R_c and uniform density ρ_w is therefore given by

$$\begin{aligned}
\langle \rho \rangle(\mathbf{r}_i) &= \sum_{j, \text{fluid}}^{N_f} m_j W(\mathbf{r}_i - \mathbf{r}_j, h) \\
&+ \frac{\rho_w}{2} \left\{ \frac{h}{\pi^{1/2} R} \left[\exp(-A_+^2) - \exp(-A_-^2) \right] + G_- \right\}.
\end{aligned} \tag{6.25}$$

6.4 Integrated Boundary Approximation for Pressure Term

The SDPD equations of motion Eqs.(6.5) and (6.6) feature three terms, *(i)* a pressure force between particle pairs, *(ii)* a viscous interaction proportional to the particles' velocity difference, and *(iii)* a random force due to thermal stresses. In this and the following two sections, we use the general approach above to derive integrated boundary terms corresponding to each of these three contributions. We first consider the conservative term due to the pressure distribution. Without the presence of boundary ghost particles to exert a pressure force, fluid particles may penetrate the solid interface. This is especially true for simulations of quasi-incompressible fluids, where the equation of state leads to strong repulsions between particle pairs that may drive them outside of the simulation box without a restraining force. Hence, we need to obtain an integrated pressure force that prevents

boundary penetration and enforces the kinematic boundary condition. We determine this integrated pressure force for planar and spherical boundaries in Subsections 6.4.1 and 6.4.2, respectively.

6.4.1 Pressure Force near Planar Boundary

Obtaining a symmetrized integrated expression for the pressure gradient term is more intuitive and simple starting from the particle perspective, which is how we proceed in this subsection. The pressure force in SPH is the first term on the right-hand-side of Eq.(6.5). Splitting this summation into wall and fluid contributions, we again focus on the sum over the wall particles and assume a constant value for the density and pressure at the wall,

$$m_i \frac{d\mathbf{v}_i}{dt} = m_i m_w \left(\frac{p_i}{\rho_i^2} + \frac{p_w}{\rho_w^2} \right) \sum_{j, \text{wall}}^N \mathbf{r}_{ij} F_{ij}, \quad (6.26)$$

where $\nabla_i W_{ij} = -\mathbf{r}_{ij} F_{ij}$ and $F_{ij} \equiv F(r_{ij}) \geq 0$. With the choice of Eq.(6.14) for the smoothing function, we have

$$F(r) = \frac{2}{\pi^{3/2} h^5} \exp \left[-\left(\frac{r}{h} \right)^2 \right]. \quad (6.27)$$

Note that components of the force in Eq.(6.26) parallel to the boundary will cancel due to symmetry. Hence, we only sum the component of this force that is perpendicular to the wall,

$$m_i \frac{d\mathbf{v}_i}{dt} \Big|_{\mathbf{n}} = m_i m_w \left(\frac{p_i}{\rho_i^2} + \frac{p_w}{\rho_w^2} \right) \sum_{j, \text{wall}}^N (\mathbf{r}_{ij} \cdot \mathbf{n}) \mathbf{n} F_{ij}. \quad (6.28)$$

Here, \mathbf{n} is the vector normal to the boundary. For a planar surface with normal in the z -direction, we replace the sum with the following integral,

$$-v_w m_i m_w \left(\frac{p_i}{\rho_i^2} + \frac{p_w}{\rho_w^2} \right) \mathbf{n} \int_{-\infty}^{\infty} dX \int_{-\infty}^{\infty} dY \int_{-\infty}^{-\Delta z} dZZF \left[(X^2 + Y^2 + Z^2)^{1/2} \right]. \quad (6.29)$$

For simplicity, we allow the integral limits to extend to infinity. Substituting Eq.(6.27) into Eq.(6.29) and integrating gives the final result,

$$= \frac{\rho_w m_i}{\pi^{1/2} h} \left(\frac{p_i}{\rho_i^2} + \frac{p_w}{\rho_w^2} \right) \exp \left[- \left(\frac{\Delta z}{h} \right)^2 \right] \mathbf{n}. \quad (6.30)$$

Hence, for a particle located within a distance κh of the wall, the equation of motion due to the pressure distribution features an additional contribution,

$$m_i \frac{d\mathbf{v}_i}{dt} \Big|_{press} = \sum_{j, fluid}^{N_f} m_i m_j \left(\frac{p_i}{\rho_i^2} + \frac{p_j}{\rho_j^2} \right) \mathbf{r}_{ij} F_{ij} + \frac{\rho_w m_i}{\pi^{1/2} h} \left(\frac{p_i}{\rho_i^2} + \frac{p_w}{\rho_w^2} \right) \exp \left[- \left(\frac{\Delta z_i}{h} \right)^2 \right] \mathbf{n}. \quad (6.31)$$

Eq.(6.31) is readily extended to situations where the fluid particle is near a planar boundary with a vector normal in a different direction, or near multiple planar boundaries. In the general case, the particle has a separate boundary term in its equation of motion for each planar surface, where \mathbf{n} is the normal for each surface, and Δz_i is the corresponding separation distance. For the case of a particle near a corner where two surfaces meet, however, including a separate boundary term for each surface may not give accurate results since some boundary-fluid interactions will be double-counted, and the integral of the kernel may need to be evaluated numerically.

6.4.2 Pressure Force near Spherical Object

Near a spherical object, the integral due to the boundary is instead

$$\begin{aligned}
& m_i m_w \left(\frac{p_i}{\rho_i^2} + \frac{p_w}{\rho_w^2} \right) \sum_{j, \text{wall}}^N (\mathbf{r}_{ij} \cdot \mathbf{n}) \mathbf{n} F_{ij} \\
& = v_w m_i m_w \left(\frac{p_i}{\rho_i^2} + \frac{p_w}{\rho_w^2} \right) \mathbf{n} \int_{R-R_c}^{R+R_c} dr \int_0^{2\pi} d\phi \int_0^{\theta_0} d\theta r^3 \sin \theta \cos \theta F(r).
\end{aligned} \tag{6.32}$$

Integrating over θ and ϕ ,

$$= \pi v_w m_i m_w \left(\frac{p_i}{\rho_i^2} + \frac{p_w}{\rho_w^2} \right) \mathbf{n} \int_{R-R_c}^{R+R_c} dr r^3 F(r) \sin^2 \theta_0. \tag{6.33}$$

Substituting $F(r)$ and θ_0 , once again specified through $R_c^2 = R^2 + r^2 - 2rR \cos \theta_0$, gives after integration the final result,

$$= \frac{\rho_w m_i h}{2R^2 \pi^{1/2}} \left(\frac{p_i}{\rho_i^2} + \frac{p_w}{\rho_w^2} \right) M(R, R_c, h) \mathbf{n}. \tag{6.34}$$

Here we have the dimensionless factor

$$M(R, R_c, h) = \exp(-A_+^2)(1+C) - \exp(-A_-^2)(1-C), \tag{6.35}$$

where we have also defined

$$C = \frac{2RR_c}{h^2}. \tag{6.36}$$

In colloidal simulations, this additional force prevents fluid particles from penetrating the suspended spheres.

6.5 Second Derivative Approximation for Viscous Term

The Laplacian of a scalar or vector field appears in the transport equations for momentum and solute diffusion, and hence integrated boundaries must approximate this quantity near surfaces. In the integral approximation, the Laplacian is typically written as [3]

$$\langle \nabla \cdot (k \nabla f) \rangle = -2k \int_{\Omega} [f(\mathbf{r}) - f(\mathbf{r}')] F(|\mathbf{r} - \mathbf{r}'|) d\mathbf{r}'. \quad (6.37)$$

As in the previous section, we separate this integral into fluid and wall contributions, and focus on the latter,

$$-2k [f(\mathbf{r}) - f_w] \int_{\Omega_w} F(|\mathbf{r} - \mathbf{r}'|) d\mathbf{r}'. \quad (6.38)$$

Dirichlet boundary conditions are once again assumed, and we now compute analytical expressions for planar and spherical boundaries that are straightforwardly incorporated into the equations of motion for the fluid particles.

6.5.1 Fluid Particle near Planar Boundary

Determining the correct form of the Laplacian boundary term merits further discussion. Note that when using ghost particles in SPH, it is necessary to take additional measures in order to enforce a boundary condition at an arbitrarily-specified surface. Takeda et al. linearly extrapolate the function into the boundary in order to enforce no-slip precisely at the fluid-solid interface. Similarly, Morris et al. assign fictitious values of the function to boundary ghost particles such that for any pair interaction, the correct boundary condition is met. This is achieved by using the value of the function in the fluid [$f(\mathbf{r})$], the value of the function in the wall [$f(\mathbf{r}')$], and the distances of the fluid and wall points relative to the boundary (Δz and $\Delta z'$, respectively) (See Section 3.3 and Fig. 3.1 for an illustration) to determine a modified function difference $f(\mathbf{r}) - f(\mathbf{r}')$. In other words, it is possible to

perform a linear extrapolation to determine what value must be assigned to the wall point, $f(\mathbf{r}')$, giving the relationship

$$f(\mathbf{r}) - f(\mathbf{r}') = \left(1 + \frac{\Delta z'}{\Delta z}\right) [f(\mathbf{r}) - f_w]. \quad (6.39)$$

As an example, when calculating the relative velocity between a fluid particle and a ghost particle, Eq.(6.39) suggests that the relative velocity can be replaced by the velocity of the fluid particle relative to the wall, where this velocity difference is rescaled by a factor that depends on the distances of the fluid and ghost particles from the boundary, $\beta = 1 + \Delta z' / \Delta z$. This ensures that the fluid velocity assumes the wall value precisely at the liquid-solid interface when the full velocity field is computed (for a derivation and more detailed discussion, see Section 3.3).

For this same reason, it is necessary to modify the function difference in Eq.(6.38) by extrapolating the function into the boundary, i.e.,

$$-2k [f(\mathbf{r}) - f_w] \int_{\Omega_w} \left(1 + \frac{\Delta z'}{\Delta z}\right) F(|\mathbf{r} - \mathbf{r}'|) d\mathbf{r}'. \quad (6.40)$$

Here, Δz is the distance of the point \mathbf{r} from the boundary (where \mathbf{r} is located inside the fluid region), and $\Delta z'$ is the distance of the point \mathbf{r}' from the boundary (where $\mathbf{r}' \in \Omega_w$). The correction factor $\beta = 1 + \Delta z' / \Delta z$ ensures that the value of the function is strictly enforced at the desired surface.

As in the previous section, we use spherical coordinates with the origin set at the point in the fluid \mathbf{r} where the function is approximated to obtain an exact result for a truncated Gaussian kernel. The expressions can be simplified by the taking the limit $\kappa \rightarrow \infty$.

In spherical coordinates, the distance between a point \mathbf{r}' inside the solid and a planar boundary is given by

$$\Delta z' = r \cos \theta - \Delta z. \quad (6.41)$$

Substituting Eq.(6.41) into Eq.(6.40) and writing the integral explicitly gives

$$-2k \left[f(\mathbf{r}) - f_w \right] \int_{\Delta z}^{\kappa h} dr \int_0^{2\pi} d\phi \int_0^{\theta_0} d\theta \left(\frac{r \cos \theta}{\Delta z} \right) F(r) r^2 \sin \theta. \quad (6.42)$$

Integrating over the angular variables,

$$-\frac{2\pi k}{\Delta z} \left[f(\mathbf{r}) - f_w \right] \int_{\Delta z}^{\kappa h} dr r^3 F(r) \sin^2 \theta_0. \quad (6.43)$$

Next, we introduce $\theta_0 = \cos^{-1}(\Delta z / r)$ into Eq.(6.43) together with the expression for $F(r)$ given by Eq.(6.27), resulting in

$$-\frac{4k}{\pi^{1/2} \Delta z h^5} \left[f(\mathbf{r}) - f_w \right] \int_{\Delta z}^{\kappa h} dr \exp \left[-\left(\frac{r}{h} \right)^2 \right] r (r^2 - \Delta z^2). \quad (6.44)$$

Integrating again, we obtain the final result for the wall term,

$$-\frac{2k}{\pi^{1/2} h \Delta z} \left[f(\mathbf{r}) - f_w \right] K \left(\frac{\Delta z}{h} \right). \quad (6.45)$$

Here, we have defined the dimensionless quantity

$$K \left(\frac{\Delta z}{h} \right) = \exp \left(-\frac{\Delta z^2}{h^2} \right) + \exp(-\kappa^2) \left[\frac{\Delta z^2}{h^2} - (1 + \kappa^2) \right]. \quad (6.46)$$

Note that if we had integrated over all space (i.e. the approximation where $\kappa \rightarrow \infty$), this equation simplifies to $K(\Delta z / h) = \exp(-\Delta z^2 / h^2)$. Due to the exponentially decaying kernel, the boundary contribution beyond the radius κh is generally small, and therefore this approximation is often useful.

As an example, the Laplacian boundary term in Eq.(6.45) is applied to each component of the velocity vector to enforce no-slip in simulations involving incompressible flows past a planar boundary, in which case the equations of motion [Eq.(6.5)] become

$$\begin{aligned}
m_i \frac{d\mathbf{v}_i}{dt} = & - \sum_{j=1}^N m_i m_j \left(\frac{p_i}{\rho_i^2} + \frac{p_j}{\rho_j^2} \right) \frac{\partial W_{ij}}{\partial r_{ij}} \mathbf{e}_{ij} \\
& + 2\eta \sum_{j=1}^N \frac{m_i m_j}{\rho_i \rho_j} \left(\frac{1}{|\mathbf{r}_{ij}|} \frac{\partial W_{ij}}{\partial r_{ij}} \right) \mathbf{v}_{ij} - \frac{2m_i \eta (\mathbf{v}_i - \mathbf{v}_w)}{\rho_i \pi^{1/2} h \Delta z_i} K \left(\frac{\Delta z_i}{h} \right).
\end{aligned} \tag{6.47}$$

Note that the boundary term diverges in the limit $\Delta z_i \rightarrow 0$, a consequence of the linear extrapolation of the function into the boundary described by Eq.(6.39). Large forces arising from lack of numerical precision are typically avoided by capping the scaling factor [22]. Some work suggests that integrated boundaries work well for compressible fluids and moderate Reynold's numbers, but may be unstable for low Reynold's number incompressible flows [22], though we do not encounter any such issues in our tests below.

6.5.2 Particle near Spherical Boundary

We now obtain an expression for the Laplacian near a spherical object, which can be used to apply a no-slip condition at the surface of a colloidal particle. In this case, the integral in Eq.(6.38) is

$$-2k \left[f(\mathbf{r}) - f_w \right] \int_{R-R_c}^{R+R_c} dr \int_0^{2\pi} d\phi \int_0^{\theta_0} d\theta \left(1 + \frac{\Delta z'}{\Delta z} \right) r^2 \sin \theta F(r). \tag{6.48}$$

The integration limit θ_0 is specified through the relationship $R_c^2 = R^2 + r^2 - 2rR \cos \theta_0$, where R_c is the radius of the spherical object, R is the separation between the center-of-mass of the sphere and point in the fluid \mathbf{r} . For this geometry,

$$\Delta z' = r \cos \theta - \Delta z. \quad (6.49)$$

Substituting into Eq.(6.48) and integrating over θ and ϕ ,

$$-\frac{2\pi k}{R-R_c} [f(\mathbf{r}) - f_w] \int_{R-R_c}^{R+R_c} dr r^3 F(r) \left[1 - \left(\frac{R^2 + r^2 - R_c^2}{2rR} \right)^2 \right]. \quad (6.50)$$

It is straightforward to obtain an exact analytical solution by replacing the upper limit in the integral in Eq.(6.50) with κh . For simplicity, we integrate over the entire colloidal particle after substituting Eq.(6.27) into Eq.(6.50), arriving at the result,

$$-\frac{hk}{\pi^{1/2} R^2 (R-R_c)} [f(\mathbf{r}) - f_w] M(R, R_c, h). \quad (6.51)$$

For simulations of fluid flow near a sphere, no-slip is applied by modifying Eq.(6.5) and including the boundary term to give

$$\begin{aligned} m_i \frac{d\mathbf{v}_i}{dt} = & - \sum_{j=1}^N m_i m_j \left(\frac{p_i}{\rho_i^2} + \frac{p_j}{\rho_j^2} \right) \frac{\partial W_{ij}}{\partial r_{ij}} \mathbf{e}_{ij} \\ & + 2\eta \sum_{j=1}^N \frac{m_i m_j}{\rho_i \rho_j} \left(\frac{1}{|\mathbf{r}_{ij}|} \frac{\partial W_{ij}}{\partial r_{ij}} \right) \mathbf{v}_{ij} - \frac{\eta m_i h (\Delta \mathbf{v}_i - R_c \boldsymbol{\omega} \times \mathbf{n})}{\rho_i \pi^{1/2} R^2 (R-R_c)} M(R, R_c, h). \end{aligned} \quad (6.52)$$

In this equation, $\boldsymbol{\omega}$ is the angular velocity of the sphere, \mathbf{n} is a normal vector pointing from the colloid center towards the fluid particle, and we have defined $\Delta \mathbf{v}_i = \mathbf{v}_i - \mathbf{V}_c$, where \mathbf{V}_c is the linear velocity of the sphere center of mass. Following Newton's third law, the colloid receives a contribution to its equation of motion [in addition to the integrated pressure contribution, Eq.(6.34)] given by

$$M_c \frac{d\mathbf{V}_c}{dt} = \frac{\eta m_i h (\Delta \mathbf{v}_i - R_c \boldsymbol{\omega} \times \mathbf{n})}{\pi^{1/2} \rho_i R^2 (R - R_c)} M(R, R_c, h). \quad (6.53)$$

Here, M_c is the total mass of the colloidal particle.

To test these results, we compute the drag on a solid sphere in uniform flow using the present numerical approach and compare it to the expected result from Stokes' law. This is done by initializing a lattice of SDPD fluid particles and placing a colloidal particle inside the box. Velocities are assigned to the fluid particles surrounding the colloid according to the flow field solution for Stokes' flow around a sphere, and the drag on the colloidal particle is calculated by summing interactions between the surrounding fluid particles and the colloid, given by Eq.(6.53). As a reference, we use parameters for a Lennard-Jones fluid at temperature $T = 1.0$ and density $\rho = 0.8$, with non-dimensional units as described in

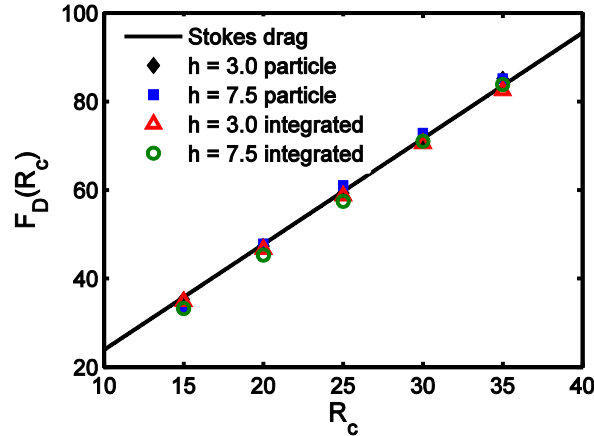


Fig. 6.4. Total force acting on spherical particle in uniform flow due to viscous forces versus particle radius. The black curve is the analytical result in the Stokes flow limit. This solution is compared to the numerically-computed drag on the particle, determined using traditional boundary particle techniques (diamond and square markers) and the same calculation using the integrated boundary approach (hollow triangle and circle markers). For the numerical results, we show data for two different fluid resolutions, a fine case where fluid particles have a smoothing length of $h = 3.0$, and a more coarse one where $h = 7.5$.

Ref. [40]. At this thermodynamic state, the fluid viscosity is $\eta = 1.9$ [41].

We consider two different resolutions for the fluid, one where the fluid particles have mass and smoothing length $m = 12.5$ and $h = 3.0$, respectively, and one with $m = 200.0$ and $h = 7.5$. For the first case, the 64000 particles are initialized on a $40 \times 40 \times 40$ lattice inside a simulation box with dimensions $100 \times 100 \times 100$. For the coarser test, 4096 particles are placed on a $16 \times 16 \times 16$ inside a volume with side lengths $100 \times 100 \times 100$. After the lattice is prepared, a solid sphere with some radius is placed at the center of the simulation box, and fluid particles located inside the colloid are deleted. Note that particles are held at their initial positions after initialization; hence, as the colloid's radius is adjusted, the distance of the nearest shell of particles around the boundary changes, affecting the error in the integral and sum approximations. The influence of the particle distribution on the numerical accuracy is the so-called “particle inconsistency” issue in SPH [42]. To reduce this effect, when creating the lattice we place particles randomly within $0.4dx$ of the ideal cubic lattice site, where dx is the lattice spacing. We initialize 10 independent random initial fluid particle distributions, and data points are obtained from an average over this ensemble of fluid particle configurations. Following this initialization, velocities are assigned to the fluid particles using the Stokes flow solution for uniform flow past a sphere, i.e., we calculate the distance r of every fluid particle from the colloid center and give it a velocity according to [43]

$$\begin{aligned} v_r(r, \theta) &= U_\infty \cos \theta \left[1 - \frac{3}{2} \left(\frac{R_c}{r} \right) + \frac{1}{2} \left(\frac{R_c}{r} \right)^3 \right], \\ v_\theta(r, \theta) &= -U_\infty \sin \theta \left[1 - \frac{3}{4} \left(\frac{R_c}{r} \right) - \frac{1}{4} \left(\frac{R_c}{r} \right)^3 \right]. \end{aligned} \tag{6.54}$$

R_c	$\langle N_c \rangle$	$\langle F_{\text{int}} \rangle$	$\langle F_{\text{par}} \rangle$	$\langle F_{\text{actual}} \rangle$	$\langle F_{\text{int}} \rangle$ % error
15	908	34.871	35.300	35.814	2.634
20	2151	46.645	47.329	47.752	2.318
25	4193	58.710	59.276	59.690	1.642
30	7244	70.523	71.178	71.628	1.543
35	11510	82.465	85.156	83.566	1.318

Table 6.1. Summary of results from Stokes' flow calculations for the net force acting on spherical colloid. Brackets denote averaging over an ensemble of fluid particle initial configurations. The table includes the colloid radius R_c , average number of fluid particles deleted when creating colloid N_c (i.e., those that fall inside it), the average force calculated using the integrated boundary approach F_{int} , the force from the traditional ghost particle method F_{par} , the actual force F_{actual} from the analytical result, and finally the percent error in the force determined from the integrated boundary technique.

U_∞ is the velocity far from the sphere, assumed in the z -direction; for the present calculations we assume $U_\infty = 0.1$. Once a velocity has been assigned to every fluid particle, we calculate the instantaneous force acting on the colloid using Eq.(6.53). For simplicity, we neglect the pressure interactions and only include viscous ones. The computed drag from this calculation is compared to the analytical result for Stokes' drag around a sphere, which, neglecting the pressure contribution, is given by [43]

$$\mathbf{F}_D = 4\pi\eta R_c U_\infty \mathbf{e}_z. \quad (6.55)$$

In addition to using the integrated boundary approach, we also perform a control test using the same SDPD calculations but without deleting the fluid particles inside the colloid, instead converting those fluid particles to boundary "ghost" particles and using traditional boundary particle techniques. Table 6.1 summarizes the number of ghost particles comprising the

colloid for each case, as well as summarizing the drag force computed from these simulations. Fig. 6.4 compares the drag force on the spherical particle computed using the integrated boundary approach to the result using traditional boundary particle methods, and to the analytical result given by Eq.(6.55). For a fixed fluid resolution, we find that the error in the integrated boundary solution decreases with increasing colloid radius, since the fluid particles with fixed resolution are able to more accurately resolve the flow field around the particle as the radius of curvature of the colloid increases. As expected, increasing the resolution of the fluid from $h = 7.5$ to $h = 3.0$ dramatically decreases the error. The integrated boundary results for the $h = 3.0$ case are always under 3%, with the largest error at 2.6% for the smallest colloid tested, and lowest error at 1.3% for the largest. Table 6.1 summarizes the data for the $h = 3.0$ tests and the associated errors. The boundary ghost particle technique gives slightly more accurate results, with errors ranging between 0.6% and 1.9%, due to a consistent particle-based description throughout. However, the gain in accuracy is modest and comes at significant computational cost.

6.6 Integrated Torque Applied to Colloid Due to Surrounding Fluid

In Section 6.5 we derived the resultant force on the colloid, which acts on the center of mass of the sphere; with this location of the force action, we must compute the associated torque on the colloidal particle about it. The torque arises due to the viscous SDPD interaction between boundary and fluid particle pairs,

$$\mathbf{f}_{ij} = \frac{2\eta}{v_i v_j} F_{ij} \mathbf{v}_{ij}. \quad (6.56)$$

For convenience, we define the number density $\nu_i = \rho_i / m_i$. The derivation in this section again proceeds from the particle perspective, where the colloid is composed of a lattice of subparticles that are later integrated out. Only the viscous interactions are relevant, since the overall pressure force will exert a force along the vector joining the fluid particle and colloid center of mass and therefore not result in a net torque. Each viscous pair interaction between fluid particle and colloid subparticle exerts a torque about an axis passing through the colloid center of mass, which is given by the cross product of the displacement vector and force

$$\boldsymbol{\tau}_{ij} = \boldsymbol{\delta}_j \times \mathbf{f}_{ij},$$

$$\boldsymbol{\tau}_{ij} = -\frac{2\eta}{\nu_i \nu_j} F_{ij} (\boldsymbol{\delta}_j \times \mathbf{v}_{ij}). \quad (6.57)$$

Here, $\boldsymbol{\delta}_j$ is the displacement vector pointing from the colloid center of mass to the j th colloid subparticle, $\boldsymbol{\delta}_j = \mathbf{r}_j - \mathbf{R}_c$, where \mathbf{R}_c is the position vector for the suspended sphere.

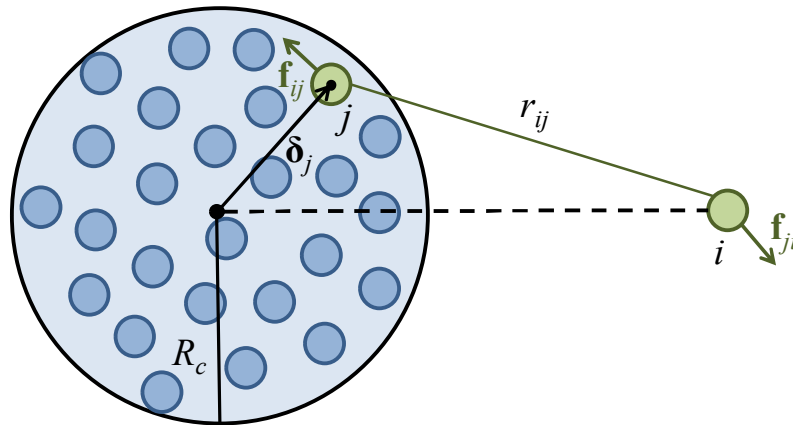


Fig. 6.5. Illustration of variables when computing the torque on a colloidal sphere due to a single fluid particle i . In order to determine the total force acting on the colloid center of mass, we begin from the particle perspective, i.e. the colloid is decomposed into a collection of particles. We write the sum of forces acting on the colloid center of mass, and then replace the summation with an integral.

Summing all torques due to each pair interaction gives the total on the colloid due to the i th particle,

$$\boldsymbol{\tau}_i = -2\eta \sum_{j=1}^{N_c} \frac{F_{ij}}{v_i v_j} (\boldsymbol{\delta}_j \times \mathbf{v}_{ij}). \quad (6.58)$$

The modified velocity difference for enforcing no-slip in this case is

$$\mathbf{v}_{ij} = \beta (\mathbf{v}_i - \mathbf{v}_s) = \left(1 + \frac{R_c - |\boldsymbol{\delta}_j| \cos \theta}{R - R_c} \right) (\Delta \mathbf{v}_i - R_c \boldsymbol{\omega} \times \mathbf{e}_z). \quad (6.59)$$

Substituting into Eq.(6.58) and splitting into two sums,

$$\boldsymbol{\tau}_i = \frac{2\eta}{v_i v_w} \Delta \mathbf{v}_i \times \sum_{j=1}^{N_c} \beta F_{ij} \boldsymbol{\delta}_j + \frac{2\eta R_c}{v_i v_w} \sum_{j=1}^{N_c} \beta F_{ij} \boldsymbol{\delta}_j \times (\boldsymbol{\omega} \times \mathbf{e}_z). \quad (6.60)$$

The second term is rewritten using the vector triple product,

$$\boldsymbol{\delta}_j \times (\boldsymbol{\omega} \times \mathbf{e}_z) = \boldsymbol{\omega} (\boldsymbol{\delta}_j \cdot \mathbf{e}_z) - \mathbf{e}_z (\boldsymbol{\delta}_j \cdot \boldsymbol{\omega}), \quad (6.61)$$

giving

$$\boldsymbol{\tau}_i = \frac{2\eta}{v_i v_w} \Delta \mathbf{v}_i \times \sum_{j=1}^{N_c} \beta F_{ij} \boldsymbol{\delta}_j + \frac{2\eta R_c}{v_i v_w} \sum_{j=1}^{N_c} \beta F_{ij} \boldsymbol{\omega} (\boldsymbol{\delta}_j \cdot \mathbf{e}_z). \quad (6.62)$$

To simplify the expression, we used the fact that $\boldsymbol{\omega}$ is orthogonal to the displacement vector $\boldsymbol{\delta}_j$ (i.e. $\boldsymbol{\delta}_j \cdot \boldsymbol{\omega} = 0$), a consequence of the rigid body motion of the particle. Assuming a number density v_w of subparticles that comprise the colloid, the sums in Eq.(6.62) can be replaced with the following integrals,

$$\boldsymbol{\tau}_i = \frac{2\eta}{v_i} \Delta \mathbf{v}_i \times \int_{\Omega_c} \beta F(|\mathbf{r}'|) \mathbf{r}' d\mathbf{r}' + \frac{2\eta R_c}{v_i} \boldsymbol{\omega} \int_{\Omega_c} \beta F(|\mathbf{r}'|) (\mathbf{r}' \cdot \mathbf{e}_z) d\mathbf{r}'. \quad (6.63)$$

We express these integrals explicitly using spherical coordinates by setting the coordinate origin at the center of the colloidal particle, with the unit vector in the z -direction \mathbf{e}_z

pointing from the colloid center towards the i th fluid particle. In this case, the dot product in the second integral is $\mathbf{r}' \cdot \mathbf{e}_z = |\mathbf{r}'| \cos \theta$.

First we address the first integral on the right-hand-side of Eq.(6.63). Note that the vector \mathbf{r}' is given by

$$\mathbf{r}' = r\mathbf{e}_r = r \sin \theta \cos \phi \mathbf{e}_x + r \sin \theta \sin \phi \mathbf{e}_y + r \cos \theta \mathbf{e}_z. \quad (6.64)$$

With our choice for the coordinate system centered inside the colloid, it is necessary to evaluate a separate integral for each of the three components of \mathbf{r}' ,

$$\begin{aligned} & \frac{2\eta}{v_i} \Delta \mathbf{v}_i \times \mathbf{e}_x \int_0^{R_c} dr \int_0^{2\pi} d\phi \int_0^\pi d\theta \left(1 + \frac{R_c - r \cos \theta}{R - R_c} \right) F(r, \theta) r^3 \sin^2 \theta \cos \phi \\ & + \frac{2\eta}{v_i} \Delta \mathbf{v}_i \times \mathbf{e}_y \int_0^{R_c} dr \int_0^{2\pi} d\phi \int_0^\pi d\theta \left(1 + \frac{R_c - r \cos \theta}{R - R_c} \right) F(r, \theta) r^3 \sin^2 \theta \sin \phi \\ & + \frac{2\eta}{v_i} \Delta \mathbf{v}_i \times \mathbf{e}_z \int_0^{R_c} dr \int_0^{2\pi} d\phi \int_0^\pi d\theta \left(1 + \frac{R_c - r \cos \theta}{R - R_c} \right) F(r, \theta) r^3 \sin \theta \cos \theta. \end{aligned} \quad (6.65)$$

We recognize that, due to our choice of coordinate origin, the function F now depends on both r and θ ,

$$F(r, \theta) = \frac{2}{\pi^{3/2} h^5} \exp \left[-\frac{r^2 + R^2 - 2rR \cos \theta}{h^2} \right]. \quad (6.66)$$

Integrating Eq.(6.65) with respect to ϕ , two of the integrals vanish due to the antisymmetry of the integrand, and only the z -component (i.e. the vector joining the centers of the colloid and the fluid particle) remains,

$$\frac{4\pi\eta}{v_i} \Delta \mathbf{v}_i \times \mathbf{e}_z \int_0^{R_c} dr \int_0^\pi d\theta \left(1 + \frac{R_c - r \cos \theta}{R - R_c} \right) F(r, \theta) r^3 \sin \theta \cos \theta. \quad (6.67)$$

Substituting Eq.(6.66) into Eq.(6.67) and integrating over θ ,

$$\begin{aligned}
& -\frac{4\eta(\Delta\mathbf{v}_i \times \mathbf{e}_z)}{\pi^{1/2}h^3v_iR^3(R-R_c)} \int_0^{R_c} dr r \exp\left(-\frac{r^2+R^2}{h^2}\right) \\
& \times \left[(h^4+h^2R^2+2r^2R^2) \sinh\left(\frac{2rR}{h^2}\right) - 2rR(h^2+R^2) \cosh\left(\frac{2rR}{h^2}\right) \right]. \tag{6.68}
\end{aligned}$$

Note that the unit vector \mathbf{e}_z appears in this expression due to our choice of coordinates for the integration such that the unit vector pointing from the colloid towards the fluid particle is in the z -direction. More generally, this vector is a normal vector pointing from the center of the colloid towards the fluid particle, regardless of the location of the fluid particle with respect to it. We therefore introduce a surface normal vector \mathbf{n} that henceforth replaces \mathbf{e}_z in the derivation. Integrating over the radial variable, we obtain the final expression for the first integral in Eq.(6.63),

$$-\frac{\eta m_i(\Delta\mathbf{v}_i \times \mathbf{n})}{\rho_i \pi^{1/2} \hat{R}^3 (R-R_c)} B(\hat{R}, \hat{R}_c). \tag{6.69}$$

Above we have defined

$$\begin{aligned}
B(\hat{R}, \hat{R}_c) &= \exp(-A_+^2) \left(1 + \hat{R}^2 + C + \frac{1}{2} C^2 \right) \\
& - \exp(-A_-^2) \left(1 + \hat{R}^2 - C + \frac{1}{2} C^2 \right) + \sqrt{\pi} \hat{R}^3 G_+, \tag{6.70}
\end{aligned}$$

where

$$G_+(R) = \operatorname{erf}(A_-) + \operatorname{erf}(A_+). \tag{6.71}$$

Next, we consider the second integral in Eq.(6.63), which is written explicitly in spherical coordinates as

$$\begin{aligned} \frac{2\eta R_c}{v_i} \boldsymbol{\omega} \int_{\Omega_c} \beta F(|\mathbf{r}'|) |\mathbf{r}'| d\mathbf{r}' = \\ \frac{2\eta R_c \rho_c}{v_i v_c (R - R_c)} \boldsymbol{\omega} \int_0^{R_c} dr \int_0^{2\pi} d\phi \int_0^\pi d\theta (R - r \cos \theta) F(r, \theta) r^3 \sin \theta \cos \theta. \end{aligned} \quad (6.72)$$

Substituting Eq.(6.66) into Eq.(6.72) and integrating with respect to ϕ ,

$$\begin{aligned} \frac{8\eta R_c}{v_i \pi^{1/2} h^5 (R - R_c)} \exp\left(-\frac{R^2}{h^2}\right) \boldsymbol{\omega} \int_0^{R_c} dr \exp\left(-\frac{r^2}{h^2}\right) r^3 \\ \times \int_0^\pi d\theta (R - r \cos \theta) \exp\left(\frac{2rR \cos \theta}{h^2}\right) \sin \theta \cos \theta. \end{aligned} \quad (6.73)$$

Integrating over the remaining variables,

$$-\frac{\eta R_c \boldsymbol{\omega}}{v_i \pi^{1/2} \hat{R}^3 (R - R_c)} B(\hat{R}, \hat{R}_c). \quad (6.74)$$

Combining Eqs.(6.69) and (6.74), we arrive at the final result

$$\boldsymbol{\tau}_i = -\frac{\eta m_i (\Delta \mathbf{v}_i \times \mathbf{n} + R_c \boldsymbol{\omega})}{\rho_i h \pi^{1/2} \hat{R}^3 (\hat{R} - \hat{R}_c)} B(\hat{R}, \hat{R}_c). \quad (6.75)$$

As expected, the torque exerted on the colloid due to fluid particle i is a function of the colloid and fluid particle's linear velocity, the colloid's angular velocity, the separation of the fluid and colloid particles, the location of the fluid particle relative to the colloid, as well as constants including the colloidal particle radius, fluid density and viscosity, and fluid resolution (i.e. smoothing length). Eq.(6.75) is the torque acting on the colloid due to a single nearby fluid particle; the total torque on the colloid is the sum of the individual torques due to all of the surrounding fluid particles, $\boldsymbol{\tau}_c = \sum_i \boldsymbol{\tau}_i$. Note that in SDPD, including the integrated boundary approach presented here, angular momentum is not conserved exactly, though formulations of SDPD that include a spin variable for each fluid particle have been recently developed [44].

We test the integrated expression for the torque by placing a stationary, non-rotating colloidal particle inside a flow field, calculating the instantaneous torque on the colloid, and comparing to the analytical result. As in subsection 6.5.2, a collection of SDPD fluid particles are initialized on a cubic lattice with spacing dx , and a colloidal particle is placed in the center of the simulation box. Ten separate particle configurations are initialized with independent random displacements from the ideal lattice positions, and fluid particles residing inside the colloid are deleted from the system. The remaining fluid particles are assigned a velocity based on the analytical solution in the zero Reynold's number limit for a particle in linear shear flow, where the spherical particle has no angular velocity [43]

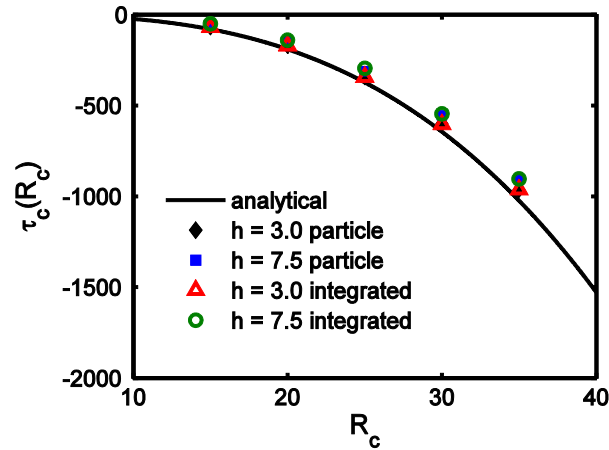


Fig. 6.6. The torque exerted on a stationary, non-rotating spherical particle in linear shear flow versus particle radius. The analytical result from Faxén's second law is shown as the black curve. This trend is exact in the zero Reynold's number limit, and compared to numerical calculations using SDPD. The diamond and square markers denote results using the traditional boundary particle method, and the hollow triangle and circle markers give the torque calculated using the integrated boundary approach. For the numerical calculations, we consider two different resolutions for the surrounding fluid, a case with $h = 3.0$ and one where $h = 7.5$

$$\begin{aligned}
v_r(r, \theta, \phi) &= \Gamma r \sin^2 \theta \sin \phi \cos \phi \left[1 - \frac{5}{2} \left(\frac{R_c}{r} \right)^3 + \frac{3}{2} \left(\frac{R_c}{r} \right)^5 \right], \\
v_\theta(r, \theta, \phi) &= \Gamma r \sin \theta \cos \theta \sin \phi \cos \phi \left[1 - \left(\frac{R_c}{r} \right)^5 \right], \\
v_\phi(r, \theta, \phi) &= -\frac{\Gamma r \sin \theta}{2} \left\{ 1 - \left(\frac{R_c}{r} \right)^3 - \cos 2\phi \left[1 - \left(\frac{R_c}{r} \right)^5 \right] \right\}.
\end{aligned} \tag{6.76}$$

Γ is the shear rate. This solution corresponds to flow in the x -direction, and velocity gradient in the y -direction. The creeping flow result for the torque on the particle due to the above flow field is given by Faxén's second law, assuming no other colloids are present and zero angular velocity for the particle [43],

$$\boldsymbol{\tau}_c = -4\pi\eta R_c^3 \Gamma \mathbf{e}_z, \tag{6.77}$$

with the torque acting in the direction of the unperturbed flow vorticity. In Fig. 6.6 we

R_c	$\langle N_c \rangle$	$\langle \boldsymbol{\tau}_{\text{int}} \rangle$	$\langle \boldsymbol{\tau}_{\text{par}} \rangle$	$\langle \boldsymbol{\tau}_{\text{actual}} \rangle$	$\langle \boldsymbol{\tau}_{\text{int}} \rangle$ % error
15	908	-69.554	-69.600	-80.582	-13.686
20	2151	-170.971	-171.334	-191.009	-10.490
25	4193	-344.272	-343.595	-373.064	-7.718
30	7244	-604.070	-600.904	-644.655	-6.296
35	11510	-962.753	-964.297	-1023.688	-5.952

Table 6.2. Summary of torques acting on non-rotating sphere in uniform shear flow. As before, brackets denote averages over an ensemble of fluid particle initial configurations. In this case, the table includes the average torque calculated using the integrated boundary approach $\boldsymbol{\tau}_{\text{int}}$, the torque from the traditional ghost particle method $\boldsymbol{\tau}_{\text{par}}$, the actual creeping flow torque $\boldsymbol{\tau}_{\text{actual}}$ given by Faxén's 2nd law, and the percent error in the torque determined from the integrated boundary technique. The integrated and particle sum calculations are for the $h = 3.0$ case.

compare numerical results using the integrated boundary SDPD approach developed in this chapter, averaged over the different random particle configurations, to the analytical result in Eq.(6.77). For completeness, we also include the same calculation using the traditional boundary ghost particle approach commonly employed in SPH and SDPD simulations. We find that errors are more significant when calculating the torque for both the integrated and boundary particle methods when compared to the linear force calculations in Subsection 6.5.2. While the errors for the integrated boundary tests in Table 6.2 appear substantial, they are comparable in magnitude to ones obtained using the established ghost particle approach. For colloidal particles with radii of curvature greater than 25.0 and fluid particles with $h = 3.0$, the error remains below 10% for both the integrated and boundary particle methods. For smaller colloids, a fluid composed of a higher number density of fluid particles is required to accurately resolve the flow around the highly curved particle in order to give the correct torque. When using particles with a larger smoothing length ($h = 7.5$), the inaccuracy in the torques is more significant, but still comparable to the error when using the ghost boundary particle method. The errors for the $h = 3.0$ case are summarized in Table 6.2.

6.7 Colloid Stochastic Force and Torque

Finally, we must consider the case in which the boundary can exchange momentum with the fluid due to random thermal stresses. Including this stochastic contribution to the dynamics is essential when the boundary is a colloidal particle, in which case these fluctuations will result in its Brownian diffusion. We treat the boundary as a super-particle such that the fluctuations have the same structure as those between two fluid particles. For

simplicity, we consider an incompressible Newtonian fluid and postulate noise in the velocity field of the form,

$$m_i d\tilde{\mathbf{v}}_i = \sum_{j, \text{fluid}}^N A_{ij} d\hat{\mathbf{W}}_{ij} \cdot \mathbf{e}_{ij} + \Upsilon_i d\hat{\mathbf{V}}_i \cdot \mathbf{n}. \quad (6.78)$$

Here, $d\mathbf{W}_{ij}$ and $d\mathbf{V}_i$ are dyadic tensors of Gaussian process increments. $d\hat{\mathbf{W}}_{ij}$ and $d\hat{\mathbf{V}}_i$ are the traceless, symmetric part of $d\mathbf{W}_{ij}$ and $d\mathbf{V}_i$, respectively. $d\hat{\mathbf{W}}_{ij}$ gives the stress between particles i and j , and $d\hat{\mathbf{V}}_i$ is the stress between the i th particle and the wall. Here, \mathbf{n} is the vector normal to the wall for a planar boundary. For a fluid particle near a spherical object, \mathbf{n} instead corresponds to a unit normal between the centers of particle i and the solid sphere. Ignoring the boundary terms, Eq.(6.78) reduces to the form of the noise for an incompressible SDPD fluid [8,14,39], Eq.(6.6). Above we assume that the stochastic fluid-boundary momentum exchange has the same structure as the random fluid-fluid interaction. This assumption is due to the fact that the integrated dissipative boundary terms have the same form as the viscous fluid-fluid force.

Following a derivation similar to the one in Chapter 4, it is possible to use the GENERIC formalism to determine the correct form of the noise amplitudes A_{ij} and Υ_i in Eq.(6.78). In Appendix 6.10 the noise amplitude due to stochastic fluxes of solute across the boundary is derived to illustrate how GENERIC is applied. The noise amplitude for the stochastic interactions between fluid particles is given by Eq.(6.7); the noise amplitude for the stochastic wall-fluid interaction for a planar boundary is

$$\Upsilon_i = \left[\frac{8k_B T m_i \eta}{\rho_i \pi^{1/2} h \Delta z_i} K \left(\frac{\Delta z_i}{h} \right) \right]^{1/2}. \quad (6.79)$$

If instead we consider a spherical object (e.g. colloid), the noise amplitude becomes

$$\Upsilon_i = \left[\frac{4\eta m_i h k_B T}{\rho_i \pi^{1/2} R^2 (R - R_c)} M(R, R_c, h) \right]^{1/2}. \quad (6.80)$$

Since there is a dissipative term that acts to reduce angular velocities, the fluctuation-dissipation theorem suggests that there is also a stochastic torque that introduces thermal noise in the angular momenta of the colloids. In other words, the stochastic interaction between fluid particle i and colloid subparticle pairs [Eq.(6.6)] results in a torque on colloid j , for which we postulate the form,

$$I_j d\tilde{\boldsymbol{\omega}}_j = \mathbb{T}_j \left(d\hat{\mathbf{V}}_j \cdot \mathbf{n} \right) \times \mathbf{n}, \quad (6.81)$$

where I_j is the moment of inertia of the j th colloidal particle, which for a sphere is simply

$I_j = \frac{2}{5} m_j R_c^2$. The noise magnitude for fluctuation-dissipation is given by

$$\mathbb{T}_j = \left[-\frac{4\eta m_i R_c k_B T}{\rho_i \pi^{1/2} \hat{R}^3 (R - R_c)} B(\hat{R}, \hat{R}_c) \right]^{1/2}. \quad (6.82)$$

6.8 Equilibrium Simulation of a Colloid Using Integrated Boundaries

In Sections 6.5.2 and 6.6, we demonstrated that the integrated boundary expressions for the instantaneous force and torque on the colloid are faithful to their traditional particle counterparts; in this section, we combine these results in a full simulation of a colloidal particle immersed in a fluid at thermal equilibrium undergoing Brownian motion, and hence validate the fluctuation-dissipation relationships given by Eqs.(6.80) and (6.82). We initialize a colloidal particle in a fluid modeled using a collection of SDPD volumes, then evolve the system in time and track the colloid's random walk. The interactions between all particles are

pairwise and symmetric. Fluid particle pairs experience the normal SDPD interactions, summarized in Section 6.2. Fluid particles interact with the colloidal particle through conservative interactions due to the pressure field [(Eq.(6.34) in Section 6.4.2], viscous forces due to friction [Eq.(6.52), Section 6.5.2], and random forces resulting from thermal fluctuations [Eq.(6.78), Section 6.7]. Since the colloid has rotational degrees of freedom, it experiences stochastic torque according to Eq.(6.81), which is balanced by a dissipative term Eq.(6.75). Densities of fluid particles near the colloid are updated using Eq.(6.25). Note that Eq.(6.34) alone does not guarantee the kinematic boundary condition and particles may penetrate the boundary unless a prohibitively small time-step is used. Moreover, the dissipative and random forces and torques diverge for zero separation between fluid particle and colloid $R = R_c$. For stability, fluid particles that penetrate the colloid ($R \leq R_c$) experience a constant repulsive pressure and dissipative forces equal to forces if the fluid particle was located a small distance outside the colloid $R = \Delta R$. For our numerical tests, we choose $\Delta R = 0.001$.

The simulation is constructed as follows: 3375 fluid particles are initialized on a $15 \times 15 \times 15$ lattice inside a $75 \times 75 \times 75$ volume. Each particle has a mass of $m = 100.0$, and the fluid density is $\rho = 0.8$, giving a smoothing length $h = 6.0$. The parameters are chosen to represent a Lennard-Jones fluid at this mass density and temperature $T = 1.0$. At this thermodynamic state point, the shear viscosity is $\eta = 1.9$. After the fluid is initialized, we place a neutrally-buoyant (i.e. $\rho_w = 0.8$) colloidal particle in the center of the simulation box, and delete any fluid particles that overlap with it. Two independent tests are performed, one for a colloid with radius $R_c = 15$ and one with $R_c = 25$. The fluid and colloidal particle positions and velocities are integrated in time using the modified velocity Verlet algorithm in

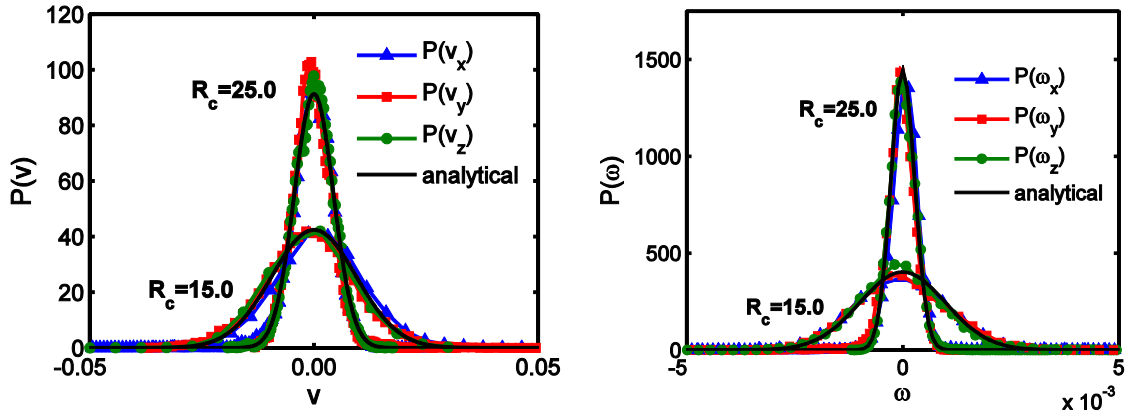


Fig. 6.7. (a) Probability distributions for colloid linear velocities from simulation of single Brownian sphere using the integrated boundary approach. (b) Distribution of suspended particle's angular velocities. The results are compared to the Maxwell-Boltzmann distribution.

Ref. [45], and the colloid angular velocity is updated at the same time as the linear velocities. We use a time-step of $\Delta t = 0.001$, which gives accuracy such that fluid particle penetration of the colloid is infrequent, and equilibrate for 5.0×10^5 steps prior to starting the production run, which lasts for 1.5×10^6 steps. In Fig. 6.7 we show the probability distributions of a) linear and b) angular velocities adopted by the suspended sphere as it undergoes Brownian motion, and compare the results from the simulation to the Maxwell-Boltzmann distribution. The results from the simulation are in good agreement with this result, showing correct diffusive behavior.

6.9 Conclusions

SDPD provides a modeling framework for colloidal suspensions that does not make physical assumptions about the flow. This generality makes SDPD more numerically expensive, hence necessitating techniques such as the integrated boundary framework

presented in this chapter, which dramatically reduces the number of pairwise force interactions calculated at each time-step. This is achieved by decomposing a suspended particle in a fluid medium into a collection of SDPD boundary particles. These particles are subsequently integrated out, giving a single bulk contribution to the equation of motion of a nearby fluid particle and the colloid center of mass, rather than determining pairwise forces between the fluid particle and each boundary one. In Sections 6.5 and 6.6, we demonstrated that for low Reynold's number flows, this integrated approach gives results consistent with the analytical creeping flow solutions. Results are obtained for the cases of a spherical particle in uniform fluid flow, as well as a non-rotating spherical particle in shear flow, and the computed forces and torques are comparable to ones obtained from existing methods for enforcing no-slip in smoothed particle techniques. Section 6.7 introduces fluctuating forces and torques into the colloid's equation of motion, which are balanced by the dissipative forces and torques derived in the previous sections. Finally, in Section 6.8, we combine these elements and perform a full simulation of the Brownian motion of a single colloidal particle. The results show that the forms for the thermal noise in Section 6.7 give the correct relationship between the random and dissipative forces, resulting in the expected Maxwell-Boltzmann distribution of linear and angular momenta for the suspended sphere.

The integrated boundary method leads to more efficient simulations of dispersed particles, but also features a number of limitations. First, we found that forces and torques computed using integrated boundaries are slightly less accurate than ones obtained using traditional boundary particle techniques owing to the discrepancy in the fluid description in different parts of the simulation box when integrated objects are present. However, this increase in error is relatively small and a minor penalty for the computational speedup. In

addition, Morris et al. suggest that integrated boundaries are well suited to compressible and moderate Reynold's number flows, but may be unstable in the creeping flow limit [22]. Another drawback of this approach is that analytical expressions for boundaries can only be obtained for simple geometries such as planar surfaces and spheres. It may be possible to obtain analytical results for ellipsoidal objects, which can approximate suspensions of rod-shaped particles. Our results assume no-slip, though analytical results for boundary conditions having a non-vanishing slip length may also be feasible. Finally, the presented approach is easily extended to include more complicated physics. For example, integrated spherical objects can be tethered using a harmonic potential to model polymers, with each integrated sphere acting as a coarse-grained monomer. Furthermore, integrated expressions for spheres interacting through van der Waals and/or electrostatic interactions exist and may be straightforwardly included. For simulations of two or more Brownian spheres, a short-ranged repulsive lubrication force can be included, which acts along the line joining colloid particle centers and prevents their unphysical overlap, even if the actual SDPD fluid particles are excluded from the region that separates the two spheres. DPD has already been used to probe the rheology of particle dispersions [46,47], and the integrated boundary approach in this chapter presents an approach that allows for similar types of studies and is more rigorous while requiring fewer particles.

6.10 Appendix

6.10.1 Application of Integrated Boundaries to Mass Transfer in Binary Ideal Mixture

We apply Eq.(6.46) to the problem of mass transfer. Starting with the diffusion equation,

$$\frac{d\Phi}{dt} = \frac{1}{\rho} \nabla \cdot (D \nabla \Phi), \quad (6.83)$$

we discretize this expression and include the extra wall contribution to the dynamics. In this expression, Φ is the concentration defined as a mass fraction and D is the diffusion constant with units $ML^{-1}t^{-1}$. Thus, we find that the evolution of the concentration of particles near a planar wall is described by the following equation of motion,

$$m_i \frac{d\Phi_i}{dt} = 2D \sum_{j=1}^{N_f} \frac{m_i m_j}{\rho_i \rho_j} \left(\frac{1}{|\mathbf{r}_{ij}|} \frac{\partial W_{ij}}{\partial r_{ij}} \right) \Phi_{ij} - \frac{2m_i D}{\rho_i \pi^{1/2} h \Delta z_i} (\Phi_i - \Phi_w) K \left(\frac{\Delta z_i}{h} \right). \quad (6.84)$$

Here, the sum over the fluid particles is the well-known SPH discretization of the diffusion equation [Eq.(6.83)]. Due to the nearby surface, there is now an additional term that also drives mass transfer if the fluid particle has a different concentration Φ_i from the boundary one, Φ_w . If instead of a flat surface we have a spherical particle loaded with an active ingredient and losing solute to the surrounding fluid, the approximation to the diffusion equation in the vicinity of the suspended particle is given by

$$m_i \frac{d\Phi_i}{dt} = 2D \sum_{j=1}^{N_f} \frac{m_i m_j}{\rho_i \rho_j} \left(\frac{1}{|\mathbf{r}_{ij}|} \frac{\partial W_{ij}}{\partial r_{ij}} \right) \Phi_{ij} - \frac{D m_i h (\Phi_i - \Phi_w)}{\rho_i \pi^{1/2} R^2 (R - R_c)} M(R, R_c, h). \quad (6.85)$$

It is possible to extend this approach to the mesoscale, where there are thermal fluctuations present in the concentration field. In this case, fluid particles can exchange solute with the boundary due to stochastic fluxes in addition to chemical potential gradients. We postulate the following form for the noise,

$$m_i d\tilde{\Phi}_i = \sum_{j, fluid}^{N_f} G_{ij} dV_{ij} + \Lambda(\Delta z_i) dU_i, \quad (6.86)$$

where we have separated the random flux between the wall and fluid particle from the fluid-fluid ones. Here we assume that the stochastic mass transfer between wall and fluid particle is a Gaussian process, with some effective unknown noise amplitude Λ that depends on the separation between particle and wall. The form of the noise between the fluid particle and wall is the same as between fluid pairs. Hence, we are treating the wall as a superparticle, which acts as a bath due to the Dirichlet boundary conditions.

Following the same derivation procedure as for the normal multicomponent SDPD, we arrive at the following equation of motion for particle i due to its interaction with wall particles,

$$m_i \frac{d\Phi_i}{dt} = -\frac{1}{2m_0} \sum_{j, fluid}^{N_f} G_{ij}^2 \left[\ln \left(\frac{\Phi_i}{\Phi_j} \right) + \ln \left(\frac{1 - \Phi_j}{1 - \Phi_i} \right) \right] - \frac{1}{2m_0} \Lambda^2(\Delta z_i) \left[\ln \left(\frac{\Phi_i}{\Phi_w} \right) + \ln \left(\frac{1 - \Phi_w}{1 - \Phi_i} \right) \right]. \quad (6.87)$$

Rewriting in terms of the solute and solvent chemical potentials $\mu_i = \ln(\Phi_i) - \ln(1 - \Phi_i)$,

$$m_i \frac{d\Phi_i}{dt} = -\frac{1}{2m_0} \sum_{j, \text{fluid}}^N G_{ij}^2 \mu_{ij} - \frac{1}{2m_0} \Lambda^2(\Delta z_i) \mu_{iw}. \quad (6.88)$$

Once more, we focus on the wall-fluid interaction, i.e. the second term on the right-hand side of Eq.(6.88). Linearizing the logarithm, we find that

$$-\frac{1}{2m_0} \Lambda^2(\Delta z_i) \mu_{iw} \approx -\frac{1}{4m_0} \Lambda^2(\Delta z_i) \left(\frac{\Theta_i + \Theta_w}{\Theta_i \Theta_w} \right) (\Phi_i - \Phi_w), \quad (6.89)$$

where we have defined $\Theta_i = \Phi_i(1 - \Phi_i)$. Comparing Eq.(6.89) to Eq.(6.84),

$$-\frac{1}{4m_0} \Lambda^2(\Delta z_i) \left(\frac{\Theta_i + \Theta_w}{\Theta_i \Theta_w} \right) (\Phi_i - \Phi_w) = -\frac{2m_i D}{\rho_i \pi^{1/2} h \Delta z_i} (\Phi_i - \Phi_w) K \left(\frac{\Delta z_i}{h} \right). \quad (6.90)$$

Solving for the noise amplitude,

$$\Lambda(\Delta z_i) = \left[\frac{8m_0 m_i D}{\rho_i \pi^{1/2} h \Delta z_i} \left(\frac{\Theta_i \Theta_w}{\Theta_i + \Theta_w} \right) K \left(\frac{\Delta z_i}{h} \right) \right]^{1/2}. \quad (6.91)$$

If instead of a planar boundary, the fluid particle is near a sphere, the noise has the same form as Eq.(6.86), but the amplitude becomes

$$\Lambda(R) = \left[\frac{4m_0 m_i h D}{\rho_i \pi^{1/2} R^2 (R - R_c)} \left(\frac{\Theta_i \Theta_w}{\Theta_i + \Theta_w} \right) M(R, R_c, h) \right]^{1/2}, \quad (6.92)$$

where R is the separation between the sphere center of mass and the fluid particle. For fluid-fluid particle fluctuations, the noise amplitude due to the fluctuation-dissipation theorem is given by [9]

$$G_{ij} = \left[-\frac{8Dm_0 m_i m_j}{\rho_i \rho_j} \left(\frac{\Theta_i \Theta_j}{\Theta_i + \Theta_j} \right) \frac{1}{|\mathbf{r}_{ij}|} \frac{\partial W_{ij}}{\partial r_{ij}} \right]^{1/2}. \quad (6.93)$$

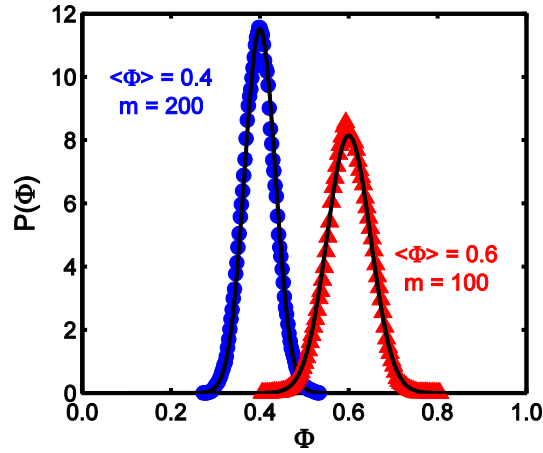


Fig. A6.1. Distribution of concentrations adopted by single particle placed near boundary, with dissipative and random fluxes of solute between the fluid particle and wall. Two cases are considered, one where the fluid particle has mass $m = 200$ and the average concentration is 0.4 (blue/circle markers), and another case where the fluid particle has mass $m = 100$ and the average concentration is 0.6 (red/triangle markers). Both tests are compared to the exact analytical result, shown in black.

In summary, the solute dynamics for a fluid particle near a solid planar boundary are governed by Eq.(6.84). For the mesoscale case, fluctuations are introduced in the particle concentrations with the form given by Eq.(6.86), and noise amplitudes for the boundary-fluid fluctuations and fluid-fluid fluctuations calculated from Eq.(6.91) and Eq.(6.93), respectively. If the solid object is a sphere (e.g. a colloidal particle loaded with some species that is miscible in the surrounding fluid), then the dynamics are described by Eqs.(6.85), (6.86), and (6.92) instead. The dissipative term has been validated in one-dimensional diffusion simulations where a concentration gradient is imposed across the system and the concentration profile evolves in time. The results from the integrated boundary approach show good agreement with the analytical solution and numerical calculations with the traditional boundary particle method (results not shown). In addition, we perform tests for the fluctuating solute model by placing a single particle near a planar boundary and allowing it to

exchange solute due to dissipative and random fluxes. The distribution of concentrations adopted by the fluid particle near the boundary is shown in Fig.A6.1 and shows good agreement with the analytical result.

6.11 References

- [1] L. B. Lucy, *Astron. J.* **82**, 1013 (1977).
- [2] R. A. Gingold and J. J. Monaghan, *Mon. Not. R. Astron. Soc.* **181**, 375 (1977).
- [3] J. J. Monaghan, *Rep. Prog. Phys.* **68**, 1703 (2005).
- [4] G. R. Liu and M. B. Liu, *Smoothed Particle Hydrodynamics: A Meshfree Particle Method* (World Scientific Publishing Company, 2003).
- [5] M. Grmela and H. C. Öttinger, *Phys. Rev. E* **56**, 6620 (1997).
- [6] H. C. Öttinger and M. Grmela, *Phys. Rev. E* **56**, 6633 (1997).
- [7] H. C. Öttinger, *Beyond Equilibrium Thermodynamics* (Wiley-Interscience, Hoboken, N.J., 2005).
- [8] P. Español and M. Revenga, *Phys. Rev. E Stat. Nonlin. Soft Matter Phys.* **67**, 26705 (2003).
- [9] N. D. Petsev, L. G. Leal, and M. S. Shell, *J. Chem. Phys.* **144**, 84115 (2016).
- [10] A. Vázquez-Quesada, M. Ellero, and P. Español, *J. Chem. Phys.* **130**, 34901 (2009).
- [11] S. Litvinov, M. Ellero, X. Hu, and N. A. Adams, *Phys. Rev. E* **77**, 66703 (2008).
- [12] S. Litvinov, X. Y. Hu, and N. A. Adams, *J. Phys. Condens. Matter* **23**, 184118 (2011).
- [13] N. Moreno, P. Vignal, J. Li, and V. M. Calo, *Procedia Comput. Sci.* **18**, 2565 (2013).
- [14] X. Bian, S. Litvinov, R. Qian, M. Ellero, and N. A. Adams, *Phys. Fluids* **24**, 12002 (2012).
- [15] M. Ferrand, D. R. Laurence, B. D. Rogers, D. Violeau, and C. Kassiotis, *Int. J. Numer. Methods Fluids* **71**, 446 (2013).

- [16] F. Macià, L. M. González, J. L. Cercos-Pita, and A. Souto-Iglesias, *Prog. Theor. Phys.* **128**, 439 (2012).
- [17] J. K. Chen, J. E. Beraun, and T. C. Carney, *Int. J. Numer. Methods Eng.* **46**, 231 (1999).
- [18] T. Belytschko, Y. Krongauz, D. Organ, M. Fleming, and P. Krysl, *Comput. Methods Appl. Mech. Eng.* **139**, 3 (1996).
- [19] G. R. Johnson and S. R. Beissel, *Int. J. Numer. Methods Eng.* **39**, 2725 (1996).
- [20] G. R. Johnson, R. A. Stryk, and S. R. Beissel, *Comput. Methods Appl. Mech. Eng.* **139**, 347 (1996).
- [21] A. Colagrossi and M. Landrini, *J. Comput. Phys.* **191**, 448 (2003).
- [22] J. P. Morris, P. J. Fox, and Y. Zhu, *J. Comput. Phys.* **136**, 214 (1997).
- [23] F. Macià, M. Antuono, L. M. González, and A. Colagrossi, *Prog. Theor. Phys.* **125**, 1091 (2011).
- [24] H. Takeda, S. M. Miyama, and M. Sekiya, *Prog. Theor. Phys.* **92**, 939 (1994).
- [25] P. J. Hoogerbrugge and J. M. V. A. Koelman, *EPL Europhys. Lett.* **19**, 155 (1992).
- [26] P. Español and P. Warren, *EPL Europhys. Lett.* **30**, 191 (1995).
- [27] Z. Li, Y.-H. Tang, H. Lei, B. Caswell, and G. E. Karniadakis, *J. Comput. Phys.* **265**, 113 (2014).
- [28] H. Lei, D. A. Fedosov, and G. E. Karniadakis, *J. Comput. Phys.* **230**, 3765 (2011).
- [29] Z. Li, A. Yazdani, A. Tartakovsky, and G. E. Karniadakis, *J. Chem. Phys.* **143**, 14101 (2015).
- [30] D. L. Ermak and J. A. McCammon, *J. Chem. Phys.* **69**, 1352 (1978).
- [31] J. F. Brady and G. Bossis, *Annu. Rev. Fluid Mech.* **20**, 111 (1988).
- [32] A. Sierou and J. F. Brady, *J. Fluid Mech.* **448**, 115 (2001).

- [33] D. R. Foss and J. F. Brady, *J. Fluid Mech.* **401**, 243 (1999).
- [34] T. N. Phung, J. F. Brady, and G. Bossis, *J. Fluid Mech.* **313**, 181 (1996).
- [35] A. J. C. Ladd, *Phys. Rev. Lett.* **70**, 1339 (1993).
- [36] A. J. C. Ladd and R. Verberg, *J. Stat. Phys.* **104**, 1191 (2001).
- [37] N. Sharma and N. A. Patankar, *J. Comput. Phys.* **201**, 466 (2004).
- [38] S. R. D. Groot and P. Mazur, *Non-Equilibrium Thermodynamics*, Dover edition (Dover Publications, New York, 2011).
- [39] X. Y. Hu and N. A. Adams, *J. Comput. Phys.* **213**, 844 (2006).
- [40] P. M. Kulkarni, C.-C. Fu, M. S. Shell, and L. Gary Leal, *J. Chem. Phys.* **138**, 234105 (2013).
- [41] K. Meier, A. Laesecke, and S. Kabelac, *J. Chem. Phys.* **121**, 3671 (2004).
- [42] M. B. Liu and G. R. Liu, *Appl. Numer. Math.* **56**, 19 (2006).
- [43] L. G. Leal, *Advanced Transport Phenomena: Fluid Mechanics and Convective Transport Processes*, 1st ed. (Cambridge University Press, 2010).
- [44] K. Müller, D. A. Fedosov, and G. Gompper, *J. Comput. Phys.* **281**, 301 (2015).
- [45] R. D. Groot and P. B. Warren, *J. Chem. Phys.* **107**, 4423 (1997).
- [46] E. S. Boek, P. V. Coveney, and H. N. W. Lekkerkerker, *J. Phys. Condens. Matter* **8**, 9509 (1996).
- [47] E. S. Boek, P. V. Coveney, H. N. W. Lekkerkerker, and P. van der Schoot, *Phys. Rev. E* **55**, 3124 (1997).

7 Conclusion

7.1 Implications

As modern chemicals and material development become increasingly reliant on nano- and micro-scale processes, the need to simultaneously probe molecular-level detail and transport phenomena over macroscopic lengths has rapidly expanded. In this thesis, we first considered surface nanobubbles, a particular example of this kind of important physical system that couples processes at both the molecular and macroscopic levels. These flat, gaseous objects, typically found along hydrophobic surfaces, are characterized by molecular length scales near the contact line due to their nanometer heights. However, another crucial aspect of the nanobubble problem is the transport of gas away from the bubble apex, which occurs over macroscopic lengths, and including both of these parts is intractable using traditional simulation methods. Beyond numerous applications that range from removing biological fouling [1] to nanoscale templating [2,3], nanobubbles pose a fundamental challenge to our understanding of hydrophobicity at interfaces because a number of their anomalous properties have eluded explanation for over two decades. The most striking feature of nanobubbles is their lifetimes, which are seven orders of magnitude greater than the prediction from simple scaling arguments [4]. Moreover, they are always flat, with small substrate-independent gas-side contact angles typically around $\sim 20^\circ$ [5].

In Chapter 2, we discussed these bubbles in detail and developed a continuum model that couples the transport of gas molecules over small scales near the bubble three-phase contact line to the diffusive outflux of gas over large scales. The resulting gas recirculation

model for nanobubble stability predicts rich behavior in their morphologies determined from the solution conditions, and we provided phase diagrams summarizing under what conditions stable bubbles exist and how factors such as the level of gas saturation in the liquid and temperature modify their properties.

While this model makes compelling predictions that are in agreement with numerous experimental studies, it is predicated on the validity of the continuum assumption for the influx process near the bubble contact line, which remains unclear. This hydrophobicity-driven influx of gas is responsible for the observed stability and occurs over nanometer scales, and hence investigating nanobubbles requires detailed simulations capable of capturing molecular features. In fact, nanobubbles are just one of a multitude of such “multiscale” problems that typically arise due to the presence of interfaces, including drug particle transport and delivery, three-phase flow, thin film dynamics, slip along hydrophobic boundaries, dynamics of biomolecules, and corrosion. We addressed in Chapter 3 this clear need to reconcile the granular, molecular picture of matter at the nanoscale with the coarse-grained continuum description over large scales, where we developed a method for embedding a detailed molecular dynamics (MD) fluid inside a continuum region simulated using the stochastic particle-based continuum fluid model known as “smoothed dissipative particle dynamics” (SDPD). The level of coarse-graining in SDPD is an input parameter, and hence by using this particle-based continuum approach, we are able to perform simulations that feature lengths ranging from the nanometer level to arbitrarily coarse continuum domains.

In the subsequent chapters, this hybrid simulation approach was generalized into a framework that allows for multiscale multicomponent simulation of continuum fluids

(Chapter 4), as well as coupled MD-continuum simulations of ideal mixtures (Chapter 5). The benefit of the coarse-graining methodology developed in Chapters 3-5 is the substantial reduction in the number of particles needed, and in Chapter 6 we described an extension of SDPD for introducing boundaries and solid objects that further reduces the system degrees of freedom. This “integrated boundary” SDPD approach was applied to the problem of Brownian particles in solution.

7.2 Future Work

One immediate next step for the multiscale framework described in this thesis is incorporating a multiple time-step algorithm. While in the preceding chapters we focus on coarse-graining single- and multicomponent fluids in space only, an important goal is to correspondingly adjust the time-step in the continuum region to account for the slower dynamics of the coarse-grained particles. Hence, the most finely-resolved region acts as a bottleneck by requiring a small time-step, which is then used to evolve the fluid at larger scales as well. Multiple time-step algorithms already exist for MD simulations [6–11], and due to the similarity between MD and SDPD, these integrators potentially may be adjusted for the coarse continuum regions in our simulations. In fact, such integrators for simulations having particles with disparate masses, where a larger time-step can be used for the more massive species, already exist [7,6]. However, decoupling time-scales in SDPD is made challenging by the presence of velocity-dependent forces, and hence such techniques cannot be immediately applied and require modification. Once developed and incorporated, however, this kind of adaptive integrator would give immense computational savings,

beyond the simple but dramatic reduction in the number of particles that our approach presently offers.

Another important future direction and major challenge for the multiscale multicomponent framework outlined in this thesis is generalizing the techniques for non-ideal mixtures, which is necessary for the simulation of nanobubbles. The ideal assumption is sufficient for problems where the dissolved species is dilute, giving solute dynamics proportional to the Laplacian of the concentration. It may be possible to model nanobubbles using a non-ideal MD region, which is sufficiently close to the ideal case that it can be coupled to an ideal-mixing continuum domain. However, many systems (e.g. electrolyte solutions) exhibit moderate to significant deviations from ideality. A simple first step to relaxing this assumption is to consider regular solutions, where the entropy of the solution is identical to the ideal case, but the fluid mixture includes an enthalpy of mixing. The existing SDPD model would require slight modification; the constant temperature assumption would have to be relaxed such that heat can flow between regions where the enthalpy results in different local temperatures. With both heat and mass transfer present, it may be necessary to allow for coupled heat/mass diffusion (e.g. thermophoresis and the Soret and Dufour effects), which is generally negligible for dilute gases, but important in many other situations [12].

Beyond small perturbations from ideality, these techniques are generalizable to problems that deviate significantly from the ideal case as well, and they have already been applied to phase-separating systems [13,14]. In general, constructing a GENERIC model that can be coupled to a MD region requires knowing the entropy $S(x)$ and total system energy $E(x)$ as a function of state variables x that represent the system (e.g. concentration or electrostatic potential). This is trivial for ideal and regular solutions, which feature simple

analytical forms for the entropy. The reversible and irreversible dynamics are proportional to the derivatives of the functions $S(x)$ and $E(x)$ with respect to the state variables x . For systems without analytical expressions for the entropy and energy, these functions can be determined numerically from equilibrium MD or Monte Carlo simulations. The resulting data from the molecular calculations can be tabulated or fit to a polynomial, then differentiated and used to build a GENERIC model. The downside of this approach is the computationally-intensive pre-calculation of the functions $S(x)$ and $E(x)$, which must be highly converged.

Despite these outstanding challenges, the multiscale multicomponent framework developed in this thesis is an important step towards a number of potential future directions and better understanding of numerous nanoscale phenomena, including nanobubbles. While there have been efforts to simulate “small” nanobubbles* using molecular dynamics [15–17], the work described in Chapters 3-6 allows for larger systems having more realistically-sized nanobubbles immersed in a fluid bath, which can be coarse-grained using our MD-continuum approach. A convenient aspect of the multiscale technique described in Chapter 5 is that the chemical potential of the bath (e.g. the continuum region far from the bubble) is easily and straightforwardly specified, giving precise control of the saturation level in the bulk fluid. Therefore it is now possible to investigate larger nanobubbles under a variety of conditions, including the solution saturation level and temperature, parameters that dramatically influence nanobubble morphology according to the analytical model in Chapter 2. The computational savings due to these multiscale methods would also allow for more realistic water and gas models, which have been absent in many MD nanobubble studies, though this

*MD simulations have probed nanobubbles with < 10 nm footprint radii in order to avoid the computational cost of larger systems, even though according to experiments, surface nanobubbles have micrometer diameters.

requires coupling molecules with internal degrees of freedom (i.e. atoms bound together with harmonic bonds) to the single-site SDPD fluid. The adaptive resolution scheme has already been applied to bridge molecules with internal features to isotropic coarse-grained models [18–22], and hence the only challenge is introducing the multicomponent aspect, where water and gas atoms transition to discrete SDPD particles with different masses, which must combine into continuous particles (and conversely, continuous SDPD particles must split into discrete ones with this mass discrepancy).

In addition to equilibrium simulations probing their stability with respect to thermodynamic variables such as the temperature and saturation, this modeling framework is also important for studying the dynamics of nanoscale bubbles and oil droplets dissolving under flow using non-equilibrium hybrid MD-continuum simulations. We demonstrated in Chapters 3-5 that our MD-SDPD framework is not only useful for coarse-graining bulk regions in equilibrium simulations, but also correctly captures the transport of momentum and solute across multiple length scales. Such non-equilibrium simulations of nanoscopic bubbles and drops can be achieved by placing a bubble or droplet along a surface in a MD region coupled to a continuum domain with gas- or oil-undersaturated fluid. The system is then subjected to shear flow, enabling the investigation of the dissolving bubble or drop dynamics. We can also consider the problem of nanobubble or nanodroplet nucleation by gradually increasing the fluid saturation under flow in a homogeneous system until a bubble or droplet nucleates along a pre-determined nucleation site in the substrate, and compare the simulation results to the scaling of theory and experiments of Zhang et al [23]. These studies would investigate the influence of flow conditions on nanodroplet/nanobubble nucleation/dissolution and effects such as stick-slip modes in nanodroplet growth.

Another important future extension of the model is the ability to model charged systems and electrolyte solutions. While in Chapter 5 we only discuss systems having neutral atoms interacting through dispersion and Pauli repulsion forces, the dissipative particle dynamics (DPD) algorithm has been generalized to include electrostatic interactions [24], and a similar approach could be straightforwardly integrated into the multiscale framework developed in this thesis. For the case of a dilute electrolyte solution with negligible correlations and mutual diffusion terms for the ionic species, the present methodology is straightforwardly extended by assigning an electrostatic potential variable to each SDPD particle and evolving these values by solving the Poisson equation at every time-step. The mass transport in the system is coupled to the electrostatics by replacing the discrete form of the diffusion equation with a discretized version of the Nernst-Planck equation. Similar to the DPD extension to charged systems described in Ref. [24], we have a flux due to the electrostatic potential gradient in addition to the flux given by Fick's first law and a stochastic one due to thermal fluctuations. One aspect that may be difficult and requires additional care is coupling the long-range electrostatic interactions in the MD region, which are typically treated using Ewald sums, to the electrostatic potential in the continuum part of the simulation. We note that similar adaptive resolution approaches have already interfaced charged MD fluids to coarse-grained ones, though these simulations use a reaction-field approach to treat the electrostatics, which is less sophisticated.

Once implemented, a first step for testing this "charged" MD-SDPD framework would be to use the MD-SDPD approach to reproduce electric double layer (i.e. the structure of an ionic solution next to an electrode) predictions from theory and simulation for a binary Lennard-Jones fluid with electrostatic interactions near a charged interface [25–28]. Using

the MD-SDPD method, we can simulate large systems while also including an explicit neutral solvent and accounting for the excluded volume of the solvent and ion molecules, which can dramatically affect the structure and ion distribution near surfaces [29]. These results can be compared to experiment [30–35] and classical density functional theory calculations [29,36]. Beyond charged surfaces in electrolyte solution, such a multiscale multicomponent framework for ionic systems is also applicable to numerous biological problems where the prevailing DLVO theory for describing the stability of aqueous suspensions is insufficient [37], including modeling of protein interactions [38] and transport of salt through cellular ion channels [39–41].

With further development, these techniques can be applied to more realistic water and salt models, as well as to design corrosion-resistant materials for the substrate, which is another important future direction for these multiscale techniques. Corrosion is inherently a problem having multiple spatiotemporal scales [42,43], with oxidation and nucleation of pits at the molecular level, transport of ions over larger scales, and bulk concentrations at the continuum level dictated by environmental conditions. The existence of these multiple scales has made corrosion process modeling difficult, even though it results in billions of dollars in damages every year in military ground, water, and air-based vehicles alone [44]. The number of available multiscale multicomponent methods in the literature is very limited at present, and hence the multi-species MD-continuum technique outlined in Chapter 5 is important for studying corrosion phenomena and other multiscale problems involving molecularly-miscible mixtures. With the simulation framework developed in this thesis, the dissolved ionic species can be included, giving atomistic detail near the interface where oxidation occurs, and a simpler description for the transport process further from the liquid-solid interface. The

continuum description can be coarsened with increasing separation from the surface, where the boundary condition at the interface is introduced through the atomically-resolved region.

Finally, the integrated boundary SDPD framework described in Chapter 6 paves the way for simulations of suspensions that are more rigorous than ones using current DPD models while having reduced computational cost. DPD has been used to probe the rheology of suspensions [45,46]; using SDPD integrated boundary techniques, it is possible to develop a parallelized code to investigate additional quantities in large systems, including the non-equilibrium structure and long-time dynamics of the colloids. Moreover, these techniques are useful for modeling many important systems, including the advection and diffusion of nano- and microparticles inside the human body, particle-membrane interactions [47–49], drug vehicle transport through membranes [50], and the margination of nanoparticles in intravascular drug delivery [51,52]. SDPD has been previously used to investigate this type of phenomena [52], though when simulating biological systems the simulation size is often problematic, and our approach allows for larger systems due to the reduced particle number.

One immediate future direction is to derive integrated boundary expressions for spheroidal particles, which can be used to approximate suspensions composed of rod-like colloids. In addition, the no-slip assumption may be relaxed to allow for a more general Navier-slip boundary condition. Beyond this generalization, it may also be possible to reconcile the SDPD integrated techniques for colloidal particles with the MD-continuum framework described in Chapters 3 through 5. One can imagine simulations where molecular resolution is used for a functionalized particle's surface, while a coarse-grained continuum description is applied to the surrounding fluid, with integrated boundaries used for other suspended particles in the bulk, or when the functionalized sphere is far from

surfaces/adjacent particles and does not require atomistic detail. As illustrated above with numerous examples, we believe that the general framework outlined in this thesis provides an important basis for an intuitive and efficient Lagrangian modeling strategy that allows for a broad spectrum of real-world applications and biological problems, and lays the foundation for investigating and understanding a variety of important physical systems.

7.3 References

- [1] Z. Wu, H. Chen, Y. Dong, H. Mao, J. Sun, S. Chen, V. S. J. Craig, and J. Hu, *J. Colloid Interface Sci.* **328**, 10 (2008).
- [2] F. Hui, B. Li, P. He, J. Hu, and Y. Fang, *Electrochem. Commun.* **11**, 639 (2009).
- [3] S. Darwich, K. Mougín, L. Vidal, E. Gnecco, and H. Haidara, *Nanoscale* **3**, 1211 (2011).
- [4] X. H. Zhang, A. Quinn, and W. A. Ducker, *Langmuir* **24**, 4756 (2008).
- [5] M. A. J. van Limbeek and J. R. T. Seddon, *Langmuir* **27**, 8694 (2011).
- [6] M. Tuckerman, B. J. Berne, and G. J. Martyna, *J. Chem. Phys.* **97**, 1990 (1992).
- [7] M. E. Tuckerman, B. J. Berne, and A. Rossi, *J. Chem. Phys.* **94**, 1465 (1991).
- [8] M. E. Tuckerman and B. J. Berne, *J. Chem. Phys.* **95**, 8362 (1991).
- [9] M. E. Tuckerman, B. J. Berne, and G. J. Martyna, *J. Chem. Phys.* **94**, 6811 (1991).
- [10] M. E. Tuckerman, B. J. Berne, and A. Rossi, *J. Chem. Phys.* **94**, 1465 (1991).
- [11] M. E. Tuckerman, G. J. Martyna, and B. J. Berne, *J. Chem. Phys.* **93**, 1287 (1990).
- [12] L. J. T. M. Kempers, *J. Chem. Phys.* **115**, 6330 (2001).
- [13] C. Thieulot, L. P. B. M. Janssen, and P. Español, *Phys. Rev. E* **72**, 16713 (2005).
- [14] C. Thieulot, L. P. B. M. Janssen, and P. Español, *Phys. Rev. E* **72**, 16714 (2005).
- [15] J. H. Weijss, J. H. Snoeijer, and D. Lohse, *Phys. Rev. Lett.* **108**, 104501 (2012).
- [16] Y. Liu and X. Zhang, *J. Chem. Phys.* **141**, 134702 (2014).
- [17] S. Maheshwari, M. van der Hoef, X. Zhang, and D. Lohse, *Langmuir* **32**, 11116 (2016).
- [18] M. Praprotnik, L. Delle Site, and K. Kremer, *J. Chem. Phys.* **123**, 224106 (2005).
- [19] M. Praprotnik, L. Delle Site, and K. Kremer, *Phys. Rev. E* **73**, 66701 (2006).

- [20] S. Poblete, M. Praprotnik, K. Kremer, and L. D. Site, *J. Chem. Phys.* **132**, 114101 (2010).
- [21] S. Matysiak, C. Clementi, M. Praprotnik, K. Kremer, and L. Delle Site, *J. Chem. Phys.* **128**, 24503 (2008).
- [22] S. Fritsch, S. Poblete, C. Junghans, G. Ciccotti, L. Delle Site, and K. Kremer, *Phys. Rev. Lett.* **108**, 170602 (2012).
- [23] X. Zhang, Z. Lu, H. Tan, L. Bao, Y. He, C. Sun, and D. Lohse, *Proc. Natl. Acad. Sci.* **112**, 9253 (2015).
- [24] M. Deng, Z. Li, O. Borodin, and G. E. Karniadakis, *J. Chem. Phys.* **145**, (2016).
- [25] M. V. Fedorov and A. A. Kornyshev, *J. Phys. Chem. B* **112**, 11868 (2008).
- [26] M. V. Fedorov and A. A. Kornyshev, *Electrochimica Acta* **53**, 6835 (2008).
- [27] B. Giera, N. Henson, E. M. Kober, T. M. Squires, and M. S. Shell, *Phys. Rev. E* **88**, 11301 (2013).
- [28] B. Giera, N. Henson, E. M. Kober, M. S. Shell, and T. M. Squires, *Langmuir* **31**, 3553 (2015).
- [29] M. E. Fleharty, F. van Swol, and D. N. Petsev, *Phys. Rev. Lett.* **116**, 48301 (2016).
- [30] T. F. Tadros and J. Lyklema, *J. Electroanal. Chem. Interfacial Electrochem.* **17**, 267 (1968).
- [31] J. N. Israelachvili and G. E. Adams, *J. Chem. Soc., Faraday Trans. 1* **74**, 975 (1978).
- [32] R. M. Pashley, *J. Colloid Interface Sci.* **80**, 153 (1981).
- [33] Y. H. Tsao, D. F. Evans, R. P. Rand, and V. A. Parsegian, *Langmuir* **9**, 233 (1993).
- [34] W. Kunz, P. Lo Nostro, and B. W. Ninham, *Curr. Opin. Colloid Interface Sci.* **9**, 1 (2004).

- [35] W. Kunz, J. Henle, and B. W. Ninham, *Curr. Opin. Colloid Interface Sci.* **9**, 19 (2004).
- [36] R. Vangara, D. C. R. Brown, F. van Swol, and D. N. Petsev, *J. Colloid Interface Sci.* **488**, 180 (2017).
- [37] M. Boström, D. R. M. Williams, and B. W. Ninham, *Phys. Rev. Lett.* **87**, 168103 (2001).
- [38] M. Lund, P. Jungwirth, and C. E. Woodward, *Phys. Rev. Lett.* **100**, 258105 (2008).
- [39] D. H. Mackay, P. H. Berens, K. R. Wilson, and A. T. Hagler, *Biophys. J.* **46**, 229 (1984).
- [40] S. W. Chiu, J. A. Novotny, and E. Jakobsson, *Biophys. J.* **64**, 98 (1993).
- [41] A. Skerra and J. Brickmann, *Biophys. J.* **51**, 969 (1987).
- [42] D. R. Gunasegaram, M. S. Venkatraman, and I. S. Cole, *Int. Mater. Rev.* **59**, 84 (2014).
- [43] I. S. Cole and A. E. Hughes, *Corros. Eng. Sci. Technol.* **49**, 109 (2014).
- [44] J. Waldman, *Rust: The Longest War*, Reprint edition (Simon & Schuster, New York, 2016).
- [45] E. S. Boek, P. V. Coveney, and H. N. W. Lekkerkerker, *J. Phys. Condens. Matter* **8**, 9509 (1996).
- [46] E. S. Boek, P. V. Coveney, H. N. W. Lekkerkerker, and P. van der Schoot, *Phys. Rev. E* **55**, 3124 (1997).
- [47] R. C. V. Lehn and A. Alexander-Katz, *Soft Matter* **7**, 11392 (2011).
- [48] R. C. V. Lehn, M. Ricci, P. H. J. Silva, P. Andreozzi, J. Reguera, K. Voitchovsky, F. Stellacci, and A. Alexander-Katz, *Nat. Commun.* **5**, 4482 (2014).
- [49] H. Ding and Y. Ma, *Small* **11**, 1055 (2015).
- [50] D. I. Kopelevich, *J. Chem. Phys.* **139**, 134906 (2013).

[51] P. Decuzzi, S. Lee, B. Bhushan, and M. Ferrari, *Ann. Biomed. Eng.* **33**, 179 (2005).

[52] K. Müller, D. A. Fedosov, and G. Gompper, *Sci. Rep.* **4**, (2014).